Shock-excited molecular hydrogen in the outflows of post-asymptotic giant branch stars

— **Kieran Patrick Forde** —

Centre for Astrophysics Research
Science and Technology Research Institute
— University of Hertfordshire —

Submitted to the University of Hertfordshire in partial fulfilment of the requirements of the degree of Ph.D.

Principal Supervisor: Dr Tim Gledhill

— July 2013 —

In memory of John Forde & Tess Brennan

"We are all in the gutter, but some of us are looking at the stars"

– Oscar Wilde

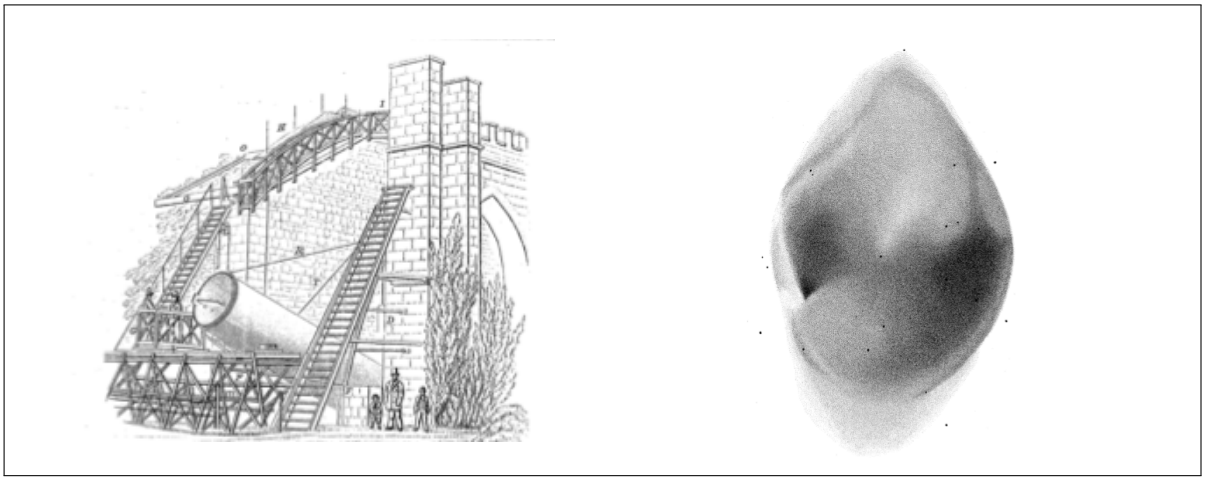

Fig. 1: (*left*) The Leviathan of Parsonstown, a 1.8 m reflecting telescope, was largest telescope in the world until 1917. It was built by William Parsons the 3rd Earl of Rosse on his estate, Birr Castle, Co. Offaly, Ireland. (*right*) A beautiful sketch of the Dumb-bell planetary nebula (M 27) as observed with the Leviathan. Images taken from: *'On the Construction of Specula of Six-Feet Aperture; and a Selection from the Observations of Nebulae Made with Them'*, Earl of Rosse, 1861.

Acknowledgements

First of all I must thank my primary supervisor Tim Gledhill who has guided me through this work and always pushed me back on track when I was getting distracted! I would also like to thank my second supervisor Michael Smith, who always had time to chat about results and provide explanations of shock physics. I am grateful to Martin Hardcastle for providing me with access to his parallel versions of the Markov Chain Monte Carlo fitting procedures. I would also like to thank John Atkinson who not only provided my IT support, but also became a good friend in the process.

There are so many members of staff that I need to thank in the department group, but I must start with Sean Ryan, Jim Hough, and Janet Drew, who interviewed me for a place in their department and since then have always been on hand to give help and advice. I would like to thank Ralf Napiwotzki who has examined my work each year throughout the process, Marc Sarzi for his running of the Bayfordbury open nights, and Elias Brinks who has always found time to chat with me about my work.

During my studies at Hertfordshire I have met some extremely smart, open and kind people, many of whom I have the privilege of calling friends. The first two people I need to mention are Roberto Raddi and Manuel Silva. From day one Roberto and Manuel have been my closest friends, always enthusiastic about astronomy, football, and women – not necessarily in that order! I am grateful to have had the opportunity to get to know: Joana, Doug, Carlos, Hywel, Simon, Federico, Lisette, Hugo, Zenghua, and James Canty.

There are equally many people outside of the university that I need to thank. I am thankful to have met some great friends, Oli, Jarred, Prev, and Antoine, while playing football on freezing cold winter mornings.

I was lucky to have the chance to get to know Jacquelin and Isabel and their daughter Cloé who have always been very kind to me.

I am grateful to my mother Carmel to whom I owe everything, she has single-handedly held our family together through some pretty tough times – an amazing woman. Of course my gratitude extends to my brother Brian, my uncle and aunt Joe and Eavon, and Cliona who at one time or another have helped me along my way. To my brother Sean, his wife Eva and their young sons John and Ruairí with whom I have spent many hours discussing topical TV programmes like Fireman Sam, Bob the Builder, and Elmo!

And finally I am indebted to my wonderful girlfriend Silvia, she has supported me along this journey. Meeting her during my studies is the most important thing that has happened to me, her kindness knows no limits and she inspires me to be a better person. Perhaps not surprisingly, her family Clemente, Ana, Esther, Joan and Laia have always made me feel welcome in their home.

I am extremely grateful to University of Hertfordshire for funding this research. This work has made use of the University of Hertfordshire Science and Technology Research Institute high-performance computing facility. I would also like to thank Krispian Lowe for observing some of the data presented in this work. Thanks to Wolfgang Steffan for help with the construction of a SHAPE model of *IRAS* 19500-1709, to Eric Lagadec providing Mid-IR VISIR images of *IRAS* 19500-1709, to Mikako Matsuura for providing information of the configuration of her ISAAC observations

of OH 231.8+4.2, and to Bruce Hrivnak for providing me with an electronic copy of his spectrum of *IRAS* 17150-3224. This research has made use of the SIMBAD database, operated at CDS, Strasbourg, France. This research has made use of NASA's Astrophysics Data System. Scanned records of early astronomical papers were provided courtesy of JSTOR. This research has made extensive use of IRAF which is distributed by the National Optical Astronomy Observatory, and is operated by the Association of Universities for Research in Astronomy (AURA) under cooperative agreement with the National Science Foundation. The STARLINK software suite was used in this research, specifically, the KAPPA, FIGARO, CONVERT, and GAIA packages.

Abstract

Since the identification of proto-planetary nebulae (PPNe) as transition objects between the asymptotic giant branch stars and planetary nebulae more than two decades ago, astronomers have attempted to characterise these exciting objects. Today many questions still elude a conclusive answer, partly due to the sheer diversity observed within this small subset of stellar objects, and partly due to the low numbers detected. Fortunately, many of these objects display a rich spectrum of emission/absorption lines that can be used as diagnostics for these nebulae.

This dissertation presents a study of six PPNe using the relatively new (at NIR wavelengths) integral field spectroscopy technique. This method has allowed the investigation of distinct regions of these nebulae, and in certain cases the application of magneto-hydrodynamic shock models to the data.

The goal of this research has been to investigate the evolution of PPNe by detailed examination of a small sample of objects consisting of a full range of evolutionary types. Near-IR ro-vibrational lines were employed as the primary tool to tackle this problem.

In all six sources the 1→0S(1) line is used to map the spatial extent of the H_2. In three of these objects the maps represent the first images of their H_2 emission nebulae. In the case of the earliest-type object (*IRAS* 14331-6435) in this sample, the line map gives the first image of its nebula at any wavelength. In the only M-type object (OH 231.8+4.2) in the sample, high-velocity H_2 is detected in discrete clumps along the edges of the bipolar outflow, while a possible ring of slower moving H_2 is found around the equatorial region. This is the first detection of H_2 in such a late-type object but due its peculiarities, it is possibly not representative of what is expected of M-type objects. In *IRAS* 19500-1709, an intermediate-type object, the line map shows the H_2 emission to originate in clumpy structures along the edges of a bipolar shell/outflow. The remaining three objects have all been the subject of previous studies but in each case new H_2 lines are detected in this work along with other emission lines (Mg II, Na I & CO). In the case of *IRAS* 16594-4656, MHD shock models have been used to determine the gas density and shock velocity.

Two new `python` modules/classes have been written. The first one to deal with the data cubes, extract flux measurements, rebin regions of interest, and produce line maps. The second class allows the easy calculation of many important parameters, for example, excitation temperatures, column density ratio values, extinction estimates from several line-pairs, column density values, and total mass of the H_2. The class also allows the production of input files for the shock fitting procedure, and simulated shocks for testing this fitting process.

A new framework to fit NIR shock models to data has been developed, employing Monte Carlo techniques and the extensive computing cluster at the University of Hertfordshire (UH). This method builds on the approach used by many other authors, with the added advantages that this framework provides a method of correctly sampling the shock model parameter space, and providing error estimates on the model fit. Using this approach, data from *IRAS* 16594-4656 have been successfully modelled using the shock models.

A full description of this class of stellar objects from such a small sample is not possible due to their diverse nature. Although H_2 was detected across the full spectral

range of post-AGB objects, the phase at which H_2 emission begins is still not clear. The only M-type object in this work is a peculiar object and may not be representative of a typical post-AGB star.

The H_2 PPNe appear to be located at lower Galactic latitudes ($b \pm 20^\circ$) than the total PPNe population, possibly pointing to an above average mass and hence younger age of these objects.

Contents

List of Figures

List of Tables

List of Equations

List of Symbols

A_λ	Extinction at wavelength, λ
$A_{\rm v}$	Visual Extinction
B	Magnetic Field Strength (G)
$E(B-V)$	Colour Excess
$M_\odot$	Solar Mass (1.989 x 10^{30} kg)
M_e	The Mass of the H envelope for AGB stars
M_{H_2}	Molecular Weight of Hydrogen (3.348 $\times$ 10^{27} kg)
$R_{\rm v}$	Ratio of Total-to-Selective Extinction
$T_{\rm rot}$	Rotational Temperature
$T_{\rm vib}$	Vibrational Temperature
$W_\lambda^{\rm abs}$	The Equivalent Width of the absorption feature at wavelength λ (Å)
$W_\lambda^{\rm em}$	The Equivalent Width of the emission feature at wavelength λ (Å)
W_λ	The Equivalent Width of the spectral feature at wavelength λ (Å)
ϵ	Filling Factor
λ	Wavelength
ϕ	Ortho-to-Para Ratio
σ	Stephan-Boltzmann Constant (5.67040 x 10^{-8} W m^{-2} K^{-4})
h	Planck's Constant (6.626068 x 10^{-34} m^2 kg s^{-1})
$n_{\rm H}$	Total Gas Density
$v_{\rm a}$	Alfvén Velocity
$v_{\rm s}$	Shock Velocity
Å	Angstrom (1.0 x 10^{-10} m)
c	Speed of Light (3.0 x 10^8 m s^{-1})
amu	Atomic Mass Unit (1.66054 x 10^{-27} kg)
AU	Astronomical Unit (1.496 x 10^{11} m)
g	Acceleration due to Gravity
Gyr	10^9 yr
$L_\odot$	Solar Luminosity (3.827 x 10^{26} W)
N_i	Upper Level Column Density
pc	parsec (3.086 x 10^{16} m)
R	Spectral Resolution

r'	Theoretical S/Q Line Ratio

Chapter 1: Post-AGB Stars

1.1 Introduction

The famous French astronomer Charles Messier in his *Catalogue des Nébuleuses & des amas d'Étoiles* [1] (Messier, 1781), lists 103 objects [2], each of which was given a Messier designation (e.g., M1 – the crab nebula). Messier was a dedicated comet hunter and it was during these nights observing the heavens with his colleague Pierre Méchain that he happened upon several diffuse objects that were fixed in position, i.e., they were not moving as expected of a comet. Messier classified these objects as either nebulae or star clusters. However, further advancements in technology showed that the catalogue contained quite a diverse list of objects – open clusters, globular clusters, Nebulae, a supernova remnant, and some planetary nebulae.

At that time, Messier did not have the equipment to further categorise these objects, although of M 57 he noted that it "resembles a planet which is fading". Nowadays M 57, commonly known as the *ring nebula*, belongs to a class of objects named *planetary nebulae* (PNe). Three more objects in the Messier catalogue also turned out to be planetary nebulae – M 27, M 76, and M 97. In spite of Messiers description of M 57, the name 'planetary nebula' is attributed to German-born British astronomer William Herschel. His paper *On the Construction of the Heavens* among other things classifies six objects as planetary nebulae, although he expresses some doubt as to their true nature (Herschel, 1785).

1.1.1 Planetary Nebulae

Messier described the PNe in his catalogue as being a "nebula without star", however it is now widely accepted that these spectacular nebulae must be powered by a hot central star. The definition of Kwok (2000) – "ionized circumstellar shells showing some degree of symmetry surrounding a hot, compact star evolving between the asymptotic giant branch and the white dwarf phases" – is a good working definition to adopt for these objects. An example of such an object is given in Figure 1.1 which shows a well-studied PN – the Helix nebula – at two distinct wavelengths. Although, many stars appear within the radius of the nebula they are either foreground or background stars. There is only a single star responsible for the expansion of the nebula – a white dwarf (WD) star. In the case of the Helix nebula the radius is approximately 200,000 AU – clearly a powerful source is required to influence the gas/dust at such distances. The central star of a PN is a hot star which can have temperatures typically of 50,000 K. The energetic photons radiated by the star will interact with the gas (specifically the elements present in the gas), exciting, dissociating or ionising it. The spatial distribution of the molecular hydrogen (H_2) in the Helix nebula, the result of internal excitation of the molecule, is apparent in Figure 1.1 (*left*); ionised gas is traced in Figure 1.1 (*right*).

As a result of these interactions the spectra of PNe are dominated by emission lines, with little continuum radiation contribution at near infrared wavelengths. These emission lines were first observed by Huggins & Miller (1864) in NGC 6543, who write that a

[1] Catalog of Nebulae and Star Clusters – A translation of the Messier Catalog is available at: http://messier.seds.org/xtra/history/m-cat81.html

[2] although, Messier 102 was reported incorrectly and was most likely a duplicate of Messier 101.

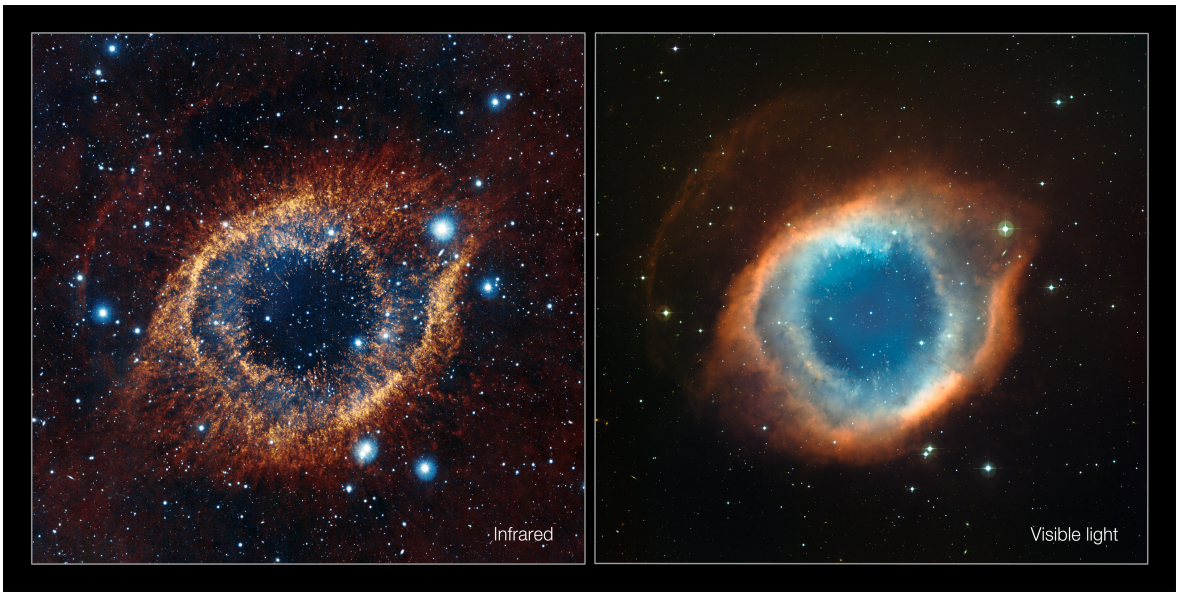

Fig. 1.1: These comparison images show two views of the famous Helix Nebula: 1) acquired with the VISTA telescope in infrared light (*left*) and 2) the more familiar view in visible light from the MPG/ESO 2.2-metre telescope (*right*). The infrared light image shows emission from clumps of dense cool molecular material, while the visible light image shows mainly ionised gas. Taken from/by: ESO/VISTA/J. Emerson. Acknowledgment: Cambridge Astronomical Survey Unit.

"derangement of the instrument" was suspected upon recording the spectrum, because of the peculiarity of the spectrum. But what process could make a spectrum appear so distinct to others? To answer this question it is important to know more about the on-going physical processes and evolutionary path followed by these spectacular objects.

The question of what preceded the PN phase was posed by Shklovsky (1957)[3], who suggested that PNe are formed from the evolution of a peculiar red giant star of high luminosity.

1.1.2 Post-AGB Stars

The missing link between the AGB and the PN stage of evolution started to become more clear with the advent of infrared (IR) technologies in the 1970's. Dust production during the AGB phase of evolution reddens the light from the star and in many cases can totally obscure the star (e.g., Figure 1.2[4]). The first candidates to display such characteristics were AFGL 2688 and AFGL 618. For example, Ney et al. (1975) describe IR, optical, and radio observations of the candidate object AFGL 2688, correctly estimating the spectral type and evolutionary stage.

At this evolutionary stage, a star will have stopped large-scale mass loss on the AGB and it will not have reached a sufficiently high temperature to ionise the surrounding circumstellar material. These stars are called *post-AGB* stars or *Proto-Planetary Nebulae* (PPNe)[5]. Post-AGB objects are statistically rare due to their short lifetimes (10^2

[3]references to an earlier paper (1956) can also be found in the literature.

[4]Images downloaded from `http://hubblesite.org/gallery/album/nebula/npp/all/`

[5]NOTE: post-AGB and PPN are sometimes used to describe the same objects however in this Thesis the former is used to represent the central star and the latter the nebulosity surrounding the central star

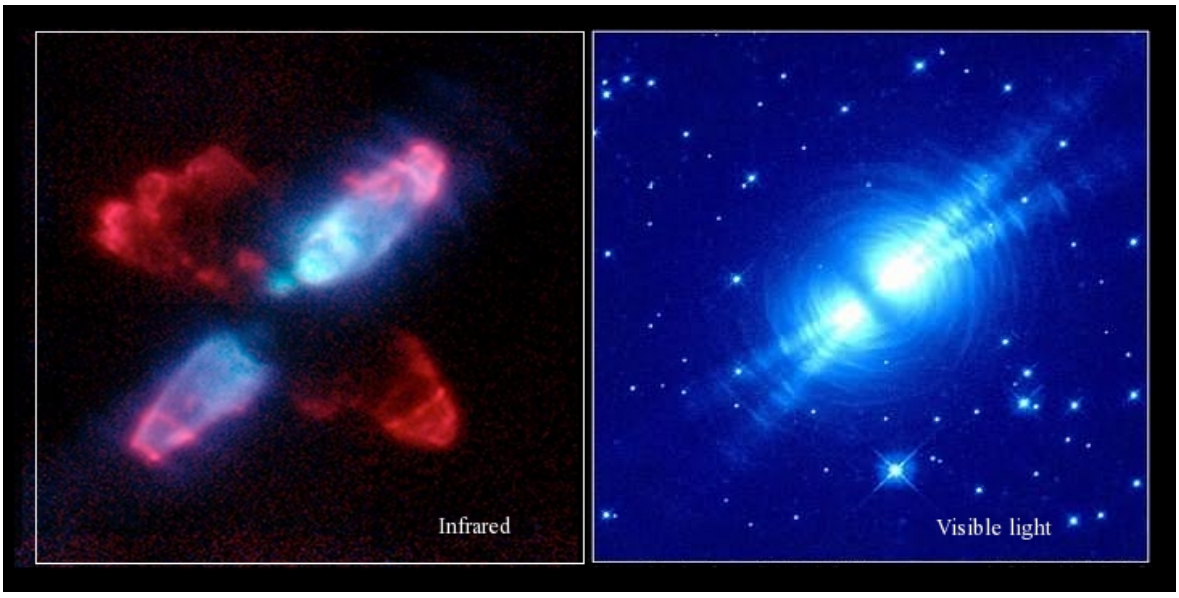

Fig. 1.2: (*left*) The egg nebula (AFGL 2688) observed in infrared light, regions of blue and red light delineate the scattered starlight and molecular hydrogen locations. Credit: Rodger Thompson, Marcia Rieke, Glenn Schneider, Dean Hines (University of Arizona); Raghvendra Sahai (Jet Propulsion Laboratory); NICMOS Instrument Definition Team, and NASA. (*right*) Visible light image of the egg nebula taken with the *Hubble Space Telescope (HST)*. Spectacular 'searchlight beams' and concentric arcs are separated by an optically thick central region. Credit: Raghvendra Sahai and John Trauger (JPL), the WFPC2 science team, and NASA.

$\rightarrow 10^5$ yrs), and are made up from a population of low- to intermediate-mass progenitor objects (0.8 $M_\odot \rightarrow 8\ M_\odot$). The above definition is theoretically correct, however further characteristics of these objects need to be defined in order to constrain the vast observational parameter space.

Luminosity - The position in the Hertzsprung-Russell (HR) diagram occupied by post-AGB objects during the transition from AGB star to becoming the central star of a PN, suggests that these stars fall between luminosity classes I $\rightarrow$ III. True luminosity values for post-AGB stars are not easily attainable due to uncertainties associated with the distance estimates to these objects. In the near future this matter should cease to be a problem with the launch of the Gaia mission. Accurate parallaxes will be obtained for all stars with a G-magnitude[6] < 20 (Perryman et al., 2001; Jordi et al., 2010).

Spectral type - Increasing stellar temperature with time is a characteristic of these transition objects. It follows that the spectral type should equally change during this phase. Assuming that O-type stars are hot enough to ionise the circumstellar material, there exists a range of spectral types corresponding to the evolutionary stage of a post-AGB star (M $\rightarrow$ B). Red giant branch and asymptotic giant branch stars can also be classified as either M-type or C-type, depending on the C/O ratio[7]. Inclusion of these objects when forming an evolutionary spectral-type sequence for post-AGB stars must be done with caution. However, many authors have investigated the correlation of the appearance of line emission within such a sequence (e.g., García-Hernández et al., 2002; Kelly & Hrivnak, 2005).

[6] a new filter passband for Gaia mission ($\lambda = 673$ nm)

[7] M-type $\rightarrow$ C/O < 1
C-type $\rightarrow$ C/O > 1

IR excess- The term *superwind* was first introduced by Renzini & Voli (1981). It refers to a dense wind created at the end of the AGB phase, essentially stripping the star of its surrounding envelope. This dense wind along with matter expelled on the AGB consists of dust and gas. This means that the usual RGB mass-loss rates, determined from the Reimers equation, cannot be used as it does not include the effects of dust formation or the sharp increase in mass loss on the AGB (Blöcker, 1995). Dust plays a vital role in mass loss as was demonstrated by several authors (e.g., Bowen, 1988; Bowen & Willson, 1991). The dense gas in the expanding envelope cools and a nucleation process occurs, whereby atoms group together collectively forming a dust grain at a nominal dust condensation temperature of $\sim$ 1400 K. Figure 1.3 shows the recent sub-mm (ALMA) imaging of the AGB star RSculptoris. This figure shows the material that has been ejected from the central star in spectacular detail, forming concentric shells of material around the star (note: RSculptoris is part a binary system and so this is not the classical single-star scenario).

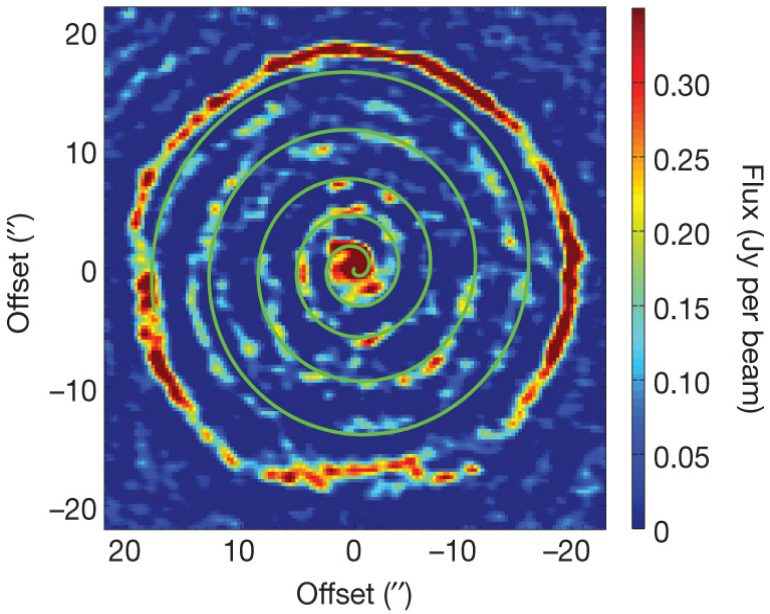

Fig. 1.3: A spectacular CO line image of the detached envelope of the AGB star RSculptoris. The observations of this star reveal the small clumpy structure present in the expanding envelope, forming a spiral pattern which is attributed to the influence of a binary. Image from Maercker et al. (2012).

The inclusion of dust in the treatment of mass loss on the AGB is vital. Radiation pressure on dust grains will drive the dust outward, which in-turn collides with expelled gas, transferring momentum to the gas – increasing the mass-loss rate. The dust cross-section is another important term that needs consideration, as the larger the cross-section the larger the mass-loss rate becomes. A dust-free model can still have significant mass loss (although still a fraction of the dust-driven model), via pressure gradients driving a slow wind (Bowen & Willson, 1991).

This envelope of dust and gas surrounds the star and can be detected as an infrared excess – a characteristic of post-AGB stars. As mentioned earlier, the use of infrared (IR) detectors meant that stars displaying such a property could be targeted by photometric surveys. The *infrared astronomical satellite (IRAS)* became a key tool in searching for objects surrounded by dust and hence emitting

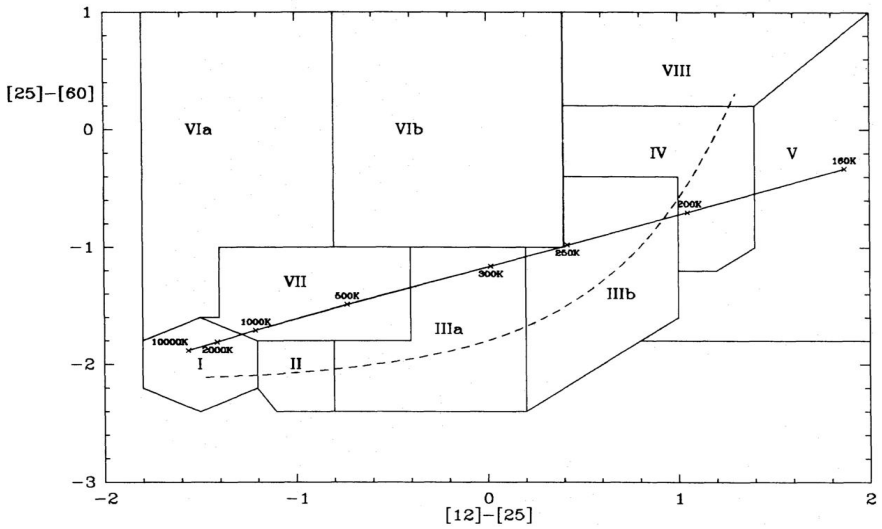

Fig. 1.4: The *IRAS* two-colour diagram demonstrating its usefulness as a classification tool for stellar objects. The regions/classes of objects are marked, with sources falling in region IIIb being pulsating stars, and PNe tend to appear in region V [figure taken from Van der Veen et al. (1989)].

light in the IR. Colour-colour diagrams constructed from the *IRAS* filters allowed the detection of large numbers of post-AGB objects (regions IV and V in Figure 1.4).

Examination of the spectral energy distribution (SED) of post-AGB stars revealed that it was double-peaked, with emission from the star peaking at shorter wavelengths and the dust emission peaking at long wavelengths. Using this to characterise post-AGB stars must be done with caution as heavily obscured stars might not display these peaks so obviously.

Molecular emission - The circumstellar envelope (CSE) surrounding a post-AGB star plays host to a rich variety of molecules. The type of molecules present is dependent on the chemistry of the AGB CSE remnant. A C-rich envelope (C/O ratio > 1) contains molecules like CO, HCN, C_2, and SiC; the 21 μm feature originally observed by Kwok et al. (1989) in post-AGB objects is also a characteristic of C-rich stars. In O-rich envelopes (C/O ratio < 1) SiO, H_2O, and OH masers are often observed; other molecules such as CO, CO_2, SO and SO_2 are some of the most numerous molecules present.

Of course, the molecule of most interest in this Thesis is that of hydrogen. Molecular hydrogen (H_2) is a good tracer of shocked gas in nebulae. Using emission line measurements it is possible to, among other things, determine the excitation mechanisms on-going in the nebulae. This molecule forms on dust grains and as discussed previously dust production is a characteristic property of AGB stars. It is still unclear why only $\sim 8\%$ of post-AGB stars exhibit H_2 emission; in many cases the nebulae can share many properties of H_2 emitting post-AGB stars (e.g., fast outflows, bipolar morphology, rich molecular envelope) and still not show shocked H_2.

Shaping of PNe & PPNe - Mass loss is a key characteristic of AGB stars. Mass-loss rates for typical AGB stars can be as high as 10^{-4} $M_\odot$ yr^{-1} or even higher. This level of mass loss cannot be sustained indefinitely and at the end of the AGB phase the mass-loss rate drops dramatically (10^{-8} $M_\odot$ yr^{-1}) while the wind speed

increases from $10 \rightarrow 10^3$ km s^{-1} (Kwok et al., 1978, and many others). Photons radiating from the central star accelerate dust particles and the gas outward. This leads to the CSE becoming detached from the central star as the star enters its post-AGB phase.

Early theoretical scenarios proposed that the detached CSE provided a simple explanation for the formation of PNe. However, PNe observations showed that their expansion velocities and densities were much higher than stellar wind speeds and envelope densities measured in AGB stars. Comparison of the sharp and diffuse boundaries of PNe shells and AGB envelopes, respectively, yielded further evidence that a more complex model of PNe formation was required. In response to these problems the Interacting Stellar Wind (ISW) model for PNe formation, was developed. In this model the detached CSE is accelerated, compressed, and shaped to form the PN — the central star rapidly evolves to higher temperatures and likewise its terminal velocity (related to escape velocity) increases driving a radiatively wind into the AGB remnant. This type of model gives the expected results for expansion velocity and PN mass given typical post-AGB input values but fails to reproduce all scenarios. The model was modified from a simple momentum-conserving model to incorporate energy-conservation to help account for the discrepancies. It is clear from this model that PNe need to be treated not as a static system but as a dynamical one where the evolution of the central star is highly linked to the nebula. As the models develop so does their complexity and they now include extreme bipolar shapes, circumstellar discs, accretion and even precessing jets (Mellema, 1995; Frank & Blackman, 2004). If all the wind components (e.g., fast wind) are isotropic then the resulting PN will be spherical in shape otherwise there will be an asymmetry introduced. Observations of PNe/PPNe show that this is normally not the case (see Figure 1.5). The cause of this asymmetry is still unclear but Kwok (2000) cite the following as possible culprits:

1. leftover protostellar disk from star formation,
2. equatorial density enhancements,
3. stellar rotation,
4. magnetic fields,
5. binary interaction

However, the interaction between the fast post-AGB wind and the axisymmetric AGB shell is largely observationally unexplored, so that models of PN shaping remain poorly constrained. For example, a protostellar disk is unlikely to survive the long main-sequence lifetime for a PN central star, or Soker (1998) states that it is unlikely the a magnetic field exists in AGB or post-AGB of sufficient strength to reproduce the asymmetries observed. The most appealing solution is the presence of a binary companion (de Marco, 2009), however observational evidence to support this is still lacking.

1.1.3 Becoming a post-AGB star

Figure 1.6 shows the evolutionary track for a 2 $M_\odot$ star of solar metallicity, represented by the red track. A star's evolution is strongly dependent on its initial mass (i.e., the

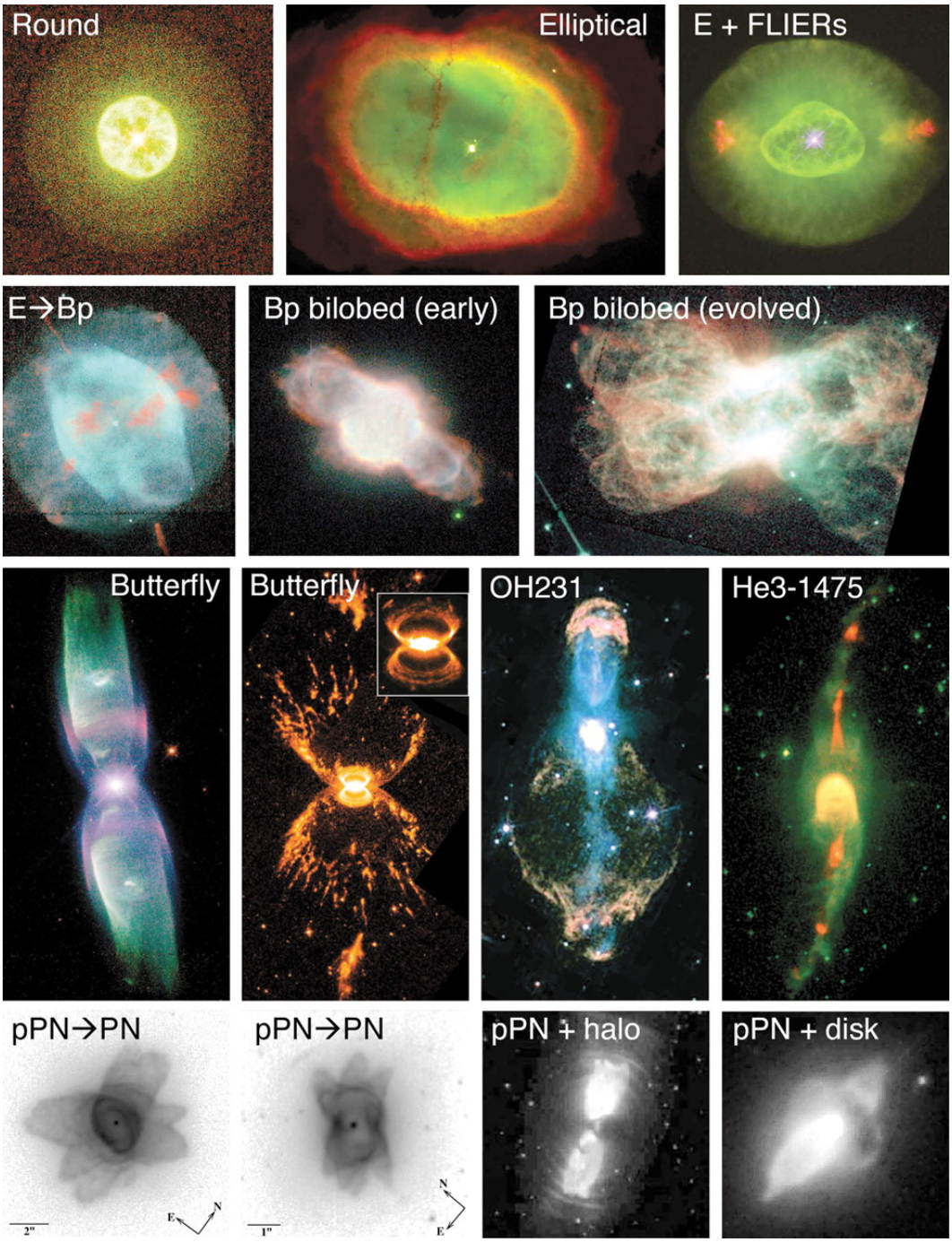

Fig. 1.5: illustrations of morphological types of PNe and PPNe. Red generally indicates regions of low ionisation (colours of NGC 3132 and OH231 have been altered for this purpose). See papers by author for details. (Top row) IC 3568 (Bond & NASA), NC 3132 (Sahai & NASA), NC 6826 with FLIERs in red (Balick & NASA); (Second row) NC 7354, NC 6886, and NC 7026 (all Hajian & NASA); (Third row) M2-9 (Balick & NASA), He2-104 (Corradi & NASA), OH231 (Bujarrabal & ESA), He3-1475 (Borkowski & NASA); (Bottom row) He2-47 (Sahai & NASA), He2-339 (Sahai & NASA), IRAS 17150-3224 (Kwok & NASA), IRAS 16594-4656 (Hrivnak & NASA). Image from Balick & Frank (2002).

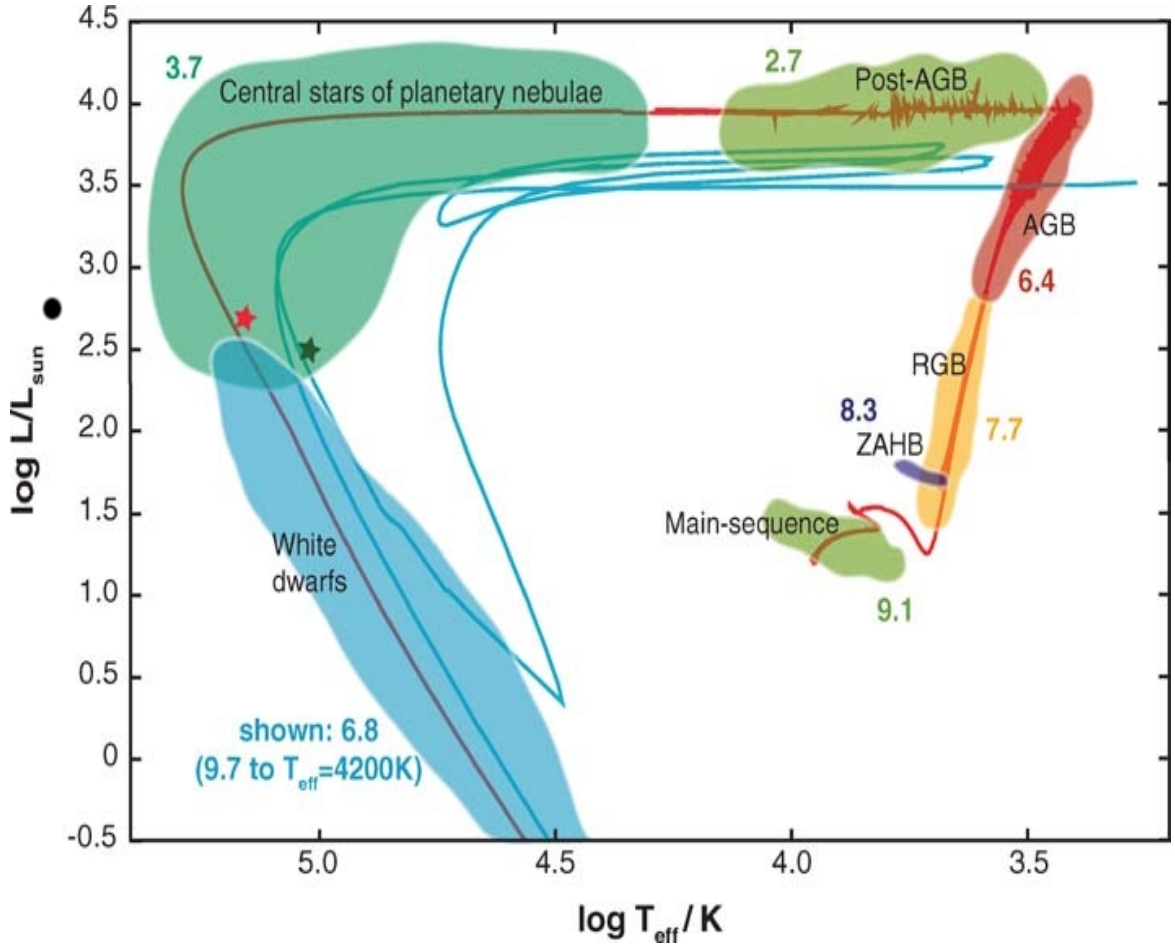

Fig. 1.6: Hertzsprung-Russell diagram of a 2 $M_\odot$ evolutionary track (red line) for solar metallicity covering the main sequence through the white dwarf phase (schematic credit: Herwig, 2005). The number labels adjacent to each evolutionary phase is the log of the time spent (in years) at that particular stage. The blue line indicates the evolution of the same mass star if there is a late thermal pulse to rejuvenate it (offset from the red track for clarity).

evolutionary timescale relies on mass); massive stars ($M_* > 10\ M_\odot$) tend to quickly run out of fuel and end their life in spectacular fashion — as supernovae; very low-mass stars ($M_* < 0.8\ M_\odot$) evolve very slowly, never initiating core He burning and so do not ascend the observable AGB (their MS lifetime is longer than the age of the universe); stars with a mass $< 8 - 9\ M_\odot$ will evolve to become post-AGB stars along the following route:

Main Sequence (MS) - Stars spend the majority of their lifetime as a main sequence object, with their position in the HR diagram dependent on their mass. At this stage they are fusing hydrogen to helium in their core via proton-proton (PP) chain reactions or the CNO cycle depending on their mass. The PP chain is most important for star of M = 1M$_\odot$ or less. The PP chain can be broken into three reactions:

$$\text{PP-I} \begin{cases} \mathrm{H}^1 + \mathrm{H}^1 \rightarrow \mathrm{H}^2 + e^+ + \nu \\ \mathrm{H}^2 + \mathrm{H}^1 \rightarrow \mathrm{He}^3 + \gamma \\ \mathrm{He}^3 + \mathrm{H}^3 \rightarrow \mathrm{He}^4 + 2\mathrm{H}^1 \end{cases} \tag{1.1}$$

PP-I is the most important of the three reactions while a star is on the main-

sequence, however there are two other PP reactions that can take place, given by:

$$\text{PP-II} \begin{cases} \mathrm{He}^3 + \mathrm{He}^4 \rightarrow \mathrm{Be}^7 + \gamma \\ \mathrm{Be}^7 + e^- \rightarrow \mathrm{Li}^7 + \nu \\ \mathrm{Li}^7 + \mathrm{H}^1 \rightarrow 2\mathrm{He}^4 \end{cases} \tag{1.2}$$

$$\text{PP-III} \begin{cases} \mathrm{He}^3 + \mathrm{He}^4 \rightarrow \mathrm{Be}^7 + \gamma \\ \mathrm{Be}^7 + \mathrm{H}^1 \rightarrow \mathrm{B}^8 + \gamma \\ \mathrm{B}^8 \rightarrow \mathrm{Be}^8 + e^+ + \nu \\ \mathrm{Be}^8 \rightarrow 2\mathrm{He}^4 \end{cases} \tag{1.3}$$

Some conditions must be satisfied for the CNO cycle to dominate energy generation in stars. Temperatures and masses must be higher than 2×10^7 K and 1.3 $\mathrm{M}_\odot$, respectively, in order to overcome the coulombic barriers of the carbon and nitrogen nuclei. Carbon must be present in the star to initiate the process, otherwise no matter the temperature the CNO cycle cannot operate. As with the PP chain, the net result of the CNO cycle is to convert hydrogen to helium, and is given by the reaction:

$$\text{CNO Cycle} \begin{cases} \mathrm{C}^{12} + \mathrm{H}^1 \rightarrow \mathrm{N}^{13} + \gamma \\ \mathrm{N}^{13} \rightarrow \mathrm{C}^{13} + e^+ + \nu \\ \mathrm{C}^{13} + \mathrm{H}^1 \rightarrow \mathrm{N}^{14} + \gamma \\ \mathrm{N}^{14} + \mathrm{H}^1 \rightarrow \mathrm{O}^{15} + \gamma \\ \mathrm{O}^{15} \rightarrow \mathrm{N}^{15} + e^+ + \nu \\ \mathrm{N}^{15} + \mathrm{H}^1 \rightarrow \mathrm{C}^{12} + \mathrm{He}^4 \end{cases} \tag{1.4}$$

In the above equations N^{13} and O^{15} both have a very short half-life, $T_{1/2} \sim$ 14 minutes and 82 seconds, respectively.

Red Giant Branch (RGB) - Upon exhaustion of the core hydrogen, the star contracts, raising the temperature and density to high enough limits to initiate hydrogen burning in a convective shell around the inert hydrogen-depleted core. This hydrogen shell burning will increase the thermal pressure inside the star and drive an expansion of the outer layers of the star – the luminosity of the star will increase.

Horizontal Branch (HB)/Clump phase - Helium burning is the source of fuel in the core of the star. The energy generation at this evolutionary point is given below and known as the triple alpha process. Two helium nuclei collide and fuse into the highly unstable beryllium nucleus. Collision by another helium nucleus is required for the reaction to continue forward and form carbon.

$$\text{Triple Alpha Process} \begin{cases} \mathrm{He}^4 + \mathrm{He}^4 \rightleftharpoons \mathrm{Be}^8 \\ \mathrm{Be}^8 + \mathrm{He}^4 \rightarrow \mathrm{C}^{12} + \gamma \end{cases} \tag{1.5}$$

A convective helium core develops and the star increases in temperature and

becomes blue and less luminous compare to the tip of the red giant branch. The star starts to move redward again once helium fuel in the core has been 'burnt' into carbon and oxygen.

Asymptotic Giant Branch (AGB) - Once it exhausts the helium in its core the star moves quickly off the HB and re-ascends the giant branch except this time on a bluer sequence of stars (AGB). This is a phase defined by hydrogen and helium burning in concentric shells, the interaction of these shells causes thermal pulses in the star's envelope. These are short phases of extreme energy generation after the helium shell has been ignited. Mass-loss is another characteristic of these stars — it is the beginning of the end for these stars with their lost mass being returned to the interstellar medium (ISM). Near the tip of the AGB the star experiences a high rate of mass loss, with solid material condensing out to form a dust-driven wind, leading to a high infrared luminosity.

Post-AGB - Evolution to this phase is signaled with the almost complete removal of the hydrogen envelope by mass loss — the star leaves the AGB and moves blueward in the HR diagram (i.e., $T_{\rm eff}$ increases). Stars in the correct mass range will reach this point, finally becoming the central stars of PNe if the star becomes hot enough ($T_* \sim 30{,}000$ K) to ionise the cast-off envelope prior to its dissipation.

1.2 Motivation

Despite much progress over the years on the topic of post-AGB objects, there remains several unanswered questions or at least the proposed answers are poorly constrained. For example, the shaping mechanism, the onset of fluorescence, the transition time between the end of the AGB and the beginning of the post-AGB phase, the onset of H_2 emission, and the role of tori/jets.

While the generalised interacting stellar wind model can explain the range of observed shapes of planetary nebulae, there is no agreement as to why the initially spherical circumstellar envelopes get distorted into a multitude of axisymmetrical structures. SINFONI integral field observations were proposed in order to perform a detailed high spatial and spectral resolution investigation of a sample of post-AGB objects of various spectral/evolutionary types. These observations will allow us to locate and differentiate shock and radiatively excited emission around these objects using a variety of modelling techniques including shock simulations.

The detection of H_2 line emission seems to depend on evolutionary phase. While many post-AGB stars with H_2 tend to be of a spectral stage earlier than A-type, there are instances where we detect H_2 emission in stars of a later spectral stage (CRL 2688 [F], IRAS 17150-3224[G], IRAS 17441-2411 [F] and many others). The implication of this, is that the mechanism for driving the onset of the observed H_2 emission and why/when it begins is unknown.

Our targets were selected from post-AGB objects with confirmed detections of molecular hydrogen emission, with two exceptions. Using these observations it was the hope to observe a total of seven post-AGB objects, of various evolutionary phases, available to investigate the types of excitation, its location and how it depends on evolutionary stage.

The goals of this work is to use H_2 as a diagnostic of excitation mechanisms in PPNe. A selection of post-AGB objects are studied spanning a range of spectral types,

and thus evolutionary types, to attempt to uncover the spectral type at which H_2 begins to emit. Magneto-hydrodynamic shock models are used to estimate various difficult to measure quantities (magnetic field strength, gas density, etc.).

1.3 Thesis Outline

Chapter 2: This chapter provides an introduction to the possible causes of H_2 emission in PPNe. Detailed derivation of equations to calculate various values using the measured line fluxes. A brief introduction to shock waves in an astronomical context and the relevant (magneto) hydrodynamic expressions. The shock models used throughout this work are also discussed here.

Chapter 3: This Chapter begins with a summary of the telescope and instrument used for this work. Next the reduction of the data and the analysis tools used are summarised. And finally, I discuss the Monte Carlo fitting technique adopted to match the observed line values to the model predictions.

Chapter 4: In this Chapter the discovery of molecular hydrogen in the outflows of the M-type star OH 231.8+4.2 is discussed. In two out of the three fields observed H_2 is detected, with the possibility that the emission is due to two different types of shock events.

Chapter 5: A detailed study of the B-type post-AGB star *IRAS* 16594-4656 is carried out. With the high number of high signal-to-noise lines available in this object, it is possible to employ a new Monte Carlo fitting technique for the shock models.

Chapter 6: The results of IFU observations of the four remaining PPNe objects in my dataset are presented, with a brief review of the relevant literature in each case.

Chapter 7: In this chapter I discuss the results obtained in this work in a broader context. Finally, the main conclusions are summarised.

Appendix A: Useful Programs

Appendix B: Useful figures or tables, from other papers, referenced in this Thesis.

References

Balick, B. & Frank, A. 2002, ARA&A, 40, 439

Blöcker, T. 1995, A&A, 299, 755

Bowen, G. H. 1988, ApJ, 329, 299

Bowen, G. H. & Willson, L. A. 1991, ApJ, 375, L53

de Marco, O. 2009, PASP, 121, 316

Frank, A. & Blackman, E. G. 2004, ApJ, 614, 737

García-Hernández, D. A., Manchado, A., García-Lario, P., Domínguez-Tagle, C., Conway, G. M., & Prada, F. 2002, A&A, 387, 955

Herschel, W. 1785, Royal Society of London Philosophical Transactions Series I, 75, 213

Herwig, F. 2005, ARA&A, 43, 435

Huggins, W. & Miller, W. A. 1864, Royal Society of London Philosophical Transactions Series I, 154, 437

Jordi, C., Gebran, M., Carrasco, J. M., de Bruijne, J., Voss, H., Fabricius, C., Knude, J., Vallenari, A., Kohley, R., & Mora, A. 2010, A&A, 523, A48

Kelly, D. M. & Hrivnak, B. J. 2005, ApJ, 629, 1040

Kwok, S. 2000, The Origin and Evolution of Planetary Nebulae (The origin and evolution of planetary nebulae / Sun Kwok. Cambridge ; New York : Cambridge University Press, 2000. (Cambridge astrophysics series ; 33))

Kwok, S., Purton, C. R., & Fitzgerald, P. M. 1978, ApJ, 219, L125

Kwok, S., Volk, K. M., & Hrivnak, B. J. 1989, ApJ, 345, L51

Maercker, M., Mohamed, S., Vlemmings, W. H. T., Ramstedt, S., Groenewegen, M. A. T., Humphreys, E., Kerschbaum, F., Lindqvist, M., Olofsson, H., Paladini, C., Wittkowski, M., de Gregorio-Monsalvo, I., & Nyman, L.-A. 2012, Nature, 490, 232

Mellema, G. 1995, MNRAS, 277, 173

Messier, C. 1781, Catalogue des Nébuleuses & des amas d'Étoiles (Catalog of Nebulae and Star Clusters), Tech. rep.

Ney, E. P., Merrill, K. M., Becklin, E. E., Neugebauer, G., & Wynn-Williams, C. G. 1975, ApJ, 198, L129

Perryman, M. A. C., de Boer, K. S., Gilmore, G., Høg, E., Lattanzi, M. G., Lindegren, L., Luri, X., Mignard, F., Pace, O., & de Zeeuw, P. T. 2001, A&A, 369, 339

Renzini, A. & Voli, M. 1981, A&A, 94, 175

Shklovsky, I. S. 1957, in IAU Symposium, Vol. 3, Non-stable stars, ed. G. H. Herbig, 83

Soker, N. 1998, MNRAS, 299, 562

Van der Veen, W. E. C. J., Habing, H. J., & Geballe, T. R. 1989, A&A, 226, 108

Chapter 2: H_2 & Shock Waves

2.1 Introduction

Molecular hydrogen (H_2) is the most abundant molecule in the universe, and so it is no surprise that it has been used to investigate a range of astrophysical objects/processes (star-forming regions, PNe, post-AGB stars, gas content of galaxies, etc.). H_2 is considered a stable molecule at low temperatures and so it was not expected to be detected in PNe — the high energy photons of their hot central star ($T_* \geq 25{,}000$ K) would dissociate the H_2. However, molecular envelopes have been detected around several PNe (for example Bieging et al., 1991, map the PN NGC 7027 in CO). By combining data from several wavelength ranges it is possible to build up a picture of the molecular envelopes that make up PNe — in general, a set of concentric shells exists: a CO-shell, furthest from the central star, encompasses a smaller H_2 shell and a HI region, which in turn surrounds a HII region. Post-AGB stars should, as progenitors of PNe and hence having lower temperatures, possess similar molecular envelopes, for example García-Hernández et al. (2002) report 13 confirmed H_2 detections in post-AGB stars. The spatial locations of the near-IR (NIR) rotational-vibrational lines of H_2 have only become easily observable since the advent of efficient large-scale IR detectors. The K-band contains many of these H_2 lines (S- and Q-branch) and as such is a useful passband to use for investigating H_2 emission.

These ro-vibrational lines of H_2 only become detectable where there is an exciting source causing the radiation. This can be from energetic UV-photons, high-energy electrons from an X-ray source, or from collisions from the interaction with a shock wave. UV excitation of H_2 is observed in post-AGB stars of early spectral type and in early PNe, however this required the central star to have $T_* > 15{,}000$ K. H_2 is readily observed in the nebulae around late-type post-AGB stars, the excitation driven by the passage of shock waves. Briefly, when a shock wave interacts with H_2 gas, it heats, compresses and accelerates, exciting the ro-vibrational degrees of freedom in the molecules; cooling via radiative decay from these excited states gives rise to the shocked H_2 NIR emission.

This Chapter will review the structure, and transitions of H_2, discuss the uses of ro-vibrational lines as diagnostic tools for studying post-AGB objects, and derive useful formulae for converting observed flux values into physical quantities. Finally, a brief introduction to shock waves is given and how shock models can produce line estimates for H_2.

2.2 Molecular Hydrogen

Hydrogen in its atomic state (HI) consists of a single positively charged particle (proton) and a single negatively charged particle (electron). In its ground state the electron occupies the lowest energy level available to it, however it can be excited to higher energy levels. There are several mechanisms for pumping these electrons to higher quantum levels (e.g. UV photons, collisions). After a certain length of time these electrons will de-excite back to lower energy levels emitting a photon at a specific frequency, ν, during the transition. An atoms configuration at any point in time is given by (1) n, its principal quantum number (where n = 1$\rightarrow \infty$), (2) ℓ, its orbital quantum number

(where $\ell = 0, 1, 2 ...$ represented by s, p, d ....) and, (3) s, its spin quantum number (where $s = \pm \frac{1}{2}$). Thus, the ground state of atomic hydrogen is $1s^1$.

The formation of molecular hydrogen in the ISM can follow two possible paths: (1) the physisorbed mechanism ($T < 100$ K), and (2) the chemisorbed mechanism ($T > 100$ K), as described in Cazaux & Tielens (2002). Both mechanisms, which depend on temperature, require the presence of dust grains as a catalyst to provide the HI with a place to combine with another hydrogen atom. The newly formed H_2 is then ejected from the grain surface into the ISM. In order to build up any substantial amount of H_2 in the ISM, there must be protection from high energy photons (≥ 4.48 eV) which would dissociate the H_2. Self- and dust-shielding provide such protection — using H_2 on the outer edge of the H_2 region and the dust in the intervening space.

Not only is H_2 a diatomic molecule (consisting of two atoms), it is also a homo-nuclear molecule (formed from identical nuclei). In a similar fashion to the electronic configuration of atomic hydrogen, the quantum state of H_2 can be described by (1) 2S+1, the spin multiplicity, (2) Λ, the total orbital angular momentum, and (3) Ω, the projection of the total electronic angular momentum onto the internuclear axis. There is a further designation, Σ, used for cases where $\Lambda = 0$. In this case, if the electron wave function changes sign upon reflection through any plane, Σ becomes Σ^-; if there is no change in sign Σ becomes Σ^+. Also, each electronic state is preceded by a letter in order to distinguish energy levels, where X represents the ground electronic state and the uppercase letters A,B,C,D ... represent levels with identical spin multiplicity as the ground state and the lowercase letters a,b,c,d ... indicate levels with different spin multiplicity than the ground state. For example, the ground configuration of H_2 is $X^1\Sigma_g^+$.

2.2.1 Ro-Vibrational Transitions

Atomic line radiation occurs when energy is released (at a certain frequency, ν) as an electron decays to a lower energy level from its excited state. Molecular line transitions can be more complex in two important ways:

- there is no longer a single centre of mass for the electrons to orbit
- the nuclei themselves move and give rise to rotational and/or vibrational motions of the atoms

However, through use of the Born-Oppenheimer approximation it is possible to deal with the electronic and nuclear wave functions individually. This means that the total wave function, $\psi_{\rm tot}$, can be represented by Equation 2.1

$$\begin{aligned} \psi_{\rm tot} &= \psi_{\rm el}\psi_{\rm nuc} \\ &= \psi_{\rm el}\psi_{\rm vib}\psi_{\rm rot} \end{aligned} \tag{2.1}$$

where $\psi_{\rm el}$, $\psi_{\rm vib}$, $\psi_{\rm rot}$ are the electronic, vibrational, and rotational wave functions, respectively. Typically, electronic transitions have energies of a few eV and are observed in the UV/visible part of the spectrum. The IR and cm/mm regimes host the vibrational and rotational transitions as they tend to have lower energies (0.1 - 0.0001 eV).

A molecule must be polar to be able to allow electronic dipole transitions. H_2 is a homo-nuclear molecule and as such, has no permanent electronic dipole moment.

This means that 'pure' electronic transitions are forbidden for H_2. However, there are permitted electronic quadrupole transitions available within H_2 — labelled O-, Q-, S-branch transitions corresponding to the change in rotational quantum number, ΔJ, of -2, 0, 2, respectively. Changes in vibrational quantum number, $\Delta\nu$, on the other hand, are unrestricted for these transitions. Other P- and R-branches can occur but not for H_2 as they obey a selection rule of $\Delta J = \pm 1$. Figure 2.1 shows the energy levels and important transitions of the H_2 molecule; in this case, the transitions shown are the main ones expected in a post-AGB object showing evidence for shock and/or fluorescent excitation (see Table B.2 in Appendix B for a list of H_2 lines, and associated values, in the K-band).

2.2.2 Emission Lines

Emission lines in nebular environments of PPNe are due to a spontaneous emission of a photon, whose rate is given by the Einstein coefficient (A_{ji}) or a collision, which depends on the collisional rate coefficient (κ_{ji}), of an atom with another particle. Lines formed from collisional bound-bound transitions occur when a bound electron within an atom moves from a higher to a lower excitation state; the ro-vibrational transitions of H_2 are a form of a bound-bound transition. The Brγ emission line is formed via a different mechanism – a free-bound transition. In this case a free electron recombines with a proton causing the atom to cascade to a lower energy level ($7 \rightarrow 4$)[1] emitting a photon. At high densities where the value is greater than a critical density the probability of observing emission from a spontaneous decay decreases, conversely the probability of observing collisionally excited lines increases. At these high densities the gas can be represented by a single temperature ($T_{\rm ex}$) and the gas is described as being in local thermodynamic equilibrium (LTE). Elastic collisions between particles under these conditions allow the particle velocity distribution to be described by the Maxwell-Boltzmann distribution function

$$n_\nu d\nu = n\left(\frac{m}{2\pi kT}\right)^{3/2} e^{\frac{-m\nu^2}{2kT}} 4\pi\nu^2 d\nu \tag{2.2}$$

where n_ν is the total number of particles per unit volume with velocity between ν and $\nu + {\rm d}\nu$. The exponent of the Maxwell-Boltzmann distribution shows that the distribution is at a maximum when the thermal energy, kT, is equal to the kinetic energy of the particles, $\frac{1}{2}m\nu^2$. This is the most likely scenario for a gas in LTE where all the thermodynamic properties (velocity distribution, excitation, ionisation) have thermodynamic equilibrium values and can be described by a single temperature ($T_{\rm ex}$). For such a gas the Boltzmann Equation gives the ratio of the number of atoms at a certain energy level (n_j) with energy (E_j) to the number/energy of atoms at a lower energy level (n_i, E_i).

$$\frac{n_j}{n_i} = \frac{g_j e^{\frac{-E_j}{kT}}}{g_i e^{\frac{-E_i}{kT}}} = \frac{g_j}{g_i} e^{\frac{(E_j - E_i)}{kT_{\rm ex}}} \tag{2.3}$$

in this case $T_{\rm ex}$ is the kinetic temperature of the electrons which is equivalent to the excitation temperature of the gas in LTE. At lower densities this expression does not remain true, in which case the level populations must be determined using a non-LTE

[1]The Brackett line series arises from transitions whose final energy level is n=4.

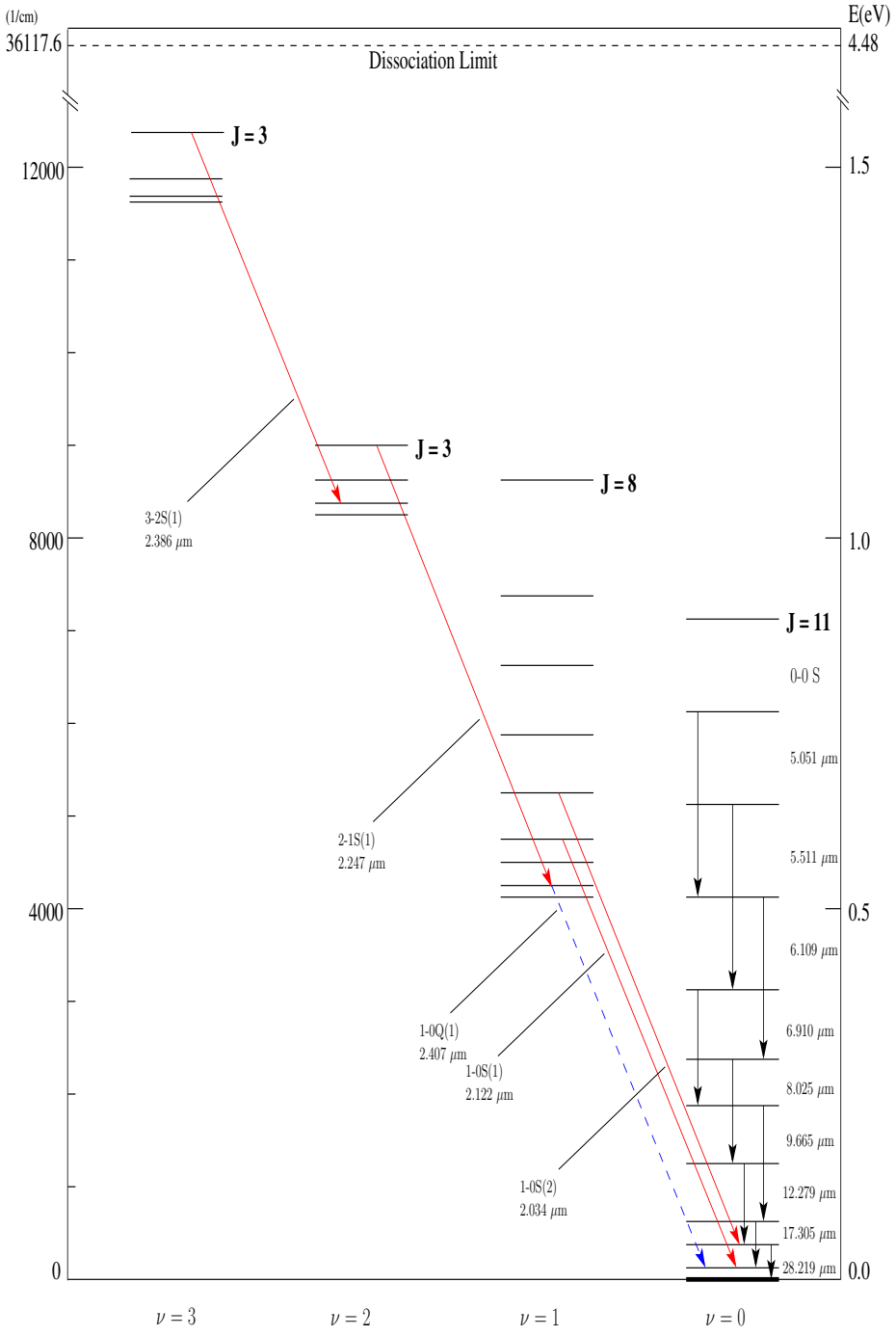

Fig. 2.1: The ro-vibrational energy level diagram for the H_2 molecule, showing some of the transitions, visible within the SINFONI wavelength range, observed in some PPNe/PNe. The S- and Q-branch ro-vibrational transitions are given by the red (solid) and blue (dashed) lines, respectively. The black (solid) lines show some of the 0-0 rotational transitions for H_2. This plot is based on the energy diagram presented in Kwok (2007)[p.62], and was also used in my Masters Thesis. Note: only a selection of levels are shown here for simplicity.

approach. To approximate non-LTE level populations it is possible to 'scale' the LTE solution for each energy level; this is the method used in the shock models to estimate non-LTE conditions.

2.2.3 Collisional Excitation

For some of the PPNe in this work the temperature of the central star is not high enough to contribute photons with enough energy to excite the H_2 lines observed in the gas. In these cases the H_2 is being excited via collisional processes such as shocks. Figure 2.2 shows the excitation/de-excitation rate coefficients (C_{ij}, C_{ji}) between two energy levels.

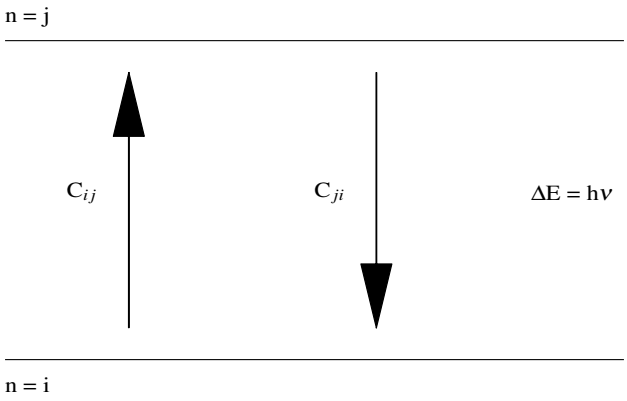

Fig. 2.2: A simple two level model, where collisions will excite electrons from level i to j depending on a rate coefficient C_{ij} and likewise will decay at a rate determined by the rate coefficient C_{ji}.

For a system in LTE the rate of excitation is balanced by the rate of de-excitation (Equation 2.4).

$$n_i n_e C_{ij} = n_j n_e C_{ji} \tag{2.4}$$

where n_e is the electron density and knowledge of the collisional excitation rate coefficient (C_{ij}) for a gas with an electron kinetic temperature (T_e) is gained by averaging the Maxwellian distribution (e.g., see Equation 3.28 in Kwok, 2007). This equation holds true if radiation plays a negligible role in the excitation of the gas – as is the case for late-type PPNe. Using the fact that

$$\frac{C_{ji}}{C_{ij}} = \frac{n_i}{n_j} \tag{2.5}$$

it is straightforward to show that for collisional excitation the level populations are given by

$$\frac{n_j}{n_i} = \frac{g_j}{g_i}\left[\frac{1}{1+\dfrac{n_{\rm crit}}{n_e}}\right] e^{\frac{(E_j-E_i)}{kT_{\rm ex}}} \tag{2.6}$$

where $n_{\rm crit}$ is the critical density given by the ratio of the spontaneous Einstein emission coefficient (A_{ji}) to the collisional de-excitation rate coefficient (C_{ji}). If $n_e \gg n_{\rm crit}$

then Equation 2.6 reverts to the Boltzmann equation, but if $n_e < n_{\rm crit}$ the fractions of atoms in the excited state is less than its LTE value by a factor of $n_e/n_{\rm crit}$.

2.2.4 UV Excitation

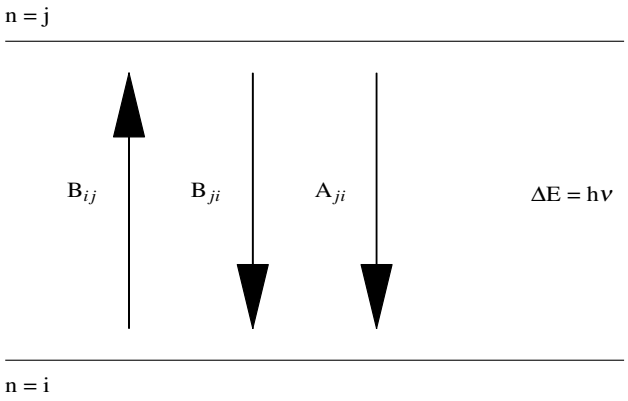

Fig. 2.3: A simple two level model, where UV radiation will excite electrons from level i to j depending on a stimulated absorption Einstein coefficient B_{ij} and likewise will decay at a rate determined by the stimulated emission coefficient B_{ji}; spontaneous emission rate is given by the A_{ji} coefficient.

Figure 2.3 shows the relevant coefficients related to gas that is excited via radiative means. UV-excited H_2 was first detected in a reflection nebula by Gatley et al. (1987) in a thin shell around the B1 star HD 37903. H_2 absorbs photons with energies in the range 11 – 13.6 eV, decaying back to ground level via the rotational-vibrational ladder, emitting NIR photons. In the K-band, observing the Brγ line in PPNe is a signature for the onset of fluorescent excitation – free-bound transitions require a free electron to recombine with an ion.

When UV photons cause excitation of molecular gas to higher energy levels, this causes the upper vibrational levels to become populated resulting in large line fluxes for these levels. Collisional excitation tends to populate the lower vibrational levels. Thus, by comparing the line strengths of higher and lower vibrational states it is possible to uncover the dominant excitation mechanism. Burton et al. (1990) note that above densities of $\sim 10^5$ cm^{-3}, the line ratios will resemble those expected for a gas in local thermal equilibrium (LTE); this means that gas density must be taken into account when using line ratios to determine the excitation mechanism. So for low density gas, the 1→0/2→1S(1) line ratio can be used as an indicator of shock or fluorescent excitation; pure fluorescence gives a value of ~ 1.8 while a value closer to $\sim$ 10–20 indicates the excitation of the gas is being driven by shocks (Hollenbach & Natta, 1995). Other useful K-band line ratios are (a) the 1→0S(1)/3→2S(3), and (b) the 1→0S(1)/Brγ. In the case of (a), it can also be used to distinguish between shock and fluorescence excitation and (b) has been linked to the evolutionary stage and morphology of bipolar PNe. Guerrero et al. (2000), in a study of 13 bipolar PNe, note that the strength of the 1→0S(1) and the 1→0S(1)/Brγ ratio are found to change with morphology; PNe exhibiting broad ring (Br) structure tend to have a higher 1→0S(1)/Brγ flux ratio than compact core (B) PNe. They consider that these two bipolar sub-classes (B & Br) are similar objects at different evolutionary stages as a

possible explanation for the 1→0S(1)/Brγ ratio correlation with morphology, provided their molecular envelopes are low density ($\leq 10^4$ cm^{-3}).

2.3 Spatial Mapping of H_2 in PPNe

The K-band hosts a multitude of strong H_2 emission lines. As explained in Section 2.2.1, these spectral features are caused by ro-vibrational transitions within the H_2 molecule. Determination of the underlying excitation mechanism is possible by the use of the measured line fluxes. Previously, studies of post-AGB objects have used longslit spectroscopy coupled with NIR imaging to determine the source of the H_2 emissions, however this approach is inefficient (in terms of telescope time). Through the use of IFUs both spatial and spectral information can be recorded, yielding a spectrum for each pixel.

2.3.1 Line Maps

Integral Field Spectroscopy (IFS) records the spectral information for each 'spaxel' on the detector, as explained in Chapter 3. For a data cube consisting of $N_{x,y,\lambda}$ elements, a map of emission features can be built up by (1) selecting an initial wavelength estimate for a particular line (e.g., $\lambda = 2.1218$ μm), and (2) stepping through the data cube in the spatial directions, and fitting the spectral line with a Gaussian profile to determine the integrated line flux for the emission line. Figure 2.4 shows a sample image of a fitted emission line map for the H_2 1→0S(1) transition.

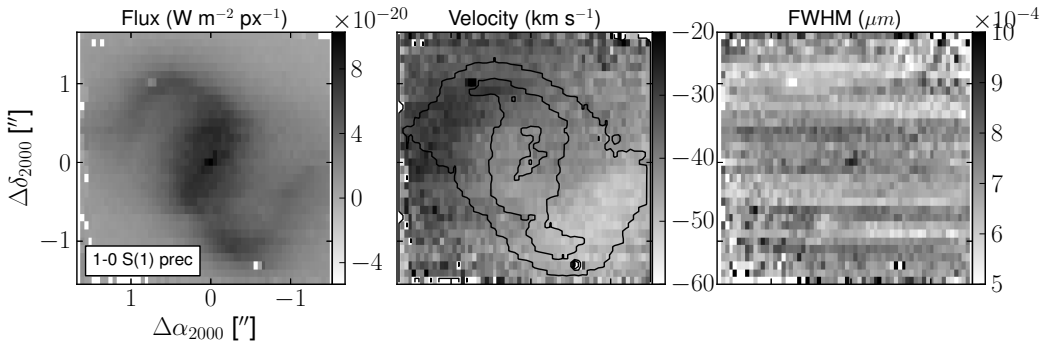

Fig. 2.4: An example of the types of line fitting maps generated using the process described in Section 3.4. In this case, the H_2 1→0S(1) transition is mapped for *IRAS* 14331-6435. *(left)* A map of the location of H_2 emission. *(middle)* Contours are overlaid on the velocity map to show the location of the strongest H_2 emission. *(right)* A map of the FWHM of the H_2 emission line. Coordinates: offset in arcseconds from central star location. Orientation: North is up, East is left.

2.3.2 Line Ratio Maps

The line maps, as discussed in the previous Section, provide a useful tool for determining the location and flux of particular emission lines. However, line maps alone do not directly provide information on the underlying physical processes driving the molecular excitation.

Once line maps have been constructed for the observed emission lines, through the process discussed in Section 2.3.1, line ratio maps can be created for the ratios discussed above. Another advantage of IFS is that the variation in ratio values can be seen across the entire Field-Of-View (FOV), provided the S/N in the weakest line is sufficient.

2.4 Extinction

The signal from astronomical sources suffers from attenuation due to the presence of dust grains along the line-of-sight. The term used to describe this attenuation is extinction, A_λ, and it consists of two processes (1) absorption, and (2) scattering. The degree of extinction is dependent on the wavelength, density, and type of dust in the intervening space.

The colour excess or reddening, $E(B-V)$, that causes an object's colour to appear to be 'redder' than it should be in the absence of dust, is caused by the difference in the level of extinction at two different wavelengths or in two different filter passbands. Thus, the reddening of an object is given by

$$E(B-V) = A_\mathrm{B} - A_\mathrm{V} \tag{2.7}$$

where A_V and A_B is the extinction value (in magnitude) in the visible and blue passbands[2], respectively. The relationship between the extinction and the reddening is given by

$$R_\mathrm{V} = \frac{A_\mathrm{V}}{E(B-V)} \tag{2.8}$$

where R_V is the ratio of total-to-selective extinction. The usual value used for R is 3.1 for the ISM as determined from observations (Cardelli et al., 1989), provided there is no over-density of gas/dust along the line-of-sight. It is possible to determine the value of extinction in any passband/wavelength using a simple empirical relation and the appropriate coefficients for that passband/wavelength (see Equations 1, 3a, and 3b in Cardelli et al., 1989), assuming we know A_V.

The comparison of certain H_2 emission lines has been used in several studies to estimate an extinction value in the direction of a source (Geballe et al., 1982; Davis et al., 2003; O'Connell et al., 2005). For the K-band, the S- and Q-branch lines are convenient for this. However, it is worth noting that, at NIR wavelengths (0.9 – 5 μm), emission line observations are hampered by strong telluric features (see Figure 3.6). These absorption features are highly variable, and so removal can cause errors in an extinction value if the emission lines being used lie on or near one of these features.

The selection of which lines can be used is determined by their upper ro-vibrational state values. For example, the 1→0S(1) and the 1→0Q(3) lines can be used as both arise from the $\nu = 1$ and $J = 3$ ro-vibrational levels (see Figure 2.1). As a result, their intrinsic flux ratio[3] is fixed, and only differential extinction can cause this value to differ. Associated with each line pair is a theoretical ratio, r′, given in Table 2.1.

[2]extinction values are usually normalised to the visible, A_V, as this is the most cited value

[3]It is worth noting (for this Section) that any symbol that is 'primed' (e.g., F') is regarded as an intrinsic measurement

Table 2.1: The theoretical ratio values for the S- and Q-branch lines; all lines given are ν = (1,0) transitions.

Line Pairs	r′
Q(2)/S(0)	1.10
Q(3)/S(1)	0.70
Q(4)/S(2)	0.56

Each value of r′ given in Table 2.1, is calculated from the quadrupole ro-vibrational transition probabilities, $A_{i,j}$, in Turner et al. (1977), the upper level degeneracy, g_i, and the wavelength of the transition, λ_i. The relationship between these quantities is given by

$$r' = \frac{\lambda_S \cdot g_Q \cdot A_Q}{\lambda_Q \cdot g_S \cdot A_S}$$

$$= \frac{F'_Q}{F'_S} \tag{2.9}$$

where F'_Q and F'_S are the intrinsic Q- and S-branch line strengths, respectively.

The derivation of the differential extinction (Δ (mags)) and absolute extinction (A_λ) is given in the following Subsections.

2.4.1 Differential Extinction

The following equation is used to convert from flux to magnitude

$$m_\lambda = -2.5 \log_{10}(F_\lambda) + \mathrm{C}_\lambda \tag{2.10}$$

where m_λ and F_λ are the magnitude and flux at a particular wavelength, λ, respectively; C_λ is a filter dependent constant.

The differential extinction can be thought of as the colour excess, E_{S-Q}. Using the equation above we can write the difference in the magnitude for an S- and Q-branch line pair as

$$(m_S - m_Q) = (m_S - m_Q)' + E_{S-Q} \tag{2.11}$$

where $(m_S - m_Q)$ is the observed colour. Rearranging equation 2.11 gives

$$\begin{aligned} E_{S-Q} &= (m_S - m_Q) - (m_S - m_Q)' \qquad \text{, or,} \\ A_S - A_Q &= m_S - m_Q - (m'_S - m'_Q) \end{aligned} \tag{2.12}$$

Now by applying equation 2.10 to equation 2.12, it becomes

$$A_S - A_Q = 2.5 \log_{10}\left(\frac{F_Q}{F_S}\right) + 2.5 \log_{10}\left(\frac{F'_S}{F'_Q}\right) \tag{2.13}$$

it is possible to rewrite this equation as

$$A_S - A_Q = 2.5 \log_{10} \left(\frac{F_Q}{F_S} \cdot \frac{F'_S}{F'_Q} \right) \tag{2.14}$$

Finally by substituting equation 2.9 into 2.14, the differential extinction is given by

$$A_S - A_Q = 2.5 \log_{10} \left(\frac{F_Q}{F_S} \cdot \frac{1}{r'} \right) \quad \text{, or,}$$

$$\Delta = 2.5 \log_{10} \left(\frac{F_Q}{F_S} \cdot \frac{\lambda_Q \cdot g_S \cdot A_S}{\lambda_S \cdot g_Q \cdot A_Q} \right) \tag{2.15}$$

2.4.2 Absolute Extinction

The power law relationship used by He et al. (1995); Stead & Hoare (2009), for NIR wavelengths (0.9 – 6 μm) is adopted here

$$\frac{A_\lambda}{E_{S-Q}} \propto \lambda^x \tag{2.16}$$

where x is either -1.7 or -2.14 as given by the above authors. This can be rearranged to give extinctions, A_Q and A_S, at wavelengths, λ_Q and λ_S, respectively

$$A_S = A_\mathrm{k} \cdot \left(\frac{\lambda_S}{\lambda_k} \right)^x \tag{2.17}$$

$$A_Q = A_\mathrm{k} \cdot \left(\frac{\lambda_Q}{\lambda_k} \right)^x \tag{2.18}$$

where A_k is the extinction at 2.2 μm and λ_k is 2.2 μm. Since $\Delta = A_S$ - A_Q, substituting Equations 2.17 and 2.18 into this gives

$$\Delta = A_\mathrm{k} \cdot \left[\left(\frac{\lambda_S}{\lambda_k} \right)^x - \left(\frac{\lambda_Q}{\lambda_k} \right)^x \right] \tag{2.19}$$

Finally, it is possible to re-arrange the above equation to yield A_k the absolute extinction as

$$A_\mathrm{k} = \frac{\Delta}{\left[\left(\frac{\lambda_k}{\lambda_S} \right)^x - \left(\frac{\lambda_k}{\lambda_Q} \right)^x \right]} \tag{2.20}$$

2.5 H_2 Diagnostics

2.5.1 Column Density

Following the method outlined in Davis et al. (2001) is is possible to calculate the column density of H_2, $N(H_2)$, in a PPN. Equation 2.22 gives the column density for an upper energy level, where the subscript i refers to a specific transition. This equation

requires that I is given in units of W m^{-2} str^{-1}. Conversion from observed flux in W m^{-2} to W m^{-2} str^{-1} can be accomplished via Equation 2.21

$$I = \left(\frac{F \cdot D^2}{\pi \cdot R^2}\right) = \left(\frac{F \cdot D^2}{Area}\right) = \frac{F}{\Omega} \tag{2.21}$$

where Ω is the solid angle of the observation, D is the distance to the object and R is the radius of the object, for a circular region, or equally $\pi \cdot R^2$ can be replaced with the area for any shaped region; F is the measured flux and I is surface brightness in W m^{-2} str^{-1}.

$$N_i = \frac{4\pi I_i}{h\nu_i A_i} \tag{2.22}$$

where A is the Einstein coefficient, ν is the frequency of the transition, and h is Planck's constant. The total column density, $N(H_2)$, can then be calculated through the use of an appropriate partition function, $Z(T)$

$$N(H_2) = \frac{N_i \cdot Z(T)}{g_i \cdot \exp\left[\frac{-h\nu_i}{kT}\right]} \tag{2.23}$$

where

$$Z(T) = \frac{0.006135 \cdot T}{1 - \exp\left[\frac{-5850}{T}\right]} \tag{2.24}$$

is a single approximation partition function over the excitation temperature range (600 K – 2450 K) which is accurate to 1% in this range (Smith et al., 1997); g_i is the statistical weight for a transition and is calculated as described in Section 2.5.4, k is the Boltzmann constant, and T is the excitation temperature.

2.5.2 Mass of H_2

The Mass of H_2, relative to the mass of the Sun, in a PPN outflow can be calculated using Equation 2.25

$$M(H_2) = Area \cdot M_{H_2} \cdot N(H_2) \tag{2.25}$$

where M_{H_2} is the mass of the H_2 molecule.

2.5.3 Column Density Ratios

This Section outlines the process of determining the Column Density Ratios (CDRs); a technique widely used as a diagnostic for differentiating excitation mechanisms (Eislöffel et al., 2000; Smith, 2000; Davis et al., 2003; O'Connell et al., 2005). A gas in Local Thermal Equilibrium (LTE) has a column density, N_i, at an energy level kT_i, which is directly proportional to the upper level degeneracy, g_i. The column density of an

energy level can be expressed in terms of the total column density of H_2 as given by

$$N_i = \frac{N(H_2) \cdot g_i \cdot \exp\left(\frac{-T_i}{T_{\rm gas}}\right)}{Z(T)} \tag{2.26}$$

where $Z(T)$ is known as the partition function or the sum over all states[4]. Rearranging this equation gives the total column density of H_2 in terms of N_i

$$N(H_2) = \frac{N_i \cdot Z(T) \cdot \exp\left(\frac{T_i}{T_{\rm gas}}\right)}{g_i} \tag{2.27}$$

Using Equation 2.22 it is possible to re-write equation 2.27 as

$$N(H_2) = \frac{4 \cdot \pi \cdot F_{\rm cor} \cdot \lambda}{\Omega \cdot h \cdot c \cdot A_i} \cdot \frac{Z(T)}{g_i} \cdot \exp\left(\frac{T_i}{T_{\rm gas}}\right) \tag{2.28}$$

where $F_{\rm cor}$ is the extinction corrected line flux. This equation[5] can be greatly simplified by 'normalising' the total column density, N(H_2), to the column density of H_2 in LTE at 2000 K

$$\frac{N(H_2)}{N(H_2)_{2000}} = \left[\frac{F^i_{\rm cor} \cdot \lambda_i \cdot \cancel{Z(T) \cdot 4 \cdot \pi}}{\cancel{\Omega \cdot h \cdot c} \cdot A_i \cdot g_i} \cdot \exp\left(\frac{T_i}{2000}\right)\right] \cdot \left[\frac{\cancel{\Omega \cdot h \cdot c} \cdot A_j \cdot g_j}{F^j_{\rm cor} \cdot \lambda_j \cdot \cancel{Z(T) \cdot 4 \cdot \pi}} \cdot \exp\left(\frac{-T_j}{2000}\right)\right] \tag{2.29}$$

where $N(H_2)/N(H_2)_{2000}$ is the Column Density Ratio (CDR). The solid angle, Ω, the constants h & c, and the partition function, $Z(T)$, all drop out of the equation leaving

$$\text{CDR} = \frac{F^i_{\rm cor} \cdot \lambda_i \cdot A_j \cdot g_j}{F^j_{\rm cor} \cdot \lambda_j \cdot A_i \cdot g_i} \cdot \exp\left(\frac{T_i - T_j}{2000}\right) \tag{2.30}$$

typically the 'normalising' is done using the 1→0S(1) line ($v = 1$, $J = 3$), using values as taken from Dabrowski (1984) for transition probabilities. CDR diagrams are usually plotted in log form, for example the y-axis would represent $\log_{10}$(CDR), while the x-axis is the upper energy level temperature, E(K). Figure 2.5 demonstrates an example of a plot of a CDR diagram. If the gas is of the order of 2000 K a horizontal straight line at $y = 0$ would represent a gas at 2000 K, while an inclined line (positive or negative) would indicate a gas at a different temperature.

2.5.4 Ortho-to-Para Ratio

The previous Subsection discussed the use of measured line fluxes as a useful tool for determining the nature of the gas temperature, i.e., whether or not the gas temperature was varying or constant.

This Section concentrates on the determination of the ortho-to-para ratio (OPR) — another probe of the excitation mechanism. Since H_2 has two identical nuclei, nuclear spin plays an important role in its spectra. Ortho- and para-H_2 exist when

[4] A partition function is simply the weighted sum of the number of ways an atom can arrange its electrons with the same energy, i.e., the sum of $(2J_i + 1)exp(-T_i/T)$ over all energy levels.

[5] Note : the subscripts i and j are used to distinguish lines arising from different energy levels.

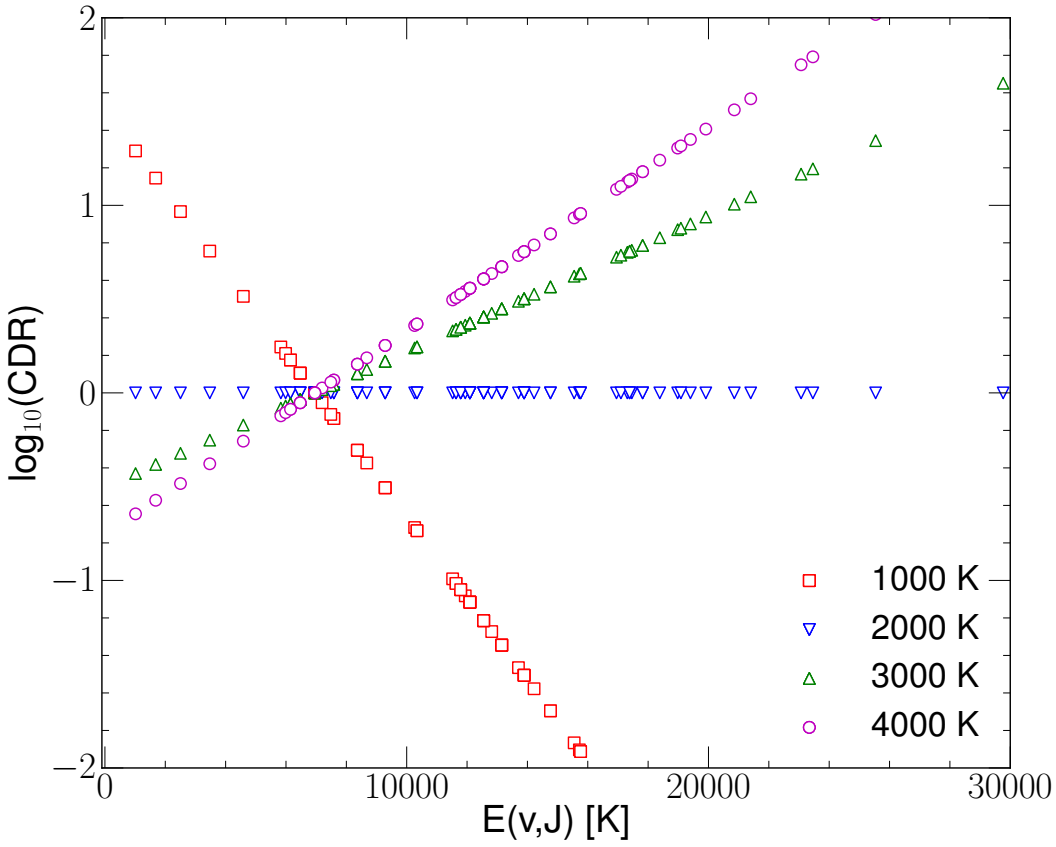

Fig. 2.5: A plot of the CDR relative to CDR of a gas in LTE having several temperatures. All possible transition lines are plotted using data values taken from Dabrowski (1984) and Turner et al. (1977).

the two protons spin in the same and opposite directions, respectively. OPR values ~ 3 are generally associated with shocked regions while values < 2 indicates a possible fluorescent component (see Martini et al., 1997). Equation 2.26 gives the column density for a particular energy level, N_i, such that the ratio of two ortho lines' column densities can be written as

$$\frac{N_{o'}}{N_o} = \frac{(2J_{o'}+1)}{(2J_o+1)} \cdot \exp\left(\frac{\Delta E}{kT_{\rm ex}}\right) \tag{2.31}$$

here $\Delta E/kT_{\rm ex}$ is given as $(To - To')/T_{\rm ex}$ [6]. This comparison can be rearranged to give an expression for the excitation temperature of a gas

$$T_{\rm ex} = (To - To') \cdot \ln\left[\frac{N_{o'}(2J_o+1)}{N_o(2J_{o'}+1)}\right]^{-1} \tag{2.32}$$

The OPR is the ratio of the total ortho-H_2 to para-H_2 column density divided by their respective statistical weight, g_u^o and g_u^p. In the case of each modification, the statistical weight is given by the product of the spin degeneracy, g_s, and the rotational

[6]Note on notation: throughout this Subsection subscripts o, and p represent ortho- and para-modifications, respectively. The 'primed' symbols are used for the third modification line, either ortho or para, which is always the transition with the higher energy.

degeneracy, g_J. For ortho-H_2 (odd J) g_s is equal to 3 and g_J is $(2J_o + 1)$, yielding a $g_u^o = 3 \cdot (2J_o + 1)$; For para-$H_2$ (even J) $g_u^p = 1 \cdot (2J_p + 1)$, in this case g_s is set to 1 as a good approximation. Taking this into consideration, the ratio of an ortho- and para-lines differs from 2.31 by the ratio of the ortho and para spin degeneracies (as they will not cancel out) and so their ratio gives the OPR using the following equation

$$\phi \equiv \frac{g_s^o}{g_s^p} = \frac{N_o(2J_p+1)}{N_p(2J_o+1)} \exp\left[\frac{(T_o - T_p)}{T_{\rm ex}}\right] \tag{2.33}$$

Use of this equation implies a prior knowledge of the excitation temperature of the gas. It is possible, using several lines of different modification, to determine the excitation temperature graphically (see Section 5.3.8) but usually means that an assumed OPR has been used (which is three in the case of using the data from Dabrowski, 1984). However, it is also possible to use a third line to calculate the OPR and so equation 2.33 can be re-written as (assuming two ortho lines and a single para line are being used)

$$\phi = \frac{N_o(2J_p+1)}{N_p(2J_o+1)} \exp\left[\frac{(T_o - T'_o)}{T_{\rm ex}}\right] \left(\frac{T_o - T_p}{T_o - T_{o'}}\right) \tag{2.34}$$

using the substitution

$$\exp\left[\frac{(T_o - T_p)}{T_{\rm ex}}\right] = \exp\left[\frac{(T_o - T'_o)}{T_{\rm ex}}\right] \left(\frac{T_o - T_p}{T_o - T_{o'}}\right) \tag{2.35}$$

This can be further re-written, by substituting $T_{\rm ex}$ in equation 2.32 into 2.34, as

$$\phi = \frac{N_o(2J_p+1)}{N_p(2J_o+1)} \cdot \frac{N_{o'}(2J_o+1)}{N_o(2J_{o'}+1)} \left(\frac{T_o - T_p}{T_o - T_{o'}}\right) \tag{2.36}$$

A similar expression can be derived for the case when working with two para lines rather than two ortho lines, as given below

$$\phi = \frac{N_o(2J_p+1)}{N_p(2J_o+1)} \cdot \frac{N_{p'}(2J_p+1)}{N_p(2J_{p'}+1)} \left(\frac{T_o - T_p}{T_p - T_{p'}}\right) \tag{2.37}$$

2.6 Shock Waves

Shocks have been widely observed in the ISM and have been approximated by various types of models. For example, pre-main sequence stars possess high velocity outflows along their jet-axes, with the higher velocities detected at the apex of the jet than along the sides and are nicely represented by shock models of Herbig Haro (HH) objects (Smith et al., 2003). The review articles of Draine & McKee (1993); Hollenbach & McKee (1979) provide an invaluable source of background information and on the physics involved in producing astronomical shock waves. Draine (1980) also present in a clear and understandable way the theory of astrophysical shocks.

As discussed in previous sections, it is possible for a shock wave to provoke the excitation of H_2. The molecular gas surrounding post-AGB stars behaves like a fluid and as such is governed by the rules of fluid dynamics. These rules allow the behavior of

the gas to be modelled as it interacts with other gases (fluids) in the interstellar medium (ISM). A fluid flow is described as supersonic if the speed of the fluid is greater than the sound speed in that particular medium. The ratio of the flow speed to the local sound speed defines the Mach number and is given by

$$M = \frac{v}{c_{\rm s}} \tag{2.38}$$

where $c_{\rm s}$ is the speed of sound in a particular medium. Since $c_{\rm s} \propto \mu^{-\frac{1}{2}}$ where μ represents the relative molecular weight, the sound speed will increase when the medium consists of light molecules – something which needs to be taken into consideration for various environments.

Normally a disturbance/signal in a fluid propagates at the sound speed, this means that if a supersonic flow is approaching a slower moving fluid, no information can be transmitted ahead of the supersonic flow to 'warn' of the impending impact between the two fluids. This is the scenario often cited as a mechanism for producing collisionally excited molecular emission around post-AGB stars – a fast moving post-AGB wind collides with the slower moving AGB cast-off envelope. At the point of interaction between the two fluids, a discontinuity of the variables (velocity, density, temperature etc.) will occur where the gas is compressed, heated and accelerated – this event is known as a shock.

The equations of mass, momentum, and energy in fluids are given by:

$$\frac{\partial \rho}{\partial t} + \nabla \cdot (\rho v) = 0 \qquad \text{[Mass Conservation]} \tag{2.39}$$

$$\rho \frac{\partial v}{\partial t} + \rho v \cdot \nabla v = -\nabla p + \rho g \qquad \text{[Momentum Conservation]} \tag{2.40}$$

$$\frac{\partial E}{\partial t} + \nabla \cdot [(E + p)v] = -\rho \dot{Q}_{\rm cool} + \rho \frac{\partial \Psi}{\partial t} \qquad \text{[Energy Conservation]} \tag{2.41}$$

where $\dot{Q}_{\rm cool}$ is the rate of cooling, Ψ is the scalar gravitational potential, and g is the gravitational acceleration. Derivations of these equations can be found in almost any textbook on fluid dynamics (e.g, Clarke & Carswell, 2007) and so I only quote the final equations here.

The relationship between pre- and post-shock variables is given by the Rankine-Hugonoit (RH) equations (below), which are always calculated in the frame of the shock. Figure 2.6 shows the variables used in these equations [7]. These equations are each derived from their respective hydrodynamic equation given above.

[7] Another symbol for velocity either side of the shock front commonly used is u when discussing the theory of shocks.

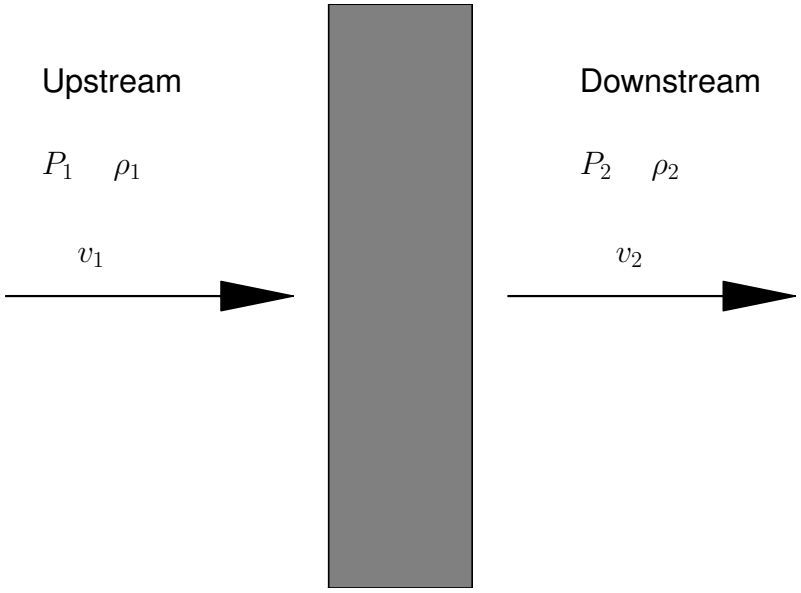

Fig. 2.6: A simplistic representation a shock front. Pre- and post-shock variables, velocity, density and pressure (v, ρ, P), change across a shock front of infinitesimal thickness.

$$\rho_1 v_1 = \rho_2 v_2 \qquad \text{[Mass Conservation]} \tag{2.42}$$

$$\rho_1 v_1^2 + P_1 = \rho_2 v_2^2 + P_2 \qquad \text{[Momentum Conservation]} \tag{2.43}$$

$$\frac{1}{2}v_1^2 + \frac{\gamma}{\gamma - 1}\frac{P_1}{\rho_1} = \frac{1}{2}v_2^2 + \frac{\gamma}{\gamma - 1}\frac{P_2}{\rho_2} \qquad \text{[Energy Conservation]} \tag{2.44}$$

where γ is the adiabatic index (=5/3 for a monotonic gas, or 7/5 for a diatomic gas), ρ is the density, v is the velocity, and P is the pressure. Using these equations and $\gamma = 5/3$, for a strong adiabatic shock[8], it can be shown that the maximum compression achievable is a factor of 4. In isothermal/radiative shocks the compression factor can be many times higher than this and is given by the square of the Mach number. Isothermal shocks, by definition, lose heat ($\dot{Q}_{\rm cool} \neq 0$) and so Equation 2.44 can not be used for these shocks – it is assumed that the gas returns to its pre-shock temperature.

The Rankine-Hugonoit conditions given above govern purely hydrodynamical flows. When this is the case and the component parts of a fluid (the neutrals, ions, and electrons) flow at the same rate in a shock, the shock is known as a *Jump*-shock or J-shock.

[8]adiabatic shocks occur when the column density is less than the characteristic cooling column density, and so the emitted radiation does not affect the gas dynamics behind the shock front (McKee & Hollenbach, 1980)

2.6.1 C-shocks

The presence of magnetic fields and a low ionisation fraction in molecular clouds means that a pure hydrodynamic treatment is no longer valid. The structure of the shock waves in these environments is drastically different, with the neutrals, ions, and electrons able to move at different velocities. These situations require a magnetohydrodynamic (MHD) treatment (e.g., Draine et al., 1983). Such shock waves are called *Continuous*-shocks or C-shocks. In such shocks, where the magnetic field strength (B_0) is greater than some minimum ($B_{\rm min}$), a magnetic precursor forms ahead of the shock at a speed faster than the sound speed in the medium Draine (1980). The effect of such a wave is that the slower moving gas can be accelerated and compressed prior to the impact of the shock front, allowing the variables (n, v, P, T) to change continuously across the shock front, without the discontinuous jump present in J-shock. This magnetic precursor is formed as a result of transverse waves called *Alfvèn waves* travelling along field lines. This MHD wave is formed from a combination of the ions moving with the field and the tension in the magnetic field lines – the transverse wave is due to the restoring force provided by the magnetic tension.

The speed at which the ions (and electrons) can propagate in directions perpendicular to the magnetic field is given in Equation 2.45 (Spitzer, 1962).

$$v_{\rm ims} = \left(\frac{\left[\frac{B^2}{4\pi} + \frac{5}{3}(n_i + n_e)kT \right]}{(\rho_i + \rho_e)} \right)^{\frac{1}{2}} \Bigg/ \left(1 + \frac{B^2}{4\pi(\rho_i + \rho_e)c_{\rm s}^2} \right) \tag{2.45}$$

where the subscripts i, e refer to the ions and electrons, respectively. The ion-magnetosonic velocity is essentially the combination of the Alfvèn speed and the ion-electron sound speed, given by Equations 2.46 and 2.47, respectively.

$$v_{\rm A} = \left(\frac{B^2}{4\pi\rho} \right)^{\frac{1}{2}} \tag{2.46}$$

$$c_{\rm s} = \left[\frac{5(n_i + n_e)kT}{3(\rho_i + \rho_e)} \right]^{\frac{1}{2}} \tag{2.47}$$

$v_{\rm ims}$ gives the ionic signal speed — a critical parameter in C-shocks. If $v_{\rm ims} > v_{\rm s}$ (the shock speed) then it is possible for the material upstream of the moving neutral gas component to become 'aware' of the impending collision — streaming ions and electrons ahead of the moving neutral gas, heat and compress the upstream material in a damping region corresponding to L in Figure 2.7. In the presence of a strong enough magnetic field ($B_0 > B_{\rm min}$) the ions and the neutral fluids decouple and the flow variables change continuously across the shock front. Figure 2.7 shows a schematic diagram summarising five different shock structures (Draine, 1980). The pure hydrodynamic J-shock is represented by Figure 2.7 (a), while (d) gives the C-shock scenario — the ion and neutral velocities (v_i and v_n) are decoupled with the ion velocity travelling ahead of the neutrals, the damping length is large and the discontinuity in the neutral fluid has disappeared.

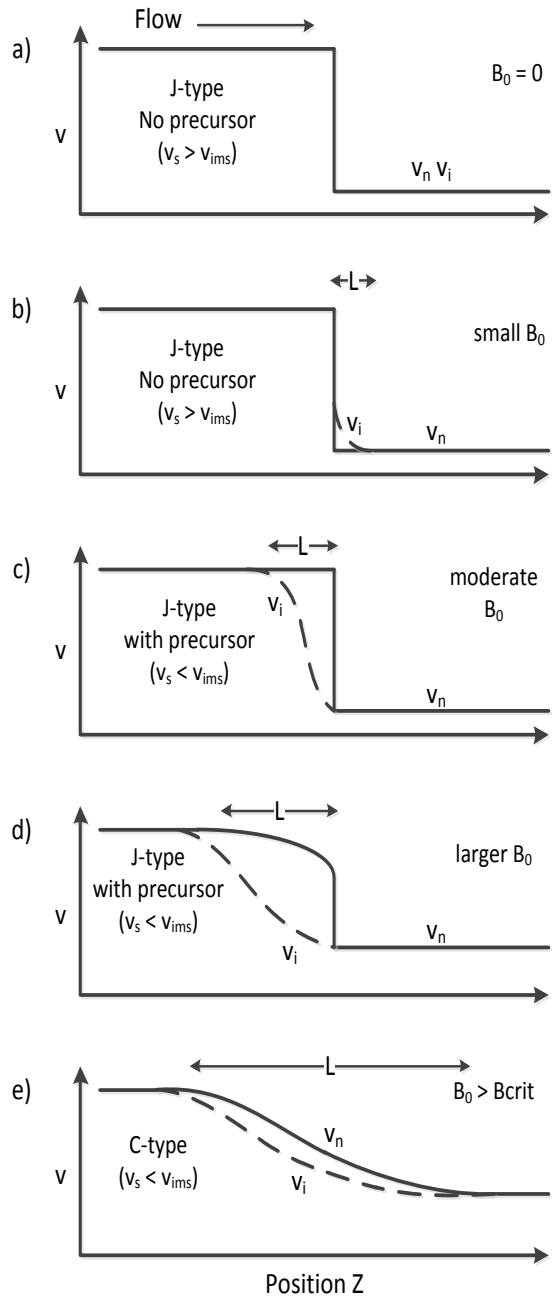

Fig. 2.7: Draine (1980) first presented this figure which shows the effect of a transverse magnetic field (B_0) on the structure of shock waves in a partially ionised gas. All variables are given in the rest frame of the shock, i.e., the neutral velocity (v_n), the ion velocity (v_i). Damping length (L) is the region in which ion-neutral collisions transfer momentum. (a) When $B_0 = 0$ the shock becomes a Jump (J) shock. (b) with a small magnetic field, there is still no magnetic precursor although the ion and neutral post-shock speeds differ. (c) when B_0 is increased further, the ion-magnetosonic speed (v_{ims}) exceeds the shock speed (v_s), magnetic field compression occurs ahead of the shock front, with v_i becoming a continuous function of position. (d) B_0 is increased again, the magnetic precursor increases the neutral gas compression ratio across the shock front decreases. And finally, (e) the J-shock front has disappeared; a strong enough magnetic field $B_0 > B_{\rm crit}$ means the hydrodynamic flow variables are continuous.

When $B > B_{\rm crit}$ the RH hydrodynamic equations require the inclusion of the magnetic field effects. Hollenbach & McKee (1979), and references therein, describe the jump conditions for an MHD shock using the following equations:

$$\rho_1 v_{1_\parallel} = \rho_2 v_{2_\parallel} \tag{2.48}$$

$$\rho_1 v_{1_\parallel}^2 + P_1 + \frac{B_{1_\perp}^2}{8\pi} = \rho_2 v_{2\parallel}^2 + P_2 + \frac{B_{2_\perp}^2}{8\pi} \tag{2.49}$$

$$\rho_1 v_{1_\parallel} v_{1_\perp} + \frac{B_{1_\parallel} B_{1_\perp}}{4\pi} = \rho_2 v_{2_\parallel} v_{2_\perp} + \frac{B_{2_\parallel} B_{2_\perp}}{4\pi} \tag{2.50}$$

$$B_{1\parallel} = B_{2\parallel} \tag{2.51}$$

$$v_{1_\parallel} B_{1\perp} = v_{2_\parallel} B_{2\perp} \tag{2.52}$$

$$v_{1_\parallel}\left(\frac{1}{2}v_1^2 + \frac{\gamma}{\gamma-1}\frac{P_1}{\rho_1}\right) + = v_{2_\parallel}\left(\frac{1}{2}v_2^2 + \frac{\gamma}{\gamma-1}\frac{P_2}{\rho_2}\right) +$$

$$\frac{(v_\parallel B_{1_\perp}^2 - v_{1_\perp} B_{1_\perp} B_{1_\parallel})}{4\pi} + F_1 \qquad \frac{(v_{2_\parallel} B_{2_\perp}^2 - v_{2_\perp} B_{2_\perp} B_{2_\parallel})}{4\pi} + F_2 \tag{2.53}$$

where the first three equations give the mass conservation and the momentum flux conservation, the following two equations are derived from Maxwell's equations, and the final equation is the energy flux conservation. F is the energy radiated in the shock front, the subscripts $\parallel$, $\perp$ refer to the component of a variable parallel to or perpendicular to the fluid motion.

From the expressions given in this section it is obvious that density, velocity, and magnetic field are critical parameters for the description of shock waves. Two other parameters worth consideration are the ionisation fraction (χ_e) and the molecular hydrogen fraction (f). Draine et al. (1983) assume a constant ionisation fraction during their shock computations given by

$$\chi_e = \frac{10^{-5}}{\sqrt{n_{\rm H}}} \tag{2.54}$$

where $n_{\rm H}$ gives the hydrogen nucleon number density ($\rm cm^{-3}$). Ion-neutral collisions may increase this fraction further, where streaming ions impact the molecular material upstream causing self-ionisation, which in turn reduces the cushioning affect.

The molecular fraction, f, is number density of hydrogen molecules, $n(H_2)$, relative to the total hydrogen nucleon number density, $n(H)$, given by

$$f = \frac{n(H_2)}{[2n(H_2) + n(H)]} \tag{2.55}$$

where $n(H)$ and $n(H_2)$ can be found from Equations 2.56 and 2.57, respectively.

$$n(H) = (1 - 2f) \cdot n_{\rm H} \tag{2.56}$$

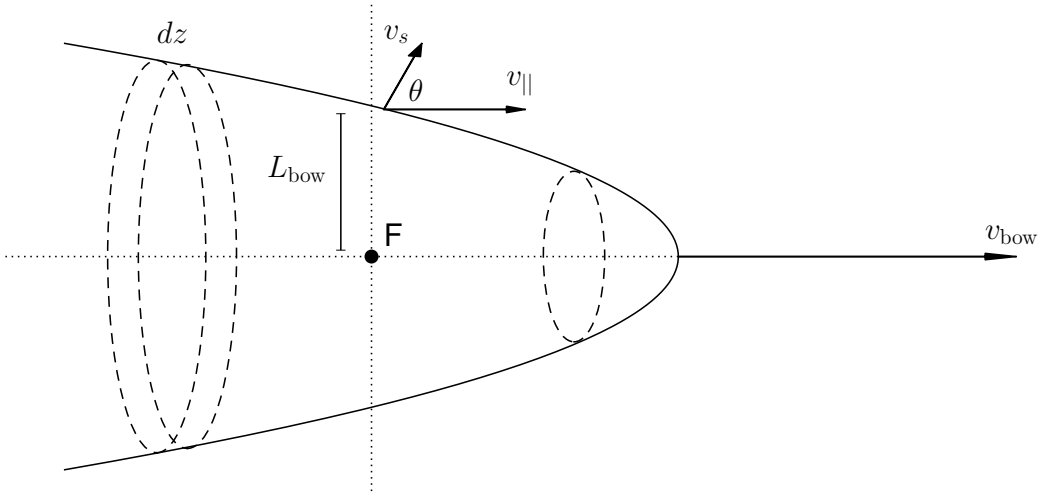

Fig. 2.8: A schematic of the bow shock geometry, where v_s is the shock velocity given as magnitude of the normal/parallel component of a surface motion, $v_{\rm bow}$ is the motion of the bow at the apex of the paraboloid, $L_{\rm bow}$ is the semi-latus rectum, which is used to calculate the total luminosity of a bow (see Section 3.5.3), dz is the thickness of a planar element (not to scale), θ is the angle between the bow velocity and the velocity normal to the shock surface, and F is the focal point of the paraboloid.

$$n(H_2) = f \cdot n_{\rm H} \tag{2.57}$$

where $n_{\rm H}$ is the total hydrogen nucleon number pre-shock density. Although often presumed that the gas is almost fully molecular, the presence of even a few percent of atomic H will set up LTE conditions far easier than by H_2–H_2 collisions alone (Smith et al., 1997).

2.6.2 Shock Models

The shock models used in this work are based on the FORTRAN codes developed by Professor Michael Smith in a series of papers (Smith & Brand, 1990a,c,b). To briefly summarise, the models allow both a pure-hydrodynamic and magneto-hydrodynamic treatment of shock waves. They are capable of producing various shock configurations based on a number of input parameters (see Table 2.2), and not only output H_2 line intensities but also many atomic species including the forbidden [OI] ($\lambda = 63$ μm). Since then various minor improvements have been included in the codes (e.g., the Non-LTE line intensities, additional atomic emission lines, etc.). These papers and the theory described in the previous sections set up the expressions required for planar shock waves. Planar shocks can be thought of as a uniform 'slab' of material, moving at a uniform velocity, impacting the ISM. However, in many cases the use of planar models to reproduce observed line intensities and velocities proved difficult. Smith et al. (1991) showed that the use of a single C-type planar shock could not provide a sensible match to the H_2 lines observed in the OMC-1 object which has velocities ~ 150 km s^{-1}. Smith et al. (1991) found that by using a parabolic shock front, also known as a bow shock, with sensible H_2O abundances ($1 - 5 \times 10^{-4}$), it was possible to fit predicted column density ratios to the observed ones in OMC-1. Bow shocks form when a fast wind flows around some dense slower-moving material or conversely where there

Table 2.2: Input model parameters for the shock models (c.g.s units).

Parameter		
H Density, n	He fraction	CO Abundance
Molecular Fraction, f	Dust fraction	O Abundance
Alfvén velocity, v_a	Breakdown velocity	C Abundance
Magnetic Field, B	Bow shape	H_2O Abundance
Shock Velocity, v_s	Bow symmetry	Field parallel
Field Angle, μ	Orientation angle	Initial temperature[¶]
Ion Fraction[*], χ	Chemistry type[†]	planar or bow
L-Bow	H_2 cooling type[△]	

[*] C-type shocks only.
[¶] J-type shocks only.
[△] Gives the option of using the analytical approximation described in Lepp & Shull (1983), or the cooling function tables given by Le Bourlot et al. (1999).
[†] Can be used to choose between an non-equilibrium or equilibrium chemistry.

is a fast moving clump of material moving into ambient material. These bow shocks possess a variety of velocities along the shock surface, Figure 2.8 shows a schematic diagram of a bow shock, where $v_{\rm bow}$ is the velocity at the apex of the paraboloid, and at each point along the surface there exists a shock velocity $v_\perp$ given by $v_{\rm bow} \times \cos\theta$ (the normal component of the bow velocity). The bow shocks are approximated by the sum of many planar elements, provided the thickness of each element (dz) is much smaller than the overall size of the curved bow shock (Smith et al., 1991).

Both curved and planar shocks were used throughout this Thesis work.

References

Bieging, J. H., Wilner, D., & Thronson, Jr., H. A. 1991, ApJ, 379, 271

Burton, M. G., Hollenbach, D. J., & Tielens, A. G. G. M. 1990, ApJ, 365, 620

Cardelli, J. A., Clayton, G. C., & Mathis, J. S. 1989, ApJ, 345, 245

Cazaux, S. & Tielens, A. G. G. M. 2002, ApJ, 575, L29

Clarke, C. & Carswell, B. 2007, Principles of Astrophysical Fluid Dynamics

Dabrowski, I. 1984, Canadian Journal of Physics, 62, 1639

Davis, C. J., Ray, T. P., Desroches, L., & Aspin, C. 2001, MNRAS, 326, 524

Davis, C. J., Smith, M. D., Stern, L., Kerr, T. H., & Chiar, J. E. 2003, MNRAS, 344, 262

Draine, B. T. 1980, ApJ, 241, 1021

Draine, B. T. & McKee, C. F. 1993, ARA&A, 31, 373

Draine, B. T., Roberge, W. G., & Dalgarno, A. 1983, ApJ, 264, 485

Eislöffel, J., Smith, M. D., & Davis, C. J. 2000, A&A, 359, 1147

García-Hernández, D. A., Manchado, A., García-Lario, P., Domínguez-Tagle, C., Conway, G. M., & Prada, F. 2002, A&A, 387, 955

Gatley, I., Hasegawa, T., Suzuki, H., Garden, R., Brand, P., Lightfoot, J., Glencross, W., Okuda, H., & Nagata, T. 1987, ApJ, 318, L73

Geballe, T. R., Russell, R. W., & Nadeau, D. 1982, ApJ, 259, L47

Guerrero, M. A., Villaver, E., Manchado, A., Garcia-Lario, P., & Prada, F. 2000, ApJS, 127, 125

He, L., Whittet, D. C. B., Kilkenny, D., & Spencer Jones, J. H. 1995, ApJS, 101, 335

Hollenbach, D. & McKee, C. F. 1979, ApJS, 41, 555

Hollenbach, D. & Natta, A. 1995, ApJ, 455, 133

Kwok, S. 2007, The Origin and Evolution of Planetary Nebulae

Le Bourlot, J., Pineau des Forêts, G., & Flower, D. R. 1999, MNRAS, 305, 802

Lepp, S. & Shull, J. M. 1983, ApJ, 270, 578

Martini, P., Sellgren, K., & Hora, J. L. 1997, ApJ, 484, 296

McKee, C. F. & Hollenbach, D. J. 1980, ARA&A, 18, 219

O'Connell, B., Smith, M. D., Froebrich, D., Davis, C. J., & Eislöffel, J. 2005, A&A, 431, 223

Smith, M. D. 2000, Irish Astronomical Journal, 27, 37

Smith, M. D. & Brand, P. W. J. L. 1990a, MNRAS, 242, 495

—. 1990b, MNRAS, 245, 108

—. 1990c, MNRAS, 243, 498

Smith, M. D., Brand, P. W. J. L., & Moorhouse, A. 1991, MNRAS, 248, 451

Smith, M. D., Davis, C. J., & Lioure, A. 1997, A&A, 327, 1206

Smith, M. D., Khanzadyan, T., & Davis, C. J. 2003, MNRAS, 339, 524

Spitzer, L. 1962, Physics of Fully Ionized Gases

Stead, J. J. & Hoare, M. G. 2009, MNRAS, 400, 731

Turner, J., Kirby-Docken, K., & Dalgarno, A. 1977, ApJS, 35, 281

Chapter 3: Data Reduction & Analysis

3.1 Introduction

This chapter will discuss the steps taken to reduce the Integral Field Unit (IFU) data and the analysis tools used/developed to examine the data. All of the data presented in this work was obtained using the Very Large Telescope (VLT) facility at Paranal, Chile (see Figure 3.1). The instrument used to obtain the data is an integral field spectrometer called SINFONI and is discussed in detail in Section 3.2.

The main advantage of IFU data over more traditional techniques (e.g., longslit spectroscopy and/or photometry) is that one can obtain both spatial and spectral information simultaneously. The resulting data set will be a three-dimensional datacube consisting of spatial X and Y information combined with wavelength/velocity information in the Z direction. Once the data has been acquired at the telescope the format of IFU data allows one to manipulate the data in a much more versatile manner than with traditional approaches. For example one can place artificial slits at any location in the field of view to simulate longslit observations, re-bin spatial/spectral spaxels/pixels to increase the signal-to-noise, extract specific regions for analysis, and many more. It is worth noting that although this format of data is quite new ($\sim$ 10 years) for optical and near-infrared instruments, it has been the normal format of radio astronomers for many years. For further information on the, now, long list of available IFU instruments and available software for analysis, the reader is directed to the IFS wiki website[1].

Fig. 3.1: Panoramic photograph of the four Unit Telescopes (UTs) that make up the VLT. Also visible in the photograph are the four Auxiliary Telescopes (ATs), and the VLT Survey Telescope (VST). Photograph taken during my observing run in February, 2010 (individual photographs stitched together using the `xmerge`[2] program).

[1] http://ifs.wikidot.com/
[2] http://xmerge.sourceforge.net/

3.2 SINFONI

The construction of an Integral Field Unit (IFU) for VLT was recommended by ESO in October 1997, conceived as a combination of IFS and Adaptive Optics (AO). First light on the newly constructed AO-assisted IFU was on 31st of May 2004. The instrument therefore consisted of two major sub-systems: (1) MACAO (**M**ultiple **A**pplication **C**urvature **A**daptive**O**ptics), and (2) SPIFFI (**SP**ectrograph for **I**nfrared **F**aint **F**ield **I**maging). The Max-Planck-Institut für Extraterrestrische Physik (MPE) developed the IFU SPIFFI in collaboration with ESO (Eisenhauer et al., 2003). The name adapted for the combined instrument was SINFONI (Spectrograph for INtegral Field Observations in the Near Infrared). In order for the two sub-systems to operate simultaneously, the visible light (450 nm to 1000 nm) is reflected to the wavefront sensor while the IR light (1.05 µm to 2.45 µm) is fed to the spectrograph. The instrument can be used with or without an AO guide star. Without AO functioning, the MACAO subsystem acts only as a light passage and the spatial resolution is dependent on current seeing conditions. Excellent spatial resolution can be achieved through the use of the AO module. A reference star of R=11 is recommended for this, however the AO will work with fainter stars down to a magnitude of R=17. To complement the AO-corrections, SINFONI is equipped with a Laser Guide Star Facility (LGSF) mounted under the Nasmyth platform of the telescope. This allows the observer to achieve AO-corrected images when there is a paucity of bright nearby reference stars, through use of the laser to stimulate Sodium in the upper atmosphere (90 km).

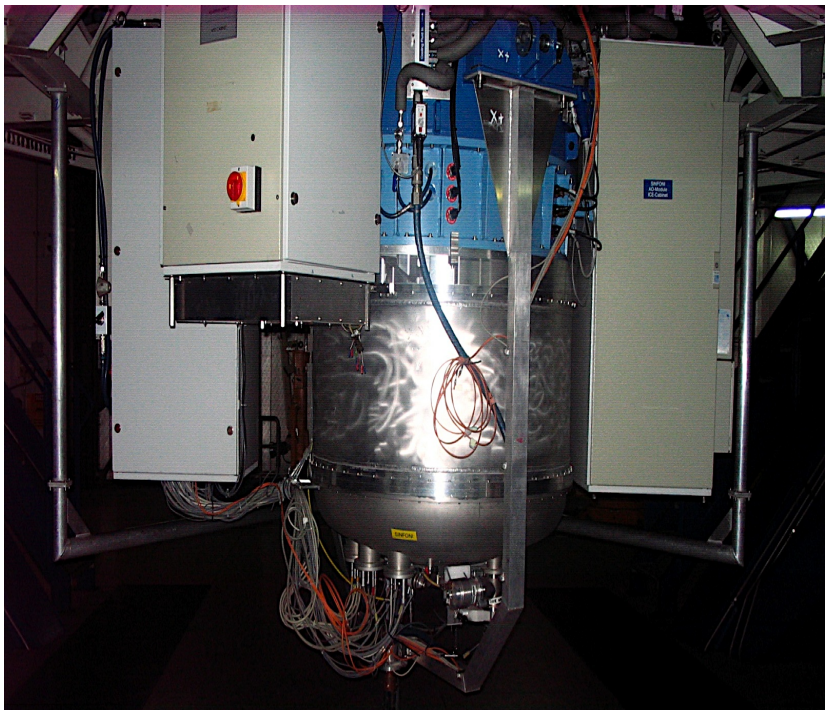

Fig. 3.2: The SINFONI instrument at Cassegrain focus located on UT4 (photograph taken during my observing run in February, 2010).

The SINFONI instrument is located at the Paranal facility on the VLT Unit Telescope 4 (UT4) a.k.a Yepun [3]. Figure 3.2 shows SINFONI attached to UT4 at Cassegrain focus.

[3]The name 'Yepun' is taken from the Mapuche language of the Chilean Indians. The other UT's 1, 2, & 3 are Antu, Kueyen, and Melipal, respectively.

Table 3.1 lists values of the three pixel scale modes available to SINFONI. The choice of pixel scale determines the field of view. SINFONI operates with four separate grating settings, J, H, K, H+K with average spectral resolutions of ∼2000, ∼3000, ∼4000, and ∼1500, respectively (see Table 3.2 for a full list of values).

3.2.1 Characteristics

Table 3.1: Information for SINFONI pixel scales and corresponding fields of view for each resolution mode, where HRM, IRM, & LRM are High-, Intermediate-, & Low-Resolution Mode.

	HRM	IRM	LRM
Pixel Scale (mas/pixel)	25.0 × 12.5	100.0 × 50.0	250.0 × 125.0
Field of View (arcsec × arcsec)	0.8 × 0.8	3.2 × 3.2	8.0 × 8.0

Equation 3.1 defines a spectrograph's resolution, which is the ability to distinguish closely spaced spectral features.

$$R = \frac{\lambda}{\Delta\lambda} \tag{3.1}$$

where $\Delta\lambda$ is the smallest detectable wavelength difference. In fact, the resolution values quoted in the SINFONI manuals and in Table 3.2, are given by

$$R = \frac{\lambda}{(pscale \cdot FWHM)} \tag{3.2}$$

where FWHM is the full width half-maximum of an arc line in pixels (typically $\sim$ 2 pixels) and pscale is the pixel scale.

Image slicer IFUs typically have spectral resolutions varying from values of $\sim$ 100 to $\sim$ 7000 (e.g., SINFONI, NIFS, PIFS). The corresponding velocity resolution is then given by equation 3.3

$$\begin{aligned} V_{res} &= c \cdot \left(\frac{\Delta\lambda}{\lambda}\right) \\ &= \frac{c}{R} \end{aligned} \tag{3.3}$$

where c is the speed of light. As with all 3D spectroscopic techniques, IFS can yield important kinematic information at various spatial locations across the FOV. This sort of data cannot be obtained as efficiently using traditional longslit techniques.

Table 3.2: Spectral & Velocity resolution information for the SINFONI instrument. All values are evaluated for each filter at their reference wavelength (J = 1.25 μm, H = 1.65 μm, K = 2.20 μm, H+K = 1.95 μm). Note that spectral/velocity resolution are dependent on wavelength and pixel scale.

Filter	HRM		IRM		LRM	
	Resolution					
	Spectral	Velocity (km s^{-1})	Spectral	Velocity (km s^{-1})	Spectral	Velocity (km s^{-1})
J (1.05 - 1.40 μm)	2360	127	1800	167	1870	160
H (1.45 - 1.85 μm)	5500	55	2730	110	2920	102
K (1.95 - 2.45 μm)	5950	50	5090	59	4490	67
H+K (1.45 - 2.45 μm)	2710	111	2050	146	1640	183

3.3 Data Reduction

The absence of any suitable astronomy package for the manipulation of NIR data cubes led me to create a quick and reliable method for examining near-IR data cube datasets. This consists of two parts: (1) a SINFONI-specific data reduction pipeline for all my data, and (2) a generic NIR data cube analysis package to be used for any instrument. Creating the former consisted of wrapping the ESO command line utility (`esorex`), in `python` code to perform the data reduction in a header-driven manner, allowing all steps to be logged and reproduced easily. The latter involved the creation of two new `python` modules which can be used to read, re-bin, line fit, create line maps, temperature maps, manipulate data cubes and much more, in the interactive `python` environment (`ipython`). The steps involved in running (1) above are discussed in this Section, while Section 3.4 discusses the details of (2).

The process of performing the data reduction is in principle quite simple. The steps involve the acquisition of several calibration frames (dark, bias, & flat-field frames), as well as the science data, for each night of observations. Achieving the necessary level of data quality can prove more difficult. IFS data in particular can be problematic to reduce from individual raw spectra to the final calibrated data products. To this end, ESO has developed a Common Pipeline Library (CPL) in order to aid the reduction for instruments located at VLT. In terms of quickly reducing and examining data, `gasgano` is an ideal tool, however we choose to adopt an automated header-driven approach to reducing the data via `esorex`.

The data reduction of SINFONI data is reliant on obtaining the optimal calibration frames for a particular set of observations. The calibration data, for each setup, are taken during the hours following the science observations. This is with the exception of the standard stars which are obtained close in time, and right ascension, & declination, to the science target. A complete set of calibration images are required to perform the reduction steps, for example: (1) linearity frames (N $\geq$ 24), (2) dark frames (N $\sim$ 3), (3) flat field frames, (4) distortion correction frames (N $\geq$ 80), (5) arc lamp frames, (6) science (plus sky) frames, (7) standard (plus sky) frames, (8) reference frames (ESO-supplied). A typical reduction cascade is illustrated in Figure 3.3 for processing the raw SINFONI data.

The caveat for fully automating a reduction process like this is that the correct

information must be supplied in the image headers and there is an assumption that the raw image is as it should be, i.e., not corrupted. Visual inspection of data frames was carried out prior to using the reduction pipeline.

The bias level for each frame is estimated from four dedicated pixels surrounding the detector. However, if a hot pixel occurs on one of these non-illuminated pixels the mean bias level is over-estimated for that particular line/row. Subtraction of this value leaves visibly dark stripes on the raw data frames. It is recommended that these artifacts are removed prior to reducing the data. A `python` program has been written to remove the dark lines. The program is based on an IDL code provided by ESO in the SINFONI data reduction cookbook (Dumas, 2007). As the code is quite short, it is supplied in Appendix A, for completeness. It is worth noting that in recent revisions (2.3.x) of the SINFONI reduction pipeline these dark line artifacts can also be removed by explicitly setting `sinfoni.general.lc_sw=True` in the each of the configuration files (`sinfo_rec_xxxxx.rc`) located in the `.esorex` directory.

3.3.1 Wavelength Calibration

A wavelength mis-calibration became apparent when calculating the radial velocity of the H_2 1→0S(1) line in the *IRAS* 16594-4656 dataset. A comparison to published literature values from high resolution position-velocity diagrams (e.g., Davis et al., 2005) showed a significant offset between the literature and the SINFONI velocities. It was found that the wavelength calibration from the ESO pipeline can be incorrect by up to a pixel in the wavelength direction (ESO private comm.). A pixel in terms of velocity, at R $\sim$ 5000, corresponds to $\sim$ 30 km s^{-1}, and can lead to large errors when the outflow velocities are low, as is the case for most of my dataset. Similar wavelength errors have been noticed by other authors using SINFONI (e.g., Epinat et al., 2009).

The ESO pipeline calibrates wavelength based on vacuum measurements. A vacuum OH line list[4] supplied reference wavelengths for these data. Figure 3.4 shows the result of over-plotting the reference OH lines against selected sky lines extracted from an ESO datacube. The inset axes shows a clear mis-match between the reference spectrum and the ESO datacube. The wavelength calibration coefficients from the ESO pipeline are given by, C0, C1, C2, and C3 and the wavelength calibration is performed using the equation:

$$\lambda = \mathrm{C0} + \mathrm{C1} \cdot X + \mathrm{C2} \cdot X^2 + \mathrm{C3} \cdot X^3 \tag{3.4}$$

so it is necessary to understand which of these coefficients are affected by the ESO pipeline wavelength calibration error. In the case that it is a simple constant offset, it would be expected that the same shift is measured across the K-band, and so only affect C0 coefficient. The following steps were used to determine if this is the case:

1. Extract from the reduced sky cube, '`out_sky_cube00.fits`', a spectrum of the sky, for this I use a median combination of the selected region.

2. Automatically select sky lines with no close neighbours that might affect line fitting.

3. Remove the slope of the local continuum by fitting a straight line to the background level (20 pixels either side of the line), and dividing this into the data.

[4] `http://www.jach.hawaii.edu/UKIRT/astronomy/calib/spec_cal/oh.html`

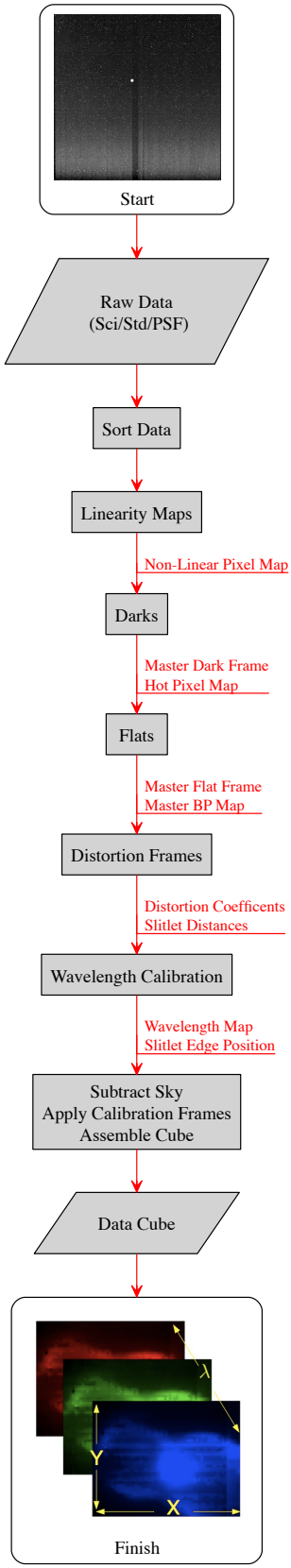

Fig. 3.3: A flow chart of the reduction process of the SINFONI data, starting with the raw data and yielding a wavelength calibrated data-cube. Flux calibration is not performed during this process. The main process flow is shown with outputs of each stage below (in red font) each process.

4. A Gaussian is used to fit each line, in the form of Equation 3.5, where μ returns the line centre, P0 the continuum level, P1 the amplitude of the Gaussian, and σ the standard deviation of the Gaussian.

5. These line centres are then cross-correlated with the reference sky OH lines in order to calculate the offset of each observed line. Examination of the cross-correlation results reveals a constant across the K-band.

6. An average offset and standard deviation is calculated from these results, for example: mean offset of 4.3×10^{-4} μm and standard deviation of 1.5×10^{-4} μm.

$$f(x) = P0 + P1 \cdot \exp\left(-0.5 \cdot \left(\frac{x-\mu}{\sigma}\right)^2\right) \tag{3.5}$$

The mean offset is used to adjust the measured line centres prior to radial velocity calculation. Similarly, the standard deviation is added to the line fitting error to give a velocity error. The above procedure has been carried out for all objects to correct the wavelength calibration.

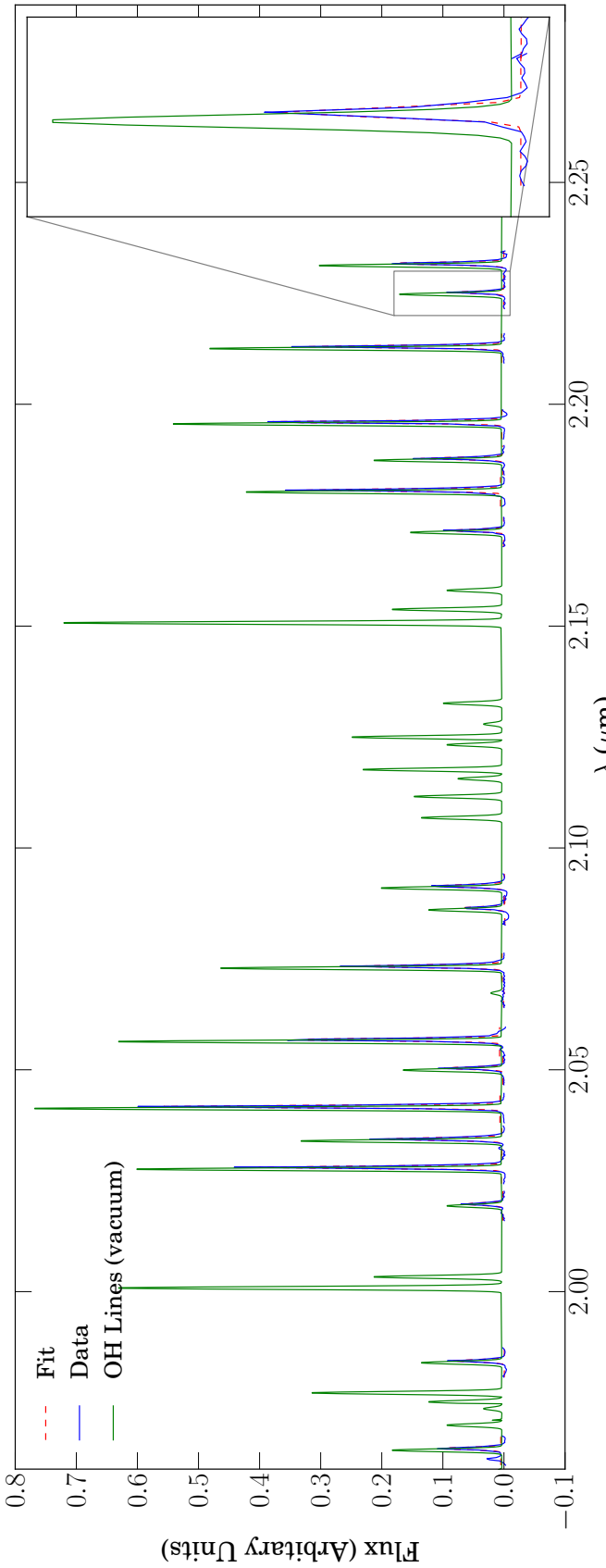

Fig. 3.4: The OH sky lines used to calculate the wavelength offset between the ESO pipeline solution (solid blue line) and an accurate reference line list (solid green line). The inset axes illustrates the offset more clearly. Lines have been normalised for an easier 'by-eye' comparison. The dashed red line gives the Gaussian fit to the observed sky lines – from which we determine the line centres.

3.3.2 Flux Calibration

Although the pipeline provided by ESO is quite powerful, it does not provide a facility for flux calibrating a dataset. Furthermore, the strong telluric absorption features, present in NIR data, need to be corrected, as evident in the K-band at 2 μm in Figure 3.5. The same standard star is used to correct for both the atmospheric absorption features and to flux calibrate the data. Figure 3.5 shows the spectrum of a G3V type standard star (HD 156153). As very few models exist for these types of stars at R=5000, a fit to a lower resolution model is used to correct for the intrinsic slope of the SED of the standard. Small differences are visible between a blackbody at the effective temperature of the standard and that of the model spectrum. A final `python` program has been written to execute existing astronomical software (ds9, STARLINK, VO-SPLAT) to allow these corrections to be applied. The program carries out the following steps :

1. Extracts the total telluric standard star spectra
2. Photospheric features present in the standard are interactively removed
3. A blackbody correction is applied (or a fit to a model spectrum)
4. Atmospheric absorption features are removed from the science data by division of the corrected telluric spectrum.
5. The resulting telluric corrected science data is flux calibrated by multiplying by the 2MASS magnitude of the telluric star, in W m^{-2} μm^{-1}, at the filter effective wavelength (e.g., 2.2 μm for the K-band).

The usual astronomical image viewer tools[5] are useful in examining the processed datacubes.

[5] QFitsview, SAOimage ds9, & GAIA

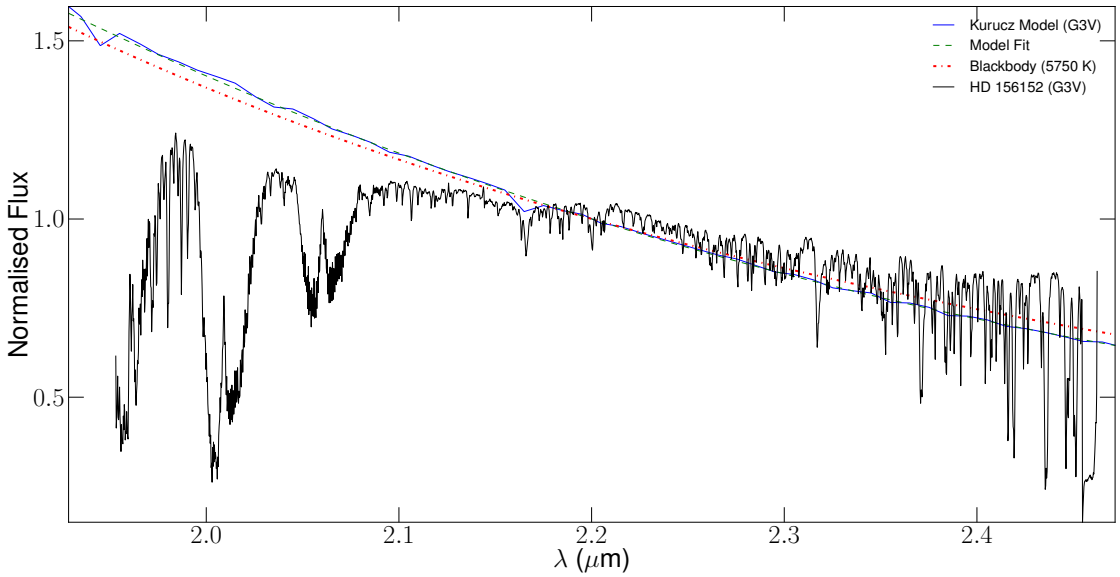

Fig. 3.5: Spectrum of the telluric G3V star (HD 156152) with SED model lines and SED blackbody at 5750 K, superposed. The model spectrum was downloaded from the Castelli and Kurucz spectral atlas located at http://www.stsci.edu/hst/observatory/crds/castelli_kurucz_atlas.html.

3.4 Analysis

This Section contains information on the procedures used to analyse/visualise the NIR datacubes. It is worth noting that many of the lines that emit in the K-band lie on/near the position of strong telluric absorption features. Figure 3.6 gives the position of a selection of lines in the K-band window superimposed on a spectrum of the atmosphere. A high resolution spectrum is resampled and convolved (see Appendix A for program to perform convolution) to match the spectral resolution of SINFONI in order to aid the distinction between 'real' features and atmospheric features.

3.4.1 Flux Measurements

In order to report accurate flux errors on the measured lines, the Signal-to-Noise (S/N) of a line is calculated, following a similar procedure to that outlined in Rosales-Ortega et al. (2012). The following subsection details the steps involved in determining the S/N for each emission line.

Signal-to-Noise Calculation

A statistical S/N value can be calculated through the comparison of the signal or flux level at a particular wavelength, f(λ), to the mean level of noise,σ_{mean}, in regions directly adjacent to that wavelength. This assumes that the adjacent continuum is free from 'real' features and the measured root mean square value truly represents the noise. An estimate for the continuum noise is therefore given by the root mean square value given by the familiar Equation 3.6.

$$\sigma(\lambda)_{\rm cont} = \sqrt{\frac{1}{N}\left(f(\lambda)_1^2 + f(\lambda)_2^2 + \ldots + f(\lambda)_N^2\right)} \tag{3.6}$$

This value is particularly appropriate for the S/N calculation for a spectral continuum region, however for an emission feature or line, this simple S/N value is not appropriate. As the signal for a line is usually found over very few data points each of which are quite distinct from each other, the approximation of a constant signal can not be applied to the S/N calculation for an emission line. The signal, s_{em}, in an emission feature is therefore defined, as given in Equation 3.7, as the pixel-weighted mean of a pixel value at λ_{em} and the mean of the values of two regions of continuum, $f(\lambda)_{c1,2}$, directly adjacent to the emission feature. Where N is the number of pixels across a given line.

$$s_{\rm em} = \frac{1}{N}\sum_{\lambda}[f(\lambda)_{\rm em} - \langle f(\lambda)_{\rm c1}, f(\lambda)_{\rm c2}\rangle] \tag{3.7}$$

The noise calculation for an emission line, n_{em}, consists of a combination of two sources of noise: (1) the mean level of noise in the adjacent continua, $\langle\ \sigma(\lambda)_{\rm c1}\ \sigma(\lambda)_{\rm c1}\ \rangle$, and (2) the contribution of noise from a given emission line, $\sigma(\lambda)_{\rm line}$. The line noise is estimated from the square root of the number of counts at the central wavelength of the emission line as given by Equation 3.8, where k is a constant conversion factor from flux to counts.

$$\sigma_{line} = \left(\sqrt{f(\lambda)_{\rm em}\cdot k}\right)\cdot k^{-1} \tag{3.8}$$

The resulting line error is then added in quadrature to the continuum error, yielding a total emission line error, n_{em}, as given by Equation 3.9.

$$n_{\rm em} = \sqrt{\sigma^2_{\rm cont} + \sigma^2_{\rm line}} \tag{3.9}$$

Finally, the total S/N for the emission line is then given as the ratio of the emission line signal, $s_{\rm em}$, to the total associated noise, $n_{\rm em}$ (see Equation 3.10).

$$\frac{S}{N_{\rm em}} = \frac{s_{\rm em}}{n_{\rm em}} \tag{3.10}$$

The flux error then is given by the line flux divided by the calculated S/N.

Line Fitting

Fitting a spectral emission line with a single (or multiple) Gaussian profile(s) (see Equations 3.5, and 3.11) can be used for construction of line maps to investigate the spatial extent of the emission. In this work the line fitting is carried out using the Levenberg-Marquardt algorithm as implemented in the `python` version of the MPFIT program (Markwardt, 2009). Using this approach four parameters are fitted simultaneously: line peak, continuum, line full width half maximum (FWHM), and centre. The spectral resolution of SINFONI, coupled with the intrinsic low velocity fields in post-AGB nebulae, means that the line profiles show no evidence of line splitting – justifying the use of a single line profile for fitting the data. Typical line FWHM are $\sim 7{\times}10^{-4}$ µm, as such fitting limits on the FWHM are imposed in order to minimise the chance of fitting spurious noise/bad pixels; we restrict the FWHM to the range $2{\times}10^{-4} \rightarrow 1{\times}10^{-3}$ µm. The line FWHM can be calculated as 2.355 $\times\sigma$, where σ is

determined from Equation 3.5.

$$f(x) = P0 + \left[P1 \cdot \exp\left(-0.5 \cdot \left(\frac{x - \mu_1}{\sigma_1} \right)^2 \right) + P2 \cdot \exp\left(-0.5 \cdot \left(\frac{x - \mu_2}{\sigma_2} \right)^2 \right) \right] \tag{3.11}$$

In Figure 3.7 the 1→0S(1) line, from an individual pixel, is shown alongside a crude continuum level estimate from a linear fit of the adjacent continuum regions. Following the extraction of an emission line, it is possible to fit Gaussian or Lorentzian line profiles to the data as illustrated in Figure 3.8. The parameters for a Lorentzian can be determined using Equation 3.12.

$$f(x) = P0 + \left[\frac{P1}{\left(1.0 + \left(\frac{(x-\mu)}{\sigma} \right)^2 \right)} \right] \tag{3.12}$$

Figures 3.10 and 3.9 shows a typical example of fitting a high S/N line and a lower S/N line, respectively. Errorbars show the total emission line noise level in each case. Examination of the residuals (dashed line) in these Figures shows that for a high S/N lines, a single Gaussian does not necessarily fit the data well enough. In fact, in these cases it requires fitting these high S/N lines with two Gaussian profiles to minimise the residuals. To avoid fitting multiple profiles, a S/N limit of 10 is imposed, whereby if the S/N is less than this value the line flux is determined from the fit, according to Equation 3.13.

$$F = P1 \cdot \sigma \cdot \sqrt{2.0 \cdot \pi} \tag{3.13}$$

where F is the flux under the fitted Gaussian in W m^{-2}. For higher S/N lines the `scipy.integrate.trapz` is used to integrate under the line using the composite trapezoidal rule.

This process has proved quite robust provided the line is not resolved (e.g., the double-peaked profile observed in the expanding shells of a PN). All objects presented in this work were carefully examined to ensure that the line profiles met this criterion.

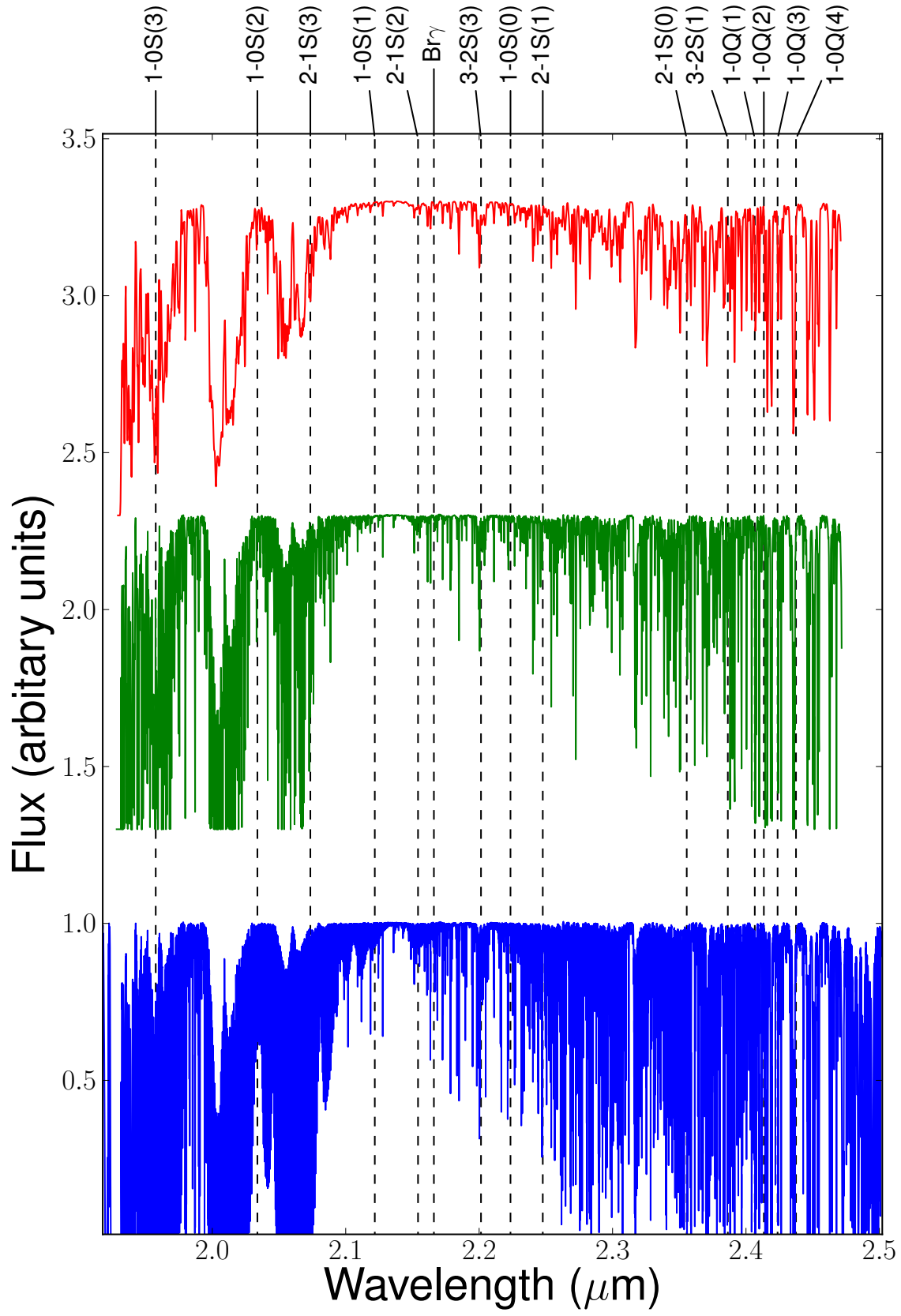

Fig. 3.6: Atmospheric transmission plot for the SINFONI K-band wavelength range. Prominent telluric features are clearly visible (e.g., at $\sim$ 2 µm). The strength of these features is dependent on the amount of water vapour in the atmosphere and distance from the zenith. H_2 lines are shown by vertical dashed lines with labels along top axis. *(Bottom)* High resolution (R$\sim$40,000) K-band transmission spectrum (From: http://www.eso.org/sci/facilities/paranal/instruments/isaac/tools/spectroscopic_standards.html). *(Middle)* High resolution spectrum resampled to wavelength range of the SINFONI K-band. *(Top)* Lower resolution spectrum convolved with Gaussian kernel to match SINFONI resolution.

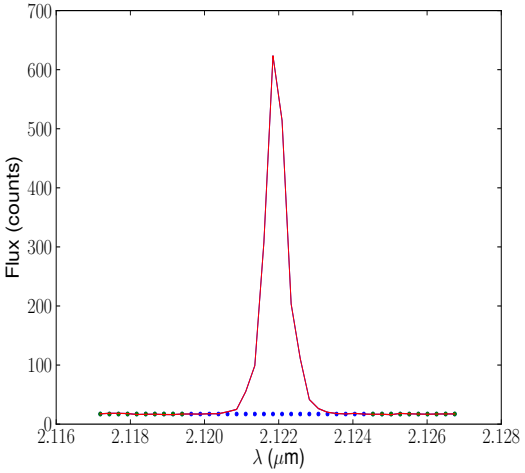

Fig. 3.7: Example of the line extraction from datacube. Dotted line shows background fit. Solid line shows data.

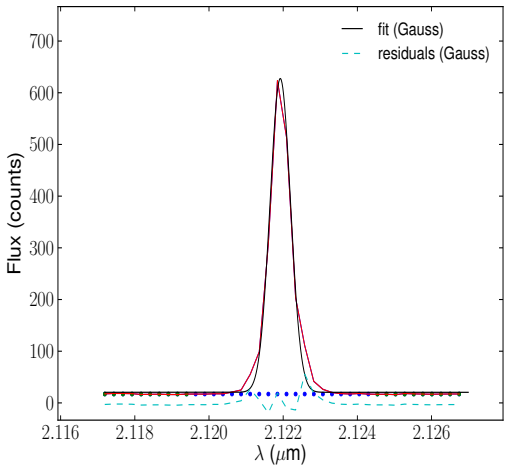

Fig. 3.8: Example fit to the line data. Black solid line shows Gaussian fit to the data. Cyan dashed line shows residuals to the fit. Data is shown by a solid red line.

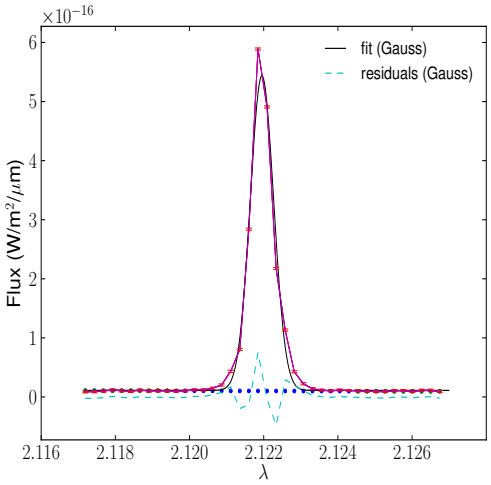

Fig. 3.9: Lines as above. Example of a high S/N line with associated small errorbars calculated from the combination of line and continuum errors.

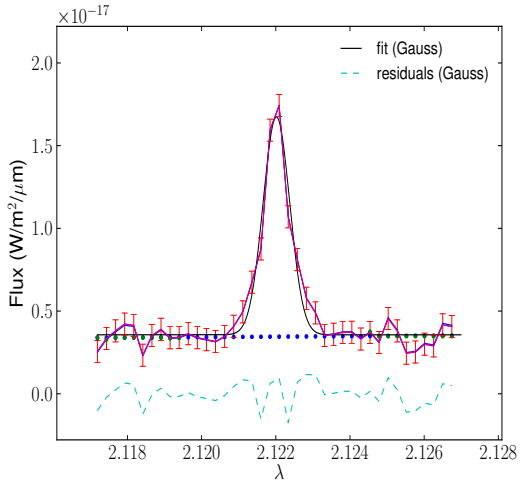

Fig. 3.10: For comparison, a moderate S/N line example, errorbars are computed as in Figure 3.9.

3.5 Shock Model Fitting Techniques

3.5.1 χ-Squared

In order to investigate in more detail the shock parameters, we used the shock models described in Smith & Brand (1990); Smith (1991, 1994). As a first attempt at fitting the shock models to real data, a grid of models was generated for a range of input parameters (see Table 3.3 for details); each density input has a set of velocity models associated with it, ranging from 1 $\rightarrow$ 80 km s^{-1}. The upper velocity limit was chosen as it is the critical velocity ($v_{\rm crit}$) for the lowest gas density used (10^3 cm^{-3}), beyond which the H_2 is dissociated. Grids for two Alfvén velocities, 2 & 4 km s^{-1}, were created. In all models the magnetic field is uniform and perpendicular to the shock direction, with the magnetic field, B, calculated from Equation 3.14:

$$B = 0.54 \cdot \mathrm{n}_H^{1/2} \cdot \mathrm{v}_a \tag{3.14}$$

where B is in units of μG, $n_{\rm H}$ in cm^{-3}, and v_a in km s^{-1}. Both C- and J-shock grids were generated in this fashion.

Table 3.3: Parameter information for the grid of models run using the Smith planar models.

Parameters	Shock Type	
	C-	J-
n_H (cm^{-3})¶	1×10^3 → 9×10^7	1×10^3 → 9×10^7
v_s (km s^{-1})◇	1 → 80	1 → 80
v_a (km s^{-1})	2, 4	—
B-field (μG)	34.2 → 10284.0‡	—
	68.5 → 20567.0*	—
B-mu	1.5708	1.5708

¶ calculated in steps of 2×10$^{3/4/5/6/7}$ cm^{-3}
◇ calculated in steps of 2 km s^{-1}
‡ calculated for v_a = 2 km s^{-1} using equation 3.14
* calculated fot v_a = 4 km s^{-1} .....

The best fit parameters were chosen from a minimisation of the χ-squared statistic of the model and observed line values. However, due to the large parameter space available in the models, using grids of this type does not allow full exploration of the true parameter space.

3.5.2 Markov Chain Monte Carlo Model Fitting

A particularly efficient Bayesian tool for estimating posterior distributions for n–dimensional models is the *Markov Chain Monte Carlo* (MCMC) method.

Literature describing the formalism for MCMC is abundant (e.g., Gregory, 2005, and references therein) and so only a short introduction is provided here, covering key concepts central to the method. Equation 3.15, also known as Bayes' theorem, is the

most important formula for performing Bayesian inference.

$$P(M \mid D, I) = \frac{P(M \mid I)P(D \mid M, I)}{P(D \mid I)} \tag{3.15}$$

where M represents the model hypothesis, D some observed data, and I the prior information. The prior probability, $P(M \mid I)$, is the probability of the model *without* prior knowledge of the data. Conversely, the posterior probability, $P(M \mid D, I)$, is the probability of the model *with* information from the data. The denominator in Bayes' theorem, $P(D \mid I)$, is the global likelihood for the full class of models. $P(D \mid I)$ also plays the role of a normalisation constant, due to the fact that the sum of the posterior probabilities over the hypothesis space of interest must equal to one.

$$\sum_i P(M_i \mid D, I) = \frac{\sum\limits_i P(M_i \mid I)P(D \mid M_i, I)}{P(D \mid I)} = 1 \tag{3.16}$$

Such that,

$$P(D \mid I) = \sum_i P(M_i \mid I)P(D \mid M_i, I) \tag{3.17}$$

the global likelihood value for a given model can be ratioed against the global likelihood of any other model in order to attempt to favour one model over the other. This ratio is known as the Bayes' factor and is used in the special case where the priors are identical. It is important to note that a more complex form of the Bayes' factor called the Odds ratio must be used when the priors are different.

One term in Equation 3.16 has been ignored so far, this is the $P(D \mid M, I)$ term. In words this is the probability of obtaining the data, D, given that some model hypothesis, M, and prior information, I, are true. This is also known as the likelihood function, $\mathcal{L}$(M), and it is proportional to the probability the model given the data and some priors. In this work the model of interest is the column density ratio (CDR) for a set of H_2 lines, and so it is possible to replace M and D in the previous equations with $\mathrm{CDR_{mod}}$, and $\mathrm{CDR_{obs}}$, respectively. Thus, the likelihood $\mathcal{L}$(M) becomes $\mathcal{L}(CDR_{\mathrm{mod}})$, as given in Equation 3.18.

$$\begin{aligned}
\mathcal{L}(CDR_{\mathrm{mod}}) &= P(CDR_{\mathrm{obs}_1} \ldots CDR_{\mathrm{obs}_N} \mid CDR_{\mathrm{mod}}, I) \\
&= P(CDR_{\mathrm{obs}_1} \mid CDR_{\mathrm{mod}_1}, I) \ldots P(CDR_{\mathrm{obs}_N} \mid CDR_{\mathrm{mod}_N}, I) \\
&= \prod_{i=1}^{N} P(CDR_{\mathrm{obs}_i} \mid CDR_{\mathrm{mod}_i}, I)
\end{aligned} \tag{3.18}$$

To determine this likelihood value analytically is a complex task, and so a Monte Carlo approach is adopted. It can then be shown, given any probability distribution $P(x)$ in the interval $a \leq x \leq b$, that

$$\int_a^b P(x)dx = \frac{1}{N}\sum_i^N P(X_i) \tag{3.19}$$

by drawing N uniform distributed random variables X_i in the same range, commonly known as Monte Carlo integration. This technique can be applied to the likelihood

function in Equation 3.18 to integrate over the product of the probability distribution for the observed data ($CDR_{\rm obs}$) and the probability distribution for the model ($CDR_{\rm mod}$), yielding an equation for the likelihood given by

$$P(CDR_{obs_i} \mid CDR_{{\rm mod}_i}, I) = \frac{1}{N}\sum_{i=1}^{N} \exp\left[\frac{-(CDR_{{\rm obs}_i} - CDR_{{\rm mod}_i})^2}{2\sigma^2_{{\rm obs}_i}}\right] \tag{3.20}$$

under the assumption that $CDR_{{\rm obs}_i}$ has Gaussian scatter (Mullin & Hardcastle, 2009).

This sort of Monte Carlo approach is fairly simple to implement. The only major requirement being that the parameter space, from which a random distribution of N points is drawn, is large enough to contain all regions where the contribution of $P(X_i)$ (e.g., Equation 3.19) to the integral is large. However, performing this sort of analysis is CPU time-intensive as the N points are randomly chosen and independent — this can lead the method to spend considerable time/resources in regions of low probability. As the number of parameters increases this method rapidly becomes computationally expensive. However, the samples need not be drawn independently. Metropolis et al. (1953) proposed an algorithm, which was later generalised by Hastings (1970), to allow the non-independent samples to be drawn from the target distribution, in this work: $P(CDR_{\rm mod} \mid CDR_{\rm obs}, I)$. This requires the construction of a Markov-Chain, which is a sequence of random variables whereby the next value in the chain is dependent only on the previous value. The chain is initiated at some value and run for a sufficiently long time for the affect of the choice of the initial value to be 'forgotten'. At this point, a.k.a post burn-in, the generated samples will then have a probability density equal to the desired posterior probability, and can be used to perform the Monte Carlo integration.

Model Parameter Estimation

Equation 3.15 allows the production of probability density functions (PDFs) for however many parameters one is interested in, for example in this work, the parameters of interest are (1) the density, (2) the shock velocity, (3) the H_2 fraction, (4) Alfvén velocity, and (5) the ionisation fraction. However, this approach only returns the Bayesian solution to the parameter estimation problem, which is a posterior PDF for each parameter. It is of course, common to give a point estimate determined from the posterior PDF which represents a best-fit value plus some errors. The Bayesian estimators, mean, median or mode, can be used to assign most likely values. In this work the median is used as the Bayesian estimator instead of the mean for the posterior distributions. This takes advantage of the property of a normal distribution whereby the mean and the median will be the same. In skewed distributions the median provides a good estimate of the best-fit value.

Credible Interval Calculation

It is possible to define a region of parameter space, for a given confidence level (e.g, C = 68% or 0.68), such that the posterior probability of the parameter lying in this region is C. This interval is more commonly known as the *credible region* for a parameter.

Once an MCMC model has been run, it is straightforward to compute the credible interval for each parameter from the results. For any given parameter, θ, the posterior probability function is binned, bearing in mind the choice of bin size can affect the

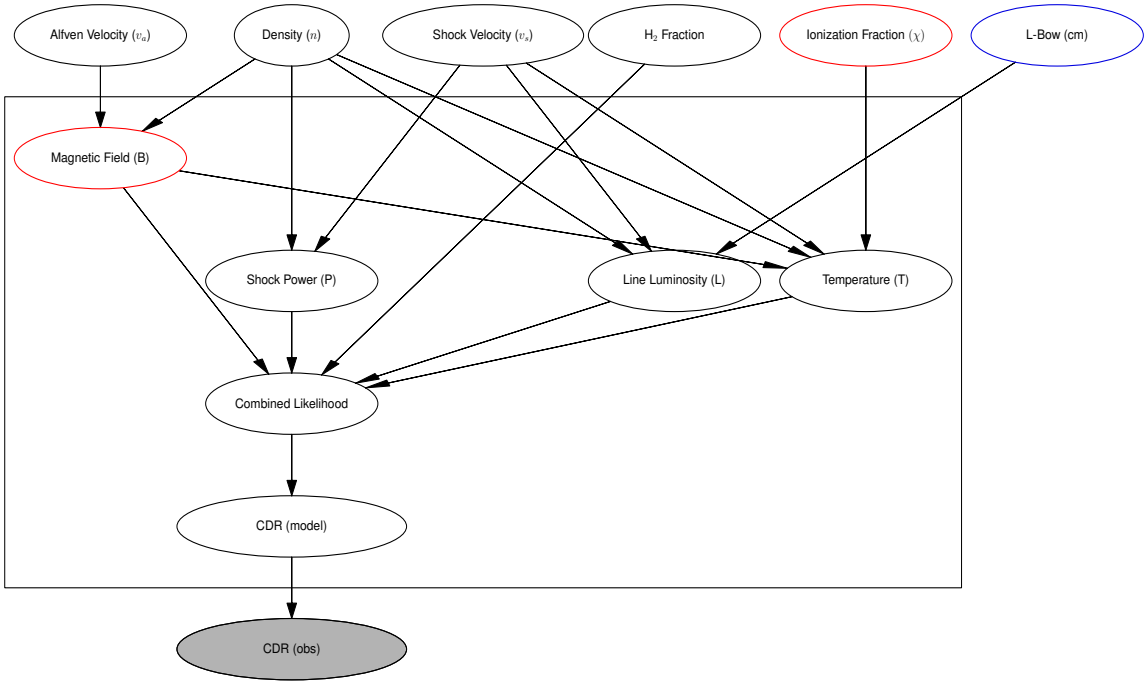

Fig. 3.11: A Bayesian network diagram showing the various dependencies between the variables in the MCMC inference model. The plate (square) encompasses the nodes for which individual likelihoods are not calculated. A combined likelihood value is used for the combination of the effect of each node. The red bordered nodes show the parameters associated with C-type models only. The blue node is the L-value for a paraboloid used to convert model flux to Luminosity. White nodes have a deterministic state while the grey node represents measurements.

results. The binned data are then normalised to produce a probability density function at each bin. These probabilities, p_i, are then sorted (largest to smallest) and the corresponding binned parameter values, θ_i, are moved accordingly to maintain the p_i – θ_i pairing. The binned probability density function is then multiplied by the width of bin, so that the cumulative sum of the resulting values is one. Starting with the largest probability value, successive values of p_i are added together until the required confidence level is reached (C=0.68). A credible interval can be estimated from the minimum and maximum values of θ_i that lie in the range $0 \leq i \leq N$, where N is the location where sum of p_i equals C.

3.5.3 Simulated Data

In order to test the effectiveness of the above MCMC fitting procedure, two different models were used, with differing numbers of free parameters, to generate a simulated shock model, and used as input for the MCMC code, as explained below.

Model Parameters and Priors

A J-type planar model, $JPLANAR$, was chosen, with three free parameters. And a C-type planar model, $CPLANAR$, was chosen with three and four free parameters. Table 3.4 gives the details of the input parameters used in these models.

The planar models return line fluxes in per unit area of the shock front (erg s^{-1} cm^{-2}). Relative errors were calculated from the observed H_2 lines, in order to assign

Table 3.4: Input model parameters for simulated shocks.

Parameter	Value			
	J-planar	C-planar	C-Bow	J-Bow
H Density, n (cm^{-3})	1×10^6	1×10^5	1×10^5	1×10^4
Molecular Fraction, f	0.25	0.4	0.2	0.4
Alfvén velocity, v_a (km s^{-1})	2	5	3	2
Magnetic Field, B (mG)	1.1	0.85	0.2	0.11
Shock Velocity, v_s (km s^{-1})	15	35	40	9
Field Angle, μ	90°	90°	0°	0°
Ion Fraction, χ	—	1×10^{-7}	1×10^{-7}	—
L-Bow (cm)	—	—	1×10^{16}	1×10^{15}
H_2O Abundance	0	0	0	0
CO Abundance	2×10^{-4}	2×10^{-4}	2×10^{-4}	2×10^{-4}
O Abundance	4×10^{-4}	4×10^{-4}	4×10^{-4}	4×10^{-4}
C Abundance	2×10^{-4}	2×10^{-4}	2×10^{-4}	2×10^{-4}

a flux error to the H_2 model lines, thus simulating real data. Using these errors, random values are drawn from a normal distribution in order to add some noise to the simulated flux values, where the simulated flux is used as the mean, and the error as the standard deviation of the distribution. These simulated H_2 fluxes (plus errors) were then converted into column density ratio values (following the method discussed in Section 2.5.3) suitable for use as input to the MCMC fitting procedure.

The choice of sensible prior values is critical for the use of Bayes' theorem. The top-level nodes in Figure 3.11 show the priors, and their relationship to other sub-nodes, that are used in this work. Once the prior values have been considered, it is equally important to consider the *type* of prior to be used. The prior for an unknown parameter, T, can be either in the form of (1) a uniform prior, or (2) a Jeffrey's prior. The main difference between the two types is that the Jeffreys prior is scale invariant, meaning that if the prior parameter space is large, all values are equally probable (Gregory, 2005). Conversely, the use of a uniform prior requires that care is taken to ensure that the parameter space of T is not too large. As discussed below, all unknown parameter priors (T) in this work are assumed to be uniform, $\mathcal{U}$, in the range $T_{\min} \leq T \leq T_{\max}$ (see Table 3.5). Details of individual priors are:

n : In PPNe there can exist regions of various densities depending on the location in the shell. For example, in nebulae where the ends of the lobes have been 'blown off' by a fast wind, at the same time the edges of the lobes can consist of denser swept-up material – there are a large range of possible values for the pre-shock density. For this reason the pre-shock density is assumed to be uniform; the densities are given in the logarithm form to reduce the range and hence avoid problems associated with large uniform ranges.

v_s : Although there is much literature on the topic of shock velocities in astrophysical nebulae, it is not clear that there is a particular distribution of velocities that could be used as a sensible prior. The shock velocity prior distribution is therefore uniform.

Table 3.5: Priors used in the J- & C-shock MCMC fitting.

Parameter	Value	
	J	C
P(n)	$\mathcal{U}$(3,7)	$\mathcal{U}$(3,7)
P(f)	$\mathcal{U}$(0.1,0.5)	$\mathcal{U}$(0.1,0.5)
P(v_a)	$\mathcal{U}$(2,10)	$\mathcal{U}$(2,2)*
P(v_s)	$\mathcal{U}$(4,30)	$\mathcal{U}$(10,70)
P(χ)	$\mathcal{U}$(-7,-3)	—†
P(L_{Bow})	$\mathcal{U}$(13,17)	$\mathcal{U}$(13,17)

* Alfvén velocity is fixed at 2 km s^{-1} in J-shocks.
† Ion fraction is not a variable input parameter in J-shocks.

v_a : The Alfvén velocity is proportional to the magnetic field strength (see Equation 3.14), and to date only a few measurements exist for this quantity in PPNe (Bains et al., 2003). Using these values as a guide (2 – 4 mG), the Alfvén velocity parameter space is uniform between 2 and 10 km s^{-1} for C-type shocks, and fixed at 2 km s^{-1} for J-type shocks.

f : The H_2 fraction parameter space is assumed to be uniform in between 0.1 and 0.5. The lower the value the more H atoms present in the gas, which in turn raises the H_2 excitation closer to LTE because H-atoms can penetrate deeper into the potential well of the H_2 than a fellow H_2 can.

χ : The value of an ion fraction is a critical difference between C- and J-type shocks. In general, the higher this value, the lower the 'cushioning' effect of the magnetic field. The range of priors is assumed to be uniform in the logarithm between -7 and -3; Higher values cause a C-shock to mimic a J-shock.

$L_{\rm bow}$: This is the semi-rectum for a paraboloid/parabola. This is half the length of a chord through a focal point parallel to the conic section directrix of a paraboloid/parabola. Hence, when using the bow shock code, the given output fluxes should be multiplied by $L_{\rm bow}^2$ to give the total luminosity of a bow. Again, the prior values are drawn from a uniform distribution in logarithm space.

Discussion

Some results of these simulations are presented in Figures 3.12 – 3.18. Figure captions distinguish each type of shock simulated and the best-fit values can be compared to those in Table 3.4. Error estimates on the fitted parameters are given by the credible regions marked by shaded regions in the 1-d posterior probability distributions. Finally, the simulated data points are superposed on the best-fit model using the determined model parameters. The planar shocks run relatively quickly and so several versions of the fitting are presented here. Parameters are held at a fixed value and added one-by-one to try to judge the effect they are having on the results; these are shown as empty

histograms in the 1-d plots. In general the addition of parameters tends to 'blur' the parameter space, as can be seen clearly in the 2-d distributions.

Although the results appear to reproduce the input values in most cases, these diagrams and Bayesian estimators should not be used blindly and a good understanding of the mechanisms at work in shocks is vital. A clear example is given by the three successive *CPLANAR* plots (Figures 3.14 – 3.16). In the first of these figures, only the density, shock velocity and H_2 fraction are allowed to vary. The Baysesian estimators for the density and shock velocity clearly recover the original input values. The H_2 fraction is not as well recovered. Nevertheless, using these values the model CDR fits the data quite well. In the following plot the ionisation fraction is included as a free parameter, and the model is re-run. In two-dimensions the 'blurring' effect is obvious and also the density and shock velocity estimates have changed slightly. The shock velocity drops by more than 5 km s^{-1}, while the density increases slightly. The best-fit ionisation fraction is determined to be higher than the input value. This suggests that a better fit is found than the original model parameters. However, the most likely reason is that increasing the ionisation fraction reduces the effect of the magnetic field and to compensate the model drops the shock velocity and increases the density. In the final plot in the sequence the Alfvén velocity is added as a free parameter. The model returns sensible estimates for shock velocity and density, however favours a higher Alfvén velocity and ionisation fraction than their respective input values. A similar case as described above is the most likely explanation except the increased Alfvén velocity is compensating for the higher fraction of ions.

MCMC Computing Requirements

Running this type of MCMC analysis is highly computing intensive. This is due the MC approach requiring hundreds of thousands of samples to be drawn, coupled with the fact that each shock model takes of the order of seconds to minutes to run (model dependent). In order to perform such an analysis in a reasonable time, the multi-threaded version of the Metropolis-Hastings algorithm, as described in Mullin & Hardcastle (2009), is used. This implementation divides into a single master and multiple slave threads at run-time. This fact is used to exploit the computing power of the University of Hertfordshire's computer cluster, whereby the MCMC will take a large portion of the cluster to run each analysis, with information exchange between threads. Table 3.6 gives the typical resources required for each model. It is clear that the planar-shock analysis runs much quicker than the bow-shock analysis, due to the fact that each bow is essentially the sum of multiple planar shocks.

The available computing cluster architecture consists of:

- 48 Xeons (E5520s) 2 socket x 4-core (no hyperthreading) with 24 Gb RAM and DDR Infiniband
- 16 Xeons (X5650s) 2 socket x 6-core (no hyperthreading) with 24 Gb RAM and QDR Infiniband
- 16 Xeons (X5675s) 2 socket x 6-core (no hyperthreading) with 24 Gb RAM and QDR Infiniband

Further information can be found at University of Hertfordshire cluster computing website (`http://stri-cluster.herts.ac.uk/wiki/index.php/Main_Page`).

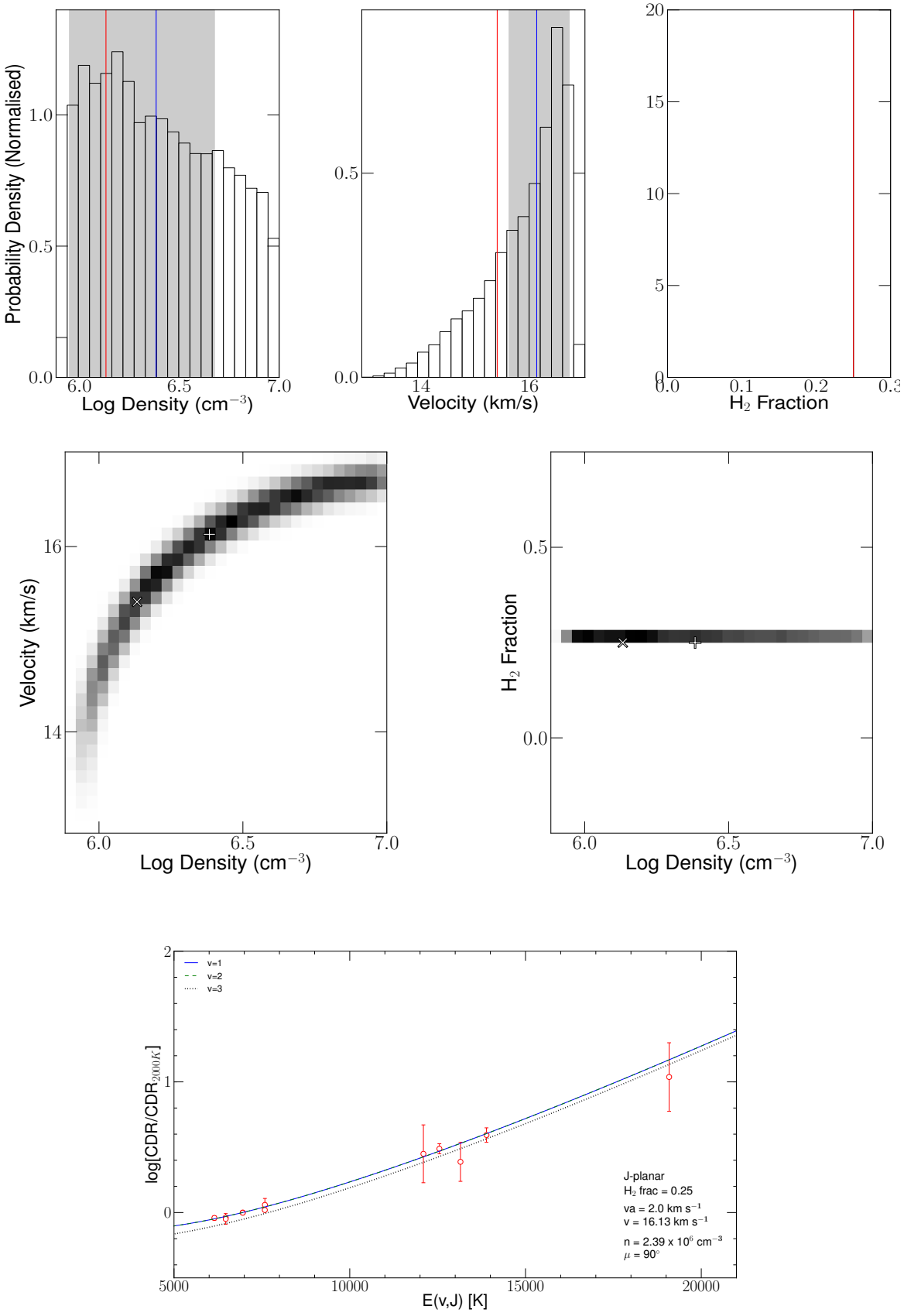

Fig. 3.12: *JPLANAR* model. (*top*) The 1-dimensional posterior probability density distribution for the MCMC fitting to the simulated model CDR values. The red solid vertical line gives the location of the best fit values, while the blue solid gives the location of the Bayesian estimator. The credible intervals for each parameter are marked by the shaded regions. (*middle*) The 2-dimensional posterior probability distributions marginalised over all other parameters. The location of the white plus sign, '+', and the white cross sign, '×', mark the positions of the mean of the distribution, and the best fit values, respectively. (*bottom*) The input CDR data points with best-fit model lines over-plotted. Fit parameters are annotated to the figure. Table 3.4 gives input values.

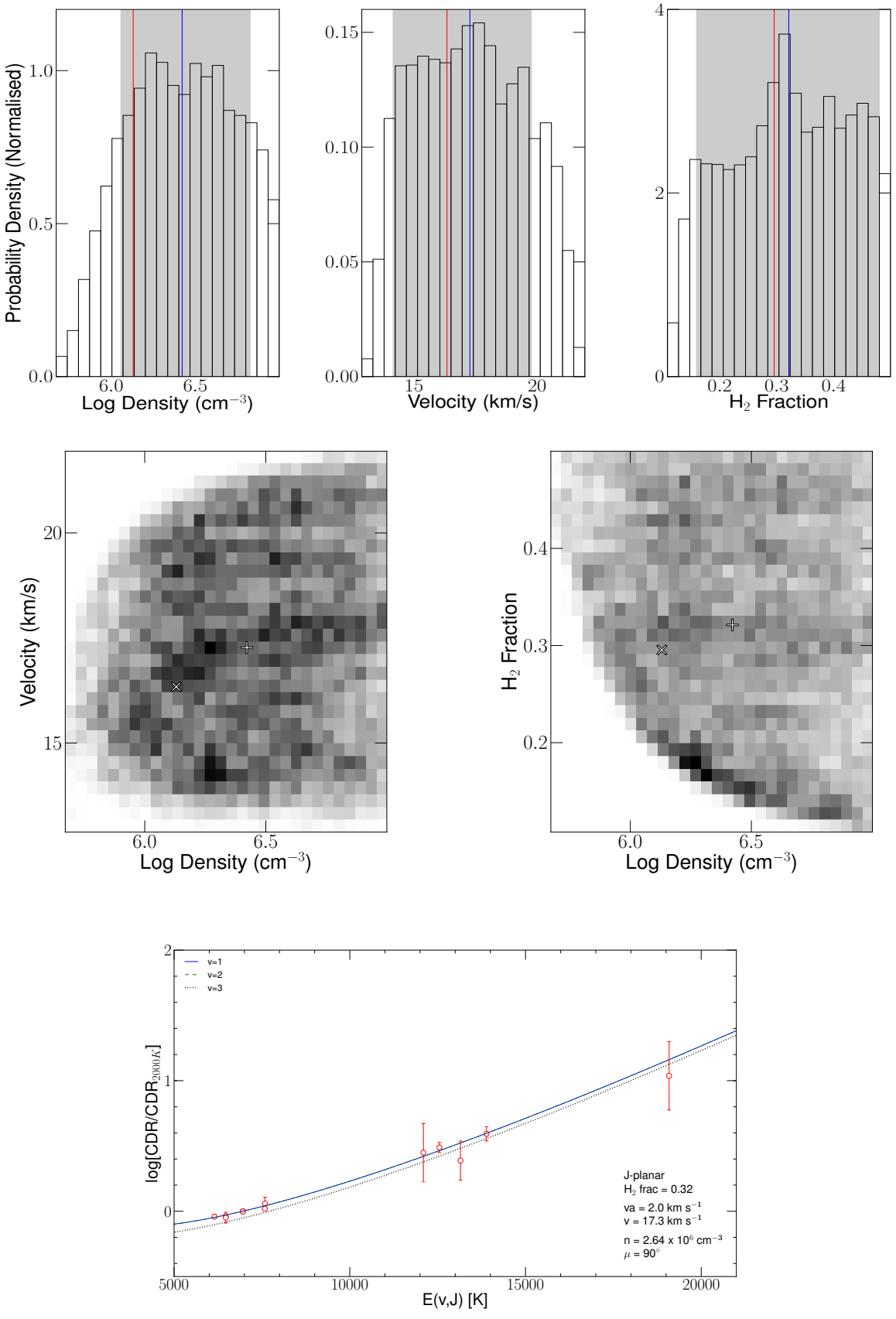

Fig. 3.13: *JPLANAR* model, with H_2 fraction allowed to vary. Details given as in the caption of Figure 3.12.

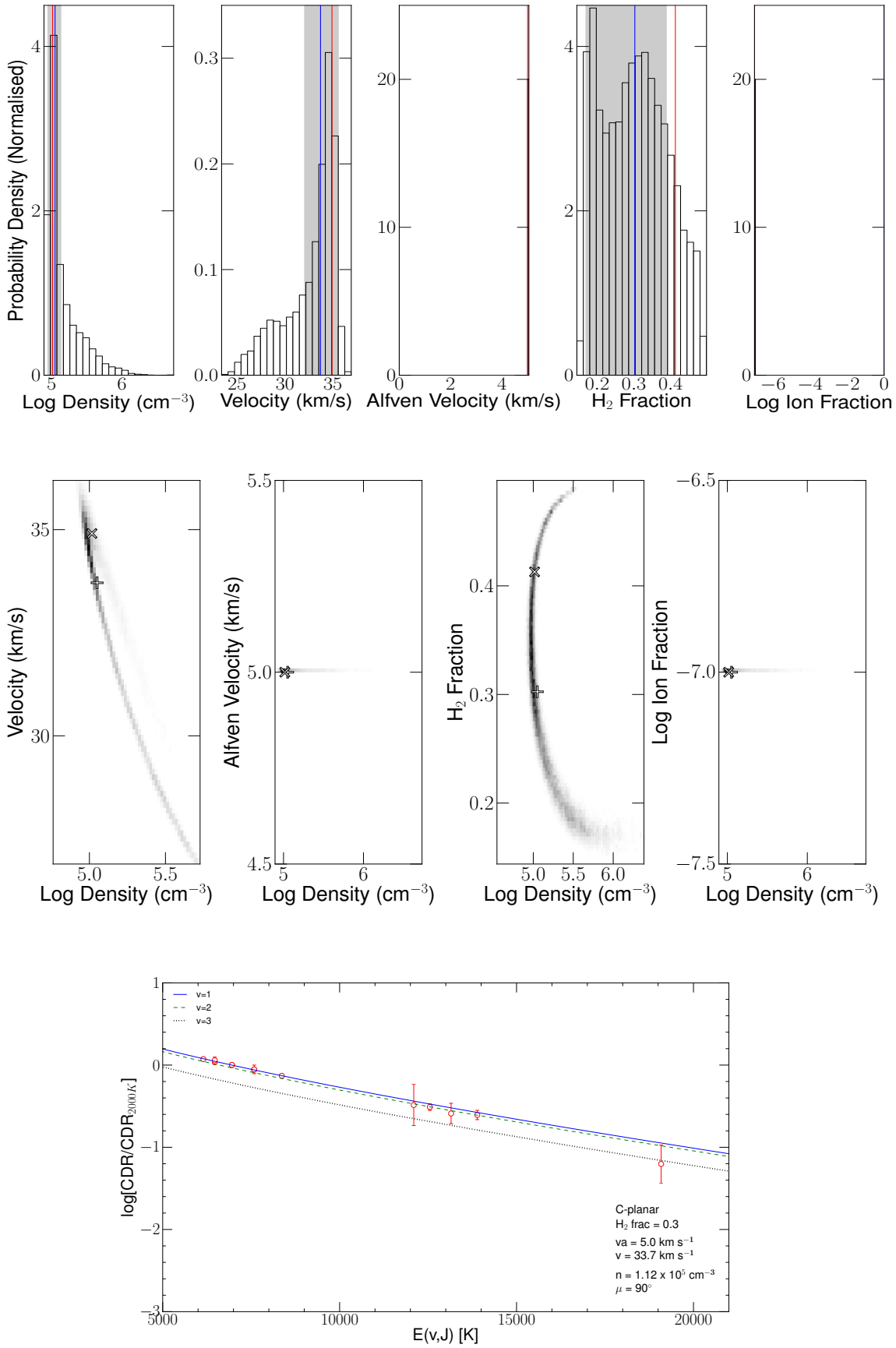

Fig. 3.14: *CPLANAR* model. Details given as in the caption of Figure 3.12. Ion fraction and Alfvén velocity held at 1×10^{-7} and 5 km s^{-1}, respectively.

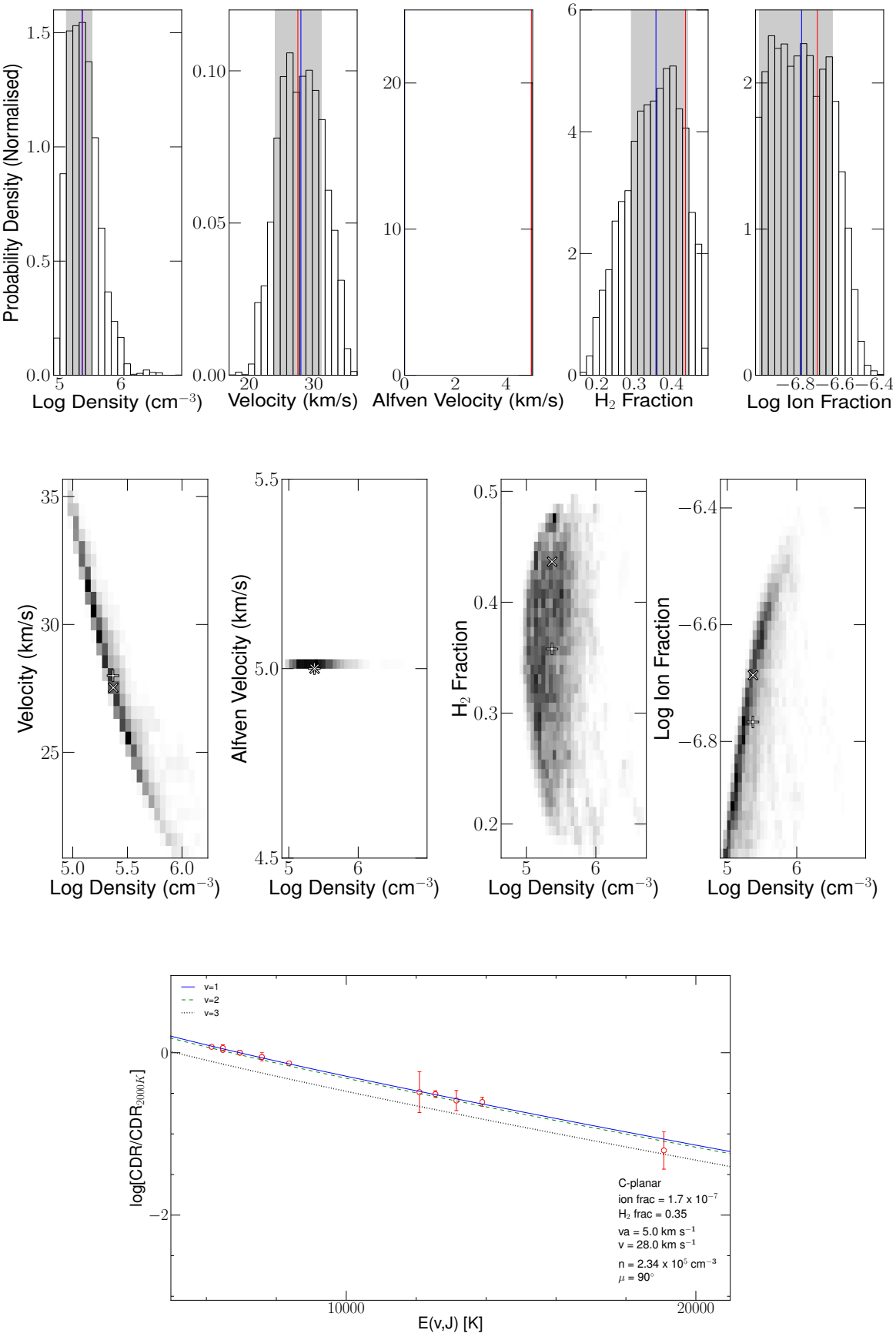

Fig. 3.15: *CPLANAR* model. Details given as in the caption of Figure 3.12. Alfvén velocity is held at 5 km s^{-1}, while ion fraction is given as a free parameter.

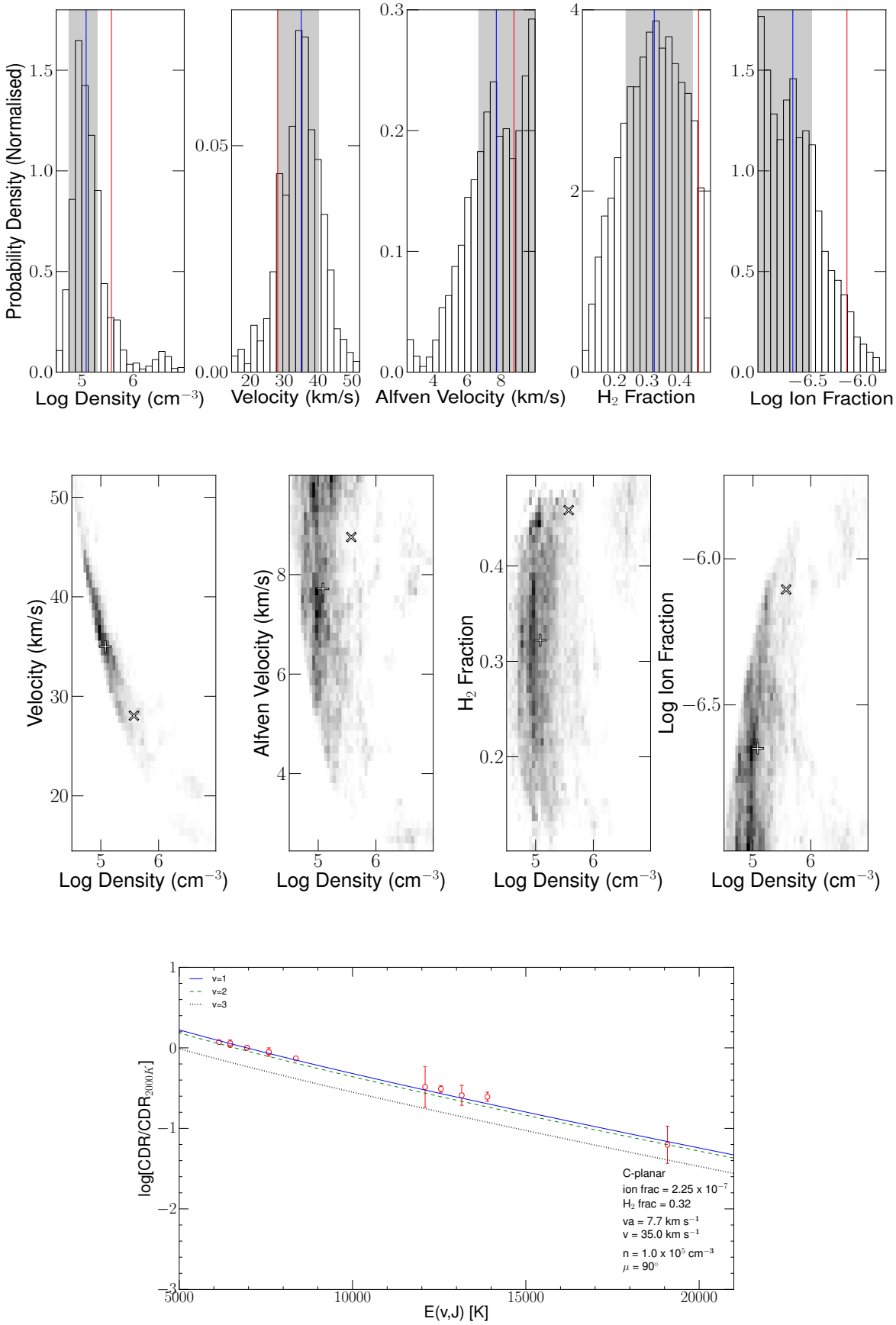

Fig. 3.16: *CPLANAR* model. Details given as in the caption of Figure 3.12. Ion fraction and Alfvén velocity are given as free parameters.

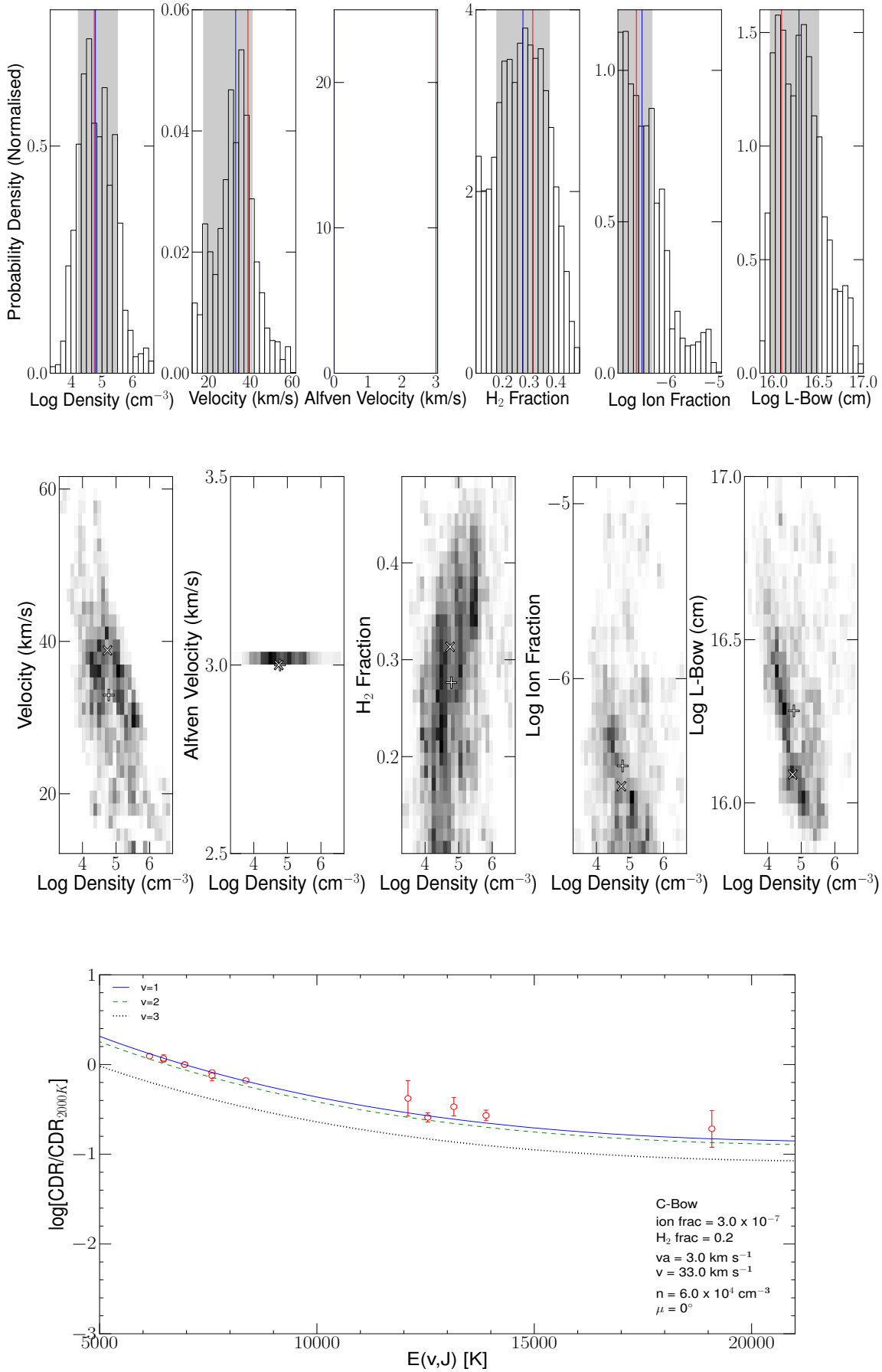

Fig. 3.17: *CBOW* model. Details given as in the caption of Figure 3.12.

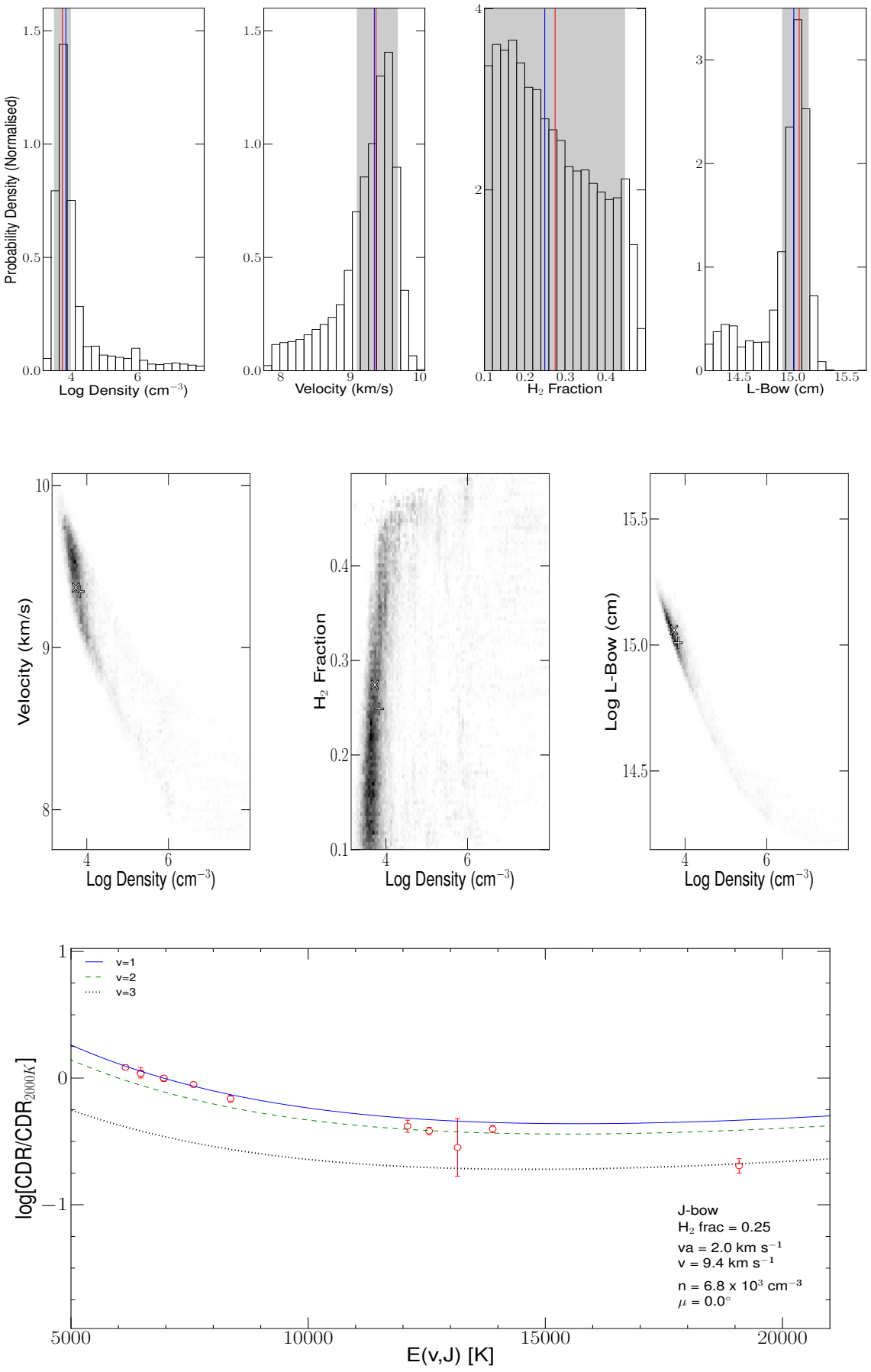

Fig. 3.18: *JBOW* model. Details given in the caption of Figure 3.12.

Table 3.6: Approximate computing resources required to run MCMC analysis.

Model	Number of free parameters	Number of CPU's	Time (hrs)
$JPLANAR$	3	80	6
$JBOW$	3	128	25
$CPLANAR$	5	80	7
$CBOW$	5	128	12

3.6 Future Work

With the exception of radio data, most generic astronomy software (e.g., IRAF) is geared toward 1- and 2-D data. With more and more telescopes offering some form optical/NIR integral field mode, it is essential that one can efficiently deal with the data. To this end I have developed a proto-type of a Graphical User Interface (GUI) for some of the code I have written throughout my PhD. At present the GUI is packaged as a single executable/binary file which runs (simply by double-clicking) on any Windows/Mac OSX, and Linux (Fedora 16) machines, allowing easy deployment of the software. The GUI is written using the `python` binding to the QT GUI toolkit — PyQT[6]. Figure 3.19 shows the interface (version 1.0.0), which allows reading in of datacubes, extraction of lines, interactive plotting tools (e.g., zoom/pan, data selection), single- or multiple-component line fitting, and sliders to examine different cube (x,y) locations. However, my aim would be to leave a piece of self-contained datacube analysis software that astronomers at the University of Hertfordshire could use for many years to come. This would involve adding the rest of my previously written code to the GUI (e.g., flux-calibration, extinction calculations, temperature plots, etc.), along with more comprehensive line lists and model atmospheres. This would give our astronomers a great advantage in the field of optical/NIR datacube analysis tools – possibly leading to the release of a software package for public download.

[6] http://www.riverbankcomputing.co.uk/software/pyqt/intro

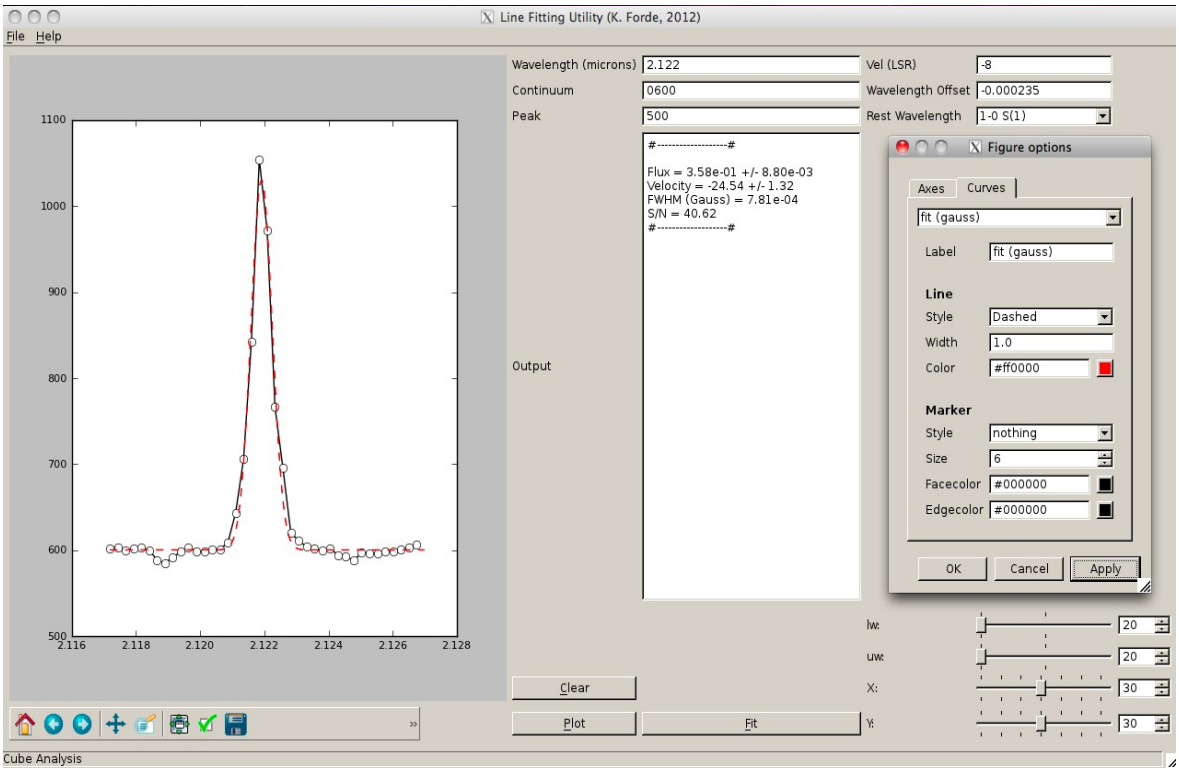

Fig. 3.19: A Graphical Analysis Interface developed for the analysis of NIR datacubes (Line-fitting, flux measurements, black-body & flux correction).

References

Bains, I., Gledhill, T. M., Yates, J. A., & Richards, A. M. S. 2003, MNRAS, 338, 287

Davis, C. J., Smith, M. D., Gledhill, T. M., & Varricatt, W. P. 2005, MNRAS, 360, 104

Dumas, C. 2007, in ESO Document No. VLT-MAN-ESO-14700-4037. Issue date 26/10/2007

Eisenhauer, F., Abuter, R., Bickert, K., Biancat-Marchet, F., Bonnet, H., Brynnel, J., Conzelmann, R. D., Delabre, B., Donaldson, R., Farinato, J., Fedrigo, E., Genzel, R., Hubin, N. N., Iserlohe, C., Kasper, M. E., Kissler-Patig, M., Monnet, G. J., Roehrle, C., Schreiber, J., Stroebele, S., Tecza, M., Thatte, N. A., & Weisz, H. 2003, in Society of Photo-Optical Instrumentation Engineers (SPIE) Conference Series, Vol. 4841, Society of Photo-Optical Instrumentation Engineers (SPIE) Conference Series, ed. M. Iye & A. F. M. Moorwood, 1548, 1561

Epinat, B., Contini, T., Le Fèvre, O., Vergani, D., Garilli, B., Amram, P., Queyrel, J., Tasca, L., & Tresse, L. 2009, A&A, 504, 789

Gregory, P. C. 2005, Bayesian Logical Data Analysis for the Physical Sciences: A Comparative Approach with 'Mathematica' Support (Cambridge University Press)

Hastings, W. 1970, Biometrika, 97

Markwardt, C. B. 2009, in Astronomical Society of the Pacific Conference Series, Vol. 411, Astronomical Data Analysis Software and Systems XVIII, ed. D. A. Bohlender, D. Durand, & P. Dowler, 251

Metropolis, N., Rosenbluth, A. W., Rosenbluth, M. N., Teller, A. H., & Teller, E. 1953, J. Chem. Phys., 21, 1087

Mullin, L. M. & Hardcastle, M. J. 2009, MNRAS, 398, 1989

Rosales-Ortega, F. F., Arribas, S., & Colina, L. 2012, A&A, 539, A73

Smith, M. D. 1991, MNRAS, 252, 378

—. 1994, MNRAS, 266, 238

Smith, M. D. & Brand, P. W. J. L. 1990, MNRAS, 242, 495

Chapter 4: Discovery of shocked H_2 around OH 231.8+4.2

4.1 Introduction

OH 231.8+4.2 (hereafter OH231) is an O-rich late spectral type (M) central star (Mira variable, QX Pup) with bipolar high-velocity dust and gas outflows (Alcolea et al., 2001), filamentary structures observed in scattered and molecular line emission, and large angular size ($10''\times60''$). Often labelled as a post-AGB object or pre-planetary nebula, the presence of both a Mira central star and a main-sequence companion of spectral type A (Sánchez Contreras et al., 2004) seems to contradict this classification. OH231 is more likely a D-type bipolar symbiotic system (Frew & Parker, 2010). However in some cases, morphological similarities do exist between post-AGB and symbiotic objects, most strikingly the presence of highly collimated bipolar nebulae. It is via fast-collimated outflows that these stars shape their surrounding nebula. Understanding the development and origin of these fast outflows is critical for advancing hydrodynamical models of wind interaction. Recent work by Lee et al. (2009) attempting to reproduce the high velocity molecular emission in AFGL 618 using collimated fast wind models, emphasises the need for further observations and model development in this area.

OH231 has been the subject of many studies spanning multiple wavelength ranges, for example: Cohen et al. (1985) were first to propose the existence of a binary companion; Bujarrabal et al. (2002) imaged the shape of the shocks using Hα (reproduced in Fig. 4.1 [a]) detected with the *Hubble Space Telescope (HST)*; Meakin et al. (2003) report *HST*/NICMOS NIR images of the dust distribution and hence a high resolution map of the extinction through the nebula. More recently, Matsuura et al. (2006) using the MIDI and NACO instruments on the Very Large Telescope (VLT) detected a compact circumstellar disc. The envelope of OH231 is also known to be rich in molecular species (e.g. H_2O, OH, and SiO) however previous studies in the NIR have all returned null detections of H_2 (e.g. Weintraub et al., 1998; Matsuura et al., 2006).

In this chapter, we present the results of preliminary observations of OH231 at NIR (K-band) wavelengths showing for the first time the presence of shock-excited H_2. Throughout this work we assume OH231 is a member of the open cluster M46 at a distance of 1.3 kpc (Jura & Morris, 1985). The origin of the coordinate system used in Figures 1,3, and 4 is given by the location of the SiO maser emission at RA=$07^h42^m16^s.93$, Dec=-14°42′50″.2 (J2000) (Sánchez Contreras et al., 2002), and the inclination angle of the bipolar axis is 36° to the plane of the sky (Kastner et al., 1992).

4.2 Observations and Data Reduction

The data were taken using the SINFONI (Eisenhauer et al., 2003) instrument located on UT4 of the VLT at Paranal, Chile, on the $1^{st}/2^{nd}$ Feb 2010. We use the lowest resolution mode (LRM), corresponding to the widest field-of-view ($8''$ x $8''$) with adaptive optics (AO) and a natural guide star (NGS). A plate scale of 250×125 mas pixel^{-1}, and a spectral and velocity resolution of 4580 and 66 km s^{-1}, respectively, are available at this resolution (for a dispersion of 2.45 Å/pix and line FWHM of 1.96 pixels). All

Table 4.1: Details of the VLT/SINFONI observations for OH231 and the telluric standard stars taken on 1st/ 2nd February 2010.

	OH231				HD	
	South	Central		North	75004	63487
Tot. Exp. (secs)	600	600	480	800	1	10
K (mag)	–	–	–	–	7.268†	7.674†
Night	1	1	2	1	1	2

† 2mass magnitude from: SIMBAD

observations utilised the K-band (2.2 μm) grating which covers many ro-vibrational H_2 emission lines. The ambient seeing varied from $\sim 0.6''$ to $1.1''$ during the observations[1]. The OH231 observations consisted of three fields focused on (1) the edge of the Northern lobe, (2) the central region, and (3) the middle of the Southern lobe (labelled N, C, S in Fig. 4.1 [b]). No H_2 was detected in the Southern field and will not be discussed further. Table 4.1 summarises exposures for each of the three fields. Telluric standard stars used for calibration are HD 75004 (G0V), and HD 63487 (G2V) for night one and two, respectively. An average AO-corrected PSF of ∼340 mas FWHM is estimated from the standard stars. These data were reduced using the ESO common pipeline library to a wavelength-calibrated datacube and further analysed as outlined in Chapter 3. The H_2 line rest wavelengths were taken from Black & van Dishoeck (1987).

4.3 Results

We report the detection of several H_2 emission lines arising from both the centre and Northern lobe of OH231. In Figure 4.1 (c,d) we present continuum-subtracted integrated line maps in the 1→0S(1) transition for both fields, showing clearly H_2 emission arising from the centre of OH231 (Fig. 4.1 [d]) and from knots of material in the Northern lobe (Fig. 4.1 [c]). In Fig. 4.1 (a) the contours of the detected H_2 are shown in relation to Hα emission, while Fig. 4.1 (b) gives the location of the H_2 relative to the strong continuum emission as imaged with a 2.12 μm filter. An integrated spectrum of the Western region of the centrally located H_2 is shown in Figure 4.2, from which we note, a) several S- and Q-branch ro-vibrational H_2 lines, and b) a CO bandhead absorption feature (∼2.3 μm).

Channel maps, extracted from the SINFONI datacube, are presented in Figures 4.3 and 4.4 for the central and Northern regions respectively, showing how the distribution of the H_2 changes across the line profile.

Table 4.2 presents the flux measurements for the central and Northern fields, for lines with flux errors less than ∼50 per cent. Accurate 2→1S(3), 1→0S(0), and 1→0Q(2) line flux measurements are not possible due to the presence of strong sky subtraction residuals at these wavelengths. We confine the calculation of the 1→0/2→1S(1) ratio for the central field to the area marked by the ellipse in Fig. 4.1 (d), where the 2→1S(1)flux error is smallest. In this region we calculate a 1→0/2→1S(1) ratio of 8.3±1.9 prior to extinction correction. We do not detect any 2→1S(1)flux in the Eastern H_2 region, instead we estimate an upper 2→1S(1)limit (3σ) for the flux in

[1]ambient seeing conditions for Paranal can be obtained from: http://archive.eso.org/asm/ambient-server?site=paranal&night=2010-02-01&data=S

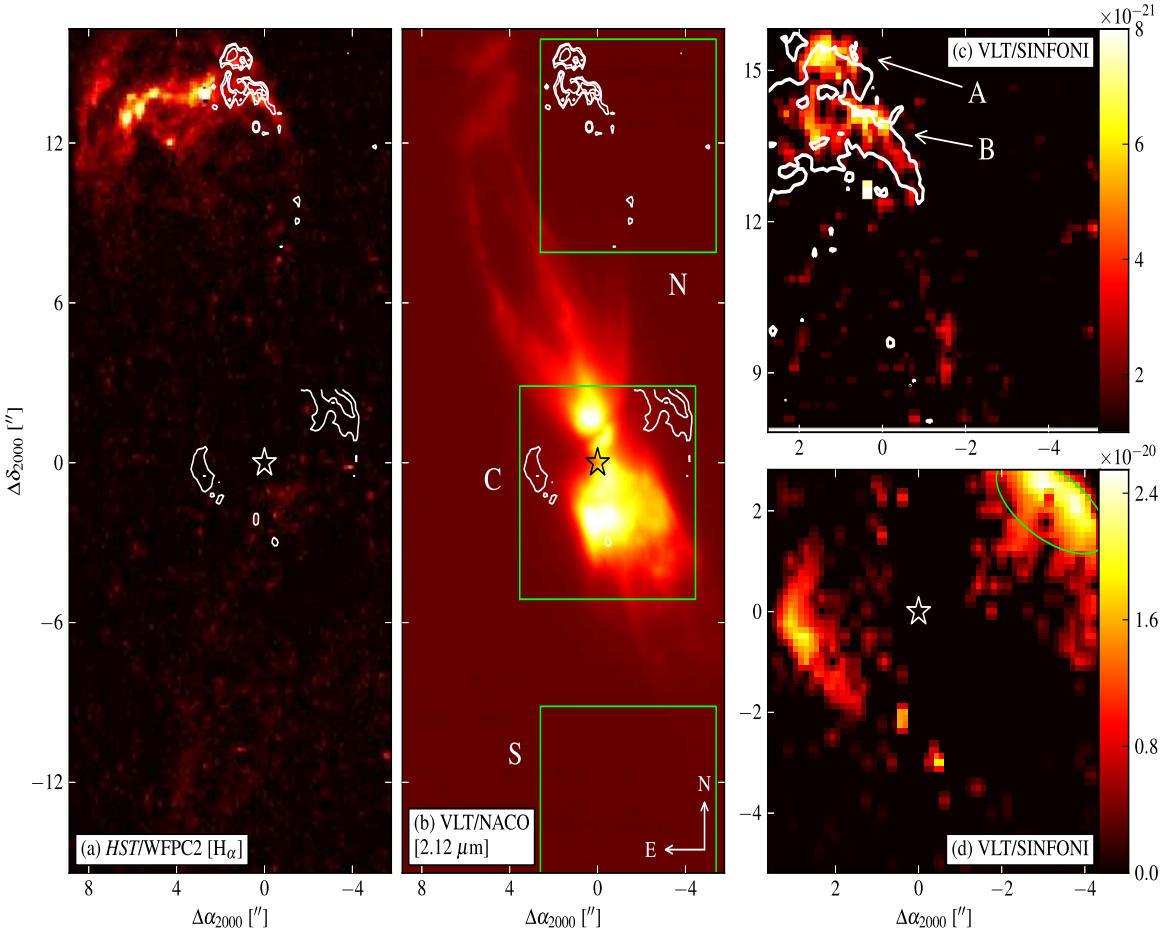

Fig. 4.1: Narrow-band images and line maps for OH231; a star symbol indicates the SiO maser position (see text), inset labels display the telescope/instrument information. (*a*) Continuum-subtracted Hα image with the 1→0S(1)H_2 contours overlaid in white, (*b*) 2.12 μm image, showing mainly scattered light, with H_2 contours overlaid, SINFONI North, Central, and South (labelled N, C, S) fields are marked by green squares, inset compass shows orientation, (*c*) 1→0S(1)H_2 line map showing the extent of the emission located along the edge of the Northern lobe, two knots (A, B) of H_2 emission are indicated by arrows; superposed contours indicate the location of the Hα emission, (*d*) 1→0S(1)H_2 line map for the central region showing the position/extent of the region used for the 1→0/2→1S(1) calculation (ellipse). Colour bar units are in W m^{-2} px^{-1}. The Hα data, from the Hubble Legacy Archive (see Acknowledgements), has been continuum-subtracted using the procedure outlined in Bujarrabal et al. (2002). The 2.12 μm data was first published in Matsuura et al. (2006) and has been reprocessed using the ESO pipeline.

Table 4.2: Line fluxes, F, (in units of 10^{-19} W m^{-2}) of the observed H_2 lines for the central and Northern fields. Measured peak line wavelengths (in μm) are given for the central field.

	Central		Northern
Line	λ_{meas}	F	F
1→0S(3)	1.9579	67.2 ± 14.2	11.5 ± 1.10
1→0S(2)	2.0342	9.71 ± 3.36$^{\diamond}$	—
1→0S(1)	2.1222	91.5 ± 6.16	9.69 ± 0.76
2→1S(1)	2.2481	7.73 ± 3.38‡	—
1→0Q(1)	2.4071	46.4 ± 14.5	11.9 ± 2.95
1→0Q(3)	2.4241	42.2 ± 24.0	13.3 ± 4.42

‡ Flux measured for Western H_2 region only.
$^{\diamond}$ Measurement confined to elliptical region (Fig. 4.1 [d]).

this region of 1.3×10^{-19} W m^{-2}, which in turn places a lower limit of ∼9.5 on the 1→0/2→1S(1) ratio for this region.

4.4 Analysis and Discussion

The 1→0/2→1S(1) ratio is a useful discriminator of excitation mechanisms. Pure fluorescence will yield a value of ≈ 2 while a value ≈ 10 indicates the excitation of the gas is being driven by shocks. However it is worth noting, these values depend on shock velocity and pre-shock gas density, with shocked H_2 capable of producing values as low as ≈4 (Smith, 1995), while fluorescence can produce values approaching those of shocks if the gas density is sufficiently high (Hollenbach & Natta, 1995). The 1→0/2→1S(1) ratio values, given above, suggest that shocks might be the main excitation mechanism, which agrees with the detection of shock-excited HCO^+ in the centre of OH231 noted in the position-velocity diagrams of Sánchez Contreras et al. (2000). In order to determine the intrinsic 1→0/2→1S(1) ratio, it is necessary to remove the effects of extinction. In the K-band, it is sometimes possible to derive the level of extinction via the comparison of S-/Q-branch H_2 emission lines (see Smith et al., 2003). Unfortunately, due to poor atmospheric transmission above 2.4 μm, it was not possible to derive a sensible estimate for extinction using the 1→0 S(1) and Q(3) lines.

Minimum values of extinction of A_K=3–4 (mag) for the central region are estimated from the $(K - L')$ colour map of OH231 (Kastner et al., 1998). They calculated an intrinsic colour of the Mira $K - L' \sim 0.5$. Under the assumption that the Mira dominates the illumination of OH 231.8+4.2, a K-band extinction for our equatorial regions can be estimated by coupling their colour map information with the intrinsic colour along with a suitable NIR extinction law. Adjusting the Western 1→0/2→1S(1) ratio for these levels of extinction yields, for example, a value of 11.7±2.6 (A_K=4). It is clear that any adjustment for extinction will increase the observed 1→0/2→1S(1) ratio, pushing it further toward the shock regime.

Using a typical value of 5.3×10^{-22} mag cm^2 (Bohlin et al., 1978) for the extinction per unit column density of hydrogen, $A_V/N(H)$, one can estimate the hydrogen column density implied by an A_K=4; yielding a $N(H)$ for the H_2 regions of $\sim7.2\times10^{22}$ cm^{-2}. Using a typical column length of the H_2 emitting regions of 1″($\sim2.0\times10^{16}$ cm), as

used in Bujarrabal et al. (2002), we estimate an average density for the H_2 regions of 3.5×10^6 cm^{-3}. This value is in good agreement with Alcolea et al. (2001) who estimate an average central density of $\sim3.0\times10^6$ cm^{-3}. The H_2 emission is most likely originating in the dense equatorial regions surrounding the central star.

4.4.1 Equatorial Region

The 1→0S(1)H_2 line map (see Fig. 4.1 [d]) shows two regions of H_2 oriented at a position angle (PA) of 113°, from brightest to faintest peak. If we assume that the distribution of the H_2 around the central region of OH231 is in a disc configuration then by measuring the major and minor axis we can estimate the inclination angle of the equatorial disc with respect to the plane of the sky from the H_2 data. Measurements for $R_{\rm max}/R_{\rm min}$ are determined by superposing a full ellipse onto the H_2 line map. We find $R_{\rm max}$= 4.06″ and $R_{\rm min}$= 2.76″from the centre of the ellipse, and using the relation $i = \sin^{-1}(R_{\rm min}/R_{\rm max})$, we find i =43°±8; errors are estimated by assuming maximum measurement errors of two pixels. This result is in good agreement with previously published values.

The location and orientation of this H_2 adds to the already complex picture of the equatorial region of OH231. Some previously reported structures, from smallest to largest, include:

- an equatorial torus of SiO maser emission ($\sim2R_\star$) that might lie on the innermost edge of an expanding SO disc (Sánchez Contreras et al., 2000, 2002);
- a centrally located compact disc of circumstellar material with inner R=0.03–0.04″/40–50 AU (Matsuura et al., 2006);
- an opaque flared disc with outer R=0.25″/330 AU revealed in mid-IR images (Jura et al., 2002);
- a slowly expanding disc with characteristic R=0.9″/1160 AU, detected via the SO (J=2_2→1_1) transition (Sánchez Contreras et al., 2000);
- a torus of OH maser emission with outer R=2.5″/3250 AU (Zijlstra et al., 2001);
- an expanding hollow cylinder of HCO^+ with a characteristic radius equal to the OH torus radius (Sánchez Contreras et al., 2000).
- a halo of scattered light at R∼4″/5200 AU (Meakin et al., 2003);

From our observations the geometry of the H_2 region is unclear, however we offer two possibilities: (1) A disc of H_2: Figure 4.1 (d) shows what might be interpreted as an incomplete disc of H_2, which fits with the series of concentric disc/tori structures listed above. To understand why we observe only emission from the edges and not the front of the disc, a comparison of the noise in the continuum at the front of the putative disc, to the amplitude of the 1→0S(1)line peak shows both to be of the same order. We might then attribute the 'missing' H_2 in this region to variations in the continuum. We would not expect to observe the back of the disc due to the high level of extinction through the nebula. (2) A shell of H_2: if the H_2 is situated in an axisymmetric shell surrounding the central star, we might explain the geometry of the H_2 regions by assuming a density contrast between the poles and equator. This, combined with an increased column depth at the edge of the shell would manifest itself as two arcs of H_2 emission situated equatorially (as noted by Lowe & Gledhill, 2005, for *IRAS* 19306+1407). This is supported by the detection of a shell of higher density gas and dust at the same location as the H_2 (Meakin et al., 2003). Both scenarios offer

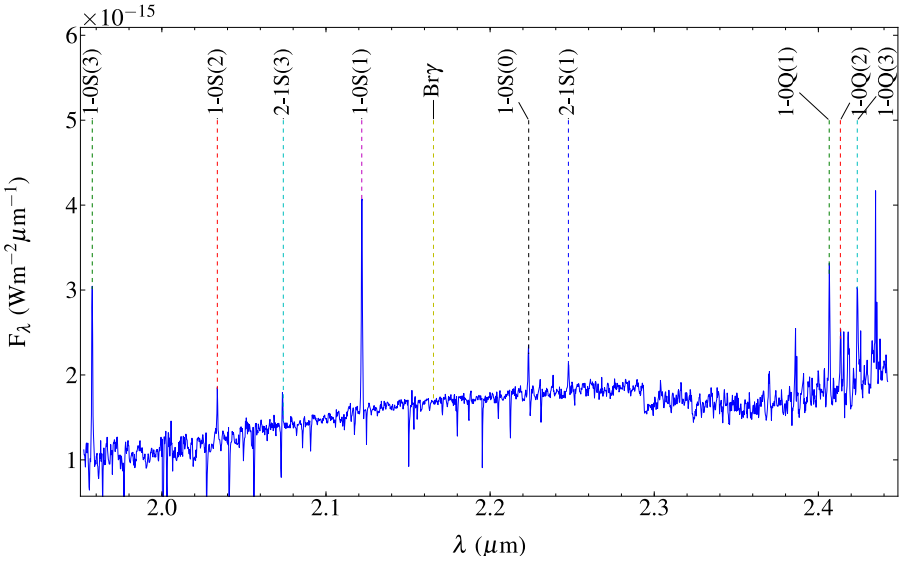

Fig. 4.2: An integrated spectrum of the Western side of the central H_2 showing the detected lines, the position of the Brγ recombination line is shown for reference. Extracted spectra location marked in Fig. 4.1 (d).

plausible explanations for the geometry of the H_2 emitting region, however further observations are needed in order to favour one.

We fit the 1→0S(1)line profile yielding a $V_{\rm LSR}$=36±17 km s^{-1} and FWHM=100 km s^{-1} for both Eastern and Western regions of H_2 emission, a value consistent with the systemic velocity. Channel maps of the 1→0S(1)line (Fig. 4.3) show no significant change in the distribution of the H_2.

In an attempt to explain the lack of reported H_2 in this object, we note two previous studies: (1) Weintraub et al. (1998) give a 3σ upper limit of 10^{-5} ergs cm^{-2} s^{-1} ster^{-1} (1σ limit =6.6×10^{-18} W m^{-2}) for the surface brightness of the 1→0S(1)line toward OH231. This places their measurement limit close to the 1→0S(1)line strength given in Table 4.2, implying that the 1→0S(1)line in their observations would be difficult to distinguish from noise, or possibly that their slit position, aligned East-West across inferred central star position, did not include the H_2 sites; (2) Matsuura et al. (2006), using the ISAAC instrument on VLT, do not report any detection of H_2. However, this can be explained due to the orientation of the slit, aligned from South-West to North-East along the major axis (private comm.), with a slit-width of 0.8″, i.e., the central H_2 emission site was not covered.

4.4.2 Northern Region

Figure 4.1 (c) shows the line map for the 1→0S(1)transition in the Northern region. Most notable are the two knots of H_2, labelled A and B for the top and bottom knot, respectively. The Hα emission contours are superposed on the H_2 line map. The peak intensity of the H_2 emission knots are slightly offset from the two Hα emission knots (Fig. 4.1 [c]), however this small offset can be accounted for by the motion of the outflow (e.g.V∼150 km s^{-1}, from Bujarrabal et al., 2002) during the 10 years between both sets of observations. It is most likely that the optical and NIR line emission arise from the same shock event. Weaker 1→0S(1)emission is noted tracing the Hα edge of the bipolar outflow in the lower portion of the 1→0S(1)line map. The NACO

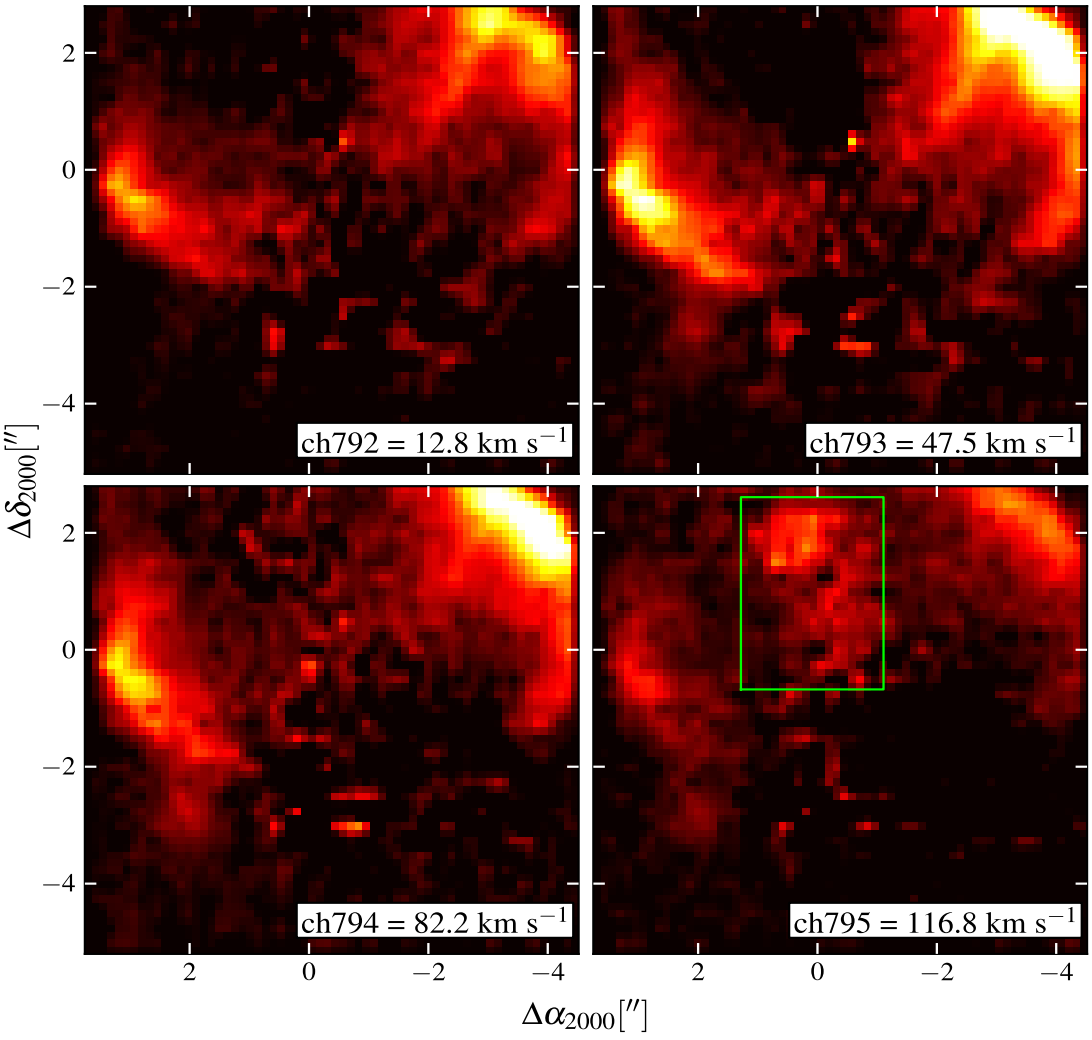

Fig. 4.3: 'Channel maps' of the four central channels of the 1→0S(1)line from the central region of OH231. Inset labels show datacube channel and corresponding $V_{\rm LSR}$ velocity. Note: in ch795, the central region (marked by a green box) is residual from the continuum subtraction and not true H_2 emission.

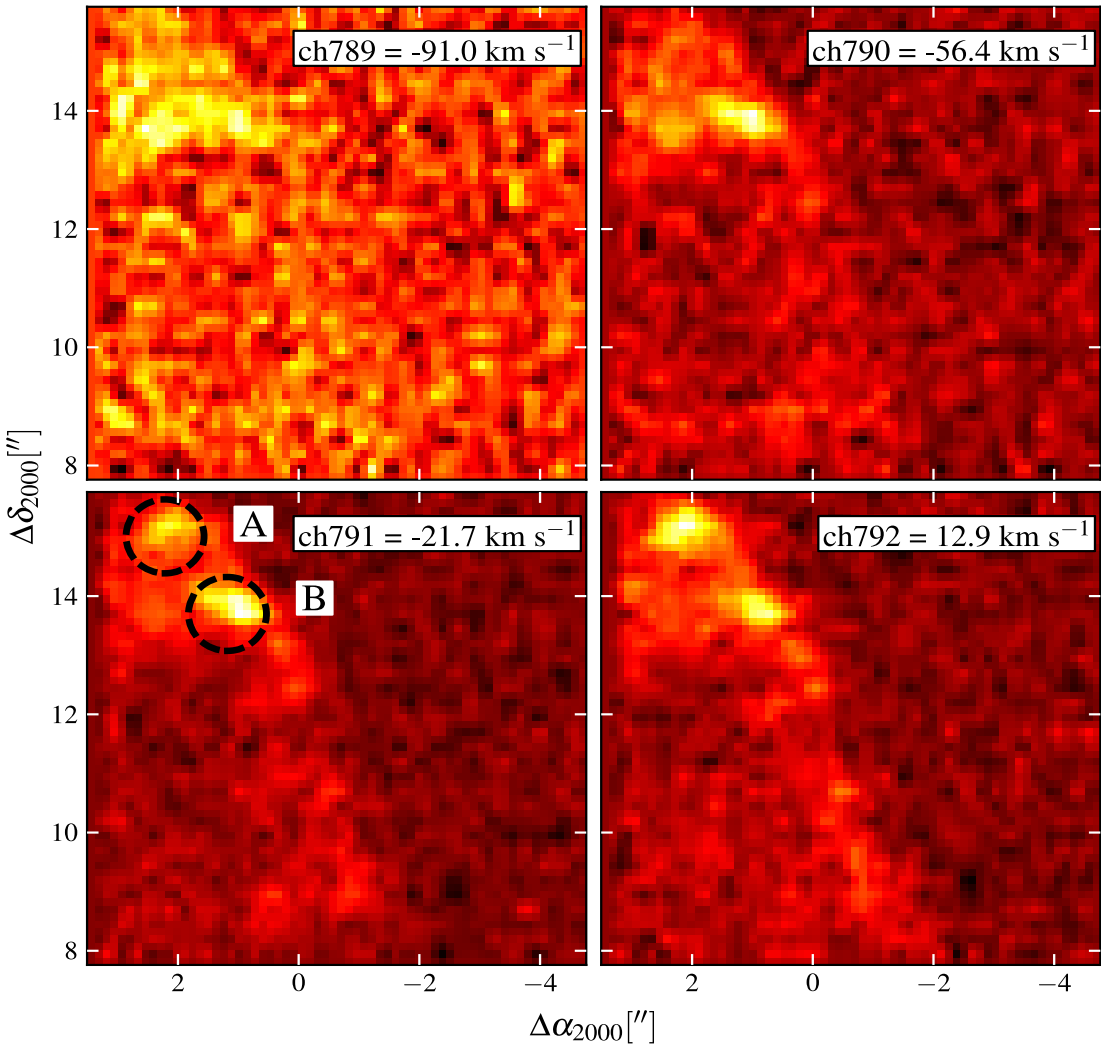

Fig. 4.4: 1→0S(1)line 'channel maps' of the four central channels extracted from the Northern region of OH231. Knot A and B are regions of most intense H_2 emission. Labels as in Fig.4.3.

2.12 μm image does not show any trace of H_2 emission in this region (see contours in Fig. 4.1 [b]).

The 1→0S(1)line is spread over ∼six spectral pixels, the four central channels are presented in Fig. 4.4. Examination of the line profile and channel maps allows us to probe the kinematics of the H_2 in this region, revealing two main features: 1) knot B which is persistent in all channel maps, 2) the reduction of peak H_2 intensity in knot A at velocities ≤ -56 km s^{-1}. Both of these H_2 structures lie in the diffuse extended region (labelled B_1 in Fig. 4 of Bujarrabal et al., 2002) perpendicular to the axial flow, with a quoted Hα velocity of 150 km s^{-1} which is in good agreement with not only our deprojected H_2 velocities (V_{H_2}∼110 km s^{-1}) but also with HCO^+ velocities (Sánchez Contreras et al., 2000).

In the case of knot A, the spectral line is strongly peaked in a single channel, while in knot B the spectral line peak is spread over two channels. Fitting the line profiles of knots A and B, yields LSR velocities of V_{LSR}=-8 km s^{-1}, and -30 km s^{-1}, with deprojected velocities of -75 km s^{-1} and -110 km s^{-1}, respectively. This might indicate that further from the Hα bow apex (Fig. 4.1 [a]), we are starting to see emission originating from the front and back of knot B, while knot A displays a narrower range

of velocities, i.e., a single peak in its spectral profile. It is worth noting that due to the slit-length of ISAAC (120″) coupled with the null H_2 detection discussed in §4.4.1, the H_2 in the Northern region might be confined to the wings of the bow shock.

The existence of fast moving shocked H_2 has previously been noted in other objects, for example, Cox et al. (2003) detect high velocity H_2 ∼220–340 km s^{-1} (dependent on adopted inclination angle) in the outflows of AFGL 618. It is currently unknown exactly how shocked H_2 can be travelling at this speed without complete dissociation. Further high resolution mapping of the H_2 is necessary in order to resolve the shock surfaces, more accurately measure the H_2 kinematics, and apply shock models to this region.

4.5 Conclusions

We have presented VLT/SINFONI integral field observations of OH231, revealing the presence of several ro-vibrational H_2 lines. The main conclusions are:

- The discovery of H_2 emission near the centre of OH231, possibly located at the edge of an axisymmetric shell or an incomplete disc.
- A 1→0/2→1S(1) value of 8.3±1.9 is found for the equatorial H_2, suggesting a collisional excitation mechanism.
- Our observations of the central shell/disc of H_2 show no velocity structure. However, higher S/N and/or velocity resolution data are needed to accurately probe the kinematics in this region.
- We detect fast-moving H_2 (∼110 km s^{-1}, along the bipolar axis) via the 1→0S(1)transition along the North-Western tip of the nebula, a region where a strong Hα bow shock exists. Due to the small FOV of our observations, the full extent of this H_2 is unknown.

References

Alcolea, J., Bujarrabal, V., Sánchez Contreras, C., Neri, R., & Zweigle, J. 2001, A&A, 373, 932

Black, J. H. & van Dishoeck, E. F. 1987, ApJ, 322, 412

Bohlin, R. C., Savage, B. D., & Drake, J. F. 1978, ApJ, 224, 132

Bujarrabal, V., Alcolea, J., Sánchez Contreras, C., & Sahai, R. 2002, A&A, 389, 271

Cohen, M., Dopita, M. A., Schwartz, R. D., & Tielens, A. G. G. M. 1985, ApJ, 297, 702

Cox, P., Huggins, P. J., Maillard, J.-P., Muthu, C., Bachiller, R., & Forveille, T. 2003, ApJ, 586, L87

Eisenhauer, F., Abuter, R., Bickert, K., Biancat-Marchet, F., Bonnet, H., Brynnel, J., Conzelmann, R. D., Delabre, B., Donaldson, R., Farinato, J., Fedrigo, E., Genzel, R., Hubin, N. N., Iserlohe, C., Kasper, M. E., Kissler-Patig, M., Monnet, G. J., Roehrle, C., Schreiber, J., Stroebele, S., Tecza, M., Thatte, N. A., & Weisz, H. 2003, in Society of Photo-Optical Instrumentation Engineers (SPIE) Conference Series, Vol. 4841, Society of Photo-Optical Instrumentation Engineers (SPIE) Conference Series, ed. M. Iye & A. F. M. Moorwood, 1548, 1561

Frew, D. J. & Parker, Q. A. 2010, PASA, 27, 129

Hollenbach, D. & Natta, A. 1995, ApJ, 455, 133

Jura, M., Chen, C., & Plavchan, P. 2002, ApJ, 574, 963

Jura, M. & Morris, M. 1985, ApJ, 292, 487

Kastner, J. H., Weintraub, D. A., Merrill, K. M., & Gatley, I. 1998, AJ, 116, 1412

Kastner, J. H., Weintraub, D. A., Zuckerman, B., Becklin, E. E., McLean, I., & Gatley, I. 1992, ApJ, 398, 552

Lee, C.-F., Hsu, M.-C., & Sahai, R. 2009, ApJ, 696, 1630

Lowe, K. T. E. & Gledhill, T. M. 2005, in Astronomical Society of the Pacific Conference Series, Vol. 343, Astronomical Polarimetry: Current Status and Future Directions, ed. A. Adamson, C. Aspin, C. Davis, & T. Fujiyoshi, 282

Matsuura, M., Chesneau, O., Zijlstra, A. A., Jaffe, W., Waters, L. B. F. M., Yates, J. A., Lagadec, E., Gledhill, T., Etoka, S., & Richards, A. M. S. 2006, ApJ, 646, L123

Meakin, C. A., Bieging, J. H., Latter, W. B., Hora, J. L., & Tielens, A. G. G. M. 2003, ApJ, 585, 482

Sánchez Contreras, C., Bujarrabal, V., Neri, R., & Alcolea, J. 2000, A&A, 357, 651

Sánchez Contreras, C., Desmurs, J. F., Bujarrabal, V., Alcolea, J., & Colomer, F. 2002, A&A, 385, L1

Sánchez Contreras, C., Gil de Paz, A., & Sahai, R. 2004, ApJ, 616, 519

Smith, M. D. 1995, A&A, 296, 789

Smith, M. D., Froebrich, D., & Eislöffel, J. 2003, ApJ, 592, 245

Weintraub, D. A., Huard, T., Kastner, J. H., & Gatley, I. 1998, ApJ, 509, 728

Zijlstra, A. A., Chapman, J. M., te Lintel Hekkert, P., Likkel, L., Comeron, F., Norris, R. P., Molster, F. J., & Cohen, R. J. 2001, MNRAS, 322, 280

Chapter 5: H_2 Tracing the Shocks around *IRAS* 16594-4656

5.1 Introduction

IRAS 16594-4656 was first identified as a proto-planetary nebula (PPN) candidate from its position in the *IRAS* two-colour diagram by Volk & Kwok (1989) and Van der Veen & Habing (1988). An imaging study by Hrivnak et al. (1999), with the *HST* Wide-Field Planetary Camera (WFPC2), allowed the multi-polar structure of *IRAS* 16594-4656 to be clearly seen for the first time. Hrivnak et al. (1999) suggest that, due to its extended nature and the fact that *IRAS* 16594-4656 possesses a double peaked SED with IR excess, it is a bi- or multi-polar PPN object. The PPN nature is supported by the fact that (1) Loup et al. (1990) detected the CO (J=1→0) transition, yielding an expansion velocity, $V_{\rm exp}$, $\sim$ 16 km s^{-1} corresponding to values expected for an AGB circumstellar envelope (CSE), (2) there is a detection of the 21 μm emission feature which is not expected for PNe or young stellar objects (YSOs) (e.g., García-Lario et al., 1999) and, (3) there is a lack of radio emission at 6 cm as would be expected from an ionised region around the hot central star of a planetary nebula.

In two recent papers (Hrivnak et al., 2008; Van de Steene et al., 2008), using high resolution spectra (R$\sim$ 50,000 - 60,000), the kinematics of the H_2 is thoroughly investigated. To briefly summarise, both papers determine that the H_2 is located in hollow bipolar lobes, with expansion velocity of 8 km s^{-1} (Van de Steene et al., 2008) and 8+2.4r/1″ km s^{-1} (Hrivnak et al., 2008). Optical forbidden lines [CI] and [OI] analysed by Van de Steene et al. (2008) display a similar double-peaked line profile to the H_2 and are assumed to arise from the same spatial location. [FeII] emission, originally detected by Van de Steene & van Hoof (2003), is shown to originate in the central region (see Figure 4 Van de Steene et al., 2008) with a line width (FWHM) of 30 km s^{-1}. A summary of important parameters for *IRAS* 16594-4656 is given in Table 5.1.

In this Chapter I present high signal-to-noise (S/N $\sim$ 60 in the continuum at 2.2 μm), K-band integral field unit data for *IRAS* 16594-4656[1]. The principal aim of this paper is to detect all the K-band ro-vibrational H_2 emission lines, only possible at high S/N, and use these line measurements to determine the shock characteristics for the H_2. Section 5.2 details the observations, while the main results are given in Section 5.3. Sections 5.4 and 5.5 give a brief discussion and conclusions.

[1]Based on observations made with ESO Telescopes at the Paranal Observatory under programme ID 075.D-0429(A).

Table 5.1: Summary of *IRAS* 16594-4656 properties from literature.

Parameter	Value	Reference
R.A. (α_{2000})	$17^h\ 03^m\ 10^s.08$	a
Dec. (δ_{2000})	-47° 00′ 27″.7	a
l	340.3924	a
b	-03.2889	a
K (mag)$^{\triangle}$	8.26	a
A_v*	3.2, 7.5	m, c
Spectral Type	B7, B5 - B7Ie	b,i
T_{eff} (K)	12,000, 14,000	c, i
log g	2.1	i
SED Class	IVa	g
Morphological Type¶	Bipolar, DUPLEX,	m, g
	Mcw∗(0.60),an,ps(m,an),h(a)	n
Distance (kpc)$^{\diamond}$	2.2 ($L = 10000L\odot$)	c
	2.6 ($L = 10000L\odot$)	e
	1.9 ($L = 6000L\odot$)	d
	1.8 ($L = 5000L\odot$)	f
Size (arcsec)	5.0 × 2.2	h
Inclination Angle (deg)†	10 - 15	j
Chemistry‡	C-rich	k,l
V_{exp} (km s^{-1})	8, 8+2.4r/1″	o,j

$^{\triangle}$ 2mass magnitude

* Derived using R_v values of 3.1 & 4.2

¶ See body of text for description of the symbols

$^{\diamond}$ Luminosity-dependent distance

† Inclination relative to the plane of the sky

‡ Originally classed as an O-rich star

References. – a. SIMBAD; b. Van de Steene et al. (2000b); c. Van de Steene & van Hoof (2003); d. Su et al. (2001); e. Hrivnak et al. (2000); f. Van der Veen et al. (1989); g. Van de Steene et al. (2000a); h. Ueta et al. (2005); i. Reyniers (2002); j. Hrivnak et al. (2008); k. García-Lario et al. (1999); l. Loup et al. (1990); m. Hrivnak et al. (1999); n. Sahai et al. (2007); o. Van de Steene et al. (2008).

5.2 Observations and Data Reduction

As described in detail in Chapter 3, the SINFONI (Eisenhauer et al., 2003) instrument was used to observe *IRAS* 16594-4656 on the 30th June 2005. The *IRAS* 16594-4656 observations consisted of 6 × 5 sub-exposures of 60 seconds (total=1800 seconds) of science & sky frames, using the medium resolution mode (100 × 50 mas/pix) with an average airmass for these frames of 1.15. Each object frame has an associated sky frame offset from the target, as there is insufficient sky available in the object frames to perform accurate sky subtraction. The science observing template used an ABBA pattern for the acquisition of the object/sky pairs, where A and B represent three object and sky exposures, respectively. Several standard stars were observed throughout the night; calibration of the data was carried out using each of these stars as a check on consistency; *HD* 113949 (B9V) is the star used to calibrate the data presented in this paper (see Table 5.2 for details).

Table 5.2: Details of the VLT/SINFONI observations for *IRAS* 16594-4656 and the telluric standard star.

	IRAS 16594-4656	HD 113949
Date	30-06-2005	30-06-2005
No. of Observations	6	1
No. of Sub-integrations	5	1
Exposure (secs)	60	10
Filter	K	K
Airmass	1.15	1.01
2MASS K (mag)	8.260	8.678
Seeing (ambient)	0.8″	0.8″
Plate Scale (mas/pix)	100 × 50	100 × 50

The reduction of *IRAS* 16594-4656 and standard star data uses calibration frames taken 12 hours following the science observations. The standard star was obtained relatively close in time, right ascension and declination, to the science target. These data were reduced in the manner described in Chapter 3.

Line measurements from the resulting flux calibrated datacube brought to light an issue with the 1→0S(3) line (λ=1.9576 μm). It appears that the telluric correction for this line is quite poor and the division by the standard star spectrum results in an enhanced line flux. Figure 3.6 in Chapter 3 shows the location of the 1→0S(3) line in the K-band. The fact that it lies in one of the large atmospheric absorption bands means that accurate telluric correction of this line is quite difficult. Figure 5.1 shows a comparison of the H_2 lines flux as measured with the SINFONI data and lines from a previous publication (Van de Steene & van Hoof, 2003). It is clear that the flux measurements, in general, agree quite well. However, there is a clear outlier – the 1→0S(3) line. For this reason this line is omitted from the shock analysis presented in this chapter.

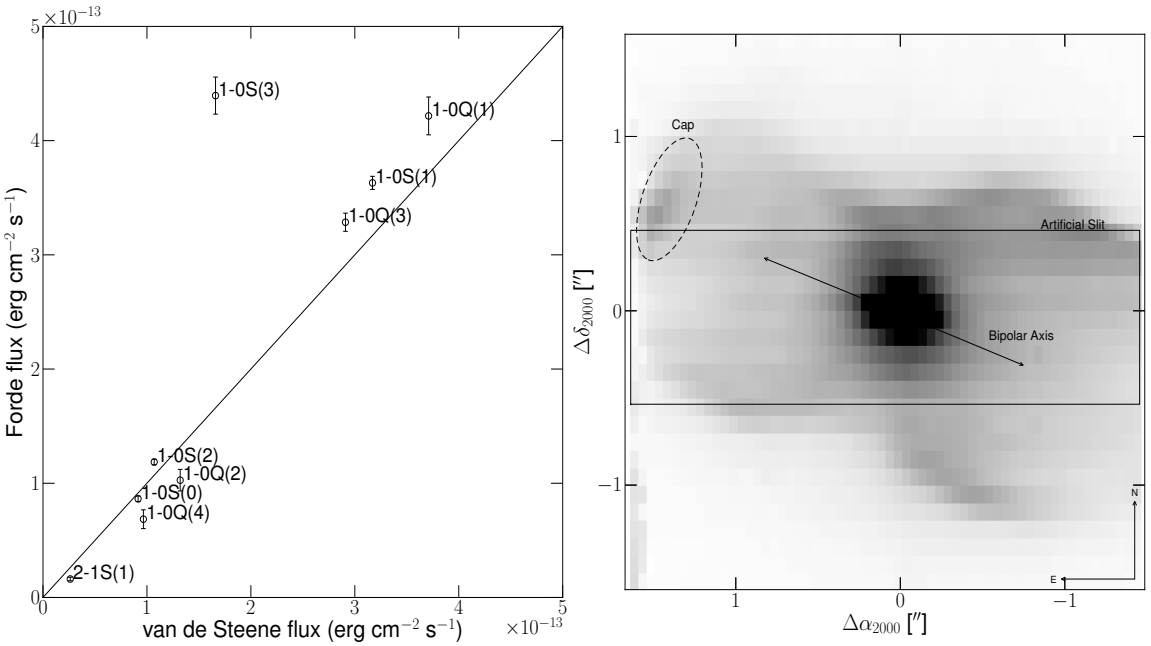

Fig. 5.1: (*left*) A comparison between the Van de Steene & van Hoof (2003) line flux measurements and this work. Y-errorbars reflect the calculated error on the flux from the extracted region in this work. Van de Steene & van Hoof (2003) do not supply errorbars and as such no x-errorbars are available. (*right*) Artificial slit position and width of Van de Steene & van Hoof (2003); flux measurements were summed in this region for comparison. The position of the 'cap' feature (dashed ellipse) and the bipolar axis (arrows) are also given.

5.3 Results

5.3.1 Integrated Spectrum

An integrated spectrum can be formed by collapsing an integral field spectral cube along both spatial directions. Figure 5.2 shows the detected NIR (K-band) lines for *IRAS* 16594-4656. The presence of 14 H_2 ro-vibrational lines (S- and Q-branch) and a single recombination line, Brγ can be clearly observed. Although García-Hernández et al. (2002) and Van de Steene & van Hoof (2003) have previously presented K-band spectra for this object, both datasets were at a lower spectral resolution, while the high resolution H_2 spectra presented by Hrivnak et al. (2008) and Van de Steene et al. (2008) cover only two lines (1→0S(1)and 2→1S(1)). The higher S/N integral field data reveal several previously undetected weaker H_2 lines. These lines arise from higher vibrational levels (v=2&3) usually associated with fluorescence but which can also be populated in shocks. The *IRAS* 16594-4656 K-band spectrum displays a continuum that decreases with wavelength. This is a familiar feature in post-AGB stars with a relatively hot photosphere plus some reddening, as noted in *IRAS* 18062+2410 (Davis et al., 2003) and almost all of the objects in Hrivnak et al. (1994), in good agreement with the spectral type of this star (B7).

5.3.2 Line Maps

Fitting a spectral emission line with a single Gaussian profile allows the construction of continuum-subtracted integrated intensity line maps displaying the spatial extent of

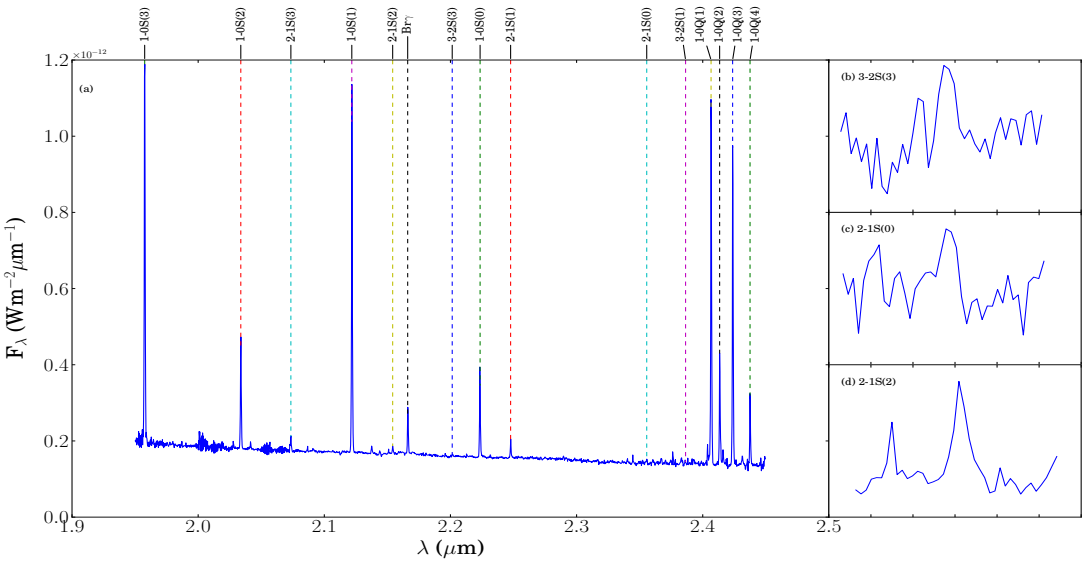

Fig. 5.2: *K*-band Spectrum of *IRAS* 16594-4656 extracted for the entire data cube, showing each detected H_2 line. The three weakest lines are shown in the subplots labelled (b), (c), and (d).

the emission. The line fitting is carried out using the Levenberg-Marquardt algorithm as implemented in the MPFIT program (Markwardt, 2009). With this approach four parameters can be fitted simultaneously: line peak, local continuum, line full width half maximum (FWHM), and line centre, allowing the construction of line maps and velocity maps for each line. Examination of the line profiles shows no evidence of line splitting, consistent with the fact that the H_2 shell is expanding at velocities below SINFONI's resolution. Typical line FWHM are $\sim 7{\times}10^{-4}$ µm ($\sim$ 85 km s^{-1}). We impose fitting limits on the FWHM in order to minimise the fitting of spurious noise; the FWHM is restricted to the range $2{\times}10^{-4} \rightarrow 1{\times}10^{-3}$ µm. The total continuum-subtracted line flux, for the whole field of view are presented in Table 5.3.

Figure 5.1 shows a channel map of *IRAS* 16594-4656 at the 1→0S(1) line wavelength. Several features can be seen: (1) the extended bipolar nature of the H_2, as seen in previous NIR studies (e.g., Hrivnak et al., 2008); (2) the relatively brighter and larger south-western lobe compared to the north-eastern lobe. Ueta et al. (2005) estimate an inclination angle of 15 degrees to the plane of the sky from a polarimetry study — such a small angle, close to the plane of the sky, would indicate that the North Eastern lobe is truly smaller than the South Western lobe. This might not be an uncommon situation in PPNe; other such objects with intrinsically different lobes are OH 231.8+4.2 (e.g., Heckert & Zeilik, 1983) and *IRAS* 17150-3224 (Hrivnak et al., 2006); and (3) the presence of a so-called 'cap' feature at the tip of the NE lobe; Figures 5.4 and 5.3 show the line maps for the H_2 lines, with high enough S/N to create a map, along with the Brγ and Mg II lines. All H_2 line maps have a similar appearance to the 1→0S(1) line map. The Brγ and Mg II line maps are distinct from the H_2 lines in that their emission is located closer to the star and their distribution is unknown, as it is only marginally resolved. The Brγ emission is slightly extended from the central star (FWHM=3.6 pix compared with 3.1 pix for the standard star).

Although not obvious from the spectrum given in Figure 5.2, there are two previously unreported lines present (located at λ=2.1375 µm and 2.1438 µm). In their spectroscopic PPNe survey, Kelly & Hrivnak (2005) detected lines at these wavelengths

Table 5.3: The total continuum-subtracted flux for each of the observed lines (prior to extinction correction).

Line	λ_{lab} (μm)*	F $\times 10^{-17}$ (W m^{-2})
1→0S(3)¶	1.9576	86.92 ± 2.80
1→0S(2)	2.0338	22.86 ± 0.85
1→0S(1)	2.1218	69.39 ± 1.59
1→0S(0)	2.2235	16.79 ± 0.76
1→0Q(1)	2.4066	77.20 ± 2.78
1→0Q(2)	2.4134	21.60 ± 1.61
1→0Q(3)	2.4237	64.08 ± 1.92
1→0Q(4)	2.4375	15.48 ± 1.53
2→1S(0)	2.4375	0.94 ± 0.47
2→1S(1)	2.2477	3.36 ± 0.46
2→1S(2)	2.1542	1.51 ± 0.55
2→1S(3)	2.0735	3.67 ± 0.62
3→2S(3)	2.2014	0.64 ± 0.35
Brγ	2.1661	8.25 ± 0.49
Mg II	2.1735	1.47 ± 0.22
Mg II◇	2.1438	– ± –

* Laboratory wavelength measurements are given in a vacuum.

¶ line flux uncertain.

◇ line flux heavily affected by defect on the detector. No measurement possible.

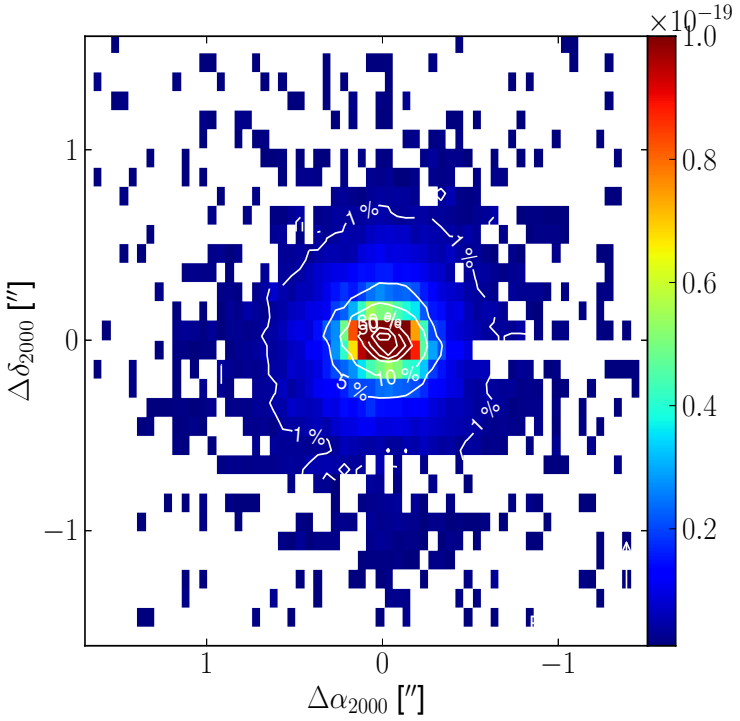

Fig. 5.3: A line map of the Mg II line (λ=2.1375 µm).

and tentatively suggest that they may be Mg II lines. Mg II has an ionisation potential of 15.03527 eV[2] and so requires photons of wavelengths $\sim$ 830 Å in order to ionise the magnesium. This requires that the post-AGB star at the centre of the nebula is hot enough to produce such photons. Figure 5.3 shows the spatial extent of one of the magnesium lines. As expected the line shows quite a similar distribution to that of the Brγ line. Excitation of the Mg II lines require more energetic photons than that of the Brγ line and so it is reasonable to expect its spatial extent to be less than the Brγ. Unfortunately the presence of a detector artifact that manifests itself in the region of the magnesium doublet means the other line cannot be measured.

5.3.3 H_2 Excitation

The line maps provide a useful tool for determining the location and flux of particular emission lines. Figure 5.5 (a) shows the result of ratioing the 1→0S(1) and the 2→1S(1)line maps. Ratio maps formed in this manner can indicate the type of excitation and its location throughout the object bearing in mind the caveats mentioned in Section 2.2.4. In this case, the image shows that the highest ratio values are located at both ends of the bipolar lobes (blue), while the northern edges of the lobes are coincident with the lowest ratio values (light green). The values presented in this map are consistent with a collisional excitation scenario, agreeing with the conclusions of previous work (García-Hernández et al., 2002; Van de Steene & van Hoof, 2003). A de-reddened average 1→0/2→1S(1) line ratio of 23.4±3.3 is calculated across the object, higher than the value of 16.2 obtained by Van de Steene & van Hoof (2003)

[2]value from the NIST database at: http://www.nist.gov/index.html

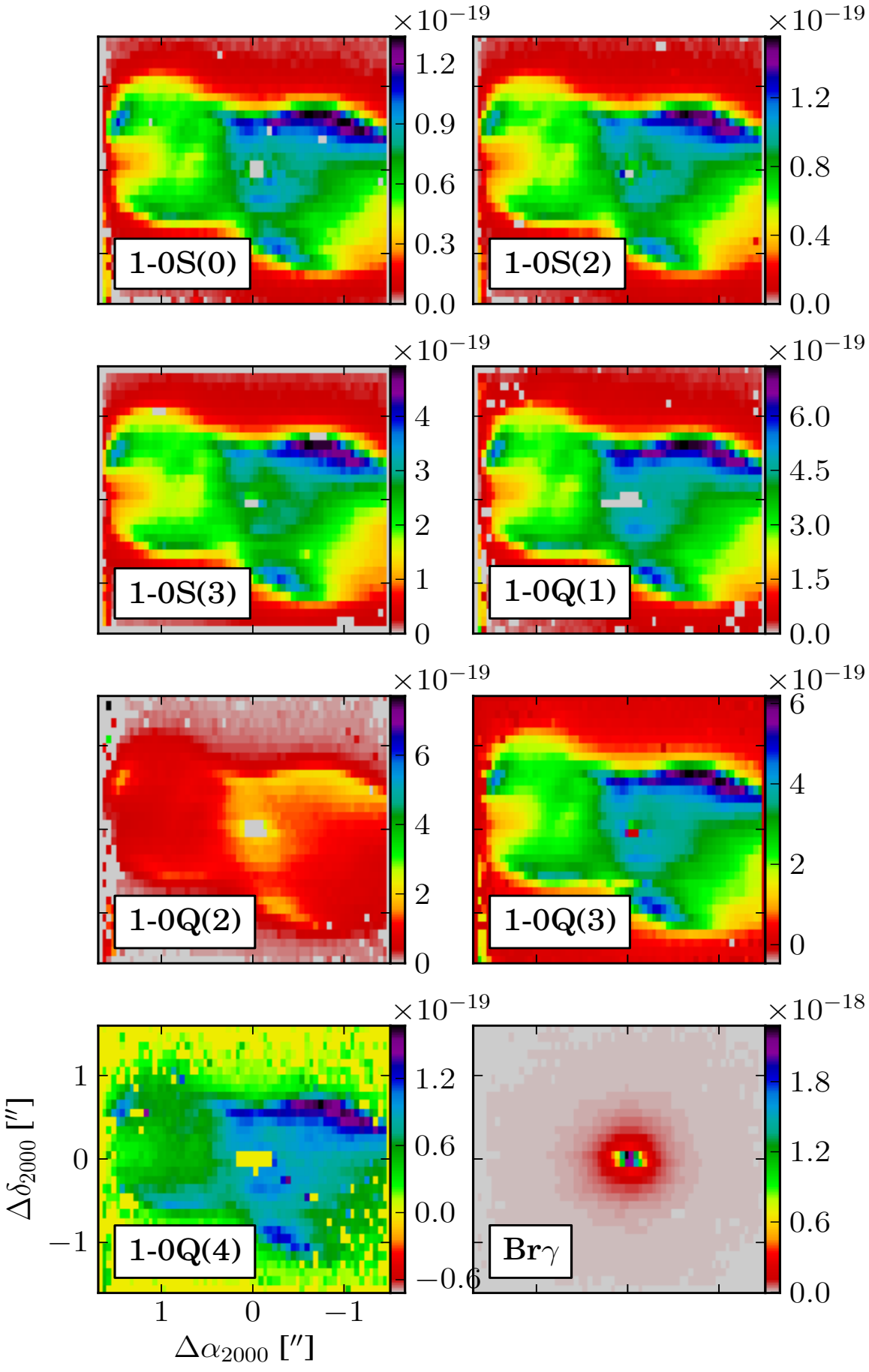

Fig. 5.4: The continuum-subtracted line maps for the strongest H_2 lines and the Brγ line. North is up, East is left, flux units are given in W m^{-2} pix^{-1}, prior to extinction correction.

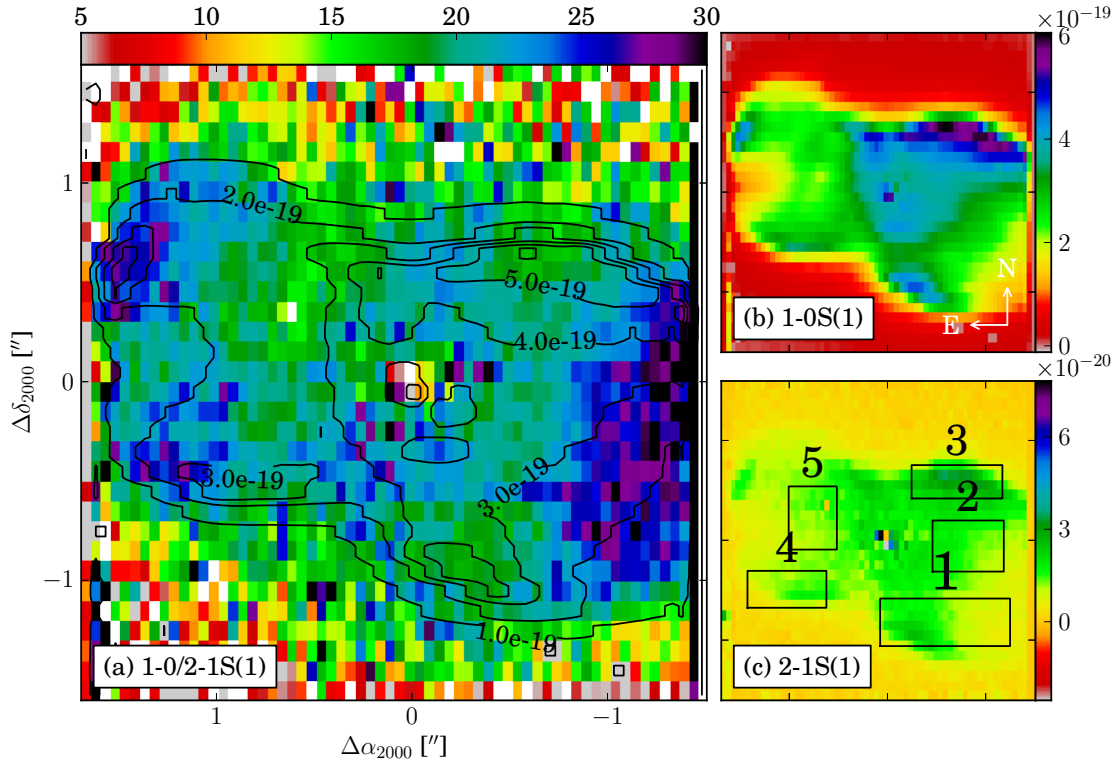

Fig. 5.5: (a) The 1→0/2→1S(1) line ratio map for *IRAS* 16594-4656 prior to extinction correction. The contours overlaid show the position of the 1→0S(1) H_2. (b) shows the 1→0S(1) line map, inset compass shows orientation. (c) show the 2→1S(1) line map, note the noisier appearance due to the weaker emission. Overlaid are the regions extracted for the shock analysis. The line intensity scale bars and numbers on the contours in (a) are in units of W m^{-2} pix^{-1}

and lower than the value of 37.5 (which is a value of 33 corrected for A_k=1.17[3] to allow comparison of values) obtained by García-Hernández et al. (2002).

A rough comparison with the line fluxes given in Van de Steene & van Hoof (2003), using a simulated slit to extract data from the same region in our SINFONI data as was covered by their longslit observations, gives 1→0S(1) flux values in good agreement. However, the 2→1S(1) values from their work are ∼ 50% higher. This is in contrast to the line fluxes given in García-Hernández et al. (2002) where the 1→0S(1) line is ∼ 50% higher than this work, while the 2→1S(1) values appear in rough agreement. The discrepancy between the H_2 line fluxes in García-Hernández et al. (2002) and Van de Steene & van Hoof (2003) has been noted previously with one possible explanation being variability in the stellar wind (Van de Steene & van Hoof, 2003). This is supported by the fact that the Brγ line flux is also varying. In our simulated slit from 2005, we measure Brγ=6.86 × 10^{-14} erg cm^{-2} s^{-1}, which is lower than the 1994 value of 9.2 × 10^{-14} erg cm^{-2} s^{-1} (García-Hernández et al., 2002), and slightly higher than the (1998) value of 4.52 × 10^{-14} erg cm^{-2} s^{-1} (Van de Steene & van Hoof, 2003).

5.3.4 Extinction

The comparison of certain H_2 emission lines has been used in several studies to estimate an extinction value in the direction of a source (Geballe et al., 1982; Davis et al., 2003;

[3]Taken as the mean extinction value from the five regions extracted from the integral field data.

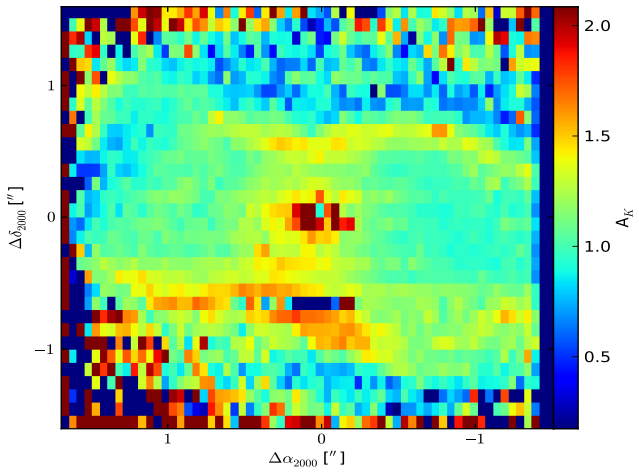

Fig. 5.6: *K*-band extinction map, created from the 1→0S(1)and Q(3) line maps, showing the regions of highest extinction located at the edges of the bipolar lobes.

O'Connell et al., 2005). The combination of three S- and Q-branch lines is used to get estimates for the extinction toward *IRAS* 16594-4656 for each of the regions given in Figure 5.5 (c). Since the Q(3)/S(1) lines are among the strongest in the *K*-band the error is much smaller on this value giving a more accurate estimate for extinction. Values of $A_{\rm K}$=1.27±0.13, 0.99±0.12, 1.2±0.1, 1.31±0.13, and 1.08±0.13 for regions 1, 2, 3, 4, and 5, respectively, were used to correct for extinction prior to calculating rotational/vibrational temperatures [see Figure 5.9]. The line fluxes were corrected for extinction using the Stead & Hoare (2009) power-law to convert the $A_{\rm K}$ obtained from the Q(3)/S(1) ratio to an extinction value at each line wavelength. The use of integral field data allowed a ratio image [for example S(1)/Q(3)] to be propagated through Equation 2.20 to yield an $A_{\rm K}$ extinction map for the whole field of view. The resulting map (Figure 5.6) shows slightly higher extinction values for the edges of the shell. This figure shows a remarkable likeness to the polarised intensity image [see Figure 7 in Ueta et al. (2007)], whereby the regions of highest extinction are mirrored by regions where the polarisation is enhanced, along the edge due to 90 degree scattering (assuming a shell).

Atmospheric transmission at wavelengths longer than 2.4 μm can vary on very short timescales and so the accuracy of the extinction estimate obtained here is dependent on the quality of the telluric correction, which depends, for example, on airmass, and on the time after observation that the telluric standard was observed. Since our science observations are taken over the course of an hour, the telluric correction will not be perfect. Substituting the flux values given in Van de Steene & van Hoof (2003) into Equation 2.20 [see Table 2 in Van de Steene & van Hoof (2003)], the extinction values for the Q3/S1, Q2/S0, and Q4/S2 line pairs are $A_{\rm k}$=1.1, 1.9, and 1.4 mags, respectively, for their slit position. We note that Van de Steene & van Hoof (2003) did not use this value to perform their final extinction correction calculation. The value used in their study was derived from multi-wavelength photometric data (Hrivnak et al., 1999) and use of a Kurucz model atmosphere (Kurucz, 1994) to determine the total extinction for the whole object.

5.3.5 Ortho-to-Para Ratio

The ortho-to-para ratio (OPR) gives the ratio of the total ortho-H_2 to para-H_2 divided by their respective statistical weight.

Using the extinction corrected fluxes for each of the extracted regions values of 2.98±0.10, 3.04±0.09, 2.99±0.08, 3.02±0.10, and 2.99±0.09 are calculated using the 1→0S(0), S(1), and S(2) lines, as outlined in Smith et al. (1997) (Equations 9 and 10). These values are similar to theoretical OPR value of 3 for collisionally excited H_2, and with a previous value of 2.77±0.19 calculated for all possible line combinations given in Van de Steene & van Hoof (2003).

5.3.6 Velocity Structure

To date, two highly detailed H_2 kinematic studies have been performed on this line in *IRAS* 16594-4656 in the recent past (Hrivnak et al., 2008; Van de Steene et al., 2008), which have shown that the H_2 emission can be modelled as a hollow shell expanding at $\sim$ 9 km s^{-1}, with a heliocentric reference velocity (which is used as the systemic velocity) of -29 km s^{-1}.

Figure 5.7 shows a velocity map derived from the 1→0S(1) line emission for *IRAS* 16594-4656 using the SINFONI data. The velocity measurements of the 1→0S(1) line, after corrections for a systematic wavelength offset and heliocentric correction, give a velocity of -36 km s^{-1} in the middle of the south-western lobe, with typical errors of $\sim$ 4–5 km s^{-1} (which do not represent the velocity resolution)[4]. As the resolution of SINFONI is not high enough to resolve the front and back of the expanding shell in this location, the interpretation of this velocity is that it represents the central velocity of the expanding shell.

Near the north-eastern lobe tip the velocity is $\sim$ -29 km s^{-1}, a region where the calculated extinction value and polarisation intensity are low. This suggests that there is less emission from the front side of the shell and so the velocity appears less blue-shifted. The high resolution position-velocity (PV) diagrams given in Figure B.4(a,b) confirm that at this location there is a lack of emission from the front of the shell. These figures are key to understanding why the velocity in the middle of the South-Western lobe is not closer to the published value of systemic velocity as would be expected from fitting a double-peaked line centred at -29 km s^{-1}. To fully understand this, requires the PV diagram given in Figure B.4(e) which is derived from a slit placed from North-South across this lobe. The emission peaks for this slit position are blueshifted slightly in this slit position, thus any velocity calculated at this position from the SINFONI data will likewise be blueshifted. The systemic velocity from this PV diagram, as measured from the published figure, is $\sim$ -35 km s^{-1}, which is in agreement with the SINFONI data and suggests that the South-Western lobe is inclined by a small angle to the plane of the sky – toward the observer.

5.3.7 Distance and Mass estimates

In order to place the central star of a planetary nebula or pre-planetary nebula on a Hertzsprung-Russell (HR) diagram, a luminosity (L) and an effective temperature $T_{\rm eff}$ are traditionally used. However, Schönberner & Tylenda (1990) observe that locating a

[4]The velocity resolution of SINFONI is given by Equation 3.3. The velocity errors give the confidence of the calculated velocity from the line fitting.

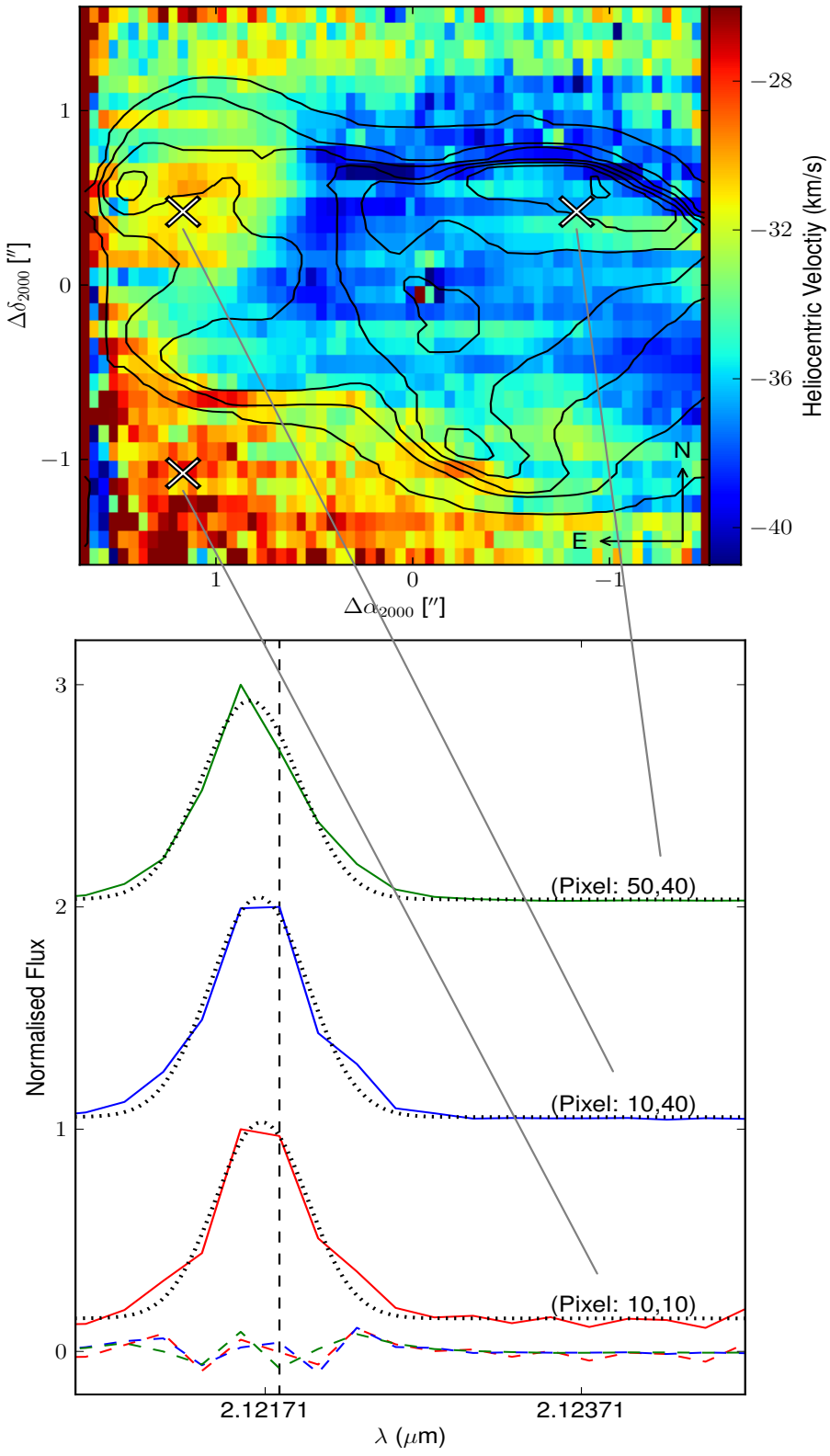

Fig. 5.7: *(top)* A velocity map of *IRAS* 16594-4656 generated from fitting the 1→0S(1) line. The adjacent colourbar indicates the fitted heliocentric velocity (km s^{-1}), while the superposed contours shows the location of the 1→0S(1) line emission. *(bottom)* Line profiles (solid lines), normalised to peak and offset for clarity, at three locations across the object. The dotted line shows the best fit Gaussian, while the horizontal dashed lines correspond to the fit residuals. The vertical dashed line gives the vacuum rest wavelength for the 1→0S(1) transition (2.1218334 μm).

star on the HR diagram in this fashion relies heavily on the accuracy of the luminosity determination.

For Pre-Planetary and Planetary nebulae, it is possible to estimate the dynamic age for the surrounding nebulae, using the assumption that the expansion of the nebulae began as the star departed the AGB, combined with an accurate expansion velocity of the nebula, and a reliable distance estimate. For example, this method was successfully applied to the central star of the planetary nebula NGC 6302 (Szyszka et al., 2009).

In Figure 5.8(*top*) the Blöcker (1995) evolutionary tracks are plotted for several post-AGB core masses. The expansion speed of this nebula is $\sim$ 9 km s^{-1} (Hrivnak et al., 2008) and the radial extent, along the major axis, of the south-western lobe is between 0.009 – 0.013 pcs (assuming distances of 1.9 – 2.6 kpc see Table 5.1). From this we estimate a dynamical age for the nebula of 1000 – 1400 years, in much the same fashion as Hrivnak et al. (2008). The positions of these times are marked on each evolutionary track with a circle ($\circ$) and a cross ($\times$), respectively. The central star of *IRAS* 16594-4656 is known to have an effective temperature of between 12,000 – 14,000 K, which we mark by a shaded green vertical band (see Table 5.1). We find that the core mass, from the intersection of the time contours and the effective temperature estimates, most likely for *IRAS* 16594-4656 is between 0.57 and 0.60 M$_\odot$, which corresponds to an initial mass of $<$ 3 M$_\odot$. From the intersection of these lines we derive an estimate for the luminosity of *IRAS* 16594-4656 of between 4000 L$_\odot$ (0.57 M$_\odot$) and 5900 L$_\odot$ (0.60 M$_\odot$). These values for luminosity would constrain the previous luminosity-based distance estimates and hence the dynamical age of *IRAS* 16594-4656 to values of $<$ 1.9 kpc and 1000 years, respectively.

For comparison, the evolutionary post-AGB tracks of Vassiliadis & Wood (1994) are presented in Figure 5.8(*bottom*). The evolutionary speeds of the post-AGB tracks are different to those presented in Blöcker (1995) due to the treatment of mass loss. Blöcker (1995) use a non-abrupt reduction in mass loss from the end of the AGB phase to post-AGB phase which is proportional to the decreasing radial pulsation period. The tracks of Vassiliadis & Wood (1994) on the other hand switch a radiation driven mass loss as the star evolves off the AGB by ΔTeff=0.3. The fact that the models of Vassiliadis & Wood (1994) switch off mass loss earlier means their transition times from the AGB are longer than the corresponding tracks of Blöcker (1995). Use of the Vassiliadis & Wood (1994) tracks to determine the mass and distance of *IRAS* 16594-4656 leads to a lower estimation of the mass range, between 0.56 M$_\odot$ and 0.59 M$_\odot$. This coupled with the luminosities $\sim$ 4000 L$_\odot$ again favour the lower distance estimate for *IRAS* 16594-4656 of $<$ 1.9 kpc.

5.3.8 H_2 Rotational and Vibrational Temperatures

Temperature estimates can be made once the dereddened line strengths are known, usually two separate estimates 1) a rotational, and 2) a vibrational temperature. If a gas is thermalised, no UV excitation present, these two temperatures should be similar, and line strengths will give a 'gas' temperature, once transformed into the standard [ln($N_{v,J}$ / $g(J)$, E(v, J))] plane. Rotational temperatures can then be obtained from the result of a linear weighted least-squares fit to the data points of same upper v-values (e.g., v=1→0 lines), while vibrational temperatures can be derived from fitting data points of same upper J-values (e.g., for J=3 usable lines might be 1→0S(1), Q(3), and 2→1S(1) lines).

Figure 5.5 (c) shows the regions extracted from the line maps to calculate temper-

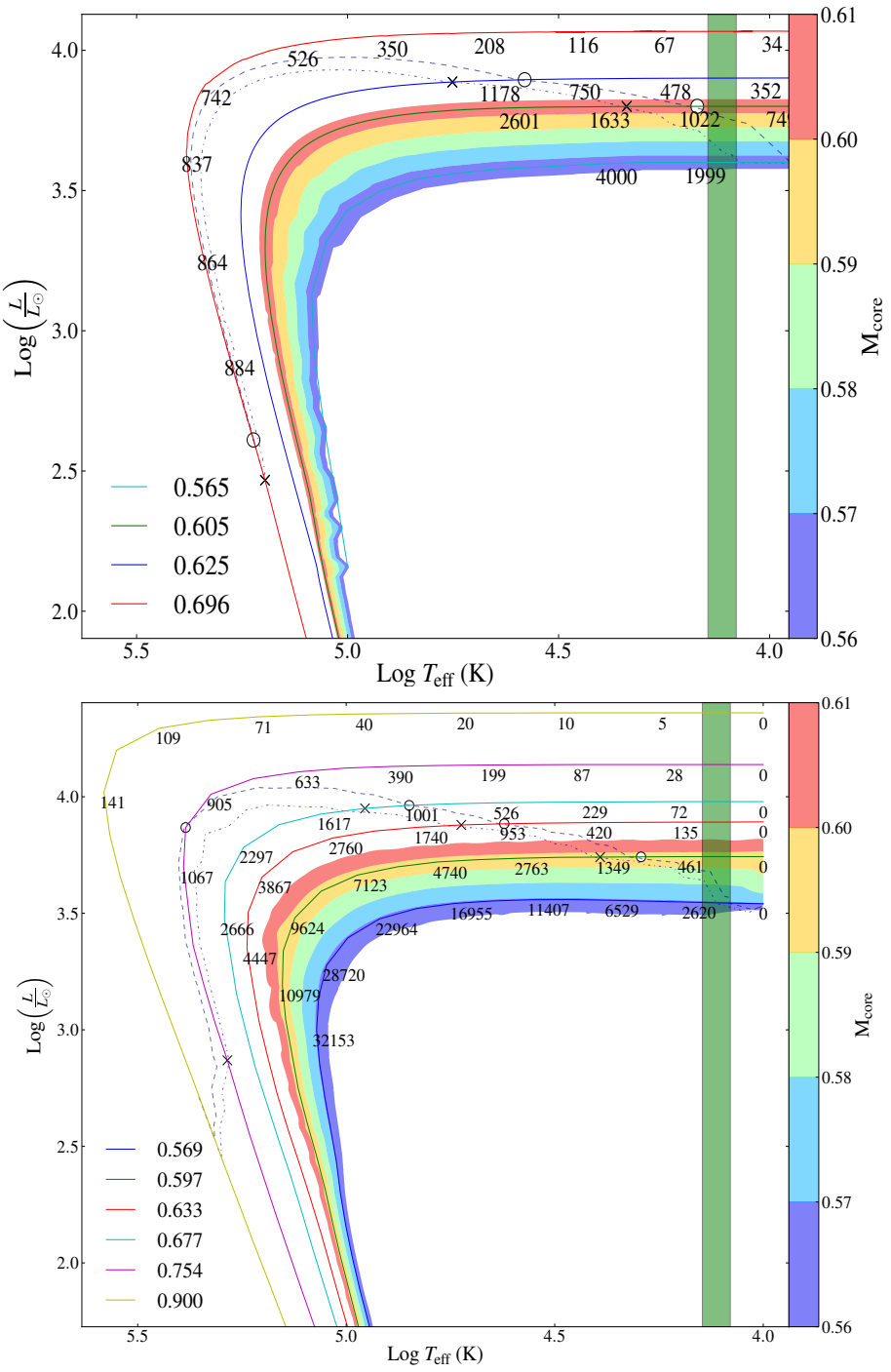

Fig. 5.8: (*top*) Post-AGB evolutionary model tracks for several core masses using the Blöcker (1995) models (solid lines). Time labels are given in years below each track. The location of *IRAS* 16594-4656 on these tracks is given by a circle (T=1000 yrs) and a cross (T=1400 yrs) symbol as determined from the age of the nebula. The shaded green vertical band gives the upper/lower $T_{\rm eff}$ determined from previous studies (see Table 5.1). Filled contours give the interpolated core mass with values indicated on the adjacent colourbar. The dashed contour line shows the interpolated T=1000 yrs locus across all model tracks. The dot-dashed contour line gives the equivalent for T=1400 yrs. The intersection of these lines with the estimates of the $T_{\rm eff}$ suggests a core mass for *IRAS* 16594-4656 of between 0.57 and 0.60 M$_\odot$. (*bottom*) a similar plot but using the tracks of Vassiliadis & Wood (1994).

atures for different regions across *IRAS* 16594-4656. These regions are chosen from the 1→0/2→1S(1) line ratio map (Figure 5.5 [a]), where the ratio (and excitation temperatures) are different. Figure 5.9 (*left*) gives the rotational temperatures for two regions (end and, top of south-western lobe), where the y-axis is the ratio (in the natural log form) of a line's column density divided by its statistical weight (e.g., $N_{\rm v,J}$ / $g(J)$) to the same quantity for the 1→0S(1) line (e.g., $N_{1,3}$ / $g(3)$) and the x-axis is the upper energy value for each line in Kelvin. The data points from each region shown are displayed prior to- and after-extinction correction, as estimated from the Q(3)/S(1) values. Taking the negative inverse of the slope for the resulting fit gives the rotational temperature. The temperature estimates vary slightly across the field-of-view and are in agreement with what is expected from the 1→0/2→1S(1) ratio map (Figure 5.5), i.e., lower temperatures at the end of the bipolar lobes with the regions nearer to the central star displaying higher temperatures.

Rotational temperatures are lower than the vibrational temperatures in *IRAS* 16594-4656. This is similar to the values given in Van de Steene & van Hoof (2003) of $T_{\rm rot}$=1440 K and $T_{\rm vib}$=1820 K. However, they note that both values are within 1.6σ of each other which is consistent the a shock excitation mechanism. They also suggest that the gas is in LTE and realistically represented by a single gas temperature.

5.4 Discussion

Several authors have found it useful to use column density ratios (CDRs) to investigate the excitation of H_2 (e.g., Burton & Haas, 1997). These CDR values, once plotted against the corresponding upper energy level (kT_j), produce a convenient diagnostic diagram (as discussed in Section 2.5.3). Figure 5.9 (*right*) shows the column density ratios (CDRs) for the end of (labelled 'Region 0') and top of (labelled 'Region 1') the south-west lobe. These CDR values can be calculated directly from the flux measurements, as given Equation 2.30. In a strict sense it is the line intensities that must be used in this equation, however, the line flux ratio can be used directly as the solid angle subtended is equal for both lines. The advantage of using this diagnostic is that for a gas at 2000 K in LTE, the data points on the CDR plot would form a horizontal line on the y-axis at zero.

As described in Section 3.5.2, the shock models described in Smith & Brand (1990); Smith (1991, 1994) were used to investigate in more detail the shock parameters in this object. The MCMC models show that C-bow type model provides a good fit to the data (see Figure 5.9 [right]), while a planar C-shock cannot reproduce the CDR values. The gas density determined from the C-bow model fitted to each region *IRAS* 16594-4656 is of the order 10^4 cm^{-3} – 10^5 cm^{-3}, with shock speeds of between 28 – 44 km s^{-1}. The posterior distributions for each parameter are shown in Figure 5.10 for the C-bow shock model with the shaded regions indicating the credible regions for each parameter (see Section 3.5.2 for more details). These densities are lower than the electron densities determined by Van de Steene et al. (2008) of 3×10^6 – 5×10^7 cm^{-3} calculated from [OI] and [CI] forbidden lines. This implies that the H_2 and the forbidden lines are not exactly coincident, however they might be produced in the same shock event. In the case of the C-bow shock, this is effectively the combination of a J-type cap where H_2 might be dissociated and atomic optical lines are produced, and C-type wings where the shock velocity and density have dropped and the H_2 can become excited without dissociating.

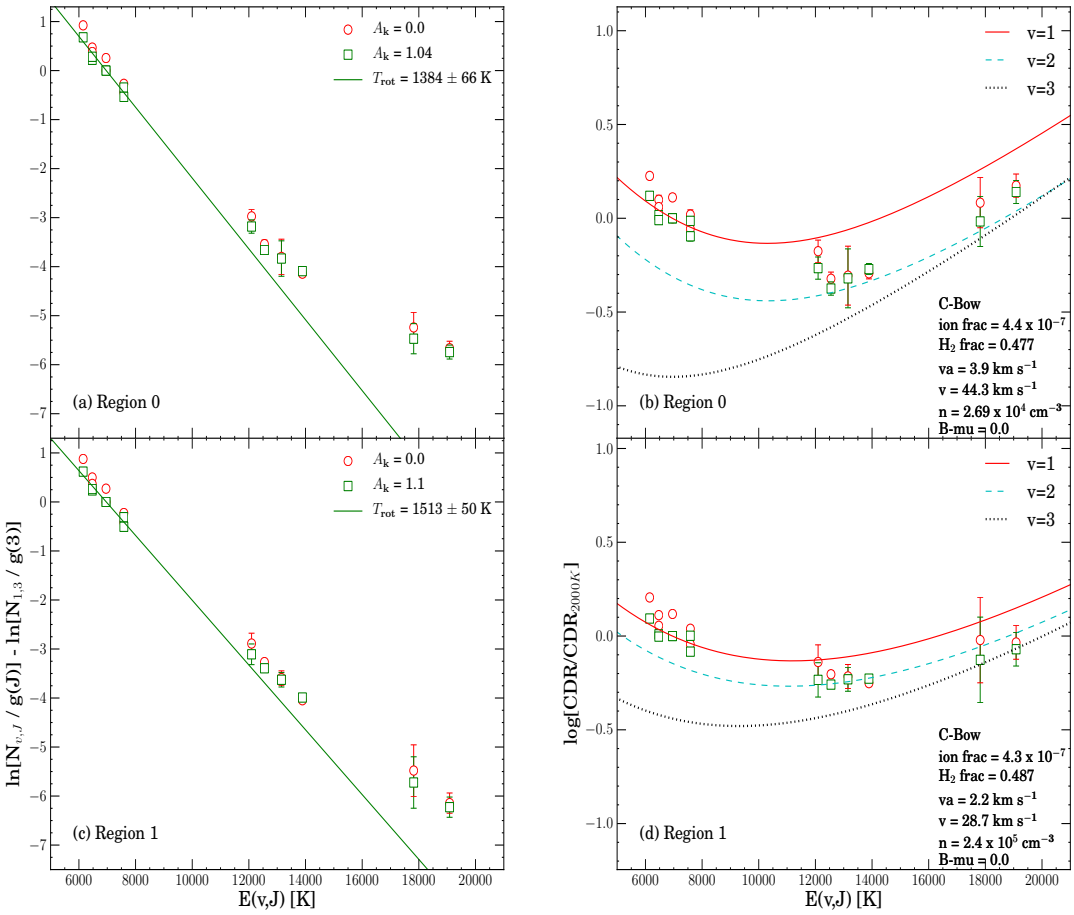

Fig. 5.9: Temperature and Column Density Ratio (CDR) plots for extracted regions across *IRAS* 16594-4656. (*left*) [ln($N_{v,J}$ / $g(J)$, E(v, J))] plots for each region from which the gas temperature is derived. Each subplot represents a different extraction region with labels inset. The red circles (○) represent the data points prior to extinction correction. Similarly, the green squares (□) represent the de-reddened data points and the solid line indicates the rotational temperature fit for the v=1 level only. Temperature values (plus errors) and the extinction values used are given in the inset labels. (*right*) the corresponding CDR diagrams for each region. Symbols are as above. Inset labels give the best-fit shock model parameters. Errorbars are propagated from flux errors, the v=1 errorbars lie within the symbols. The solid, dashed, and dot-dashed lines represent the v=1, 2, and 3 CDR models for the fitted C-bow model.

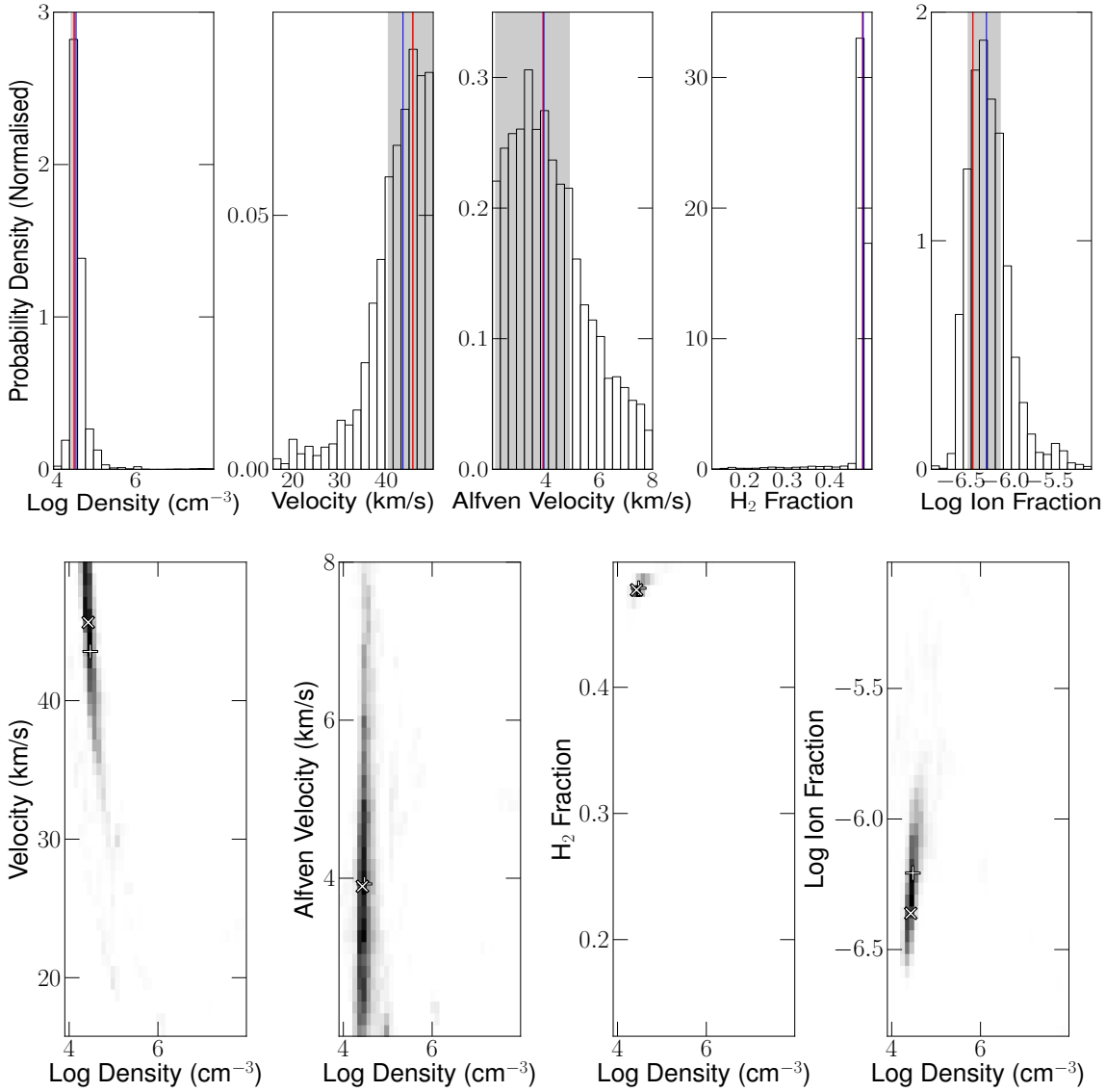

Fig. 5.10: The 1-d and 2-d posterior distributions from the MCMC shock model fitting technique for Region 0 in Figure 5.9. The red solid vertical line gives the location of the best fit values, while the blue solid gives the location of the Bayesian estimator. The credible intervals for each parameter are marked by the shaded regions. Individual values of n=$4.48^{0.0018}_{-0.12}$ cm^{-3}(log$_{10}$), v=$43.6^{6.1}_{-3.1}$ km s^{-1}, v_a=$3.9^{0.95}_{-1.8}$ km s^{-1}, f=$0.47^{0.0019}_{-0.0019}$, χ=$-6.2^{0.16}_{-0.21}$.

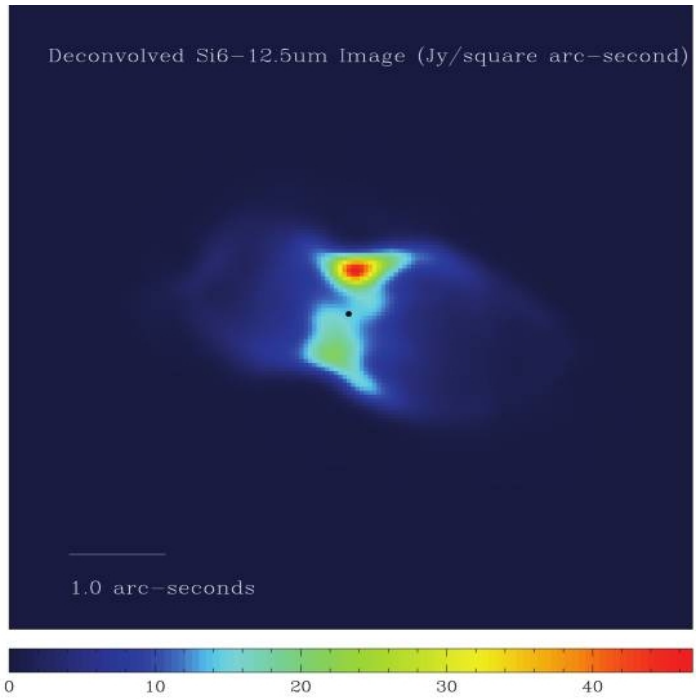

Fig. 5.11: A deconvolved mid-IR false-colour image of *IRAS* 16594-4656, clearly showing the thermal emission from the dust forming a torus around the object. Note also, the fainter thermal emission tracing the H_2 in the lobes [*image from* Volk et al. (2006)].

A shock propagation speed of $\sim$ 60 km s^{-1} is needed to drive the C-bow shock model at a shock speed of 44 km s^{-1} assuming that the surrounding ambient medium is moving outward at a velocity of $\sim$ 16 km s^{-1} (Loup et al., 1990). It can be shown that the escape velocity for the central star would be of the order of 125 km s^{-1}, using the luminosity, and the core mass determined in § 5.3.7, and an effective temperature of 13,000 K. Interestingly, Van de Steene et al. (2000b) determine a terminal wind velocity of 126 km s^{-1} from the Hα line, and confirming the presence of a fast wind in this object. This wind speed is higher than the speed required for our C-bow model and most likely represents the highest speed component in the system. The speed the shock is propagating at is most likely found between this fast wind speed and the slower AGB wind speed. Interaction with the remnant torus material, as seen in Figure 5.11, leads to the excitation of other species present nearer the central star; For example Van de Steene et al. (2008) detect centrally located [FeII] emission moving at 30.0 km s^{-1}, and Paβ at 48.2 km s^{-1}, which may be slowing the fast wind to a lower velocity. One possible method of uncovering the speed of the of the wind that is shocking the H_2 is by measuring the distance to four ansae (see Figure 3a in Hrivnak et al., 2008) which are presumably blown off the end of the lobes of *IRAS* 16594-4656 at the same time the nebula began expanding. The south-western ansae is located at a distance of $\sim$ 5.5 arcseconds (after deprojection using a tilt to the plane of the sky of 10°) equivalent to a distance of 1.6 $\times$ 10^{12} km. Assuming the dynamical age of the nebula is 1000 years (see §5.3.7), the wind must be moving at a velocity of at least 50 km s^{-1}.

The presence of Mg II lines in *IRAS* 16594-4656 has not been detected before. For example, Van de Steene & van Hoof (2003) present a longslit *K*-band spectrum for this object (see Figure B.2) in which they do not detect the lines. The only previous reference to these lines found in the PPNe literature was that of Kelly & Hrivnak (2005). They list four PPNe with these lines in emission all four are B-type stars.

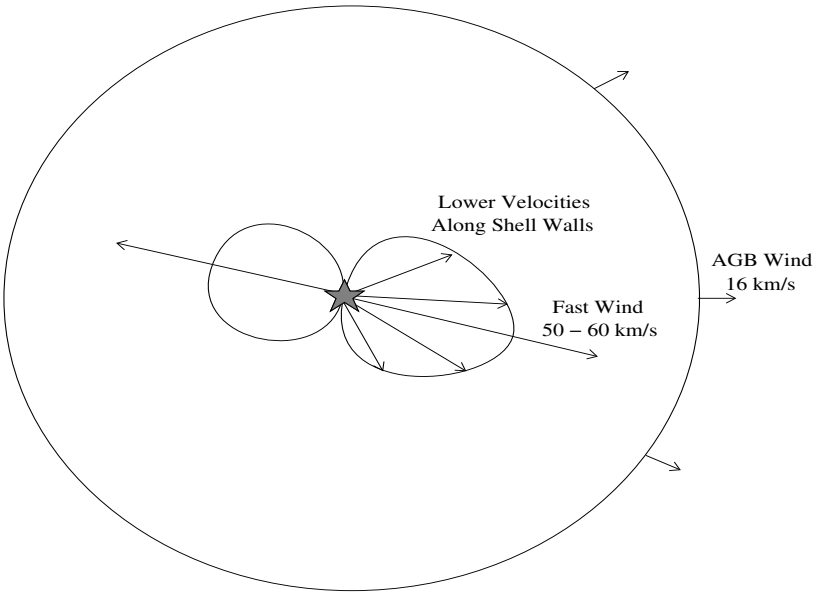

Fig. 5.12: Schematic of the model assumed for *IRAS* 16594-4656, where a bipolar fast wind is driving the expansion of the bubble, leading to higher shock velocities along the axis and lower velocities along the edge of the lobes. Orientation is as the same as the SINFONI line maps, North is up and East is left.

IRAS 16594-4656 also being a B7-type star suggests that theses lines might be another indicator that the nebula is near the onset of the ionisation process. In Chapter 6 another B-type star is added to the list of objects displaying these emission lines. This increases the number of PPNe from 4 → 6, however these lines might be more common than these low numbers might suggest. A further 5 B-type PPNe are known to exhibit Mg II line emission (private comm. Tim Gledhill). The spatial distribution of the Mg II in *IRAS* 16594-4656 is centrally located, however it is not clear if this will be the case for all B-type PPNe. The fact that these lines have only been observed in B-type PPNe with H_2 is puzzling but further observations would be required to prove/disprove if this is always the case.

The expansion of the nebula might be driven by a fast bipolar wind whose radial component is observed as the expansion velocity of the lobes (9 km s^{-1}), giving rise to lower density and higher velocity shocked gas at the end of each lobe, and higher density and lower velocity shocked gas along the walls.

Alternatively, both J-bow and J-planar type shocks are also capable of fitting the data at shock velocities of 13 km s^{-1} and 25 km s^{-1}, pre-shock densities of 2×10^7 cm^{-3} and 7×10^7 cm^{-3}, and Alfvén velocities of 5 km s^{-1} and 2 km s^{-1}, respectively. The densities returned by the J-shock models also seem unreasonably large. For example, estimating a column length of H_2 of 1.1×10^{16} cm from the shell thickness, as measured from our images (0.4 arcseconds at 1.9 kpcs)[5], and using the standard visual extinction to total hydrogen column density conversion, A_v / N(H)=5.3×10^{-22} mag cm^{-2}, gives A_v values of between $\sim$ 110 – 500 mags, far in excess of what is estimated from the line ratios. Therefore this suggests that a J-shock model is not appropriate to model the H_2 shocks in *IRAS* 16594-4656.

[5]The distance used here is not critical to this calculation. For example, at the largest estimated distance to *IRAS* 16594-4656 the column length only increases to 1.6×10^{16} cm.

5.5 Conclusions

IRAS 16594-4656 displays a multi-polar morphology when viewed at optical wavelengths, while at near-IR wavelengths the appearance is strongly bipolar. The H_2 lobes are pinched in at the 'waist' of the object by a dusty torus of mid-IR emission, with the two H_2 lobes mirrored in the dust emission (Volk et al., 2006; García-Hernández et al., 2006). The H_2 and the dust appear spatially coincident and Volk et al. (2006) raise the possibility that the dust is at least partially heated by the shock. The line maps described in § 5.3.2 further confirm the bipolar nature of *IRAS* 16594-4656 at NIR wavelengths.

- Through the use of line maps the spatial extent of each line can be easily uncovered. Figure 5.4 shows that the Brγ for *IRAS* 16594-4656 is located in close proximity to the central star and does not extend out into the H_2 lobes of the object. This is an expected result as it is a recombination line and higher energies are required to excite it.

- Three new v=2 and two v=3 ro-vibrational H_2 lines have been detected in the K-band, all of which are most likely generated in shocks.

- A C-shock bow model is required to the fit the column density ratio and luminosity values. An average pre-shock hydrogen nucleon density of 10^5 cm^{-3}, shock velocities of above 30 km s^{-1}, and low ionisation fraction are determined for *IRAS* 16594-4656. At these densities the magnetic field strength would be $\sim$ 0.5 mG.

- The Mg II doublet at λ=2.1375 and 2.1438 μm has been detected for the first time. The longer wavelength line is not reliable and so only flux measurements for the shorter wavelength line is provided. Construction of a line map for this line shows that it is centrally located in a very similar fashion to the location of the Brγ line. Most likely these lines are being excited from the higher energy photons at this position, although further detailed investigation is required to confirm this.

References

Blöcker, T. 1995, A&A, 299, 755

Burton, M. G. & Haas, M. R. 1997, A&A, 327, 309

Davis, C. J., Smith, M. D., Stern, L., Kerr, T. H., & Chiar, J. E. 2003, MNRAS, 344, 262

Eisenhauer, F., Abuter, R., Bickert, K., Biancat-Marchet, F., Bonnet, H., Brynnel, J., Conzelmann, R. D., Delabre, B., Donaldson, R., Farinato, J., Fedrigo, E., Genzel, R., Hubin, N. N., Iserlohe, C., Kasper, M. E., Kissler-Patig, M., Monnet, G. J., Roehrle, C., Schreiber, J., Stroebele, S., Tecza, M., Thatte, N. A., & Weisz, H. 2003, in Society of Photo-Optical Instrumentation Engineers (SPIE) Conference Series, Vol. 4841, Society of Photo-Optical Instrumentation Engineers (SPIE) Conference Series, ed. M. Iye & A. F. M. Moorwood, 1548, 1561

García-Hernández, D. A., Manchado, A., García-Lario, P., Cañete, A. B., Acosta-Pulido, J. A., & García, A. M. 2006, ApJ, 640, 829

García-Hernández, D. A., Manchado, A., García-Lario, P., Domínguez-Tagle, C., Conway, G. M., & Prada, F. 2002, A&A, 387, 955

García-Lario, P., Manchado, A., Ulla, A., & Manteiga, M. 1999, ApJ, 513, 941

Geballe, T. R., Russell, R. W., & Nadeau, D. 1982, ApJ, 259, L47

Heckert, P. A. & Zeilik, II, M. 1983, MNRAS, 202, 531

Hrivnak, B. J., Kelly, D. M., Su, K. Y. L., Kwok, S., & Sahai, R. 2006, ApJ, 650, 237

Hrivnak, B. J., Kwok, S., & Geballe, T. R. 1994, ApJ, 420, 783

Hrivnak, B. J., Kwok, S., & Su, K. Y. L. 1999, ApJ, 524, 849

Hrivnak, B. J., Smith, N., Su, K. Y. L., & Sahai, R. 2008, ApJ, 688, 327

Hrivnak, B. J., Volk, K., & Kwok, S. 2000, ApJ, 535, 275

Kelly, D. M. & Hrivnak, B. J. 2005, ApJ, 629, 1040

Kurucz, R. 1994, Solar abundance model atmospheres for 0,1,2,4,8 km/s. Kurucz CD-ROM No. 19. Cambridge, Mass.: Smithsonian Astrophysical Observatory, 1994., 19

Loup, C., Forveille, T., Omont, A., & Nyman, L. A. 1990, A&A, 227, L29

Markwardt, C. B. 2009, in Astronomical Society of the Pacific Conference Series, Vol. 411, Astronomical Data Analysis Software and Systems XVIII, ed. D. A. Bohlender, D. Durand, & P. Dowler, 251

O'Connell, B., Smith, M. D., Froebrich, D., Davis, C. J., & Eislöffel, J. 2005, A&A, 431, 223

Reyniers, M. 2002, PhD thesis, AA(Departement Natuurkunde en Sterrenkunde, K.U.Leuven, Celestijnenlaan 200B, 3001 Leuven, Belgium)

Sahai, R., Morris, M., Sánchez Contreras, C., & Claussen, M. 2007, AJ, 134, 2200

Schönberner, D. & Tylenda, R. 1990, A&A, 234, 439

Smith, M. D. 1991, MNRAS, 252, 378

—. 1994, MNRAS, 266, 238

Smith, M. D. & Brand, P. W. J. L. 1990, MNRAS, 242, 495

Smith, M. D., Davis, C. J., & Lioure, A. 1997, A&A, 327, 1206

Stead, J. J. & Hoare, M. G. 2009, MNRAS, 400, 731

Su, K. Y. L., Hrivnak, B. J., & Kwok, S. 2001, AJ, 122, 1525

Szyszka, C., Walsh, J. R., Zijlstra, A. A., & Tsamis, Y. G. 2009, ApJ, 707, L32

Ueta, T., Murakawa, K., & Meixner, M. 2005, AJ, 129, 1625

—. 2007, AJ, 133, 1345

Van de Steene, G. C., Ueta, T., van Hoof, P. A. M., Reyniers, M., & Ginsburg, A. G. 2008, A&A, 480, 775

Van de Steene, G. C. & van Hoof, P. A. M. 2003, A&A, 406, 773

Van de Steene, G. C., van Hoof, P. A. M., & Wood, P. R. 2000a, A&A, 362, 984

Van de Steene, G. C., Wood, P. R., & van Hoof, P. A. M. 2000b, in Astronomical Society of the Pacific Conference Series, Vol. 199, Asymmetrical Planetary Nebulae II: From Origins to Microstructures, ed. J. H. Kastner, N. Soker, & S. Rappaport, 191

Van der Veen, W. E. C. J. & Habing, H. J. 1988, A&A, 194, 125

Van der Veen, W. E. C. J., Habing, H. J., & Geballe, T. R. 1989, A&A, 226, 108

Vassiliadis, E. & Wood, P. R. 1994, ApJS, 92, 125

Volk, K., Hrivnak, B. J., Su, K. Y. L., & Kwok, S. 2006, ApJ, 651, 294

Volk, K. M. & Kwok, S. 1989, ApJ, 342, 345

Chapter 6: Rest of the Sample

6.1 Introduction

The remaining observations consisted of three late-type post-AGB objects and a single early-type post-AGB object. Table 6.1 gives a summary of the details of the observations. This Chapter will detail these remaining post-AGB objects for which data was obtained, *IRAS* 17441-2411, *IRAS* 17150-3224, *IRAS* 19500-1709, and *IRAS* 14331-6435.

6.2 Observations

Each object frame has an associated sky frame offset from the target, as there is insufficient sky available in the object frames to perform accurate sky subtraction. Several telluric standard stars were observed throughout the night; calibration of the data was carried out using each of these stars as a check on consistency. The selected standard used for each science target is given in Table 6.1.

Accurate telluric correction relies upon the telluric calibrator star being observed at similar atmospheric conditions to the science target. This is especially important in spectral regions where there are strong telluric features caused by the absorption by gaseous oxygen (O_2), water vapour (H_2O), and carbon dioxide (CO_2), e.g., the region between 1.9 and 2.1 μm. Figure 6.1 gives the details of the changes in the airmass throughout the observations. As each observation can last up to 20 mins in total, the values given by the ESO header keywords `HIERARCH ESO TEL AIRM START` and `HIERARCH ESO TEL AIRM END` are used to calculate the average airmass per observation. The observations of *IRAS* 19500-1709 are spread over the longest period and, as might be expected, suffer from the largest change in airmass. In this case, the telluric star used was taken in the middle of the observation sequence. Telluric stars used to correct *IRAS* 17441-2411 and *IRAS* 17150-3224 were taken at the beginning of each sequence, as these were the closest calibrator stars, in time, to the science targets.

The majority of telluric calibrator stars observed were G-type stars which display weak absorption lines in the NIR. The use of these types of stars complicates the process of differentiating between real features and 'introduced' features if the science target is of a similar spectral type (see Figure 6.4).

Table 6.1: Details of the observations *IRAS* 17441-2411, *IRAS* 17150-3224, *IRAS* 19500-1709, and *IRAS* 14331-6435 and associated telluric standard stars used for atmospheric correction and flux calibration.

	IRAS 17441-2411	*HD* 159033	*IRAS* 17150-3224	*HD* 156152	*IRAS* 19500-1709	*HD* 186853	*IRAS* 14331-6435	*HD* 152432
Date	30-06-2005	30-06-2005	29-06-2005	29-06-2005	29-06-2005	29-06-2005	04-02-2010	04-02-2010
No. Images	6	1	6	1	8	1	1	1
No. Sub-Images	1	1	3	1	20	1	4	5
Exposure (secs)	180	10	100	10	10	10	120	2
Filter	K	K	K	K	K	K	K	K
Airmass (mean)	1.03	1.02	1.08	1.15	1.12	1.097	1.35	1.37
2MASS K (mag)$^{\triangle}$	9.380	6.991	9.391	6.591	6.858	6.098	8.887	6.765
Spectral Type$^{\triangle}$	F5	G3V	G2	G3V	F2/F3I	G5V	B3I	G3V

$^{\triangle}$ 2MASS magnitudes and spectral types taken from SIMBAD

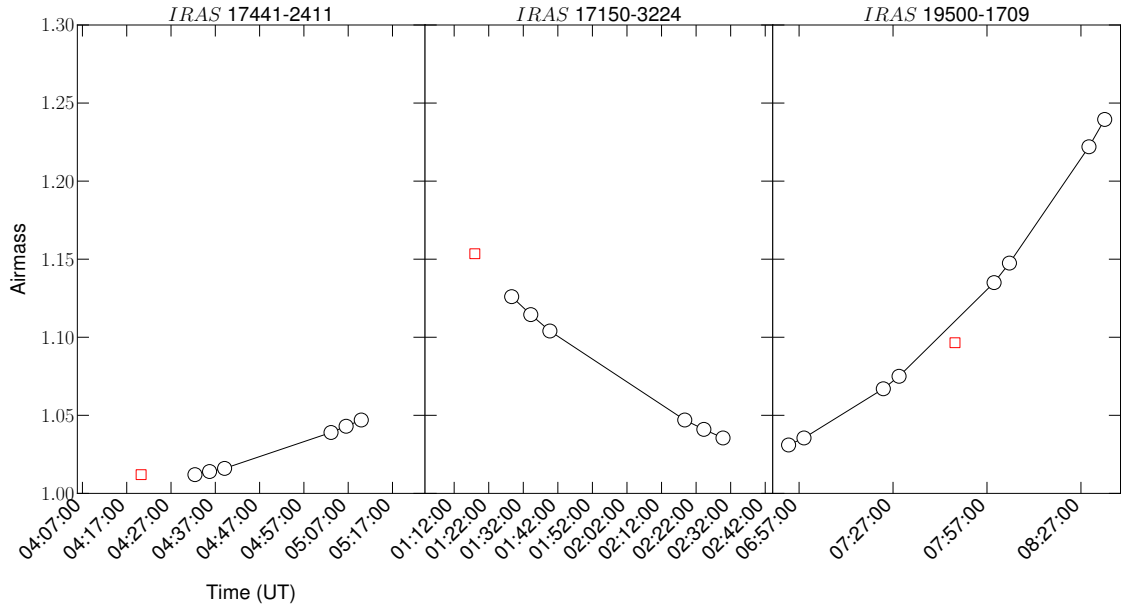

Fig. 6.1: The change in airmass values for each observation as each observing block was executed. Black circles (○) represent a science observation, while a red square (□) represents the telluric standard star. Note: *IRAS* 14331-6435 observation is not displayed here as it consists of a single observation, the average airmass for that observation is given in Table 6.1.

6.3 H_2 Emission Sources

6.3.1 *IRAS* 17441-2411

IRAS 17441-2411, also known as the "Silkworm Nebula" (Su et al., 1998), is a late-type (F5) post-AGB star with an extended nebula. Kwok et al. (1996) produced the first high-resolution (0.13″/pix), V- and I-band images of *IRAS* 17441-2411 using the Canada-France-Hawaii Telescope (CFHT). The images in both filters showed *IRAS* 17441-2411 to have a bipolar morphology with its axis at a position angle (PA) of $\sim 17°$. These V - I images also showed a redder component located along the waist of the nebula, which the authors suggest might be a possible disc; the central star is not seen in the visible. *IRAS* 17441-2411 displays a double-peaked SED with IR excess, typical of PPN. With *Hubble Space Telescope (HST)* imaging of *IRAS* 17441-2411 using the Wide-Field Planetary Camera 2 (WFPC2), Su et al. (1998) detected two circular arcs at the end of each lobe and hints of two more beyond the lobes, probably indicating intervals of enhanced mass loss. *IRAS* 17441-2411 shows a distinct S-shaped morphology in the visible (F606W) images (Su et al., 1998), which is also noted in NIR images. This S-shaped appearance is typical of point-symmetric nebulae. High-resolution NIR imaging and polarimetry allowed Su et al. (2003) to construct colour and polarimetric maps for this nebula. These maps show (1) that the lobes are bluer than the equatorial region, (2) that the Southern lobe is fainter and redder than its Northern counterpart, and (3) that both lobes are highly polarised. This suggests that lobes are seen almost entirely in scattered light and that the Southern lobe is inclined away from the observer.

H_2 was first detected by Weintraub et al. (1998) via the 1→0S(1) line. Although the

spectrum was not spatially resolved, it is proposed that the H_2 might be confined to an expanding equatorial torus, as was the case for another object in their study, namely, *IRAS* 17150-3224. In a low S/N spectrum of *IRAS* 17441-2411, no H_2 or CO bandhead emission is detected in either the core or the lobes by Davis et al. (2003) (attributed to the higher shot-noise in the observations); the Brγ line was detected in absorption. Hrivnak et al. (2004) show a NICMOS continuum-subtracted H_2 image of the object, which identifies the emitting regions to be located in the bipolar lobes. Kelly & Hrivnak (2005) report the detection of a weak 1→0S(1) line in their reduced spectrum, however suggest that much of the H_2 emitting regions might have been missed by their small slit width (2.4″); no other H_2 lines were noted in this study. Davis et al. (2005) carried out the only other H_2 study of this object to date. Using NIR echelle spectroscopy (R $\sim$ 18,750), discrete knots of H_2 are detected at the ends of the bipolar lobes, with the H_2 spectra from each lobe showing narrow profiles ($\sim$ 25 km s^{-1}).

Volk et al. (2007) discuss the possible precession of a disc in *IRAS* 17441-2411, using mid-IR data from Gemini (Si-2 & Si-5 wavelengths). These data reveal dust emission in both bipolar lobes and the equatorial region. An IR torus is detected offset, in PA, by 23° to the optical dark lane. The authors suggest that this might be the result of rapid precessional motion of the torus (1°/yr) for the past $\sim$ 100 years. The size (1000 AU at 1 kpc) of this structure is large, and unlikely to be the primary reason for precession. The authors suggest that this torus is formed in response to a smaller central disc.

Table 6.2 gives some important details found in the literature regarding this object.

Table 6.2: Summary of *IRAS* 17441-2411 properties from literature.

Parameter	Value	Reference
R.A. (α_{2000})	$17^h\ 47^m\ 13^s.49$	a
Dec. (δ_{2000})	-24° 12′ 51″.4	a
K (mag)$^{\triangle}$	9.38	a
Spectral Type	F5,F4-5	a,d
Morphological Type	Bipolar	b,c
Distance (kpc)	4, 1.9*	b,d
Inclination Angle	< 30	c
Anglular Size (arcsec)	12 × 7	d

$^{\triangle}$ 2mass magnitude

* minimum distance ($L = 3000\ L_{\odot}$).

References. – a. SIMBAD; b. Davis et al. (2005); c. Su et al. (1998); d. Sánchez Contreras et al. (2008); d. Kwok et al. (1996).

Results & Discussion

The IFU observations of this late-type (F5) star reveal the presence of many previously undetected ro-vibrational H_2 lines. A wavelength correction of -2.8 × 10^{-4} (± 5.0 × 10^{-5}) μm was determined from the sky lines (as described in Subsection 3.3.1), and all velocities presented take this into account.

Table 6.3: The total continuum-subtracted flux for each of the observed lines (prior to extinction correction).

Line	λ_{lab} (μm)*	F $\times 10^{-18}$ (W m^{-2})	
		North Lobe	South Lobe
1→0S(3)	1.9576	5.89 ± 0.612	5.90 ± 0.447
1→0S(2)	2.0338	1.63 ± 0.184	1.47 ± 0.120
1→0S(1)	2.1218	4.66 ± 0.290	3.82 ± 0.236
1→0S(0)	2.2235	1.02 ± 0.119	7.79 ± 0.943
1→0Q(1)	2.4066	4.48 ± 0.696	3.63 ± 0.473
1→0Q(2)	2.4134	2.23 ± 0.812	1.71 ± 0.620
1→0Q(3)	2.4237	4.10 ± 0.471	3.33 ± 0.375
1→0Q(4)¶	2.4375	—	—
2→1S(1)	2.2477	0.55 ± 0.084	0.44 ± 0.088

* Laboratory wavelength measurements are given in a vacuum.
¶ line heavily affected by a telluric feature.

Previous studies of this object (as discussed above) have focused on the detection of the 1→0S(1) line. For example, Davis et al. (2005) show from their position-velocity diagrams that the H_2 emission is located in discrete knots in the bipolar lobes. Figure 6.2 shows integrated intensity line maps for the 1→0S(1) and 2→1S(1) transitions, alongside a 1→0/2→1S(1) line ratio map. These maps confirm that the H_2 is confined to two distinct regions North and South of the central star. Where possible, the construction of line maps using other transitions yields the same emission structure. For the first time, the 2→1S(1) line is detected in this object, which allows the construction of a line ratio map for this object (see Figure 6.2 [a]). The map reveals that the 1→0/2→1S(1) values in both lobes are similar with a value of 8.5±1.8 in the North lobe and a value of 8.7±2.0 in the South lobe, prior to extinction correction. These values suggest that shocks are the primary mechanism for the H_2 excitation. As seen in Figure B.1, the 1→0/2→1S(1) value will increase once an extinction correction is applied. Using the 1→0S(1) and 1→0Q(3) line pair, an A_k of ~ 0.9 is calculated for both lobes. Correcting by this amount increases the 1→0/2→1S(1) values to 9.4±1.6 and 9.7±2.0 for the North and South lobes, respectively — confirming that the H_2 is emitting due to thermal excitation. Figure 6.2 [c] shows that the 2→1S(1) emission extent appears to be less than the 1→0S(1) emission. This is most likely due to the much lower S/N of the 2→1S(1) image per pixel.

Kelly & Hrivnak (2005) report the only 1→0S(1) flux measurement published to date for this object — 0.54×10^{-17} W m^{-2}. Using a simulated slit of the same width, the 1→0S(1) flux measured in the SINFONI observations was 0.57×10^{-17} W m^{-2}, which is in good agreement with their value. This offers reassurance of the flux calibration and telluric correction of the data.

Fitting one of the H_2 lines, 1→0S(1), with a Gaussian profile allows the construction of a velocity map for *IRAS* 17441-2411. Figure 6.3 presents the resulting map, which shows a good agreement with the echelle data presented in Davis et al. (2005). The map shows that the Southern lobe is slightly blueshifted, while the Northern lobe is slightly redshifted. If this H_2 emission is being shocked by an axial outflow, then

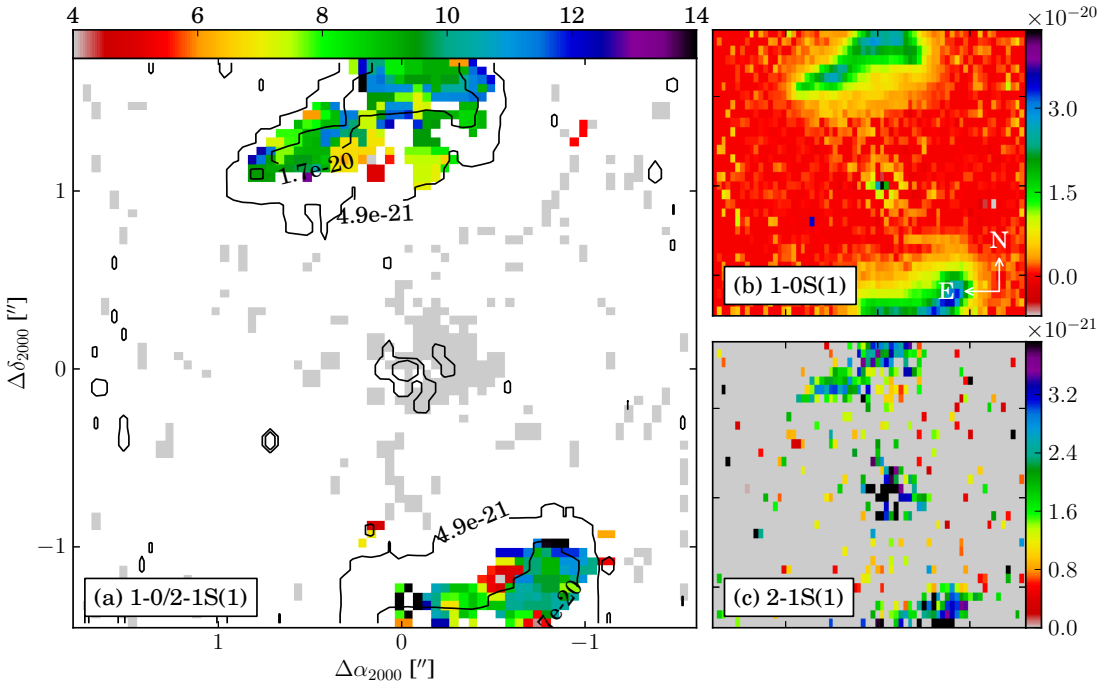

Fig. 6.2: (a) The 1→0/2→1S(1) line ratio map for *IRAS* 17441-2411 prior to extinction correction. The contours overlaid show the position of the 1→0S(1) H_2. (b) shows the 1→0S(1) line map, inset compass shows orientation. (c) show the 2→1S(1) line map, note the noisier appearance due to the weaker emission.

these velocities would suggest that the nebula bipolar axis is tilted ,to a small degree, with the Southern lobe toward the observer. This is contrary to the suggestion by Su et al. (1998), who suggest that due to the difference in peak intensities of both lobes, the South lobe is tilted away from the observer. Later observations show that the South lobe is redder and fainter, possibly due to increased extinction (Su et al., 2003). However, the extinction values obtained from the H_2 lines are, within errors, the same for both lobes, which would not support this explanation. The velocity of the system as estimated from the Brγ absorption line is 2.3±6 km s^{-1}, which is similar to the velocity of 4.9 km s^{-1} estimated by Davis et al. (2005).

Figure 6.4 shows three spectra, centred on the NIR Na I doublet region. The telluric corrected spectrum shows two peaks at the Na I wavelengths (2.206242 & 2.208969 μm), however interpreting this emission as real is complicated by the fact that the telluric calibrator star used is of type G3V, and shows evidence for weak NaI absorption. For comparison, the same region from the raw spectrum of *IRAS* 17441-2411 is shown, which also shows two peaks at the same wavelength as in the corrected spectrum. For this reason, the Na I is interpreted as real and coming from a region of dense gas close to the central star. The spatial distribution of these lines is peaked at the continuum peak with weaker extended emission along the bipolar axis, as is the case for *IRAS* 17150-3224 (see following Section). We suggest that the Na I emission originates near the star and is scattered into the lobes. This is supported by polarisation maps produced by Su et al. (2003) which show that the lobes of *IRAS* 17441-2411 are highly polarised (> 40%) and so are almost entirely observed in scattered light. As noted in many young stellar objects (YSOs), the presence of the Na I emission lines is often accompanied by CO bandhead emission. *IRAS* 17441-2411 displays this CO bandhead

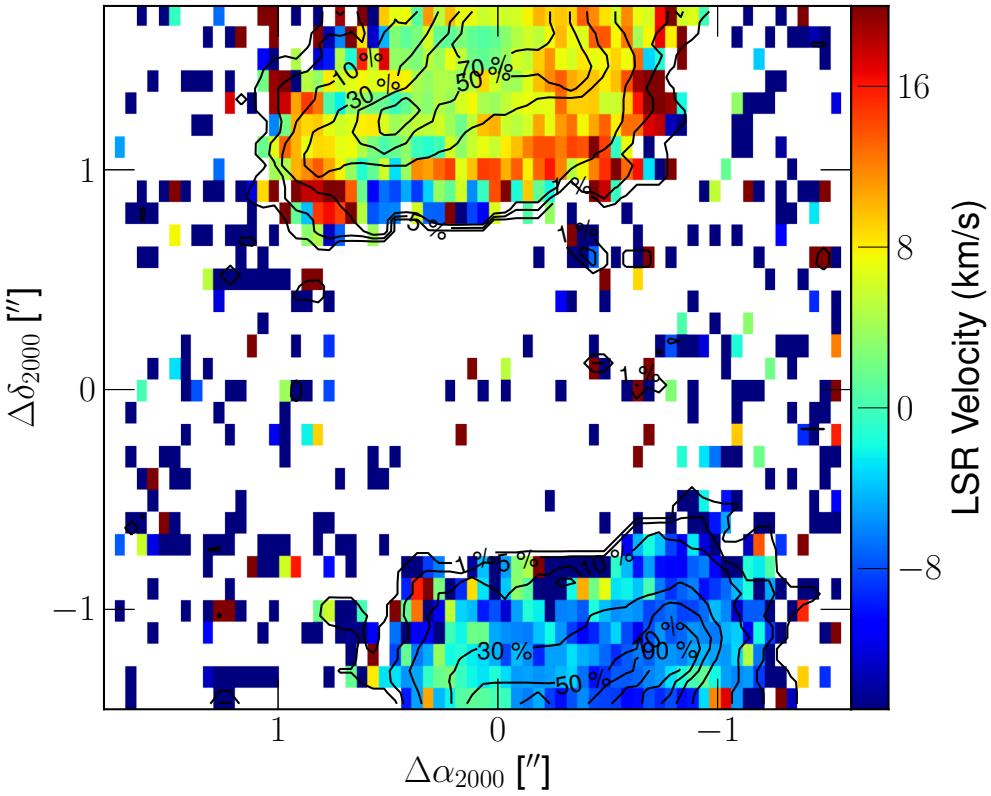

Fig. 6.3: *IRAS* 17441-2411 velocity map showing LSR velocities for the 1→0S(1) line. Contours show the 1, 5, 10, 30, 50, 70, and 90% of the peak.

emission (v=2-0, v=3-1, v=4-2, and possibly v=5-3), however as mentioned above the use of a G3V-type calibrator introduces some uncertainty in the actual presence of these lines. Reassuringly, the spectrum of the adjacent star (see Figure 6.5) shows strong CO bandhead absorption, one might expect these features to be adversely affected by the division by a standard star with CO also in absorption — this does not seem to be the case. The presence of these two spectral features is thought to be the result of emission from a dense region of gas (n=10^{10} cm^{-3}) possibly held in a disc configuration as models have suggested (Gledhill et al., 2011; Gledhill & Forde, 2012).

A NIR continuum image of *IRAS* 17441-2411 is formed by extracting a channel free of any spectral lines from the datacube (see Figure 6.6). The S-shaped morphology is clearly evident, as was noted in previous NIR studies (Su et al., 2003) — another PPNe with point-symmetric structures. The image also shows in the SINFONI FOV the presence of an adjacent star. If both *IRAS* 17441-2411 and this star were located at the same distance (e.g., 2 kpc) then the star would lie ∼ 2400 AU from the post-AGB star. This distance could make it a wide binary companion, however comparison of the Na I doublet absorption features in the adjacent star and the Na I emission in *IRAS* 17441-2411 shows that there is an offset between the two line wavelengths. This should not be the case if they were a co-moving system. Of course the source of the absorption and the emission are completely different and as such must not be used as absolute proof that the objects are independent.

The excitation diagrams presented in Figures 6.7 and 6.8 reveal the temperature,

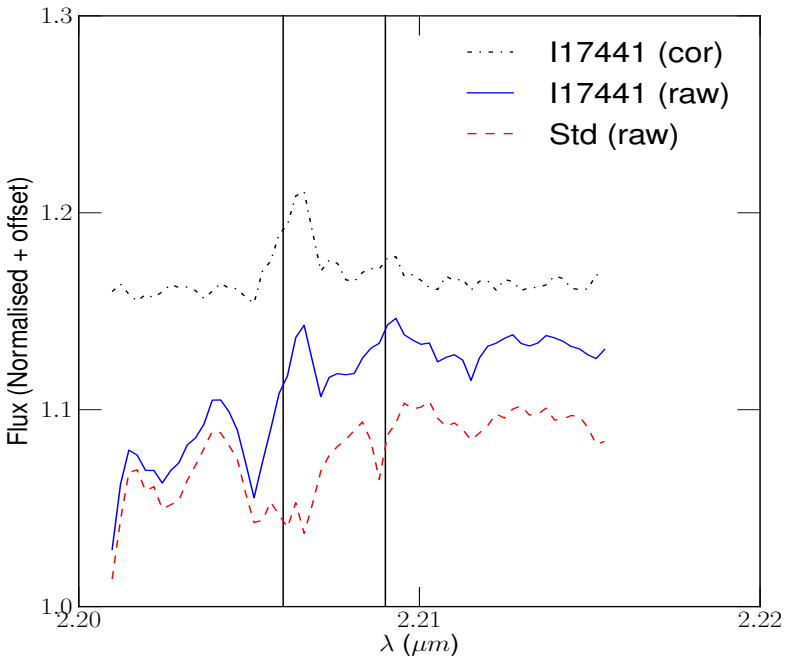

Fig. 6.4: Na I doublet feature in emission in *IRAS* 17441-2411. Vertical solid lines give the vacuum lab wavelengths for the Na I doublet (2.206242 & 2.208969 μm). The solid line spectrum represents the raw (before telluric correction) spectrum of the target. The dashed spectrum gives the telluric standard spectrum appearing to show Na I in absorption to some degree. The dot-dashed spectrum is the target spectrum after telluric correction. The spectrum was extracted from a $0.5'' \times 0.5''$ region centred on the object using a mean combination method to reduce the noise in the spectrum. Note: no correction for wavelength mis-calibration or LSR has been applied to the spectrum.

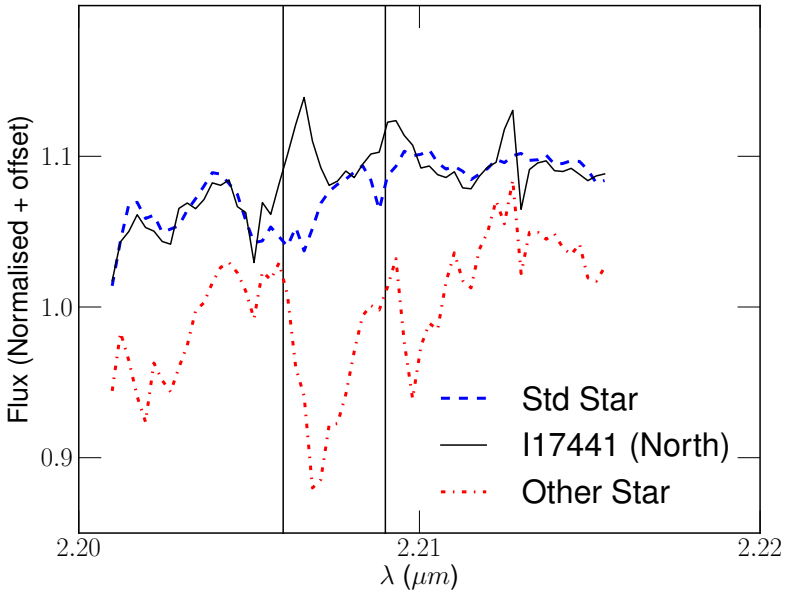

Fig. 6.5: Na I doublet feature in emission in *IRAS* 17441-2411 compared to the absorption feature in the adjacent star. Details as given in 6.4.

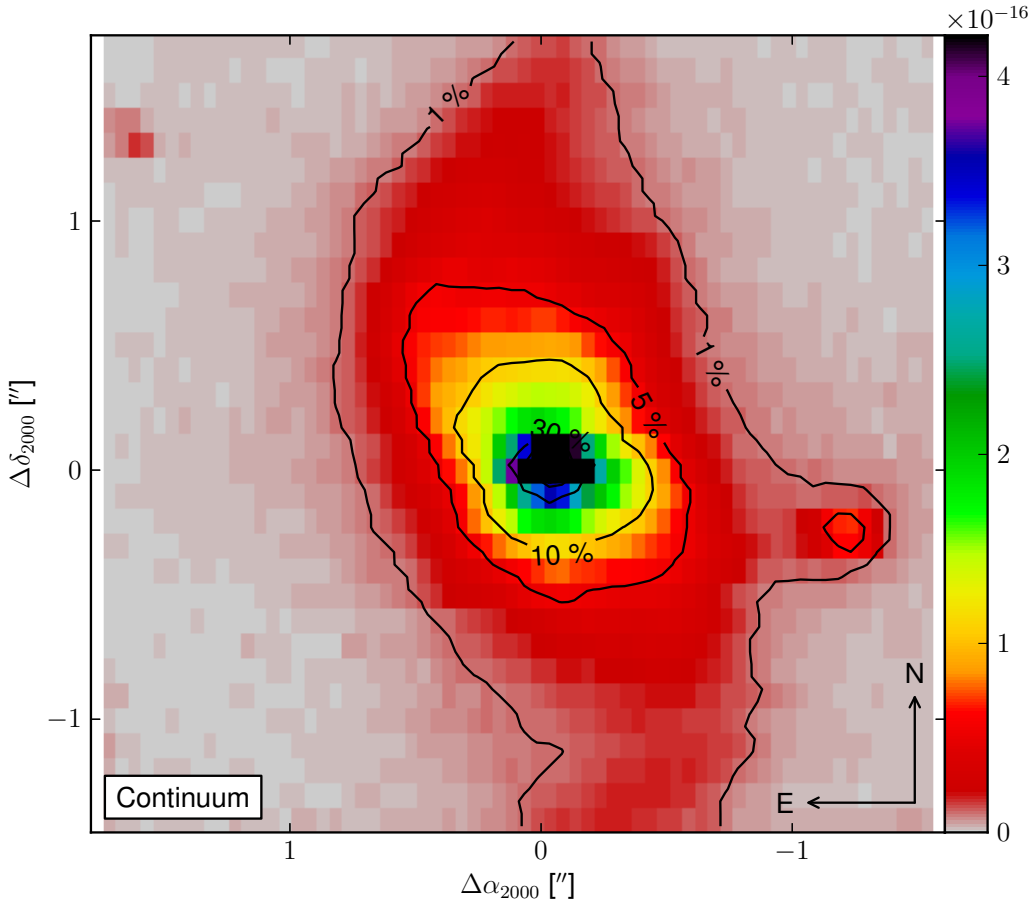

Fig. 6.6: *IRAS* 17441-2411 continuum map (taken from channel 760). Contours show the 1, 5, 10, 30, 50, 70, and 90% of the peak. Units are in W m^{-2} μm^{-1} pix^{-1}. The companion star offsets from the central star are: 1.18″ West and 0.28″ South.

as derived from the H_2 lines, to be similar in both lobes. In each case two temperature estimates are inset in the top right-hand corner of each diagram. Both the rotational and vibrational temperatures are quite similar, $\sim$ 2000 K, which is the temperature expected for a shocked gas in which the level populations are thermalised.

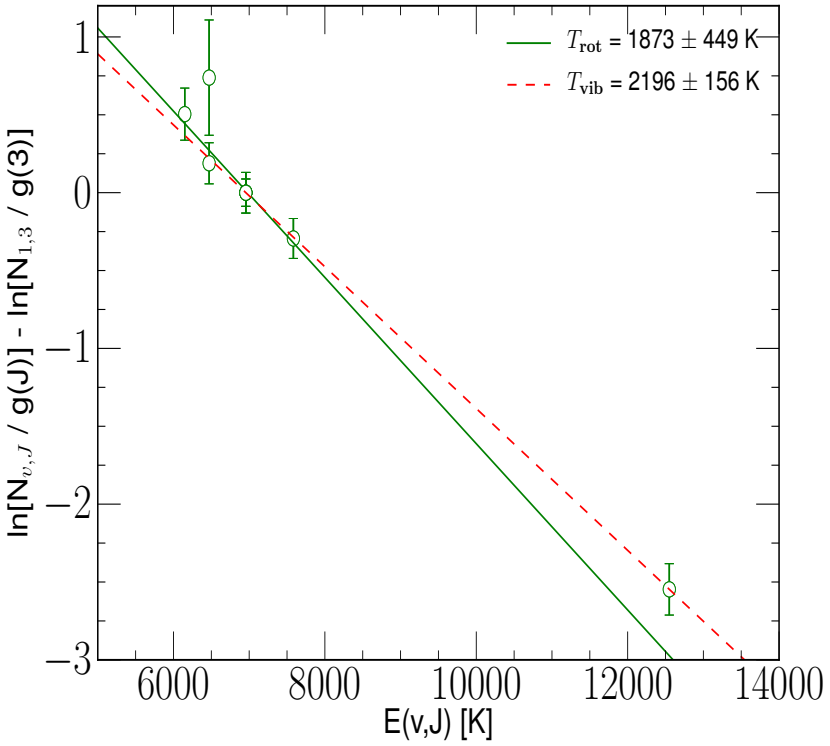

Fig. 6.7: Excitation diagram for a portion of the Northern lobe of *IRAS* 17441-2411. A vibrational and rotational temperature is calculated for both regions. Dashed line represents a fit to the vibrational levels, while the solid line is fit to the 1→0 rotational levels. Note: the 1→0S(3) line is removed from this plot. Lines are corrected for extinction (using a value of A_k=0.9) calculated for this region.

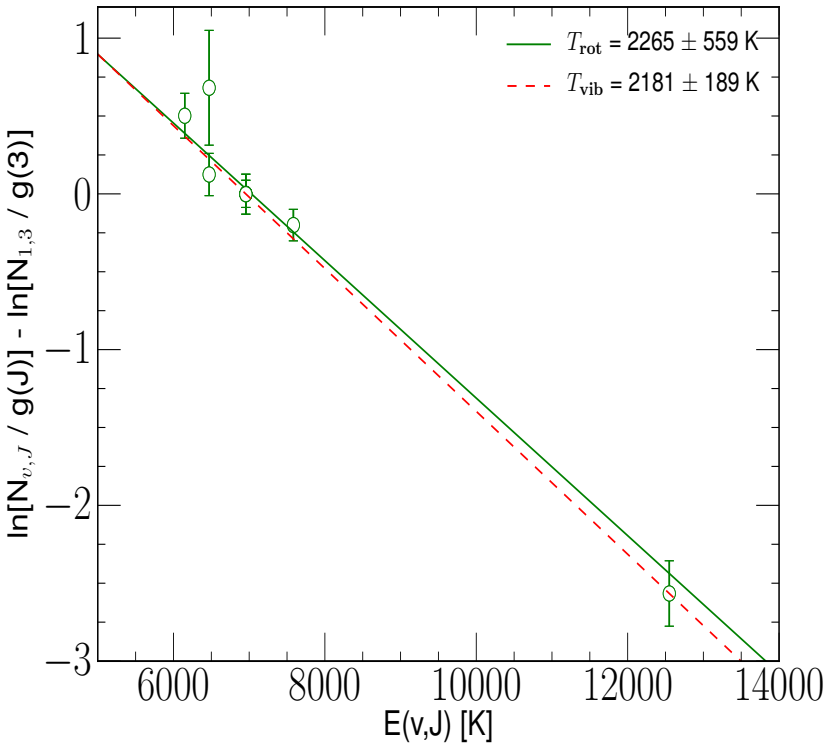

Fig. 6.8: Excitation diagram for a portion of the Southern lobe of *IRAS* 17441-2411. Labels as given in Figure 6.7. Extinction correction was carried out using an A_k value of 0.9.

6.3.2 *IRAS* 17150-3224

IRAS 17150-3224, also commonly known as the "Cotton Candy Nebula" and AFGL 6815S, is a bipolar PPN whose central star is obscured by a dust lane in the optical, but is visible in the near-IR. Figure 6.9 shows a *Hubble Space Telescope (HST)* image in the 1→0S(1) line. The lobes are oriented at a PA of 112 – 122° (Lagadec et al., 2011; Ueta et al., 2007) and much of the H_2 emission arises from 'clumps' of material near the ends of each lobe. The bipolar lobes are hollow structures evident from the polarisation (I_p and P) maps of Ueta et al. (2007), where the polarised light is observed along the lobe edges and polar caps. A series of concentric arcs were detected surrounding this object by Kwok et al. (1998) using the *HST* Wide Field Camera 2 data. This source, along with *IRAS* 17441-2411, *IRAS* 18276-1421 and AFGL 2688, is one of the small number of post-AGB objects displaying these arcs which are illuminated by 'searchlight beams' believed to be the result of light escaping through dust cavities. The bipolar lobes of *IRAS* 17150-3224 are most likely quite low density and are observed through scattering of light from the walls of the cavity (Su et al., 2003).

The first detection of H_2 was made by (Weintraub et al., 1998) via near-infrared longslit spectroscopic observations. In this paper, three slit positions were used to sample the nebula along the Western, Central, and Eastern region. The observed spectrum was taken during an engineering run without a flux calibrator, so measurement of the absolute flux of the 1→0S(1) line was not possible. However, an integrated flux (central region) ratio between the line and the continuum of 14 is calculated. The slit was 1.4″ × 60″ in extent and orientated East-West across the suspected position of the central star. A splitting of the 1→0S(1) line in the central region gives rise to the possibility for the presence of an expanding torus, with an expansion speed of 11 km s^{-1}, in the core of *IRAS* 17150-3224 (Weintraub et al., 1998). However, this was not found to be the case in the high-resolution spectra of Hrivnak et al. (2006), who carried out a near-IR spectroscopic (both high and low resolution) and imaging study on this object. The high-resolution images were taken using three filters: F212N, F215N, and F222M. By first scaling the F215N image appropriately, and then subtracting this scaled image from the F212N image, Hrivnak et al. (2006) produce the first accurate H_2 map for *IRAS* 17150-3224. This H_2 image reveals that the majority of the emission is coming from the clumpy structures near the end of each bipolar lobe; a faint loop/ear structure of equatorial H_2 is also reported. Kelly & Hrivnak (2005) used longslit low-resolution spectroscopy to calculate a 1→0/2→1S(1) ratio of 14.2, which they conclude suggests a collisional excitation mechanism is responsible for the H_2 emission. Using this information coupled with an estimation for both the vibrational excitation temperature (1900±130 K) and the speed of the shock (35 km s^{-1}), Hrivnak et al. (2006) make a comparison of the data to the shock model grids of Le Bourlot et al. (2002) and Wilgenbus et al. (2000). A measurement for the magnetic field strength in the nebula of 300±150 μG (Hu et al., 1993) from the OH 1665 MHz maser line suggests the H_2 excitation is caused by C-shocks occurring in a gas with a density of 10^4 cm^{-3}, at a velocity of 40 km s^{-1} (Hrivnak et al., 2006). The orientation of *IRAS* 17150-3224 is also estimated by comparison of the visible brightness of each lobe coupled with knowledge of the extinction, which would indicate that the Northwest lobe is pointing out of the plane of the sky. However, this is at odds with the radial velocity information which suggests that both lobes are nearly in the plane of the sky (Hrivnak et al., 2006). A similar result was noted in *IRAS* 17441-2411. An earlier lower resolution spectroscopic study (R ∼18,750) also reported similar velocity results (Davis et al.,

2005), however it is noted that there appears to be a mislabelling of their PV diagrams (left should be right and vice-versa). Brγ spectral information is also reported in this study; *IRAS* 17150-3224 is one of two G-type stars in their study exhibiting Brγ in absorption. Line fitting of their Brγ line yielded a velocity (LSR) of 20.4 km s^{-1}, which is most likely the systemic velocity. Hu et al. (1993), from CO observations, determine a systemic velocity of 14 km s^{-1}, while Hrivnak et al. (2006) report a systemic velocity from the H_2 lines of 11±1 km s^{-1}. There is possible evidence for outflow rotation in *IRAS* 17150-3224 which might be expected if magneto-centrifugal disc winds were present. This is the only source in their sample to exhibit signs of rotation.

Table 6.4 gives some important details found in the literature regarding this object.

Table 6.4: Summary of *IRAS* 17150-3224 properties from literature.

Parameter	Value	Reference
R.A. (α_{2000})	17^h 18^m $19^s.85$	a
Dec. (δ_{2000})	-32° 27′ 21″.6	a
K (mag)$^{\triangle}$	9.391	a
Spectral Type	G2, F3-7	a,d
Morphological Type	Bipolar	b
Distance (kpc)	2.4	b
Inclination Angle	Plane of Sky	b,e
Position Angle (PA)	112, 122	g,h
Anglular Size (arcsec)	7 × 2	e
V_{LSR} (km/s)	14, 11, 20.4 & 10-12	f,e,b

$^{\triangle}$ 2mass magnitude

References. – a. SIMBAD; b. Davis et al. (2005); c. García-Hernández et al. (2006); d. Sánchez Contreras et al. (2008); e. Hrivnak et al. (2006); f. Hu et al. (1993); g. Lagadec et al. (2011); h. Ueta et al. (2007).

Results & Discussion

Several H_2 lines are detected across the K-band for this object. The final reduced spectrum suffers from poor sky subtraction, evident from the P Cygni-like profiles at locations across the spectrum. These profiles appear due to the instrument settings occasionally becoming unstable allowing shifts of a significant fraction of a pixel (Sinfoni Pipeline User Manual, issue 16, p. 106). The procedure recommended to try to correct for this problem in the manual in this case gave very little improvement. Instead, a careful examination of the H_2 line profiles was carried out to determine to what extent the residuals affected the measurements. The only line found to severely suffer from this subtraction is the 2→1S(3) line at 2.0735 μm.

The total 1→0S(1) flux, in a simulated slit similar to the one used in Kelly & Hrivnak (2005), is 4×10^{-14} erg s^{-1} cm^{-2}. The flux value given in Kelly & Hrivnak (2005) is 7.8×10^{-14} erg s^{-1} cm^{-2}. The difference between both measurements can be attributed to the fact that it is not possible to recreate the full slit with the SINFONI data, which lacks coverage of the ends of both lobes. García-Hernández et al. (2002) quote a 1→0S(1) flux measurement of 5.5×10^{-14} erg s^{-1} cm^{-2}, which is similar to the results above.

To investigate the excitation across the object, three mean spectra were extracted from the regions across the datacube (see Figure 6.9 [*top*]). The first from the South-Eastern lobe (Region 1), the second from the weaker H_2 emission around the waist of the object (Region 2), and third from the North-Western lobe (Region 3). From these spectra we determine 1→0/2→1S(1) ratios of 10.7±1.7, 9.1±2.1, and 12.8±2.3, for the SE lobe, waist, and NW lobe, respectively. These values, the same within errors, are consistent with a shock excitation mechanism. Calculation of the extinction via the 1→0S(1) and 1→0Q(3) lines indicates lower values in the lobes and a higher value, circumsteller plus interstellar, around the waist (A_k=0.82±0.55 mags). The H_2 line ratios are not corrected for extinction, however any correction would push the ratios further into the shock regime. For example the application of this extinction correction to the values obtained for the waist of the object yields a 1→0/2→1S(1)=11.8±1.8. These ratios are consistent with the H_2 gas being shock excited. The Brγ line is only detected in absorption for this object, which is consistent with the spectrum given in García-Hernández et al. (2002); interestingly, the spectrum given in Figure 5 of Davis et al. (2003), shows what appears to be Brγ in emission, although the Brγ line is again observed in absorption in Davis et al. (2005).

The Brγ absorption line can be fit with a Lorentzian profile to give a velocity of V_{LSR}=19.6±6 km s^{-1}, in good agreement with the measured velocity for this line of 20.4 measured by Davis et al. (2005). Figure 6.9 (*bottom*) shows a velocity map for *IRAS* 17150-3224 with the locations of the H_2 emission shown by the superposed contours.

Figure 6.10 shows a portion of the *K*-band spectrum for *IRAS* 17150-3224. The reduced spectrum shows the presence of the Na I doublet at 2.206242 μm and 2.208969 μm, which is centrally located, and traces the presence of high density gas which can be excited in accretion discs or at the base of a disc wind. To confirm that this is a real detection and not an artifact due to the use of a G3V telluric calibrator star, both the raw and the telluric star spectra are plotted next to the corrected spectrum. The presence of the feature in the raw spectrum confirms that it is not introduced to the data in error. Examination of the corrected spectrum shows that 2.206 μm doublet line is stronger than the 2.209 μm line, however in the raw spectrum they appear similar. Although, these lines are interpolated out of the telluric star spectrum, the increase of the 2.206 μm line strength might be the result of the division by the G3V spectrum or due to correction for an atmospheric feature suppressing the 2.206 μm feature in the raw data. Measurement of the central wavelength of each emission line allowed the calculation of a wavelength separation of 2.7 × 10^{-3} μm. This compares well with the difference of the vacuum wavelengths for these features, which should always remain constant. Previous studies have not reported a detection of the Na I doublet in this object (e.g., Hrivnak et al., 2006; Kelly & Hrivnak, 2005). Figure B.3 in Appendix B shows a plot of the region around the doublet from the data in Hrivnak et al. (2006), the proximity of the two peaks to the vacuum wavelengths of the Na I doublet suggests that the emission is in fact real.

As described previously, it is possible to calculate the H_2 rotational and vibrational temperatures from the line strengths. Figure 6.11 shows the excitation diagrams for the three regions. Region 1 is the South-Eastern lobe, Region 2 is the from the waist, and Region 3 is the North-Western lobe. The 2→1S(3) line is not included and as is the case for all the data the 1→0S(3) line is over-estimated due to poor telluric correction. The rotational temperatures for Region 1 and 2 are the same within errors while Region 3 shows a significantly higher temperature. It is apparent from the diagram that the

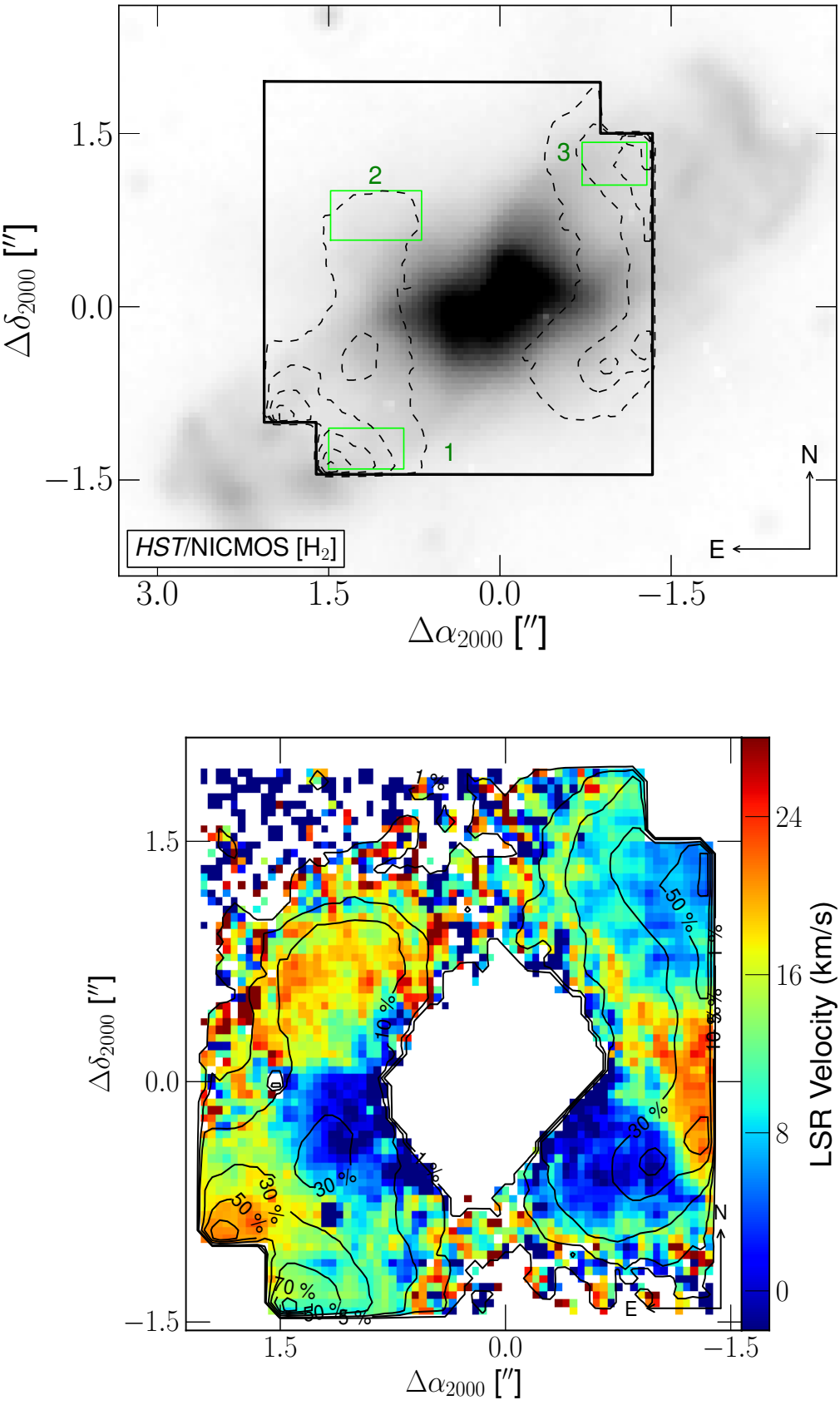

Fig. 6.9: (*top*) A *Hubble Space Telescope* image (F212N) showing the bipolar morphology of *IRAS* 17150-3224 (taken under the General Observer program ID 7840, PI: Kwok, S.); the image is not continuum subtracted. The SINFONI field-of-view and the position of the detected H_2 is shown by the solid squared and dashed contours, respectively. (*bottom*) *IRAS* 17150-3224 velocity map showing LSR velocities for the 1→0S(1) line. Contours shown as percentages of the peak.

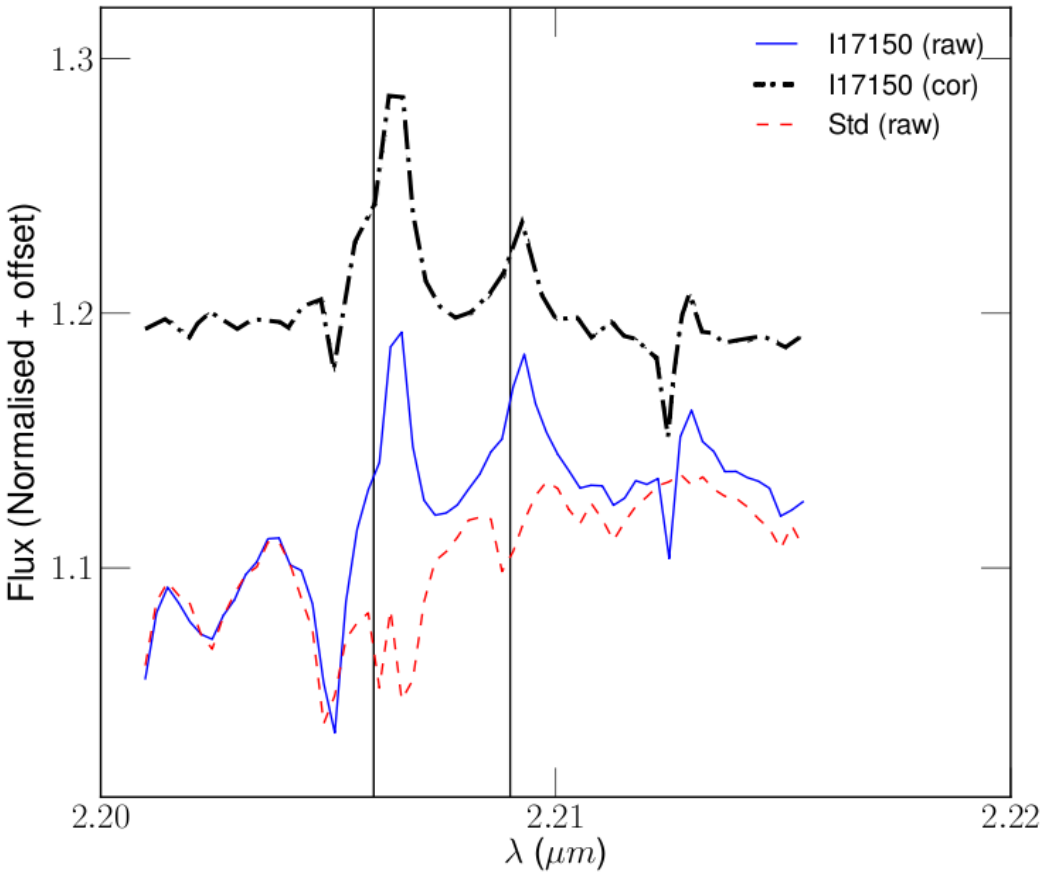

Fig. 6.10: Na I doublet feature in emission in *IRAS* 17150-3224. Vertical solid lines give the vacuum lab wavelengths for the Na I doublet (2.206242 & 2.208969 μm). The solid line spectrum represents the raw (before telluric correction) spectrum of the target. The dashed spectrum gives the telluric standard spectrum appearing to show Na I in absorption to some degree. The dot-dashed spectrum is the target spectrum after telluric correction. The spectrum was extracted from a 0.5″ × 0.5″ region centred on the object using a mean combination method to reduce the noise in the spectrum. Note: no correction for wavelength calibration or LSR has been applied to the spectrum.

1→0S(3) line is having too large an affect on the fit. Removal of this line from the fit lowers the temperature to 1233±102 K. These temperatures are in good agreement with Hrivnak et al. (2006) who quote a vibrational temperature of 1900±130 K, and Davis et al. (2003) who quote a rotational temperature of 1300 K.

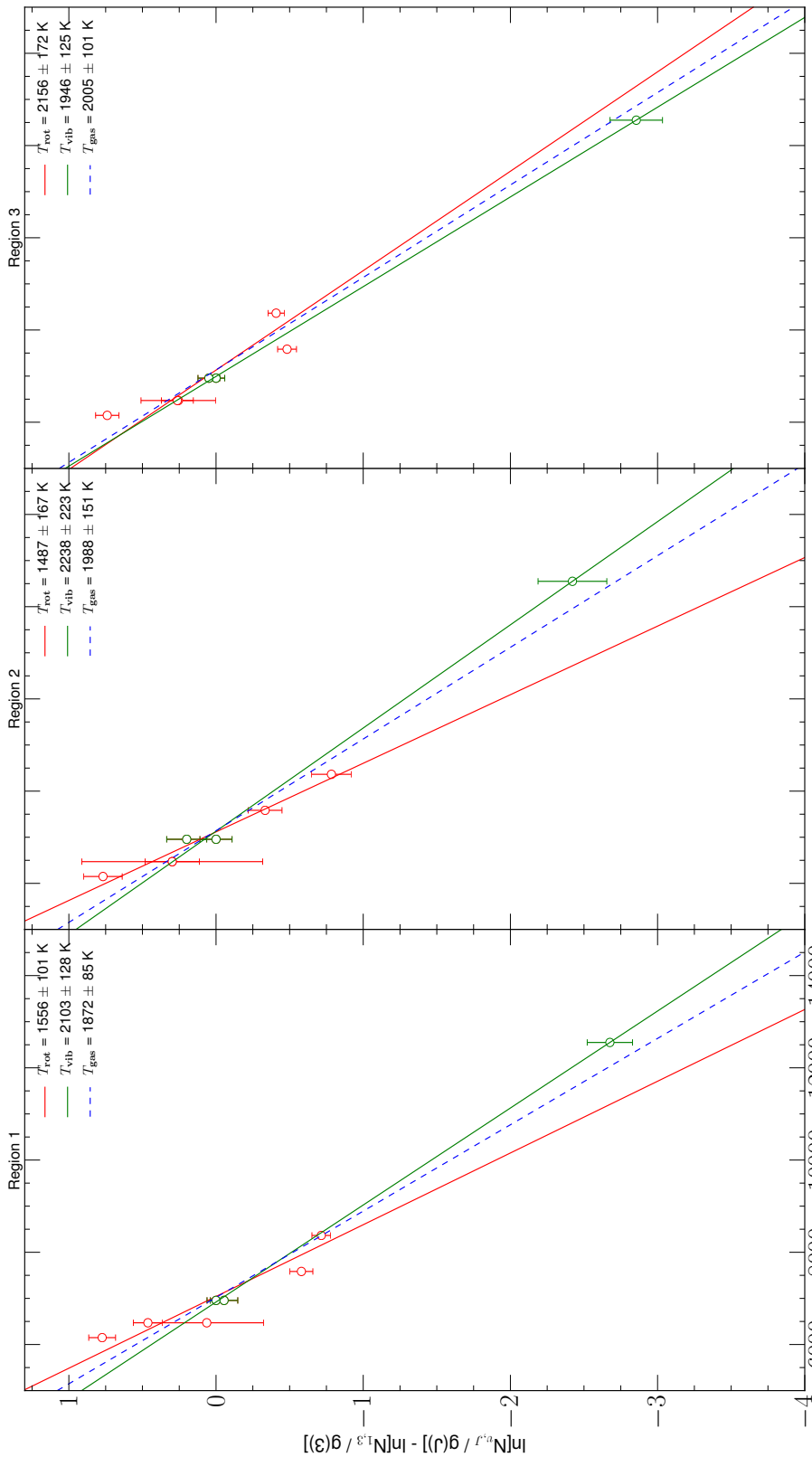

Fig. 6.11: Regions 1, 2, and 3 are marked in Figure 6.9. Dashed line is the fit to all data points. The solid red line gives the rotational temperature and the solid green line gives the vibrational temperature. The data points have been corrected for extinction; Regions 1 & 3 using an A_k=0.6 and Region 1 with an A_k=0.8 mag.

6.3.3 *IRAS* 19500-1709

Likkel et al. (1987) first detected *IRAS* 19500-1709 in the CO J=2→1 line, measuring an expansion velocity of 10 km s^{-1}. In a further study of 77 AGB and post-AGB objects Likkel et al. (1991) comment that the CO J=2→1 line profile includes wide blue and red wings yielding an outflow velocity of $\sim$ 30 km s^{-1}. The broad wings, with a velocity range from -25 → 60 km s^{-1}, in the ^{12}CO J=2→1 line are confirmed in an independent study by Bujarrabal et al. (1992). Other lines detected in this study are: ^{12}CO J=1→0, ^{13}CO J=2→1, ^{13}CO J=1→0, and HCN J=1→0. They do not detect either the SiO J=3→2 or HCO^+ J=1→0 lines. Analysis of the relative intensity of these CO lines shows that the presence of the broad wings is not an artifact and most likely due to the presence of much of the molecular mass in an outflow (Bujarrabal et al., 1992). This is confirmed in a follow-up study of mass, momentum, and kinetic energy of bipolar post-AGB outflows; the calculated mass of the bipolar outflow is 6.7 × 10^{-3} $M_\odot$, with a momentum of 5.3 × 10^{37} g cm s^{-1} (Bujarrabal et al., 2001).

Imaging in the mid-IR for the first time tentatively suggested that an axial symmetry was present in the dust emission structures of *IRAS* 19500-1709 (Meixner et al., 1997); typically these structures are interpreted as due to an equatorial density enhancement. Gledhill et al. (2001) presented $J-$ and $K-$band imaging polarimetry of 16 PPNe, from which 15 objects have extended circumstellar envelopes, and 14 show axisymmetry. *IRAS* 19500-1709 was one of the observed sources, and both the $J-$ and $K-$band polarised flux images clearly show the illumination is not isotropic but it appears as a bipolar nebula in scattered light. These polarized flux images also show the Eastern lobe to be brighter than the opposing lobe, leading to the suggestion that the bipolar axis is slightly tilted toward the observer – out of the plane of the sky. Mid-IR imaging at 10 and 20μm, using OSCIR on the Gemini North telescope, combined with modelling of the SED with a detached shell radiation transport code led Clube & Gledhill (2004) to propose the existence of an optically thin detached axisymmetric dust shell around *IRAS* 19500-1709, due to enhanced equatorial mass-loss, with a maximum inner radius of 0.4″. The presence of this detached shell was confirmed using VISIR on the VLT at three mid-IR wavelengths (8.59, 11.85, and 12.81μm) by Lagadec et al. (2011).

Hrivnak et al. (1994) do not report any detection of H_2 in this object in their K-band low-resolution spectroscopic study of several PPNe. Kelly & Hrivnak (2005) are the first authors to report a detection of H_2 in this object, albeit a tentative detection. This is quite remarkable, as from a visual examination of their published spectrum (see their Figure 2.) it is difficult to see the emission. So much so, that 'if' the spectrum was slightly lower S/N *IRAS* 19500-1709 would be classed with other F–G type stars without H_2 emission.

Important information from the literature is summarised in Table 6.5 for *IRAS* 19500-1709.

Table 6.5: Summary of *IRAS* 19500-1709 properties from literature.

Parameter	Value	Reference
R.A. (α_{2000})	$19^h\ 52^m\ 52^s.7$	a
Dec. (δ_{2000})	-17° 01′ 50″.3	a
K (mag)$^{\triangle}$	6.858	a
Spectral Type	F2/F3I	a
Morphological Type	Bipolar	c
$T_{\rm eff}$ (K)	8000	b
Distance (kpc)	4,1,2	b,h
Inclination Angle	??	–
Position Angle (PA)	100°	c
Chemistry	C-rich	e
Anglular Size (″)	3.6 × 2.2, 4.0 × 3.0	c,z
$V_{LSR}{}^{\dagger}$	24 km/s	e,g
V_{exp}	$10^{\diamond}$; $40^{\dagger}$km/s	f,e

$^{\triangle}$ 2mass magnitude
† From CO J=2→1
$^{\diamond}$ From CO J=1→0
References. – a. SIMBAD; b. Clube & Gledhill (2004); c. Gledhill et al. (2001); d. Kelly & Hrivnak (2005); e. Bujarrabal et al. (1992); f. Likkel et al. (1987), g. Bujarrabal et al. (2001); h. Meixner et al. (1997), z. this work.

Results & Discussion

The integral field observations of *IRAS* 19500-1709 show the presence of the strongest 1→0 H_2 lines. A wavelength offset of -1.4±0.2 × 10^{-4} (± 0.2 × 10^{-4}) μm was determined from the OH lines (as discussed in Subsection 3.3.1). A local standard of rest correction of +21.45 km s^{-1} was applied to the data when constructing the velocity map. A 1→0S(1) line flux of 1.44 × 10^{-17} W m^{-2} is measured from constructing a line map, and summing the values. Not surprisingly this value is not in good agreement with the value of 0.16 × 10^{-14} erg s^{-1} cm^{-2} supplied in Kelly & Hrivnak (2005). In fact, it is nearly an order of magnitude larger than their measurement. This might be explained by slit losses by not observing some of the strongest H_2 regions, or by the low S/N of the line in their data. There is no detection of the Na I doublet or CO bandhead emission in this object.

Figure 6.12 shows the mean spectrum extracted over a small region centred on the continuum peak (0.5″× 0.5″). The spectrum, whose flux drops as wavelength increases, is mainly featureless apart from the strong Brγ absorption, as would be expected in a star at this phase of its evolution.

Figure 6.13 shows the location of the H_2 emitting regions (solid lines) in relation to the mid-IR dust shell (Lagadec et al., 2011) and the polarised flux (dashed lines) (Gledhill et al., 2001). The large-scale H_2 structures consist of three 'arms' of emission, which appear to be outlining a bipolar outflow. The fourth arm is not detected in these observations, in the expected position, i.e., South-Western region of the nebula; only a

small region of weak emission is detected in this region. The spatial region covered by the observations is $\sim 3'' \times 3''$, and so it is entirely possible that there exist regions of H_2 at a larger extent. It is worth noting that the sharp cut-off of the North-Western lobe is due to the edge of the SINFONI field-of-view. On a smaller scale the H_2 emission is strongest in discrete clumps along the outflow. The *J*-band polarised flux contours appear to be located within the H_2 emission regions, where there may be multiple scattering occurring in the lobes.

The deconvolved image of the mid-IR torus (Figure 6.13), shows for the first time, the presence of the dust shell around *IRAS* 19500-1709. The solid white contours show the locations of strong emission from this shell; two arcs of strong emission are represented by the innermost contours (95% of peak). These arcs most likely represent a dust shell surrounding the central star with a large equator-to-pole density enhancement. This type of axisymmetric dust structure was resolved, for the first time, by Gledhill & Yates (2003), using OSCIR on Gemini North for the post-AGB star HD 161796 (*IRAS* 17436+5003). Likewise, the dust structure in *IRAS* 19500-1709 shows a clear sign of axisymmetry. The arcs of dust emission are not positioned directly either side of the central star, but are located closer together along the Eastern side of the dust shell, i.e., the shell is brighter along this side. This can be seen by the gap in the weakest contour level in Figure 6.13. This type of structure is also observed in HD 161796. In this case Gledhill & Yates (2003) found that modelling the mid-IR images and the SED with an axisymmetric dust model requires an equator-to-pole density contrast of 6:1 and an inclination of the symmetry axis of 10° to achieve a good fit to the observations. A visual comparison of the dust shell in *IRAS* 19500-1709 to the model images (Figure 5 in Gledhill & Yates, 2003) suggests that *IRAS* 19500-1709 would be best represented by a shell inclined at between 20 – 30°, as it is the inclination angle that determines the position of the arcs. Although, tilting the axis of the dust shell in the manner described in their paper – out of the plane of the sky with North-East quadrant pointing toward the observer – would lead to the Eastern lobe being pointed away from, and Western lobe pointed toward the observer. If that were the case then it would be reasonable to assume that any radial velocity measurements might reflect this, however the velocity map constructed from the 1→0S(1) line yields the opposite result (Figure 6.14). This velocity map shows that the South-Eastern arm of H_2 is the most blueshifted, with a velocity, V_{LSR}, of $\sim$ -5 km s^{-1}, the North-Eastern arm is less blueshifted with V_{LSR}, of $\sim$ 20 km s^{-1}, and the North-Western arm is redshifted with V_{LSR}, of $\sim$ 60 km s^{-1}. The average velocity of the map is V_{LSR}=29.0 km s^{-1}, which is in rough agreement with the value given in Table 6.5. Further investigation led to the conclusion that the tilt of the IR model dust shells, given in Gledhill & Yates (2003), should be have the North-East quadrant pointing *away* from the observer (private communication).

Combining all the above information with previous studies allows the construction of a model for this object. From the radial velocity measurements, the previously suggested inclination of the lobes is confirmed. The VISIR imaging of the dust shell combined with the mid-IR models suggest that the inclination of the symmetry axis of the shell is $\sim$ 30° to the plane of the sky. The past CO observations reveal the presence of a fast axial wind. Although, at a minimum distance of 4 kpc Clube & Gledhill (2004), the inner radius of the mid-IR dust shell would be 1600 AU, too large to collimate the fast axial wind. However, as seen in *IRAS* 17441-2411 the mid-IR shell/torus could be the result of an inner disc of material, such as an accretion disc, although the lack of CO bandhead emission might not support this. This might suggest that *IRAS* 19500-1709 could have a close binary companion. Figures B.7, B.8, B.9 show

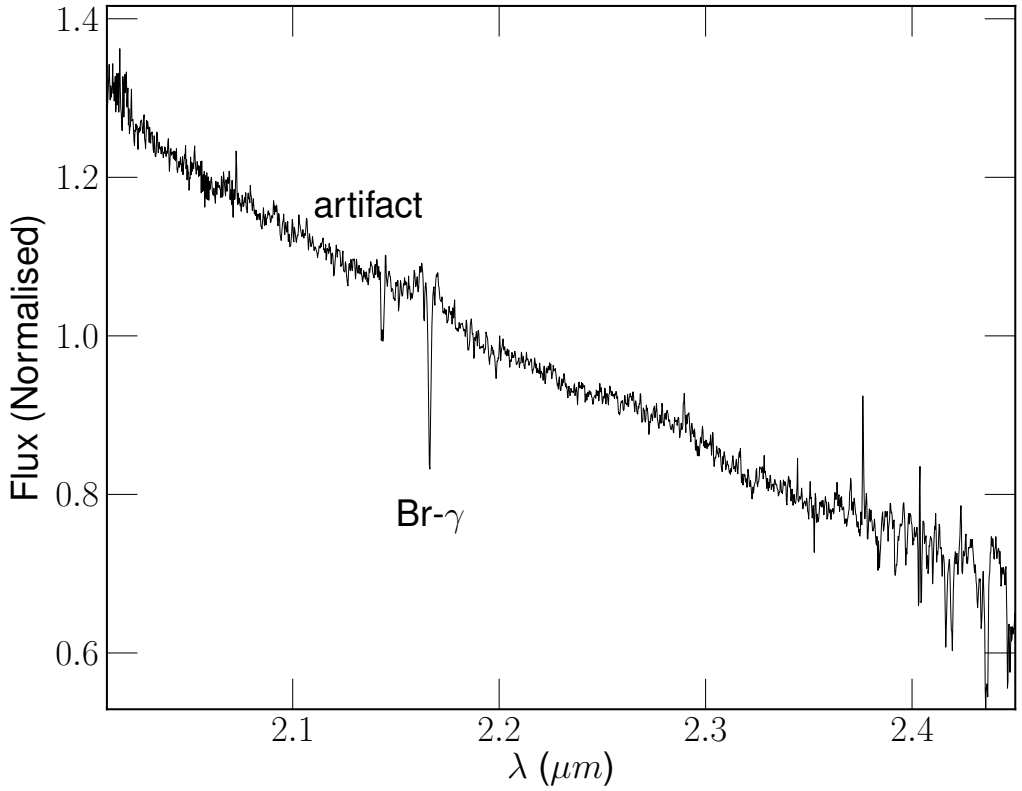

Fig. 6.12: Spectrum of the central region of *IRAS* 19500-1709 extracted from the region around the peak of the continuum ($0.5'' \times 0.5''$).

a basic model of *IRAS* 19500-1709, constructed using SHAPE[1] (Steffen et al., 2010). In this case the H_2 is being emitted by discrete filaments of material along the outer shells of the bipolar lobes.

[1] http://bufadora.astrosen.unam.mx/shape/index.html

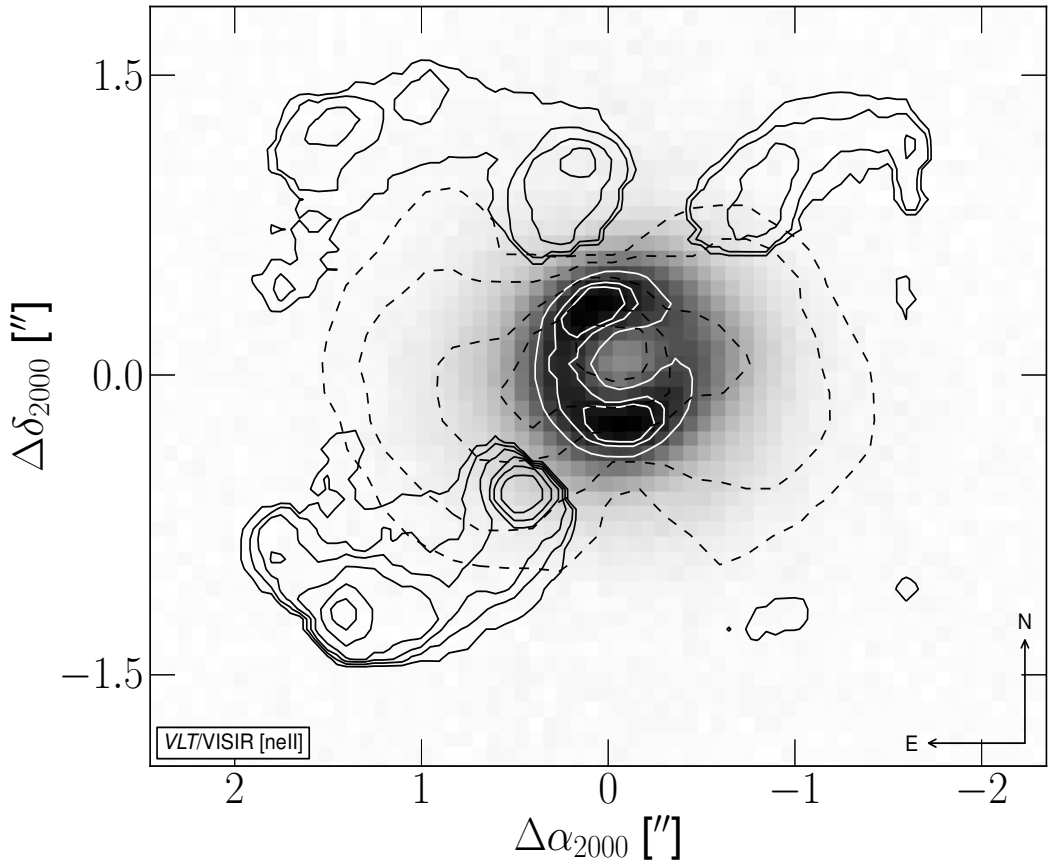

Fig. 6.13: *IRAS* 19500-1709 VISIR image (background) showing the location of the mid-IR emission (the mid-IR images were provided by Eric Lagadec private communication). White contour lines give 70, 90, and 95% of peak flux locations. The locations of the H_2 emission and J-band polarised emission are shown by solid black contours and dashed contours, respectively.

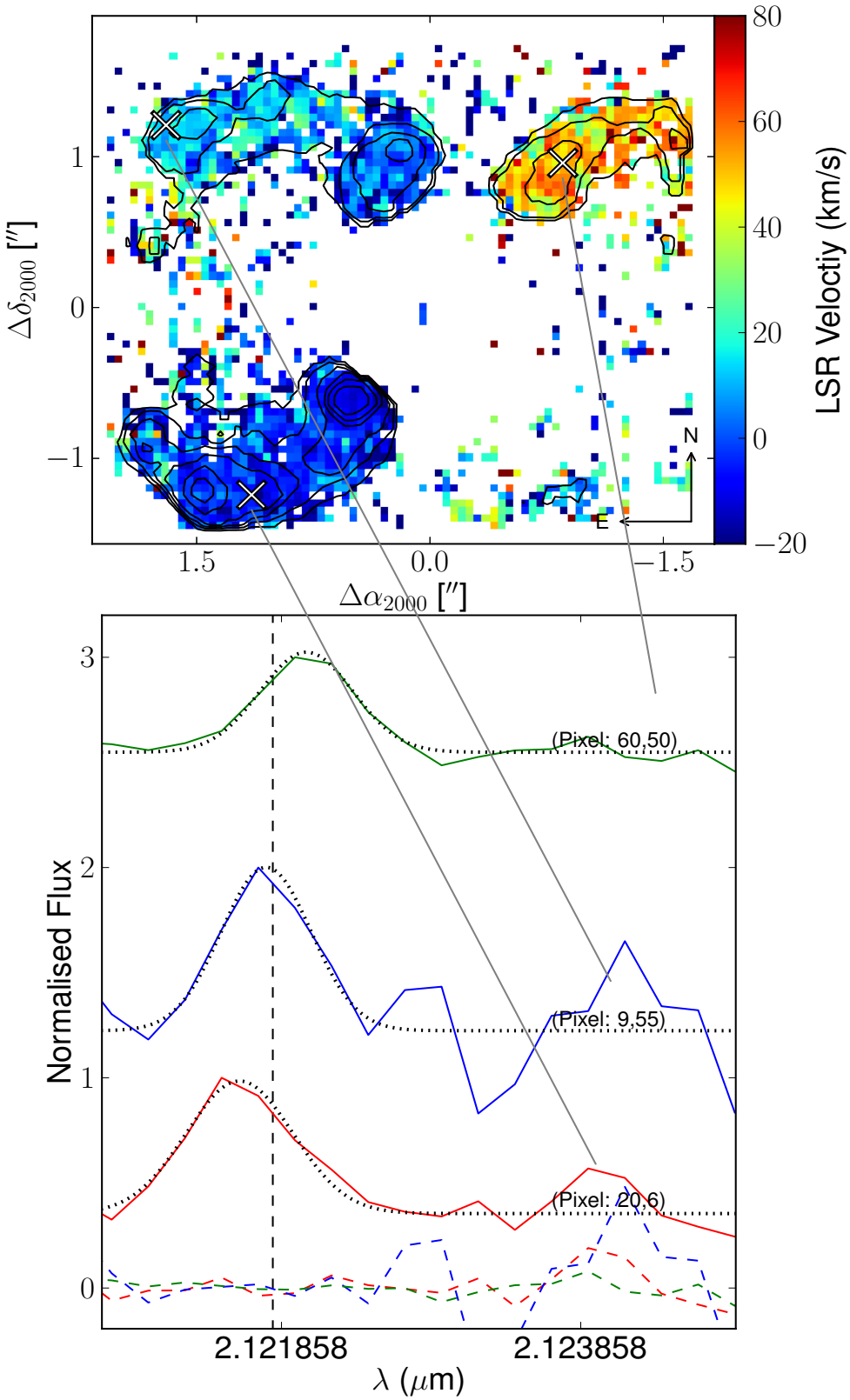

Fig. 6.14: *(top)* A velocity map of *IRAS* 19500-1709 generated from fitting the 1→0S(1) line. The adjacent colourbar indicates the fitted local standard of rest (LSR) velocity (km s^{-1}), while the superposed contours shows the location of the 1→0S(1) line emission. To reduce the noise in the image, lines with a S/N < 1 are removed from the plot. *(bottom)* Line profiles (solid lines), normalised to peak and offset for clarity, at three locations across the object. The dotted line shows the best fit Gaussian, while the horizontal dashed lines correspond to the fit residuals. The vertical dashed line gives the vacuum rest wavelength for the 1→0S(1) transition (2.1218334 μmas given in Bragg et al., 1982).

6.3.4 *IRAS* 14331-6435

IRAS 14331-6435 was listed in the catalogue of Henize (1976) as a Hα emission source, and later classified as a post-AGB object based on its far-IR (FIR) flux (Parthasarathy & Pottasch, 1989). Although the line strengths of Si IV and N IV are normal for a B-type supergiant (from its UV spectrum), the lack of C IV means this star is carbon poor. No information exists in the literature on the morphology of this object, however the integrated FIR flux to integrated stellar flux ($F_{\rm fir}$ to $F_{\rm star}$)[2] ratio of 3.42 for *IRAS* 14331-6435 indicates the presence of dust around the star, possibly in a disc. Gauba & Parthasarathy (2003) use the 2200Å UV feature to correct for circumstellar extinction ($A_{\rm v}$=2.20) for *IRAS* 14331-6435. From CO observations Loup et al. (1990) report an expansion velocity of 15 km s^{-1} for the envelope of *IRAS* 14331-6435. In terms of NIR studies, there has been very little published, García-Hernández et al. (2002) report the detection of the 1→0S(1), 2→1S(1), and the Brγ lines in emission and measure 1→0/2→1S(1) of 8.4 which suggests that shocks are the most likely source of H_2 emission. The 1→0S(1)/Brγ line ratio for this object is 2.97 and Guerrero et al. (2000) discuss the correlation of this ratio value with the degree of bipolarity in a sample of PNe. Low values of the 1→0S(1)/Brγ (0.1 – 0.5) are associated with small PNe with bright central stars, while values > 5 are linked with larger well-defined rings and faint central stars. García-Hernández et al. (2002) also suggest that relatively high values of this ratio may also be a good indicator of shocks in PPNe.

Table 6.6 gives a summary of the information for *IRAS* 14331-6435 gathered from the literature.

Results & Discussion

This early B-type star is visible in the NIR, and shows many H_2 lines in emission across the *K*-band, the strongest of which are easily seen in the raw data prior to atmospheric correction. This is also the case for Brγ (2.1661 μm) and a line at 2.1375 μm which has previously been observed in PPNe, with a tentative identification that it may be the Mg II recombination lines (Kelly & Hrivnak, 2005). The position of the 1→0S(3) line in the *K*-band atmospheric window appears to again had an effect on the measured flux for this line (as became apparent from the excitation diagrams discussed below). In this instance the 1→0S(3) line flux is underestimated significantly. The 1→0Q(4) line also shows signs of poor atmospheric correction and a measurement for this line is not attempted. Visual examination of the other lines show them to be free from these effects. The flux measurements given in Table 6.7 are the total measurements plus error estimates, as derived from extracting a spectrum of the full object and fitting the lines. A wavelength mis-calibration of -2.9 × 10^{-4} (± 0.5 × 10^{-4}) μm is calculated for this object; wavelength/velocity measurements are corrected by this amount. To this, a further local standard of rest correction is of 15.57 km s^{-1} is applied.

García-Hernández et al. (2002) were the first to report the presence of H_2 around this object and report H_2 line flux values of 10.1 × 10^{-17} W m^{-2} for the 1→0S(1) line, quite close to the flux reported in Table 6.7. The slight increase in the IFU flux measurement is most likely due to the slightly larger spatial area integrated. Similarly, García-Hernández et al. (2002) provide 2→1S(1) and Brγ lines values of 1.2 and 3.4 × 10^{-17} W m^{-2}, respectively — both agreeing reasonably well with this work. Once again, these comparisons act as an added check on the flux calibration and telluric

[2] $F_{\rm star}$ is the integrated stellar flux from 1150 Å to 5500 Å.

Table 6.6: Summary of *IRAS* 14331-6435 properties from literature.

Parameter	Value	Reference
R.A. (α_{2000})	14^h 37^m $10^s.092$	a
Dec. (δ_{2000})	-64° 48′ 04″.72	a
l	313.8867	a
b	-04.2026	a
K (mag)$^{\triangle}$	8.887	a
Spectral Type	B3Iab:e,B8Ie	a,e
Morphological Type	Bipolar	z
$T_{\rm eff}$ (K)	16,200	b
Log g	2.6	b
Distance (kpc)	2.1;2.49*;1.3$^{\triangle\triangle}$	b, b, d
Size (arcsec)	3 × 3	z
Inclination Angle (°)	Unknown	—
$V_{\rm exp}$ (km s^{-1})	15.0	d

$^{\triangle}$ 2mass magnitude
‡ Based on presence of CO emission
$^{\diamond}$ Calculation carried out for post-AGB star with core mass of 0.565 M$\odot$
* as above with core mass of 0.605 M$\odot$
$^{\triangle\triangle}$ Based on an assumed luminosity of 10^4 $L_{\odot}$
References. – a. SIMBAD; b. Gauba & Parthasarathy (2003); c. Gauba & Parthasarathy (2004); d. Loup et al. (1990); e. Suárez et al. (2006); z. This work.

correction of the IFU data in this work.

Prior to this work there was no NIR imaging of this object, the choice of medium resolution mode of SINFONI appears to have been extremely fortuitous as the FOV (3″× 3″) appears to have been sufficient to image the nebula. Figure 6.15 presents 1→0S(1)and 2→1S(1) integrated intensity line maps alongside a 1→0/2→1S(1) ratio map. The 1→0S(1) clearly shows, for the first time, that the nebula of *IRAS* 14331-6435 is bipolar in the NIR, displaying an S-shape distribution of the gas. These point symmetric structures are not uncommon in both PPNe (e.g., *IRAS* 19475+3119 in scattered light) and PNe (e.g., *IRAS* 16585-2145). The 1→0S(1) flux is most intense in the bar-like structure oriented along the NW-SE direction. There is some evidence that some of the H_2, at least, in the lobes is in clumps in the bipolar direction, for example, the bright region in the SW lobe. The observations of such point symmetric nebulae is most likely in large part due to the viewing angle and in fact these types of structures have been reproduced by using two bipolar lobes offset azimuthally from one another, with a non-uniform density distribution (Chong et al., 2012).

The 2→1S(1) line map is noisier in appearance, and the line emission traces the general spatial locations of the 1→0S(1) line. The 1→0/2→1S(1) line ratio map shows where the excitation changes across the object. It is evident that the ratio is higher at the ends of both lobes and lower closer to the central star location. However, the

Table 6.7: The total continuum-subtracted flux for each of the observed lines (prior to extinction correction).

Line	λ_{lab} (μm)*	F $\times$ 10^{-17} (W m^{-2})
1→0S(3)	1.9576	3.19 ± 0.588
1→0S(2)	2.0338	3.13 ± 0.200
1→0S(1)	2.1218	10.6 ± 0.260
1→0S(0)	2.2235	2.85 ± 0.166
1→0Q(1)	2.4066	10.8 ± 0.656
1→0Q(2)	2.4134	3.74 ± 0.580
1→0Q(3)	2.4237	8.37 ± 0.304
1→0Q(4)¶	2.4375	—
2→1S(0)	2.3556	0.618± 0.251
2→1S(1)	2.2477	1.80 ± 0.102
2→1S(2)	2.1542	0.713± 0.290
2→1S(3)	2.0735	1.79 ± 0.370
3→2S(1)	2.3864	0.525± 0.400
3→2S(3)	2.2014	0.519± 0.182
Brγ	2.1661	3.48 ± 0.130
Mg II	2.1375	1.68 ± 0.180

* Laboratory wavelength measurements are given in a vacuum.

¶ line heavily affected by a telluric feature.

lowest values are noted in two regions along an axis through the central star position from the SE to NW direction.

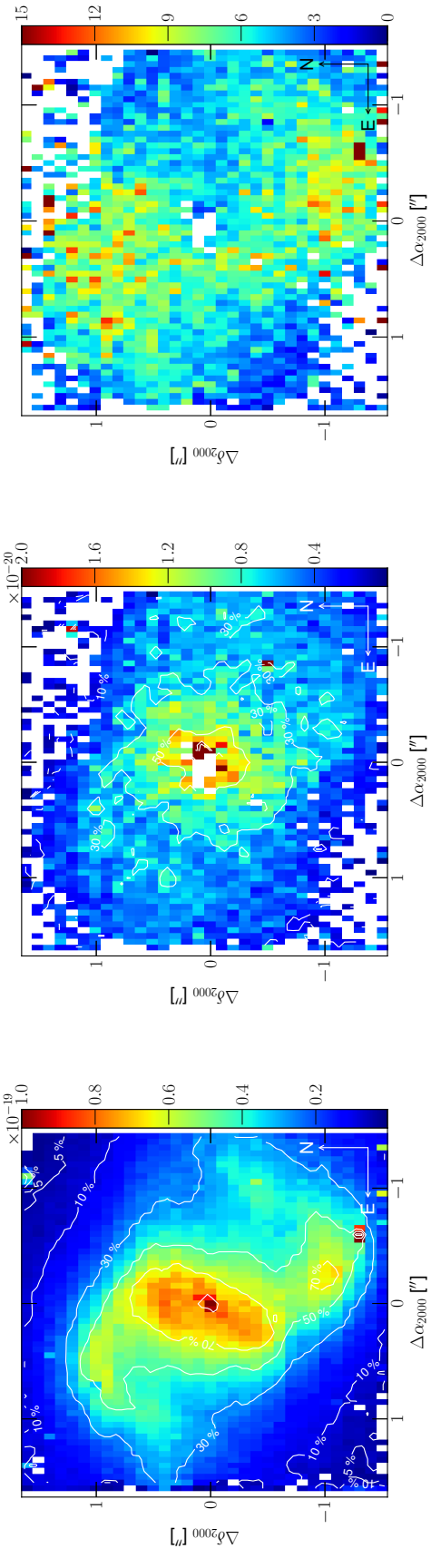

Fig. 6.15: (*left*) Continuum-subtracted integrated intensity line map of the 1→0S(1) emission from the central region *IRAS* 14331-6435. White contour lines give 5, 10, 30, 50, 70, and 90% of peak flux locations. (*middle*) Line map of the 2→1S(1) emission., and (*right*) The line 1→0/2→1S(1) line ratio map.

Figure 6.16 is a velocity map with two example line profiles (and fits) given in the lower panel. It is quite clear from this map that there is a significant velocity gradient across the object. This map is the first clue to the true orientation of the object, for example, a bipolar object with its' lobes in the plane of the sky should yield similar radial velocities for both lobes. As a system the whole object is moving toward the observer, with the nebula Southern lobe more blueshifted and the Northern lobe. An estimate of the systemic velocity can be directly estimated from this map as the average value of the H_2 gas of $\sim$ 40 km s^{-1}. This systemic velocity can be compared to the value obtained from the Brγ line. Figure 6.17 presents both a line and velocity map for the Brγ line. This shows that the line emission originates close to the star it so should give a good a good estimate of the stellar velocity. A systemic velocity of -42$\pm$7 km s^{-1} is estimated using this velocity map, which is very good agreement with the velocities obtained above. A 2-d Gaussian fit to the line map gives a FWHM of 4.95 $\times$ 4.25 pixels (0.25$''\times$ 0.21$''$).

Brγ is not the only recombination line detected in this spectrum. Figure 6.17 (*right*) shows a the line map derived from fitting a line at 2.1375 μm, most likely the Mg II line. Again, this image reveals the Mg II to be centrally located in a similar way to the Brγ emission. The emission has a FWHM of 4.46 $\times$ 4.31 pixels (0.22$''\times$ 0.22$''$). The line map appears much noisier than the Brγ map, however the contour levels indicate that at the 5% level the spatial extent of both lines are spatially coincident. This suggests that the recombination line emission is being driven by a common source. Although, this is the first report of this line in *IRAS* 14331-6435, it is not the first time that this line has been noted in PPNe. Kelly & Hrivnak (2005) have also reported tentative detections of this line in 4/22 PPNe, plus the detection in *IRAS* 16594-4656 (Chapter 5).

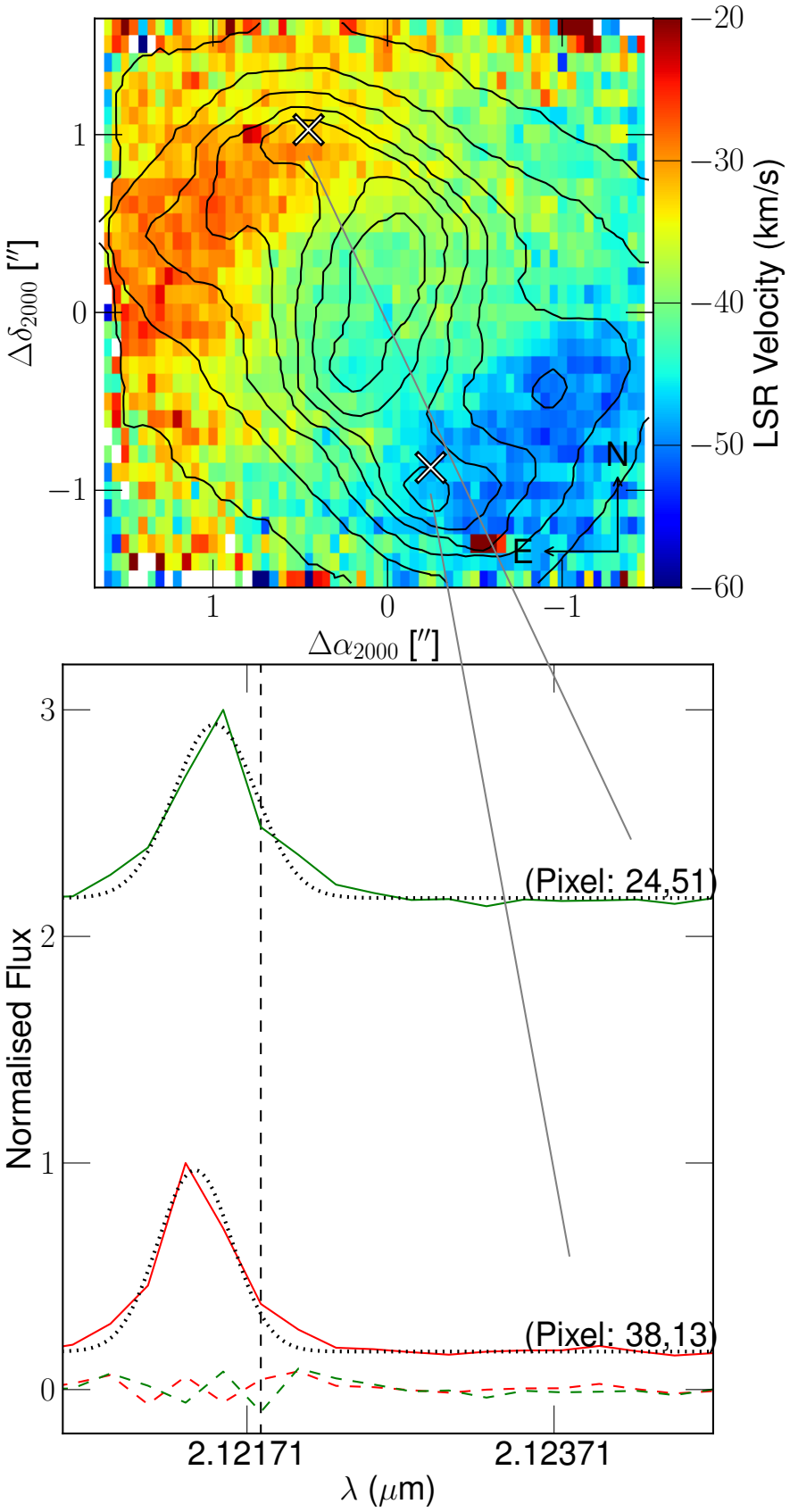

Fig. 6.16: *(top)* A velocity map of *IRAS* 14331-6435 generated from fitting the 1→0S(1) line. The adjacent colourbar indicates the fitted local standard of rest (LSR) velocity (km s^{-1}), while the superposed contours show the location of the 1→0S(1) line emission. *(bottom)* Line profiles (solid lines), normalised to peak and offset for clarity, at two locations across the object. The dotted line shows the best fit Gaussian, while the horizontal dashed lines correspond to the fit residuals. The vertical dashed line gives the vacuum rest wavelength for the 1→0S(1) transition (2.1218334 μm as given in Bragg et al., 1982).

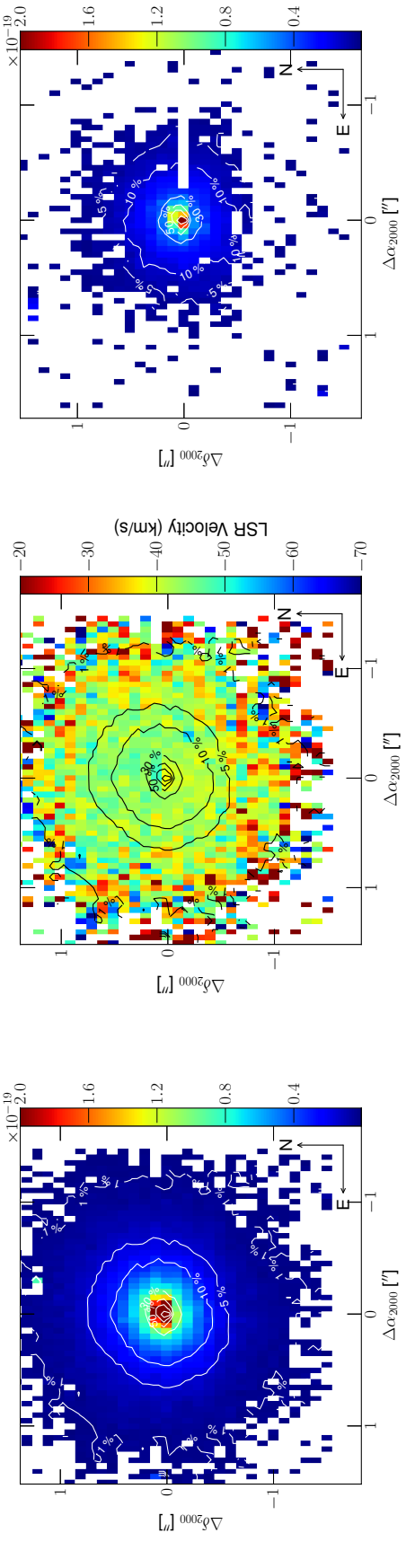

Fig. 6.17: (*left*) Line map of the Brγ emission detected in *IRAS* 14331-6435. White contour lines give 1, 5, 10, 30, 50, 70, and 90% of peak flux locations. (*middle*) Velocity map of the Brγ emission of the central region *IRAS* 14331-6435. Black contour lines give Brγ flux locations for reference. Note: the images are shifted slightly up and left to show the compass. (*right*) Line map of the Mg II emission from the central region *IRAS* 14331-6435. Note: White horizontal region at Y=0″ is an artifact and not a real 'lack' of emission. To eliminate some noise in the final image, lines with a S/N < 2 are removed. Orientation is given by inset compass.

Excitation diagrams constructed from the H_2 line fluxes are presented in each lobe (Figures 6.18 and 6.19). In both cases it is found that the vibrational temperature exceeds the rotational temperature by a significant amount; this is also the case in the other B-type object in this work (*IRAS* 16594-4656). These plots reveal that there must be a higher temperature component to the gas as evident from the presence of the 3→2S lines. Pure thermal excitation would tend to yield similar vibrational and rotational temperatures with all points lying along a straight line. Each plot is corrected for the effects of extinction as determined from the 1→0S(1)/1→0Q(3) lines. A_k values of 0.98±0.18 and 0.74±0.21 are estimated, allowing the calculation of corrected 1→0/2→1S(1) ratios of 8.9±0.6 and 8.98±0.7 for both the North and South lobes, respectively. These values are similar to the value of 8.4 presented by García-Hernández et al. (2002). Examination of the spectrum in each spaxel shows that the 3→2S(3) line is very difficult to distinguish from the continuum noise. However, in the extracted Northern lobe the mean spectrum quite clearly shows the line in emission. Measurement of the 1→0S(1)/3→2S(3) in this lobe yields an extinction corrected value of 29.4±5.5, consistent with the value expected in regions where shocks are the primary excitation mechanism (e.g., 10-100). Likewise for the Southern lobe, a 1→0S(1)/3→2S(3) value of 26.2±3.7 is determined from the mean spectrum.

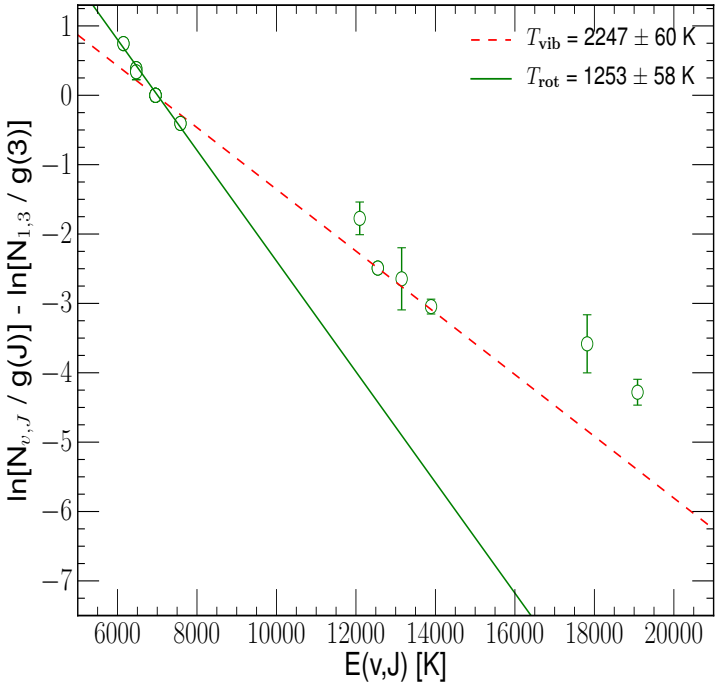

Fig. 6.18: Excitation diagram for a portion of the Northern lobe of *IRAS* 14331-6435. A vibrational and rotational temperature is calculated for both regions. Dashed line represents a fit to the vibrational levels, while the solid line is fit to the 1→0 rotational levels. Note: the 1→0S(3) line is removed from this plot. Lines are corrected for extinction (using a value of A_k=0.98) calculated for that region.

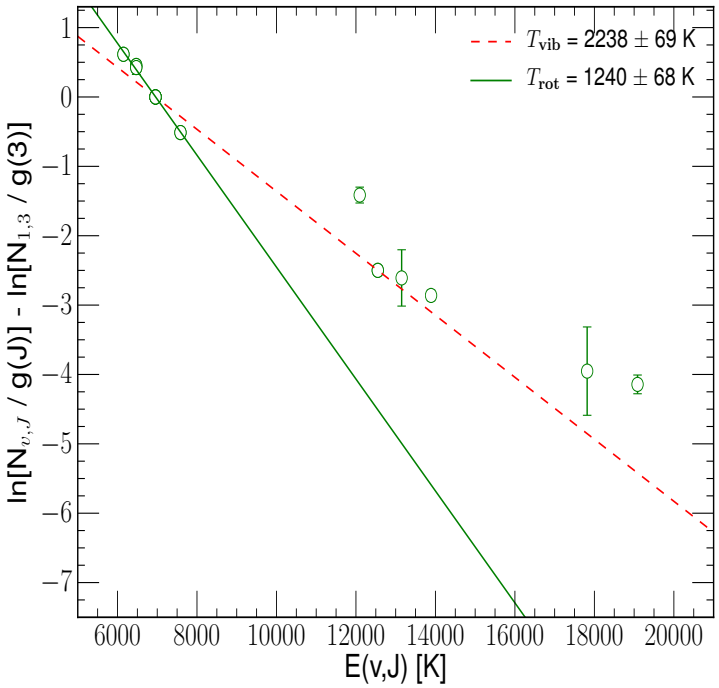

Fig. 6.19: Excitation diagram for a portion of the Southern lobe of *IRAS* 14331-6435. Labels as given in Figure 6.18. Extinction correction was carried out using an A_k=0.74.

6.4 Summary

Four post-AGB objects have been analysed in this Chapter: three late-type objects and a single early-type object. These observations add to the objects presented in Chapters 4 and 5 giving a dataset of six PPNe observed with the same instrument and reduced in a consistent manner.

The central stars of two of the late-type post-AGB stars, *IRAS* 17441-2411 and *IRAS* 17150-3224, presented in this Chapter are visible in the NIR, while at optical wavelengths the stars are obscured by a dark lane. The detection of Na I and possibly CO bandhead emission originating close to the central star indicates that these dark lanes might be part of a system of tori/discs at this location. Several newly detected H_2 lines are presented and extinction estimates and excitation temperatures are calculated for each object. These results combined with the 1→0/2→1S(1) ratio are consistent with the a thermal excitation source in shocks.

In the remaining late-type object, *IRAS* 19500-1709, only the 1→0S(1) line is measured with any degree of confidence, due to the low S/N per pixel of the line. A line map of this transition shows, for the first time, the spatial distribution of the H_2 in this object. The H_2 is mostly emitting from clumps located in three 'arms' forming a bipolar shape. Velocites from this line also show the first clues as to the orientation of the bipolar axis.

Finally, *IRAS* 14331-6435, the earliest-type PPNe in the IFU dataset (B3I) is discussed. The line and ratio maps show the first NIR H_2 images of *IRAS* 14331-6435 which exhibits a point symmetric (S-shaped) morphology. A blue- and red-shifted nebula is evident from the velocity map, which offers evidence for an intermediate inclination angle of the bipolar axis. The line ratios are consistent with the H_2 being shock excited, however the presence of strong Brγ and possibly Mg II recombination lines coupled with the significantly different H_2 temperatures indicates that the star is at a much more evolved stage of evolution near the onset of photoionization of the nebula.

References

Bragg, S. L., Smith, W. H., & Brault, J. W. 1982, ApJ, 263, 999

Bujarrabal, V., Alcolea, J., & Planesas, P. 1992, A&A, 257, 701

Bujarrabal, V., Castro-Carrizo, A., Alcolea, J., & Sánchez Contreras, C. 2001, A&A, 377, 868

Chong, S.-N., Kwok, S., Imai, H., Tafoya, D., & Chibueze, J. 2012, ApJ, 760, 115

Clube, K. L. & Gledhill, T. M. 2004, MNRAS, 355, L17

Davis, C. J., Smith, M. D., Gledhill, T. M., & Varricatt, W. P. 2005, MNRAS, 360, 104

Davis, C. J., Smith, M. D., Stern, L., Kerr, T. H., & Chiar, J. E. 2003, MNRAS, 344, 262

García-Hernández, D. A., Manchado, A., García-Lario, P., Cañete, A. B., Acosta-Pulido, J. A., & García, A. M. 2006, ApJ, 640, 829

García-Hernández, D. A., Manchado, A., García-Lario, P., Domínguez-Tagle, C., Conway, G. M., & Prada, F. 2002, A&A, 387, 955

Gauba, G. & Parthasarathy, M. 2003, A&A, 407, 1007

—. 2004, A&A, 417, 201

Gledhill, T. M., Chrysostomou, A., Hough, J. H., & Yates, J. A. 2001, MNRAS, 322, 321

Gledhill, T. M. & Forde, K. P. 2012, MNRAS, 421, 346

Gledhill, T. M., Forde, K. P., Lowe, K. T. E., & Smith, M. D. 2011, MNRAS, 411, 1453

Gledhill, T. M. & Yates, J. A. 2003, MNRAS, 343, 880

Guerrero, M. A., Villaver, E., Manchado, A., Garcia-Lario, P., & Prada, F. 2000, ApJS, 127, 125

Henize, K. G. 1976, ApJS, 30, 491

Hrivnak, B. J., Kelly, D. M., & Su, K. Y. L. 2004, in Astronomical Society of the Pacific Conference Series, Vol. 313, Asymmetrical Planetary Nebulae III: Winds, Structure and the Thunderbird, ed. M. Meixner, J. H. Kastner, B. Balick, & N. Soker, 175

Hrivnak, B. J., Kelly, D. M., Su, K. Y. L., Kwok, S., & Sahai, R. 2006, ApJ, 650, 237

Hrivnak, B. J., Kwok, S., & Geballe, T. R. 1994, ApJ, 420, 783

Hu, J. Y., Slijkhuis, S., de Jong, T., & Jiang, B. W. 1993, A&AS, 100, 413

Kelly, D. M. & Hrivnak, B. J. 2005, ApJ, 629, 1040

Kwok, S., Hrivnak, B. J., Zhang, C. Y., & Langill, P. L. 1996, ApJ, 472, 287

Kwok, S., Su, K. Y. L., & Hrivnak, B. J. 1998, ApJ, 501, L117

Lagadec, E., Verhoelst, T., Mékarnia, D., Suáeez, O., Zijlstra, A. A., Bendjoya, P., Szczerba, R., Chesneau, O., van Winckel, H., Barlow, M. J., Matsuura, M., Bowey, J. E., Lorenz-Martins, S., & Gledhill, T. 2011, MNRAS, 417, 32

Le Bourlot, J., Pineau des Forêts, G., Flower, D. R., & Cabrit, S. 2002, MNRAS, 332, 985

Likkel, L., Forveille, T., Omont, A., & Morris, M. 1991, A&A, 246, 153

Likkel, L., Morris, M., Omont, A., & Forveille, T. 1987, A&A, 173, L11

Loup, C., Forveille, T., Omont, A., & Nyman, L. A. 1990, A&A, 227, L29

Meixner, M., Skinner, C. J., Graham, J. R., Keto, E., Jernigan, J. G., & Arens, J. F. 1997, ApJ, 482, 897

Parthasarathy, M. & Pottasch, S. R. 1989, A&A, 225, 521

Sánchez Contreras, C., Sahai, R., Gil de Paz, A., & Goodrich, R. 2008, ApJS, 179, 166

Steffen, W., Koning, N., Wenger, S., Morisset, C., & Magnor, M. 2010, ArXiv e-prints

Su, K. Y. L., Hrivnak, B. J., Kwok, S., & Sahai, R. 2003, AJ, 126, 848

Su, K. Y. L., Volk, K., Kwok, S., & Hrivnak, B. J. 1998, ApJ, 508, 744

Suárez, O., García-Lario, P., Manchado, A., Manteiga, M., Ulla, A., & Pottasch, S. R. 2006, A&A, 458, 173

Ueta, T., Murakawa, K., & Meixner, M. 2007, AJ, 133, 1345

Volk, K., Kwok, S., & Hrivnak, B. J. 2007, ApJ, 670, 1137

Weintraub, D. A., Huard, T., Kastner, J. H., & Gatley, I. 1998, ApJ, 509, 728

Wilgenbus, D., Cabrit, S., Pineau des Forêts, G., & Flower, D. R. 2000, A&A, 356, 1010

Chapter 7: Discussion & Conclusions

This dissertation has presented a study of six Pre-Planetary Nebulae (PPNe) using the relatively new (at NIR wavelengths) integral field spectroscopy technique. This method has allowed the investigation of distinct regions of these nebulae, and in certain cases the application of Magneto-HydroDynamic (MHD) shock models to the data.

The goal of this research has been to investigate the evolution of PPNe by detailed examination of a small sample of objects consisting of a (nearly[1]) full range of evolutionary types. Near-IR (NIR) ro-vibrational lines were employed as the primary tool to tackle this problem.

In all six sources the 1→0S(1) line is used to map the spatial extent of the H_2. In three of these objects the maps represent the first images of their H_2 emission nebulae. In the case of the earliest-type object (*IRAS* 14331-6435) in this sample, the line map gives the first image of its nebula at any wavelength. In the only M-type object (OH 231.8+4.2) in the sample, high-velocity H_2 is detected in discrete clumps along the edges of the bipolar outflow, while a possible ring of slower moving H_2 is found around the equatorial region. In *IRAS* 19500-1709, an intermediate-type object, the line map shows the H_2 emission to originate in clumpy structures along the edges of a bipolar shell/outflow. The remaining three objects have all been the subject of previous studies but in each case new H_2 lines are detected in this work along with other emission lines (Mg II, Na I & CO). In the case of *IRAS* 16594-4656, MHD shock models have been used to determine the gas density and shock velocity.

Two new `python` modules/classes have been written. The first one to deal with the data cubes, extract flux measurements, rebin regions of interest, and produce line maps. The second class allows the easy calculation of many important parameters, for example, excitation temperatures, CDR values, extinction estimates from several line-pairs, column density values, and total mass of the H_2. The class also allows the production of input files for the shock fitting procedure (discussed below), and simulated shocks for testing this fitting process. A prototype standalone executable providing a Graphical User Interface (GUI) has been developed to provide an easy-to-use tool for these classes.

A new framework to fit NIR shock models to data has been developed, employing Monte Carlo techniques and the extensive computing cluster at the University of Hertfordshire (UH)[2]. This method builds on the Column Density Ratio (CDR) approach used by many other authors (e.g., O'Connell et al., 2004; Davis et al., 2003), however this framework provides a method of 1) correctly sampling the shock model parameter space, and 2) providing error estimates on the model fit. Using this approach, *IRAS* 16594-4656 (B7 star) has been modelled using shocks.

7.1 Galactic Distribution of PPNe

Figure 7.1 shows the distribution of the 326 *'most likely'* PPNe as given in the Toruń catalogue (Szczerba et al., 2007), in Galactic (7.1) and Equatorial (7.2) coordinates.

[1] No A-type stars are in this sample. Reasons for this are discussed later in this chapter.

[2] *see* Acknowledgements

The stars in this study are marked with blue star symbols, and two objects added to the list of H_2 emitting PPNe in Kelly & Hrivnak (2005) are plotted with green squares. Stars added to the Toruń catalogue (Szczerba et al., 2007) are OH 231.8+4.2, *IRAS* 10178-5958, *IRAS* 06556+1623, while *IRAS* 19336-0400 is removed from the list of PPNe H_2 emitters given in (Kelly & Hrivnak, 2005) — it is most likely a PN. This assumption is further justified by relatively recent (2006) integral field data from Gemini/NIFS in which no NIR H_2 lines are detected (private communication – Tim Gledhill). In constructing Figure 7.3 the spectral type for *IRAS* 22574+6609 and *IRAS* 16342-3814 are assigned to F and K type, respectively. Neither of these stars have confirmed spectral types in the literature, however due to the weak 1→0S(1) emission in *IRAS* 22574+6609 combined with the lack of other strong emission lines in the *K*-band suggests that this object is of intermediate spectral type. *IRAS* 16342-3814 shows strong bipolar morphology, fast outflows along the polar axis, and an optically thick equatorial region (Gledhill & Forde, 2012), suggesting that it is most likely a late-type object. A list of all objects considered/plotted in this chapter as a H_2 PPNe are given in Table B.1 in Appendix B.

As expected the PPNe are concentrated at low latitudes close to the Galactic plane (Figure 7.1). Weston et al. (2011) recently found that very few post-AGB stars populate the halo and those that do are of low masses ($M < 0.55 M_{\odot}$). Interestingly, a discrepancy exists in that their synthetic galactic model predicts many more post-AGB stars in the halo than are currently observed. An increased number of PPNe at low Galactic longitudes is also evident in Figure 7.1, as would be expected in the direction of the Galactic centre. This low-latitude population of the PPNe indicates that they must come from relatively massive progenitors, as one would not expect to observe massive stars at very high latitudes, unless in extra-ordinary circumstances (e.g., the case of runaway stars or nearby objects). The distribution of PPNe with H_2 emission appears to be also focused toward low Galactic latitudes, with only two objects with latitudes greater than 15° (*IRAS* 19500-1709 and *IRAS* 18062+2410) — there is a paucity of objects at high Galactic latitudes. Similarly, Kastner et al. (1996) found the distribution of PNe exhibiting H_2 emission seems to be concentrated at low Galactic latitudes ($| b | = 6° \pm 1°$).

Figure 7.3 (a) shows the total number of PPNe with H_2 in emission to be 25 (with the inclusion of OH 231.8+4.2). The total number of PPNe observed for H_2 is estimated at between 75 – 80, with the majority of these coming from just two spectroscopic surveys (Kelly & Hrivnak, 2005; García-Hernández et al., 2002). Therefore ∼30%of the objects from these observations of PPNe display H_2 emission. Interestingly, Kastner et al. (1996) have reported that around 40% of PNe observed for H_2 exhibit some H_2 emission.

The distribution of H_2 emitting PPNe in terms of spectral type shows that B-type stars are most likely to show some H_2. However, it is worth noting that H_2 emission is detected in PPNe with a variety of spectral types. There is a 'gap' in this distribution at 10,000 K (A-type), which might be attributed to the acceleration of evolution since $\Delta M_{\rm env}/\ \Delta T_{\rm eff}$ becomes very small at this point (Blöcker, 1995). This gap is also evident for all PPNe (see Figure 6 in Szczerba et al., 2007).

Figures 7.3 (b) and (c) compares the distribution of all PPNe to the H_2 emitting PPNe in Galactic longitude and latitude. These show that the distribution of H_2 PPNe with latitude is limited to ± 20°, while the total PPNe population is much more extended ∼ ± 70°. Figures 7.3 (d) and (e) show the same data in Equatorial coordinates.

As can be seen from these plots, the PPNe objects presented in this Thesis are all located (with the exception of *IRAS* 19500-1709) at low Galactic latitudes, and might lie in the Galactic plane. Table 7.1 gives a list of distances for each object studied in this Thesis. Where possible, a range of distances taken from the literature is given alongside near and far kinematic distance estimates determined from the Brγ line; a flat rotation curve is assumed, V(R)=220 km s^{-1}, and a distance of the Sun to the Galactic centre of 8.5 kpc. Using the lowest and highest overall values, an altitude is calculated for each object. These altitudes confirm the PPNe lie within the Galactic disc, with the exception of *IRAS* 19500-1709 (assuming a disc scale height of 300 pcs).

As discussed above, there is a strong anti-correlation between high Galactic latitude and H_2 PPNe. The distances to five out of the six nebulae in this study show that they all lie within the Galactic disc. If this trend were to extend to all H_2 emitting PPNe then we might expect a large proportion emitters to lie at relatively low Galactic altitudes. This would be a similar result to the distribution of H_2 emitting PNe (Kastner et al., 1996) which are likewise considered to be descendants of relatively massive stars.

Kelly & Hrivnak (2005) find that all F-G type PPNe emitting H_2 exhibit a bipolar morphology. The integral field data of four PPNe supports this hypothesis, and possibly extends it to include M-type PPNe. Kelly & Hrivnak (2005) calculate the mean Galactic latitude of these spectral types is $\mid b \mid = 3^\circ.6 \pm 1^\circ.2$, while B-type PPNe with H_2 are located at a higher Galactic latitude ($8^\circ.1$) and display H_2 emission irrespective of morphology.

Such small numbers of H_2 emitting PPNe and their morphological diversity make it quite difficult to determine if the apparent correlations between spectral type and Galactic location, and H_2 emission and morphology, hold true for this class of objects. To tackle this problem a systematic survey is needed.

In the past there have been searches for PN candidates in Hα (e.g., the IPHAS survey, Drew et al., 2005). However, in the case of PPNe the majority have been discovered as a result of their strong IR excess detected by the *IRAS* satellite. The PPNe detected in this survey are biased toward dusty objects which tend to be younger, bipolar and more extreme. To date, only two spectroscopic surveys have been attempted (Kelly & Hrivnak, 2005; García-Hernández et al., 2002). Many of their candidates were chosen from the *IRAS* database and so are biased to the same types of objects.

Froebrich et al. (2011) are currently undertaking a Galactic plane H_2 survey ($6<l<65$; $-1.5<b<+1.5$) – the UKIRT Widefield Infrared Survey for H_2 (UWHIS2). The narrow-band images are centred on the $1\rightarrow0$S(1) line. The apparent concentration of H_2 PPNe in the Galactic plane from the previous studies suggests that this systemmatic approach should uncover many new H_2 PPNe emitters. Data mining is already underway by various teams of people with a handful of PPNe objects already discovered.

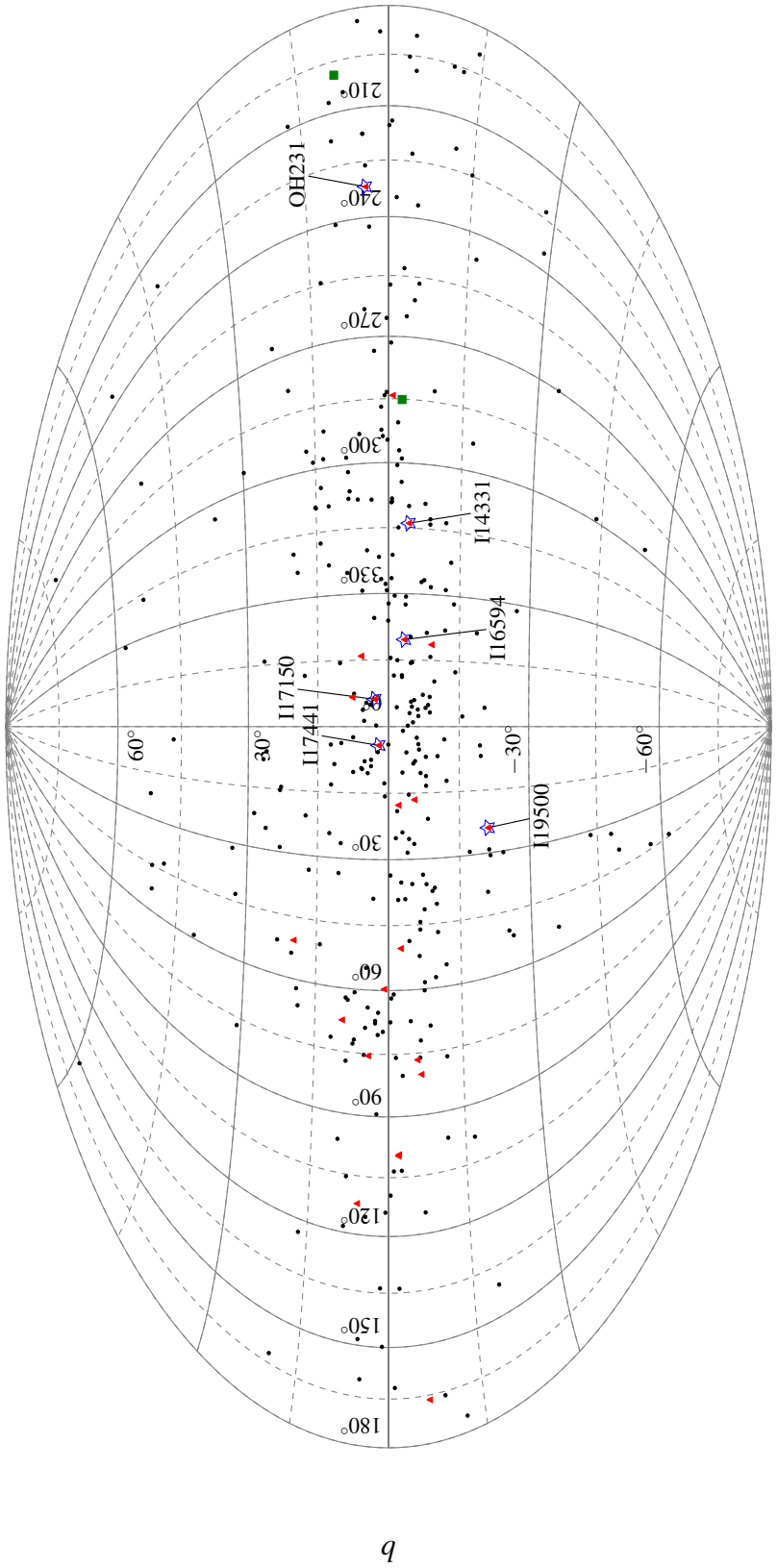

Fig. 7.1: Aitoff projection of the positions of PPNe in Galactic coordinates. PPNe with H_2 are displayed with red triangles, while black circles give the positions of other *'most likely'* PPNe objects as defined in the Toruń catalogue (Szczerba et al., 2007). Labelled blue stars give the locations of objects presented in this Thesis. Two green squares mark the position of two objects not included in the Toruń catalogue (see text).

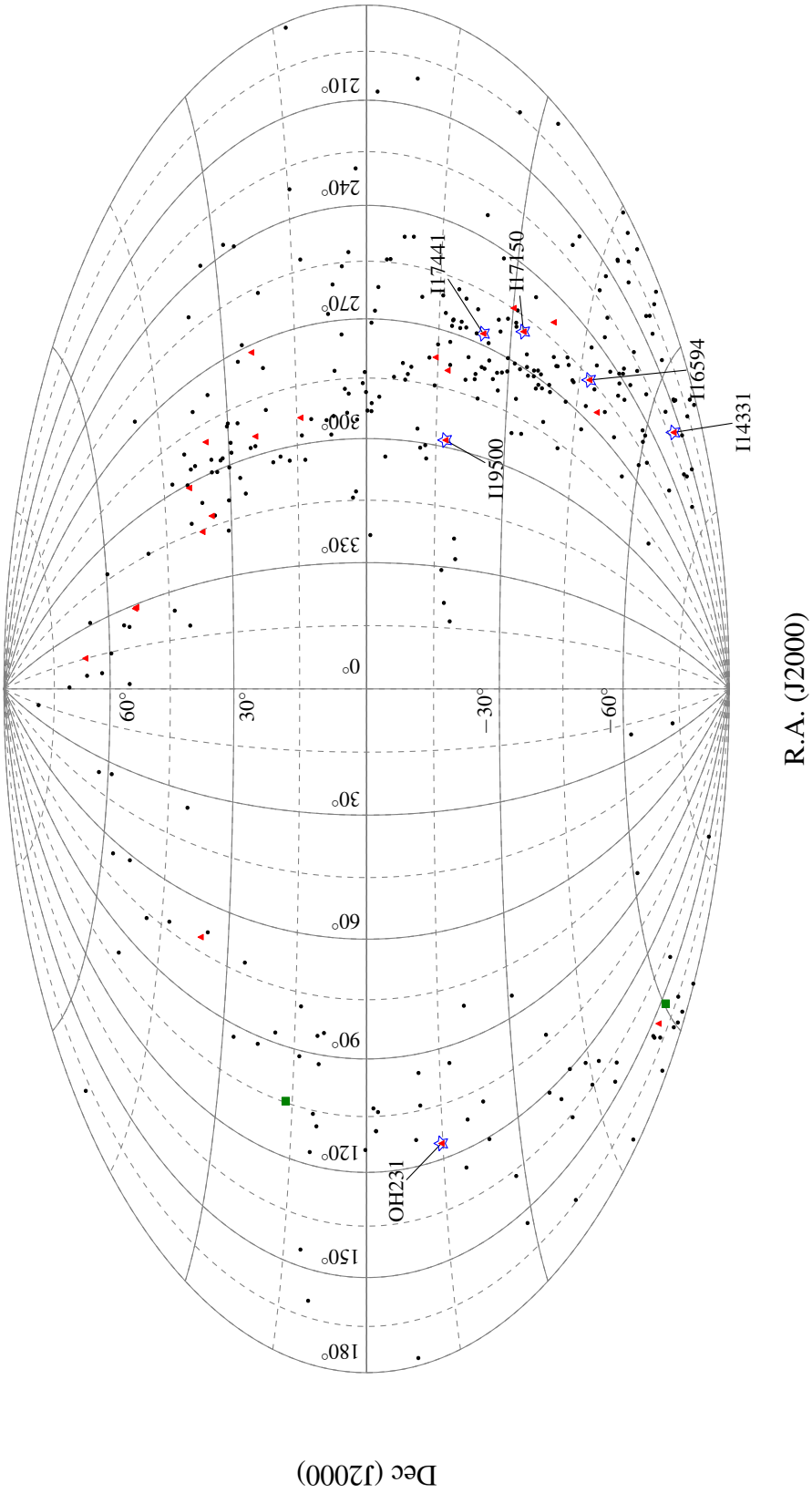

Fig. 7.2: Aitoff projection of the positions of PPNe in Equatorial coordinates. Symbol definitions given in Figure 7.1.

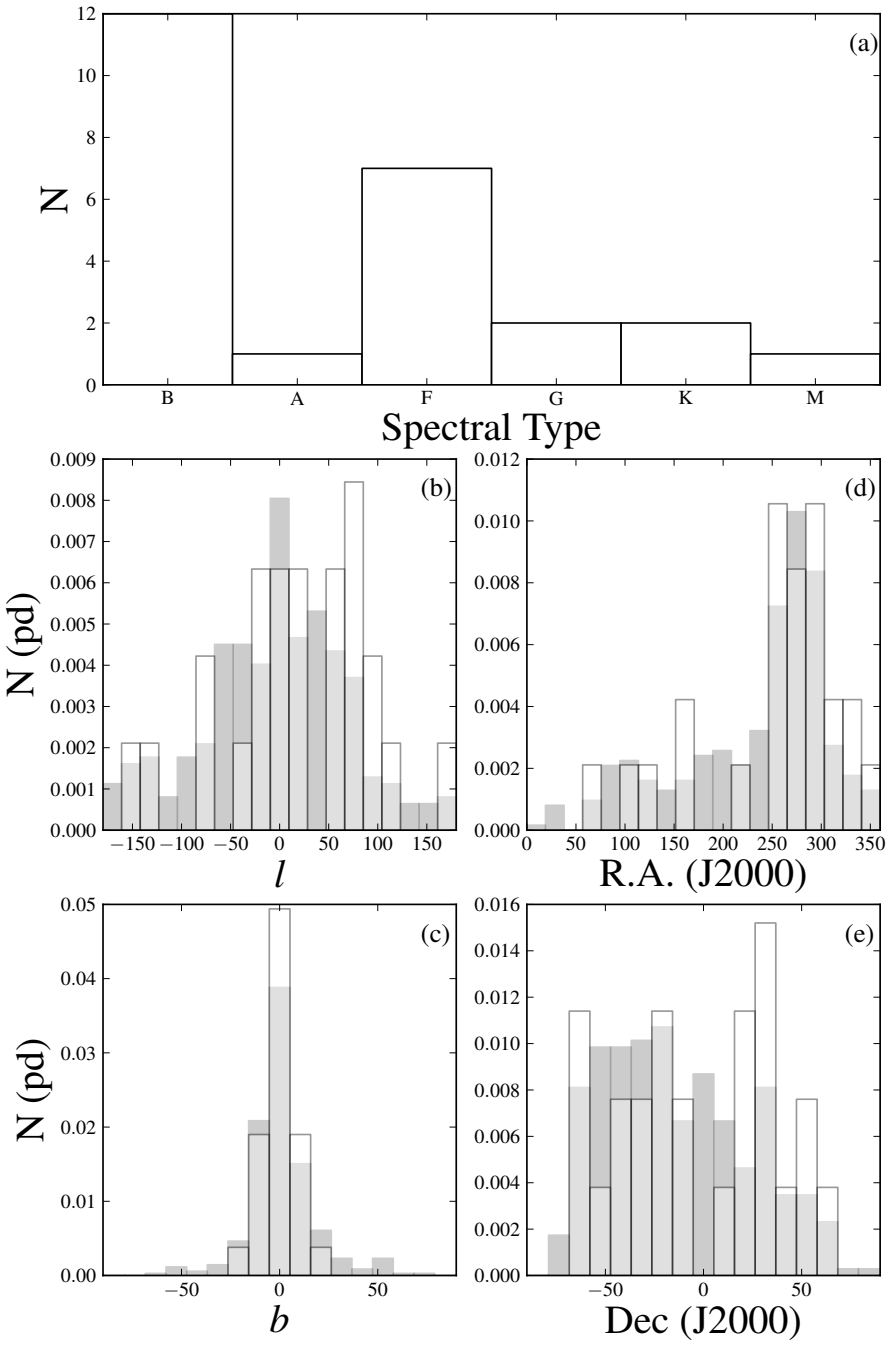

Fig. 7.3: (*a*) Histogram of the Galactic PPNe that exhibit H_2 emission in terms of spectral types, (*b*) Galactic longitude distribution for all *'most likely'* PPNe, and (*c*) Galactic latitude distribution. (*d*) The distribution of PPNe in Right Ascension , and (*e*) in Declination. White histograms are the PPNe with H_2 emission, gray histograms are all (as defined previously) PPNe. The Y-axis is the number of objects normalised to form a probability density, this is purely to allow a comparison of the distributions.

7.2 Dependence on evolutionary phase

Weintraub et al. (1998) was one of the first authors to show that the presence of H_2 in PPNe is linked to spectral type, using a sample of seven objects at various different evolutionary stages. García-Hernández et al. (2002) proposed that the onset of H_2 emission takes place during the post-AGB phase, shortly before photoionization of the nebula. In this longslit NIR study of 30 *IRAS* sources from M→B-type star, nine show H_2 emission lines, however none of the stars (with the exception of *IRAS* 17150-3224) earlier than A-type showed any H_2 lines. To explain these observations, they suggest a scenario whereby fluorescent excitation is experienced by stars earlier than A-type, while shocks dominate the bipolar nebulae with stars of later types. A later NIR spectroscopic survey carried out by Kelly & Hrivnak (2005), on a selection of 51 PPNe of different spectral types, resulted in the detection of H_2 emission in 16 of these sources. Many of these objects were of later spectral types, three of which were M-type stars with null detections reported in each case. A similar result was reported by Weintraub et al. (1998) for the three M-type objects in their sample (OH 231.8+4.2, *IRAS* 09371+1212, and *IRAS* 07131-0147). These results led Kelly & Hrivnak (2005) to suggest that H_2 emission begins at a spectral class of mid-G in PPNe, in fact all the F→G-type stars in their dataset with bipolar morphology plus optically thick equatorial regions exhibit collisionally-excited H_2 emission.

As H_2 is present in the ejecta of all post-AGB precursors, and there is a high mass-loss rate at the tip of the AGB (up to 10^{-4} $M_\odot$/yr), it seems reasonable that shocked H_2 should be present in the nebulae surrounding M-type stars – provided there is time for a fast wind and the AGB cast-off envelope to interact. This most likely means that there must be some mechanism present in the nebula to accelerate the formation of the fast wind (e.g., a close binary companion) – which is probably the case for a minority of post-AGB objects.

CO observations of late-type PPNe (Bujarrabal et al., 2001) show that many of these objects possess high-velocity massive molecular outflows (e.g., OH 231.8+4.2, *IRAS* 09371+1212), with optical imaging showing the presence of the shocked Hα line, and dense equatorial regions obscuring the central star. CRL 2688 is a well-studied object with an F5 type star at its heart, a different spectral type star but it certainly shares some very obvious morphological characteristics with some these objects. CRL 2688 also has a fast molecular bipolar outflow, an optically thick equator, and most importantly shock H_2 emission. Similarly, *IRAS* 22036+5050 (F5-type) harbors massive molecular bipolar outflows along the axis of the optical bipolar nebula (Sahai et al., 2006). These comparisons allows the question to be asked of later-type objects which share the same morphological characteristics – why has H_2 not been detected in their outflows?

Following a successful VLT observing proposal[3] based on this argument, a search of two extended PPNe objects was carried out to try to locate H_2 in their outflows. The first object OH 231.8+4.2 shares almost the morphological characteristics as CRL 2688, however in two different attempts with different instruments, no H_2 has been reported. As discussed in Chapter 4, the IFU observations revealed the presence of two distinct regions of H_2 emission: 1) around the waist of the object and 2) along the edge of the bipolar outflow. This is quite a similar situation to that of CRL 2688, whose H_2 emission sites are similarly distributed (Sahai et al., 1998). Unfortunately,

[3]Programme ID 084.D-0487(A)

a positioning error meant that the full bow-like shock front at the end of the bipolar outflow in OH 231.8+4.2 was not imaged. This work is the first to report the detection of H_2 in an object with an M-type central star.

The second object, not discussed prior to this, imaged during this observing run was *IRAS* 09371+1212 (Frosty Leo). Unfortunately, after taking some short acquisition images, an actuator on one of the deformable mirrors malfunctioned and no further images of this object were possible. These images showed no obvious H_2 emission in the raw spectrum. It is unfortunate that the planned regions were not properly imaged, as Frosty Leo shows evidence for collimated outflows, equatorial structures, and bipolar morphology, similar to OH 231.8+4.2 (e.g., Sahai et al., 2000). Searches by previous authors (Weintraub et al., 1998; Davis et al., 2005) report null detections of H_2 in this nebula, however stating that due to the extended nature of this object the emission sites may have been missed. Sahai et al. (2000) point out that the high energy outflow is located at low latitudes in this object ($< 10''$); this could mean that shocked H_2 might be found associated with these jets. To resolve this question, an IFU survey of three locations (A_N, A_S, and J1/3 as labelled in Figure B.5) would be required to provide an ideal comparison study to OH 231.8+4.2.

7.3 Tori & Jets

Equatorial structures have been detected in PPNe via many different indicators (e.g., CO, H_2, dust, SiO, and OH masers). Sahai et al. (1998) show high-resolution NIR imaging of CRL 2688, showing a spectacular example of a large equatorial H_2 structure perpendicular to the main outflow direction (see image B.6). Recently, more of these H_2 equatorial structures have been detected in IFU studies of PPNe: *IRAS* 19306+1407, *IRAS* 18276-1431, and from this work OH 231.8+4.2. In these three objects the H_2 appears as two arcs of emission either side of the central star. This configuration is most likely the result of viewing a torus or equatorially enhanced shell of material at some intermediate angle. Objects with their bipolar axis in the plane of the sky (e.g., *IRAS* 16594-4656) would also be expected to display H_2 emission peaks either side of the central star. This does not seem to be the case for *IRAS* 16594-4656, although a dense mid-IR dust torus is present at the expected location in this object (Volk et al., 2006).

The three objects mentioned above, are at three distinct evolutionary stages (B, F, and M), and as such the arcs do not trace the evolution of the PPNe. The presence of these H_2 arcs might be dependent on the nature and/or density of material in the equatorial plane. Holes/gaps in the central optically thick material might allow the H_2 further away from the star to become shock excited. In several PPNe these holes/gaps give rise to 'searchlight beams' illuminating the surrounding nebula in spectacular fashion (e.g., *IRAS* 18276-1431).

The equatorial H_2 in OH 231.8+4.2 is located at a distance of $\sim$ 5200 AU from the central star and as such can not be the collimating structure for the bipolar outflow. In fact, there are a series of concentric structures, mapped via different lines, which are most likely the response of the equatorial material to the collimating mechanism. The 1→0/2→1S(1) ratio in the central region (8) is consistent with a shock origin, as observed in CRL 2688 (11), and also in *IRAS* 18276-1431 (9).

The connection of these structures to fast-moving material moving perpendicular to these equatorial enhancements has been noted both observationally (Huggins, 2007)

and theoretically (Soker & Rappaport, 2000). Huggins (2007) found that the tori and the bipolar jets are formed at similar times with the jets lagging the tori formation by $\sim$ 100 years. Indeed, in the case of OH 231.8+4.2 where massive fast-moving material has been found in the outflows, with regions of shocked gas present in discrete clumps. From the data presented in this thesis, H_2 has been detected along the edges of the bipolar outflow of OH 231.8+4.2. Under the reasonable assumption that the outflow is mainly moving in the bipolar direction, the H_2 is moving at deprojected velocities between 100 – 150 km s^{-1}. The presence of fast-moving H_2 is common in young stellar objects (YSOs) and has now been detected in several PPNe objects (e.g., AFGL 618, CRL 2688, *IRAS* 16342-3814). The presence of a transverse magnetic field allows C-type shocks to occur without dissociation of the H_2 at speeds up to 70 km s^{-1} for densities $\sim 10^4$ cm^{-3} (e.g., Le Bourlot et al., 2002). Yet it is unclear how H_2 can exist at the high velocities observed in these PPNe without destruction of the molecule. Table 7.1 shows some characteristics of the nebula studied in this Thesis. In all objects, independent of spectral type, H_2 is detected, apart from Frosty Leo (possibly due to instrument failure). In 4/6 objects there is some evidence for a fast wind/outflow from the literature. While equatorial enhancements of some material is detected for 5/6 of these objects. Due to the small numbers of objects and the selection bias involved, it is difficult to draw any great conclusions from these statistics.

However, what is clear from these observations, when coupled with some literature imaging data, is that most G$\rightarrow$A-type H_2 emitters are bipolar with optically thick material around the waist of the objects, further supporting the scenario of the tori preceding the formation of the jets. The detection of the Na I doublet lines in the objects *IRAS* 17441-2411 and *IRAS* 17150-3224 might suggest that they are coming from a disc of material near the central source – the low ionisation potential of these lines (5.1 eV) means that photons with λ=2430 Å can cause the ionisation. A higher resolution spectrum would be necessary to confirm the disc configuration of the Na I. B-type stars showing significant levels of fluorescence (e.g., *IRAS* 14331-6435 and *IRAS* 19306+1407 [unpublished work of Krispian Lowe]) are all found to be bipolar when imaged in H_2. This is contrary to the conclusions of Kelly & Hrivnak (2005), who suggested that there is no correlation with morphology. However, 9 out of 13 of their objects had no imaging data available. With the more efficient integral field techniques it might be possible, in the near future, to resolve this debate. Interestingly, *IRAS* 16594-4656 is an object of spectral type (B7) and so will begin to photo-excite the H_2 quite soon, however it still shows quite strong evidence that the H_2 in the nebula is shock excited. The Mg II doublet has been detected in the two B-type objects in this Thesis. The high ionisation potential of the Mg II means that it most likely originates quite close to the central star, inside the Brγ emission region. This line can act as a further indicator that the central star is on the brink of becoming the central star of the planetary nebula.

Table 7.1: Characteristics of the post-AGB H_2 emitters in this work.

Source	Spectral Type	Morphology¶ (NIR)	H_2	l (deg)	b (deg)	Distance (kpc)		Altitude (pc)		Evidence of Fast wind?	Equatorial Enhancement
						other	kinematic*	low D	high D	(km s^{-1})	
IRAS 14331-6435	B3I	B	√	313.8867	-04.2026	1.3 – 2.5	3.1, 8.7	95	230	×◇	??
IRAS 16594-4656	B7	B	√	340.3924	-03.2889	1.8 – 2.6	2.3, 13.7	105	150	√ (126)	√
IRAS 17150-3224	G2,F3–7△	B	√	353.8437	+02.9842	2.4	—†	125	125	×	√
IRAS 17441-2411	F5	B	√	004.2227	+02.1453	1.9 – 4	1.7, 15.3	70	150	√ (50)	√
IRAS 19500-1709	F2/F3I	B	√	023.9837	-21.0361	1 – 4	2.0, 13.5	360	1435	√ (30)	√
OH 231.8+4.2	M6	B	√	231.8354	+04.2196	1.3	2.85‡	95	155	√ (150)	√

* Two values given when object is inside the solar circle (kinematic distance ambiguity).
† Kinematic distance estimate unreliable due non-circular motion close to Galactic centre.
‡ Using V_{LSR} = 33 km s^{-1} from mm observations (Sánchez Contreras et al., 2000).
◇ No evidence for a Hα P-Cygni profile (e.g., Suárez et al., 2006).
¶ B = Bipolar.
△ updated classifictaion based on high-resolution data, in particular the Ca II H and K lines, which are useful for discriminating between F- and G-type stars (Sánchez Contreras et al., 2008).

7.4 Shocked H_2

In each object considered in this work the 1→0/2→1S(1) ratio has been a key indicator for the presence of shocks in the nebulae. In all objects the values measured have all pointed toward the H_2 being shock-excited. These lines have upper energies of E = 6956 K (1→0S(1)) and 12550 K (2→1S(1)), and so gas temperatures > 1000 K are required to observe the lines. The use of the 1→0/2→1S(1) ratio can only be used as an indicator for shock excitation at low densities, as at high densities (10^5 – 10^7 cm^{-3}), H_2 that has been UV-excited can be collisionally de-excited giving similar 1→0/2→1S(1) values, thus incorrectly pointing towards a collisional mechanism. Another problem with relying on a single ratio to determine the excitation is the existence of a degeneracy between the pre-shock density and the shock velocity for the 1→0/2→1S(1) ratio. This situation can be seen in Figure 7.4, where e.g. a 1→0/2→1S(1) ratio of 20 can be obtained from a C-type shock at 25 km s^{-1} and a pre-shock density of 10^7 cm^{-3}, or equally from the combination of a shock velocity of 65 km s^{-1} and a pre-shock density of 10^5 cm^{-3}. Figure 7.4 also shows a similar degeneracy can exist for 1→0S(1)/3→2S(3) ratio, while comparison of rotational and vibrational temperatures in certain circumstances might allow you to break this degeneracy.

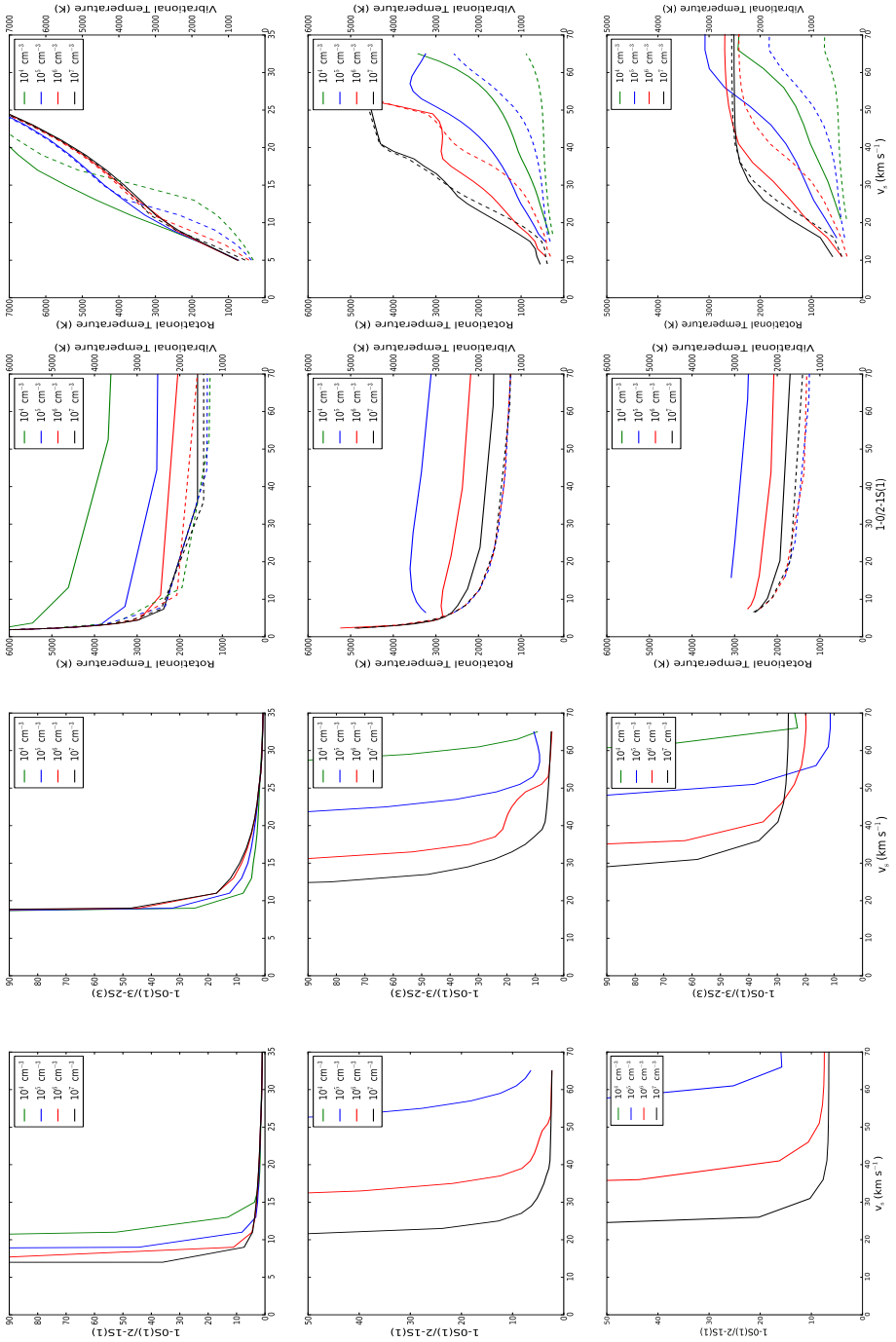

Fig. 7.4: Shock diagnostic plots are presented to show the degeneracy that can occur from using a single line ratio to determine the excitation mechanism. Three shock models were created to illustrate this: (*top*) J-type shock, (*middle*) Planar C-type shock, (*bottom*) C-bow shock.

In an attempt to overcome these problems, a Markov Chain Monte Carlo (MCMC) approach was used to fit as many line fluxes as possible coupled with CDR diagrams and line luminosities. The Markov Chain allows a more time/resource efficient exploration of the parameter space than conventional Monte Carlo techniques. This is mainly because of the advantage that in constructing the Markov Chain each new sample does not necessarily have to be independent.

This technique was used to fit the CDR diagrams at various regions in the nebula of *IRAS* 16594-4656. It was found that no C-planar type model could reproduce the line values. C- and J-bow shocks could both find a satisfactory fit to the data, a J-planar model also fit the data points. The predicted pre-shock densities for the J-type shocks when converted into extinction estimates yielded values an order of magnitude too high (100 – 500) and so could be ruled out. This level of extinction is not observed in the nebula. Several $v = 2$ and two $v = 3$ lines were detected for the first time in this object. The $v = 2$ lines show a similar morphology to the $v = 1$ lines and are therefore generated through the same process. The S/N per pixel of $v = 3$ lines is too low to generate a line map and so it is unclear whether the line shows the same spatial extent as the lower levels. Due to the hollow bipolar lobes of *IRAS* 16594-4656 it might be possible that the $v = 3$ lines have a fluorescent component in regions nearer to the bipolar axis, although, the 1→0S(1)/3→2S(3) ratio (> 100) appears to agree with a shock origin for the line.

The 1→0/2→1S(1) line ratio map for *IRAS* 16594-4656 shows that lower excitation regions exist at the ends of both lobes, while the highest excitation is originating along the walls of the shell. Low-excitation regions like this can exist where either the shock velocity drops or the density drops. The best-fitting C-bow shock model that resulted from the application of the MCMC technique, returns a lower density at the end of the lobes than along the edges of the lobe. A lower density is a reasonable result, as in wider field-of-view images two pairs of ansae are observed in H_2 past the ends of each lobe. This is most likely the result of the axial fast wind breaking out of the lobes and a much different component to the slower wind giving rise to the radial expansion speed of the nebula.

As discussed in Chapter 6, in *IRAS* 17441-2411 (F5) the H_2 emission confined to the ends of the bipolar outflow, with a 1→0S(1) line width (FWHM) of 25 km s^{-1} measured from NIR echelle spectroscopy (Davis et al., 2005). The velocity resolution of these observations, as estimated from arc lamp lines, is $\sim$ 16 km s^{-1}, so any linewidth above this value might represent a convolution of the spectral resolution and the true intrinsic line width. However, as is the case for many PPNe (e.g., *IRAS* 16594-4656) the H_2 emission is usually coming from expansion of the nebula both toward and away from the observer. This situation will result in a blending of the emission from the front and back of the nebula, increasing the linewidth and leading to possible mis-interpretation of the intrinsic velocities. Typically the intrinsic line profiles from C-type bow shocks tend to be quite narrow (< 70 km s^{-1}), while J-type shocks produce even narrower lines (< 25 km s^{-1}), due to dissociation limiting the normal component of the velocity (Smith et al., 1991).

Of the remaining objects in the sample, *IRAS* 19500-1709 and OH 231.8+4.2 are too low S/N to run the shock analysis code, *IRAS* 17150-3224 does not have resolved structures that could be modelled reasonably. *IRAS* 14331-6435 is the most evolved object in the sample with the most significant difference in rotational and vibrational temperatures, the presence of the strongest v=3 lines, and an unclear morphology. This is most likely a PPNe on the 'brink' of becoming a PN and excitation modelling

would most likely require the inclusion of UV excitation models.

7.5 Future Work

The Bayesian Markov-Chain Monte Carlo (MCMC) shock fitting method allows an efficient approach to modelling H_2 shock lines via CDR diagrams. This technique could also be applied to early-type post-AGB stars (B1-5) undergoing the onset of the fast-wind stage of evolution. In this case, a combination of the above technique with a H_2 fluorescence model, to attempt to disentangle the contributions from the collisional and fluorescence components would be necessary if one wants to be able to say anything meaningful about the physical conditions in these nebulae. Also, previous published work could be re-analysed to explore the possibilities of more than one fit to the data.

With the data in this Thesis it has not been possible to resolve any clear bow-like shock fronts. High resolution NIR images of the Helix planetary nebula (e.g., see Figure 1.1) have revealed the presence of many cometary knots and clumpy structures (Matsuura et al., 2009); in the future it should be possible to resolve these structures in the nebulae of post-AGB objects – if they are present. This would allow a more accurate modelling to be performed using not only the H_2 line fluxes but also the size and shape of the shocked material.

The new KMOS NIR integral field unit on VLT will be a useful tool to study the PPNe with large angular size. KMOS will operate in the J-, H-, and K-bands and cover a wavelength range of between 0.8→ 2.5μm. It will consist of 24 individual IFUs each of a spatial extent 2.8″× 2.8″. KMOS achieved first light on the 21st of November 2012 and is located on the Nasmyth platform in the VLT/UT1. The large angular size of OH 231.8+4.2 limited the amount of fields and time that was possible to search for H_2, with KMOS this could all be done is a fraction of the time, covering the northern bow shock and the southern lobe to search for further H_2 emission sites. Frosty Leo is another PPNe which could be investigated with KMOS as it 'should' display H_2 given its physical characteristics.

References

Blöcker, T. 1995, A&A, 299, 755

Bujarrabal, V., Castro-Carrizo, A., Alcolea, J., & Sánchez Contreras, C. 2001, A&A, 377, 868

Davis, C. J., Smith, M. D., Gledhill, T. M., & Varricatt, W. P. 2005, MNRAS, 360, 104

Davis, C. J., Smith, M. D., Stern, L., Kerr, T. H., & Chiar, J. E. 2003, MNRAS, 344, 262

Drew, J. E., Greimel, R., Irwin, M. J., Aungwerojwit, A., Barlow, M. J., Corradi, R. L. M., Drake, J. J., Gänsicke, B. T., Groot, P., Hales, A., Hopewell, E. C., Irwin, J., Knigge, C., Leisy, P., Lennon, D. J., Mampaso, A., Masheder, M. R. W., Matsuura, M., Morales-Rueda, L., Morris, R. A. H., Parker, Q. A., Phillipps, S., Rodriguez-Gil, P., Roelofs, G., Skillen, I., Sokoloski, J. L., Steeghs, D., Unruh, Y. C., Viironen, K., Vink, J. S., Walton, N. A., Witham, A., Wright, N., Zijlstra, A. A., & Zurita, A. 2005, MNRAS, 362, 753

Froebrich, D., Davis, C. J., Ioannidis, G., Gledhill, T. M., Takami, M., Chrysostomou, A., Drew, J., Eislöffel, J., Gosling, A., Gredel, R., Hatchell, J., Hodapp, K. W., Kumar, M. S. N., Lucas, P. W., Matthews, H., Rawlings, M. G., Smith, M. D., Stecklum, B., Varricatt, W. P., Lee, H. T., Teixeira, P. S., Aspin, C., Khanzadyan, T., Karr, J., Kim, H.-J., Koo, B.-C., Lee, J. J., Lee, Y.-H., Magakian, T. Y., Movsessian, T. A., Nikogossian, E. H., Pyo, T. S., & Stanke, T. 2011, MNRAS, 413, 480

García-Hernández, D. A., Manchado, A., García-Lario, P., Domínguez-Tagle, C., Conway, G. M., & Prada, F. 2002, A&A, 387, 955

Gledhill, T. M. & Forde, K. P. 2012, MNRAS, 421, 346

Huggins, P. J. 2007, ApJ, 663, 342

Kastner, J. H., Weintraub, D. A., Gatley, I., Merrill, K. M., & Probst, R. G. 1996, ApJ, 462, 777

Kelly, D. M. & Hrivnak, B. J. 2005, ApJ, 629, 1040

Le Bourlot, J., Pineau des Forêts, G., Flower, D. R., & Cabrit, S. 2002, MNRAS, 332, 985

Matsuura, M., Speck, A. K., McHunu, B. M., Tanaka, I., Wright, N. J., Smith, M. D., Zijlstra, A. A., Viti, S., & Wesson, R. 2009, ApJ, 700, 1067

O'Connell, B., Smith, M. D., Davis, C. J., Hodapp, K. W., Khanzadyan, T., & Ray, T. 2004, A&A, 419, 975

Sahai, R., Bujarrabal, V., Castro-Carrizo, A., & Zijlstra, A. 2000, A&A, 360, L9

Sahai, R., Hines, D. C., Kastner, J. H., Weintraub, D. A., Trauger, J. T., Rieke, M. J., Thompson, R. I., & Schneider, G. 1998, ApJ, 492, L163+

Sahai, R., Young, K., Patel, N. A., Sánchez Contreras, C., & Morris, M. 2006, ApJ, 653, 1241

Sánchez Contreras, C., Bujarrabal, V., Neri, R., & Alcolea, J. 2000, A&A, 357, 651

Sánchez Contreras, C., Sahai, R., Gil de Paz, A., & Goodrich, R. 2008, ApJS, 179, 166

Smith, M. D., Brand, P. W. J. L., & Moorhouse, A. 1991, MNRAS, 248, 451

Soker, N. & Rappaport, S. 2000, ApJ, 538, 241

Suárez, O., García-Lario, P., Manchado, A., Manteiga, M., Ulla, A., & Pottasch, S. R. 2006, A&A, 458, 173

Szczerba, R., Siódmiak, N., Stasińska, G., & Borkowski, J. 2007, A&A, 469, 799

Volk, K., Hrivnak, B. J., Su, K. Y. L., & Kwok, S. 2006, ApJ, 651, 294

Weintraub, D. A., Huard, T., Kastner, J. H., & Gatley, I. 1998, ApJ, 509, 728

Weston, S., Napiwotzki, R., & Catalan, S. 2011, in Asymmetric Planetary Nebulae 5 Conference, 29P

Glossary

AFGL	**A**ir **F**orce **G**eophysics **L**aboratory
AGB	**A**symptotic **G**iant **B**ranch
ALMA	**A**tacama **L**arge **M**illimeter **A**rray
ATCA	**A**ustralia **T**elescope **C**ompact **A**rray
Brγ	**B**rackett **G**amma
C	**C**arbon
CASPIR	**C**ryogenic **A**rray **SP**ectrometer/**I**mage**R**
CDR	**C**olumn **D**ensity **R**atio
CFHT	**C**anada-**F**rance-**H**awaii Telescope
CPL	**C**ommon **P**ipeline **L**ibrary
CSD	**C**ircum-**S**tellar **D**isk
CSE	**C**ircum-**S**tellar **E**nvelope
CTIO	**C**erro **T**ololo **I**nter-american **O**bservatory
DGE	**Dust**/**G**as **E**nvelope
DUPLEX	**DU**st-**P**rominet **L**ongitudinally **EX**tended
EDE	**E**quatorial **D**ensity **E**nhancement
ESO	**E**uropean **S**outhern **O**bservatory
FEL	**F**orbidden **E**mission **L**ine
FOV	**F**ield **O**f **V**iew

GB	**G**iant **B**ranch
GISW	**G**eneralized **I**nteracting **S**tellar **W**ind
H	**H**ydrogen
H_2	Molecular Hydrogen
HB	**H**orizontal **B**ranch
He	**H**elium
HH	**H**erbig **H**aro
HI	Atomic Hydrogen
HII	Ionised Hydrogen
HR	**H**ertzsprung-**R**ussell
HST	**H**ubble **S**pace **T**elescope
IFS	**I**ntegral **F**ield **S**pectroscopy
IFU	**I**ntegral **F**ield **U**nit
InSb	Indium antimonide is a narrow gap semiconductor material used in IR detectors, sensitive in the 1-5μm wavelengths
IRAF	**I**mage **R**eduction and **A**nalysis **F**acility
IRAS	**I**nf**R**ared **A**stronomical **S**atellite
IRSPEC	**I**nfra**R**ed **SPEC**trograph
ISM	**I**nter-**S**tellar **M**edium
ISO	**I**nfrared **S**pace **O**bservatory
ISW	**I**nteracting **S**tellar **W**ind
LGS	**L**aser **G**uide **S**tar
LGSF	**L**aser **G**uide **S**tar **F**acility
LIS	**L**ow **I**onisation **S**tructures
LRS	**L**ow **R**esolution **S**pectrometer

LSR	**L**ocal **S**tandard of **R**est
LWS	**L**ong **W**avelength **S**pectrograph
MACAO	**M**ultiple **A**pplication **C**urvature **A**daptive **O**ptics
MCMC	**M**arkov **C**hain **M**onte **C**arlo **M**odel
MHEL	**M**olecular **H**ydrogen **E**mission **L**ine
MPE	**M**ax-**P**lanck-Instituts für **E**xtraterrestrische Physik
NACO	**NA**os **CO**nica
NGS	**N**atural **G**uide **S**tar
NIC2	*see NICMOS*
NICMOS	**N**ear **I**nfrared **C**amera and **M**ulti-**O**bject **S**pectrometer
NIR	**N**ear **I**nfrared **R**ed (800nm - 2.5μm)
NTT	**N**ew **T**echnology **T**elescope
O	**O**xygen
OSCIR	**O**bservatory **S**pectrometer and **C**amera for the **I**nfra**R**ed
P-Cygni Profile	A combination of features in a star's spectrum that points to an outflow of material in the form of either an expanding shell of gas or a powerful stellar wind
PA	**P**osition **A**ngle
PAGB	**P**ost-**A**symptotic **G**iant **B**ranch
PAH	**P**olycyclic **A**romatic **H**ydrocarbon

PDR	**P**hoto-**D**issociation **R**egion
PN(e)	**P**lanetary **N**ebula(e)
PPN(e)	**P**roto-**P**lanetary **N**ebula(e)
PSC	**P**oint **S**ource **C**atalogue
PSF	**P**oint **S**pread **F**unction
SED	**S**pectral **E**nergy **D**istribution
SEST	**S**wedish-**E**SO **S**ubmillimetre **T**elescope
SINFONI	**S**pectrograph for **IN**tegral **F**ield **O**bservations in the **N**ear **I**nfrared
SOFI	**S**on **O**f **I**SAAC
SOLE	**S**tar-**O**bvious **L**ow-level **E**longated
SPAXEL	**SPA**tial pi**X**ture **EL**ement
SPIFFI	**SP**ectrograph for **I**nfrared **F**aint **F**ield **I**maging
SPIPE	**S**INFONI **PIPE**line
SSO	**S**iding **S**pring **O**bservatory
SWS	**S**hort **W**avelength **S**pectrograph
T-ReCS	**T**hermal-**Re**gion **C**amera **S**pectrograph
TIMMI	**T**hermal **I**nfrared **M**ulti-**M**ode **I**nstrument
TIMMI2	**T**hermal **I**nfrared **M**ulti-**M**ode **I**nstrument 2
UIST	**U**KIRT **I**mager **S**pectrometer
UKIRT	**U**nited **K**ingdom **I**nfrared **T**elescope
UT4	**U**nit **T**elescope 4
UV	**U**ltra**V**iolet
UVES	**U**ltraviolet and **V**isual **E**chelle **S**pectrograph

VISIR	**V**LT **I**mager and **S**pectrometer for the mid-**I**nfra**R**ed
VLT	**V**ery **L**arge **T**elescope
WD	**W**hite **D**warf
WFPC2	**W**ide-**F**ield **P**lanetary **C**amera
YPN(e)	**Y**oung **P**lanetary **N**ebula(e)

Appendix A: Useful python Programs

A.1 SINFONI Dark Line Removal

```
#!/usr/bin/python

def cleanLines(indir,outdir):

"""
This Routine cleans the dark lines from the VLT/SINFONI frames.
It takes 2 arguements:

1) The input directory (containing raw images)
2) The output directory (destination directory for processed images)

exmample usage (from command line) : python darkLineRemov.py raw/ cleaned/

NOTE :  The original code was written in IDL and provided by
ESO. It can be found in the SINFONI reduction cookbook (Appendix A)

NOTE2 : This program was adapted by Kieran Forde.
This was a very quick adaptation of the IDL code and
I'm sure it can be made to run faster. Please feel free
to upgrade it. I would appreciate it if you emailed me
any improvements just so I can upgrade my own verion.
Contact : k.forde(AT)herts.ac.uk

"""

# These modules should be standard on all systems no need to test for them
import os
import sys
```

```
import re
import string
import glob
# Test for numpy and pyfits modules to see if they are installed
try:
import pyfits
except ImportError:
print '*****************  The module pyfits is NOT installed  *****************'
sys.exit(1)

try:
import numpy
except ImportError:
print '*****************  The module numpy is NOT installed  *****************'
sys.exit(1)



dir='./'
dim=2048
width=4
nsigmaback=18

dir_in=indir+'/'
dir_out=outdir+'/'

# build the template mask for non illuminated edge pixels (background
# pixels)
# Here I have to _NOT_ subtract the 1 from the high end of the array
# because python replaces everything less than the high end of the selection
# whereas IDL replaces everything including the high end value
mask_back=numpy.zeros((dim,dim),dtype=int)
mask_back[width:dim-width,0:width]=1
mask_back[width:dim-width,dim-width:dim]=1
# define subscripts of background pixels
# I am doing this to mimic the IDL 'where' command ...
# this command flattens 2-d arrays in this manner
```

```
backposY = numpy.where(mask_back == 1)
backpos = numpy.where(mask_back == 1,1,0)
backpos_array = numpy.ndarray.flatten(backpos)
# reason for diffeerence in the values in backpos is
# because of the way IDL and python handle rounding
# define y position of back pixels
ybackpix = backposY[0]

# read list of raw data files and produce corresponding cleaned image
filextn = glob.glob(dir_in+'*.fits')
for item in filextn:
# read input file
im = pyfits.open(item)
# read input file and save unmodified images
im1 = im[0].data
# get the header info
hhddrr=pyfits.getheader(item)
# reset the background mask
backpix = numpy.compress(backpos_array,im1)
# search for back pixels too deviant
diffbackpix = backpix-numpy.median(backpix)
#Calculate the Median
# split into chunks of 3
chunk_size=3
med_array=[]
i=0
while i < len(diffbackpix)-1 :
if len([diffbackpix[i],diffbackpix[i+1],diffbackpix[i-1]]) == chunk_size:
med = numpy.round(numpy.median([diffbackpix[i],diffbackpix[i+1],diffbackpix[i-1]]),4)
med_array.append(med)
i+=1
# Here we are just appending on the final element of the array seeing as it
# won't have an item x+1 to do a median with ... we just leave it as is
med_array.append(diffbackpix[-1])

sigmaback = numpy.std(med_array)
```

```
bad = numpy.where(numpy.abs(diffbackpix) > nsigmaback*sigmaback)
cntbad = numpy.shape(bad)
# If there is bad pixels
if cntbad[1] > 0:
# define background median value of good back pixels
ybad = ybackpix[bad]
good = numpy.where(abs(diffbackpix) <= nsigmaback*sigmaback)
medvalue = numpy.median(backpix[good])
yprev = -1
for k in range(0,int(cntbad[1])-1):
yval=ybad[k]
if yval != yprev :
yprev=yval
kline = [im1[yval,0:width],im1[yval,dim-width:dim]]
kline_mean=numpy.sum(kline)/(2.0*width)
im1[yval,width:dim-width]=im1[yval,width:dim-width]+kline_mean-medvalue
# Get the proper name of the data frame without the ./raw/ in front of it
item_split = string.split(item,'/')
# Write the image plus original header to the data
pyfits.writeto(dir_out+item_split[-1],im1,hhddrr)
im.close()
print item_split[-1]+' ..... Completed\n'



if __name__ == '__main__':

# These modules should be standard on all systems no need to test for them
import os
import sys
import re
import string
import glob
# Test for numpy and pyfits modules to see if they are installed
try:
import pyfits
except ImportError:
```

```
print '*****************  The module pyfits is NOT installed  *****************'
sys.exit(1)

try:
import numpy
except ImportError:
print '*****************  The module numpy is NOT installed  *****************'
sys.exit(1)

if len(sys.argv) != 3:
print cleanLines.__doc__
print "****** ---> Not enough arguments given ... see above     doc.string <--- ******"
sys.exit(1)
cleanLines(sys.argv[1],sys.argv[2])
```

A.2 Gaussian Convolution of Spectra

```
from numpy import *
import scipy
import scipy.interpolate
import sys

def gconv(x, y, fwhm,  ppr=3, nsigma=None, inter=None, original=None):
   """
   Gaussian convolution

   IN: x -fltarr independent variable
    y -fltarr array of data to smooth
    fwhm -float FWHM of the Gaussian kernel (pixels)

   OUT: nx -fltarr new sampled x-axis
    ny -fltarr smoothed data
```

```
KEYWORDS: ppr -integer pixels per resolution element
 (default  is ppr=3)

   nsigma -float how far the convolution goes

   inter   if set, the x-axis is interpolated
 to force a constant step; if the step
 already constant, 'inter' will have no
 effect

   original if set, the original sampling is kept
 for the output arrays, unless inter is
 also set and an interpolation is
 performed, in which case, the output
 x-axis  will just have the same
 number of points as the input x, but
 resampled to constant step.

EXAMPLES:  1) Smooth an input spectrum with a Gaussian of FWHM=2.0 AA
 assuming the spectrum is given on a uniform (linearly sampled)
 wavelength scale with a step of 0.1 AA.

 IDL> fwhm=2.0/0.1
 IDL> gconv,w,f,fwhm,w2,f2

    2) Smooth the same spectrum with a Gaussian of FWHM=50. km/s

 IDL> step=(max(alog(w))-min(alog(w)))/n_elements(w)
 IDL> fwhm=50./299792.458/step
 IDL> gconv,alog(w),f,fwhm,w2,f2,/inter

 Because of the keyword inter, the spectrum will be internally
 interpolated to a step in ln (w) of
 step=(max(alog(w))-min(alog(w)))/n_elements(w)
 Then the 50 km/s (or V/c = 0.000166782) is equivalent to
```

```
    50./299792.458/step pixels.

   C. Allende Prieto, Univ. of Texas, March 2006

   # ------------------------------------------------------------------------------------------
   Typical procedure:

   1) resample the high-res spectra to your wavelength range.
    >>>
   2) run :
      # fwhm = res_of_your_spectra_Angstroms e.g 7.5 / delta_step of model spectra e.g 3.99e-2
# fwhm = 187
    >>> hg = gconv.gconv(wav,flux, 187, ppr=3, inter=True, original=True)
# or in microns
# if you've resampled first to make the model spectrum the same as your spectrum
# then the calc is: 7.5 Ang / 2.45 A = 3
>>> hg = gconv.gconv(wavmic,flux, 3, ppr=3, inter=True, original=True)

# To resample do:
>>> import scipy.interpolate as sint
>>> fin = numpy.loadtxt('atmos_k_band.txt')
>>> wav = fin[:,0]
>>> flux = fin[:,1]
>>> wavmic = wav / 1e4
>>> f = sint.interp1d(wavmic,flux)
>>> xnew = numpy.linspace(1.928295, 2.471705, 2218)
>>> ynew = f(xnew)
>>> hg = gconv.gconv(xnew,ynew,3,original=True)
>>> plot(hg[3], hg[4])
>>> plot(xnew,ynew)

Or I find it better to do ... as it gets the same number of pixels in the output as the input.
>>> import scipy.interpolate as sint
>>> fin = numpy.loadtxt('atmos_k_band.txt')
>>> wav = fin[:,0]
>>> flux = fin[:,1]
```

```
>>> wavmic = wav / 1e4
>>> hg = gconv.gconv(wavmic,flux,187.5,original=True)
>>> f = sint.interp1d(hg[3],hg[4])
>>> xnew = numpy.linspace(1.928295, 2.471705, 2218)
>>> ynew = f(xnew)
>>> plot(hg[3], hg[4])
>>> plot(xnew,ynew)
```

```
   # ------------------------------------------------------------------------------------------#

   """

   n_params = 5
   _opt = (ppr, nsigma, inter, original)
   def _ret():
      _optrv = zip(_opt, [ppr, nsigma, inter, original])
      _rv = [x, y, fwhm, nx, ny]
      _rv += [_o[1] for _o in _optrv if _o[0] is not None]
      return tuple(_rv)



   #initialize
   tol = 1e-3
   nx = 0.0
   ny = 0.0
   if (inter is not None):
      nel = array(x, copy=0).shape
      xinput = x
      yinput = y
      minx = array(x, copy=0).min()
      step = (max(x) - minx) / nel
      ftmp = scipy.interpolate.interp1d(xinput, yinput)
      x = arange(nel[0]) * step + minx
      y = ftmp(x)
      #y = interpol(yinput, xinput, x)
```

```
   else :
      #checking that the input x is evenly sampled
      nel = array(x, copy=0).shape # nel input pixels
      #step = abs(x - shift(x, 1))
      step = abs(x - roll(x, 1))
      if max(step[1:(nel[0])] / x[0:nel[0]-1]) > tol:
         #not linearly spaced, maybe logarithmically
         lx = log10(x)
 step = abs(lx - roll(lx, 1))
         #step = abs(lx - shift(lx, 1))
         if max(step[0:(nel[0] - 1)+1] / lx) > tol:
            print 'not log spaced, cannot handle it without interpolation'
            return _ret()

   #set default params
   if bitwise_not((ppr is not None)):
      ppr = 3      #sample output function with ppr
   #points per FWHM
   if bitwise_not((nsigma is not None)):
      nsigma = 3.0 #how far the convolution goes
   #Gaussian kernel ; units are pixels
   sigma = fwhm / 2.0 / sqrt(-2. * log(0.5)) # equivalent sigma for kernel
   grange = floor(nsigma * sigma) # range for kernel (-range:range)
   psf = psf_gaussian(npix=2 * grange + 1, fwhm=fwhm, normalize=True)

   #select output x-axis
   if (original is not None):
      #keep input sampling on output arrays
      sampling = arange(nel[0])
   else :
      rate = int(floor(fwhm) / ppr) # 1/rate pixels will be kept
#      tmpind = []
#      ident = 0
#      aaa = (arange(nel[0]) / rate) - rate / 2
#      while ident < len(unique(aaa)) :
#       tmp1 = (searchsorted(aaa,unique(aaa)[ident],'right')-1)
```

```
# tmpind.append(tmp1)
# ident+=1
      sampling = uniq(arange(nel[0]) / rate) - rate / 2

   #trim edges
   wtrim = where(ravel(bitwise_and(sampling > grange, sampling < nel[0] - grange)))[0]
   if max(wtrim) <= 0:
      print 'The Gaussian is too wide for the input range'
      return _ret()
   sampling = sampling[wtrim]
   print sampling
   print len(sampling)
   nx = x[sampling] # new x-axis
   nel2 = array(nx, copy=0).shape # nel2 output pixels
   ny = zeros([nel2[0]], dtype=float32)

   #convolve
   for i in arange(0, nel2[0]):
      ny[i] = sum(psf * y[sampling[i] - grange:(sampling[i] + grange)+1], axis=0)

   #return the original values of x and y if resampled
   if (inter is not None):
      x = xinput
      y = yinput



   return _ret()



def uniq(data):
'''
Took this from mmath.py in /home/kforde/prog
Remove the duplicate value per returning one index for each value.
ee numpy.unique.
'''
data = array(data)
```

```
#Sort by frequency
idsort = argsort(data)
data_sorted = data[idsort]
#Remove duplicate frequency.
#Add a disctinct element since the prcedure selects only the
#last element of each serie. Hence, the last SERIE
#of the array is not taken into account.
data_sorted = r_[data_sorted, data_sorted[-1]+1]
id_uniq_sorted = nonzero(data_sorted[1:]-data_sorted[0:-1])
return sort(idsort[id_uniq_sorted])
```

```
def psf_gaussian(npix, fwhm, normalize=True):
"""
Works as IDL 1-d psf_gaussian does. Tested Jan 31 2013, K.Forde
"""

# Initialize PSF params
cntrd = (npix - 1.0) * 0.5
st_dev = 0.5 * fwhm / sqrt( 2.0 * log(2) )

# Make PSF
i = arange(npix)
psf = array( [exp(-(((x-cntrd)/st_dev)**2)/ 2.) for x in i] )

# Normalize
if normalize:
  psf /= psf.sum()

return psf
```

Appendix B: Reference Material

Table B.1: List of all PPNe with H_2.

Name		
OH 231.8+4.2*†	*IRAS* 16559-2957	*IRAS* 19016-2330
AFGL 2688	*IRAS* 16594-4656	*IRAS* 19200+3457
IRAS 04395+3601	*IRAS* 17150-3224	*IRAS* 19306+1407
IRAS 06556+1623*	*IRAS* 17311-4924	*IRAS* 19336-0400△
IRAS 10178-5958*	*IRAS* 17441-2411	*IRAS* 19374+2359
IRAS 10197-5750	*IRAS* 18062+2410	*IRAS* 19500-1709
IRAS 14331-6435	*IRAS* 18379-1707	*IRAS* 20028+3910
IRAS 16342-3814†	*IRAS* 18276-1431†	*IRAS* 20462+3416
IRAS 22036+5306†	*IRAS* 22574+6609	*IRAS* 22023+5249

△ Removed from the list in Kelly & Hrivnak (2005) due to be presence of Balmer line emission.
† Added to the list in Kelly & Hrivnak (2005).
* Added to the PPNe in Szcerba et al., (2007).

Table B.2: A list of important H_2 lines observable with SINFONI.

Line	Wavelength (μm)	Frequency (cm^{-1})	g(J)	E_{upper} K	A 10^{-7} s
1→0 S(0)	2.2235	4497.41	5	6471	2.53
1→0 S(1)	2.1218	4712.91	21	6956	3.47
1→0 S(2)	2.0338	4917.01	9	7584	3.98
1→0 S(3)	1.9576	5108.40	33	8365	4.21
1→0 Q(1)	2.4066	4155.25	9	6149	4.29
1→0 Q(2)	2.4134	4143.47	5	6471	3.03
1→0 Q(3)	2.4237	4125.87	21	6956	2.78
1→0 Q(4)	2.4375	4102.57	9	7586	2.65
1→0 Q(5)	2.4548	4073.72	33	8365	2.55
2→1 S(0)	2.3556	4245.15	5	12095	3.68
2→1 S(1)	2.2477	4448.95	21	12550	4.98
2→1 S(2)	2.1542	4642.04	9	13150	5.60
2→1 S(3)	2.0735	4822.82	33	13890	5.77
2→1 S(4)	2.0041	4989.84	13	14764	5.57
3→2 S(0)	2.5014	3997.73	5	17387	3.88
3→2 S(1)	2.3864	4190.33	21	17818	5.14
3→2 S(2)	2.2870	4372.49	9	18386	5.63
3→2 S(3)	2.2014	4542.57	33	19086	5.63

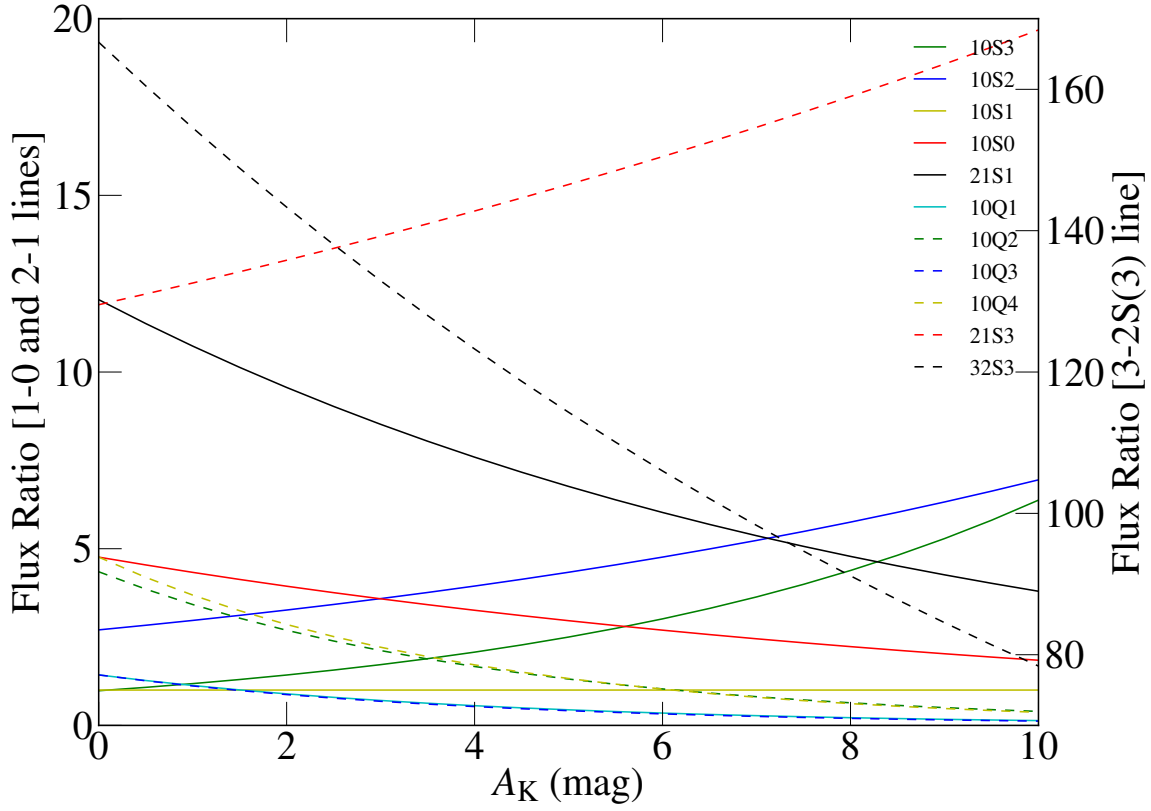

Fig. B.1: The effect of extinction on the ratio of the K-band H_2 lines to the 1→0S(1) line. Data is for an LTE gas at 2000 K.

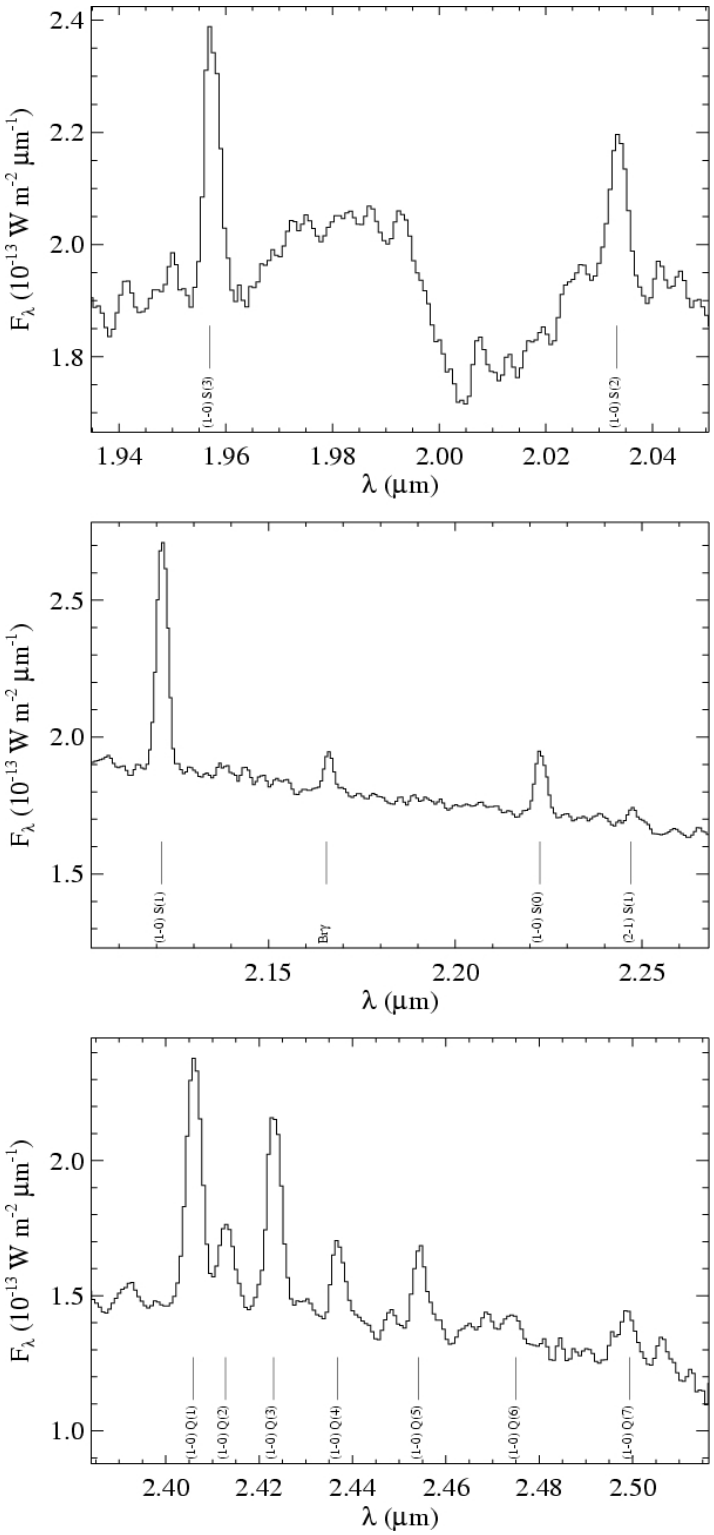

Fig. B.2: A portion of the K-band spectrum from van de Steene (2003). Note there is no obvious Mg II emission at 2.1375 μm.

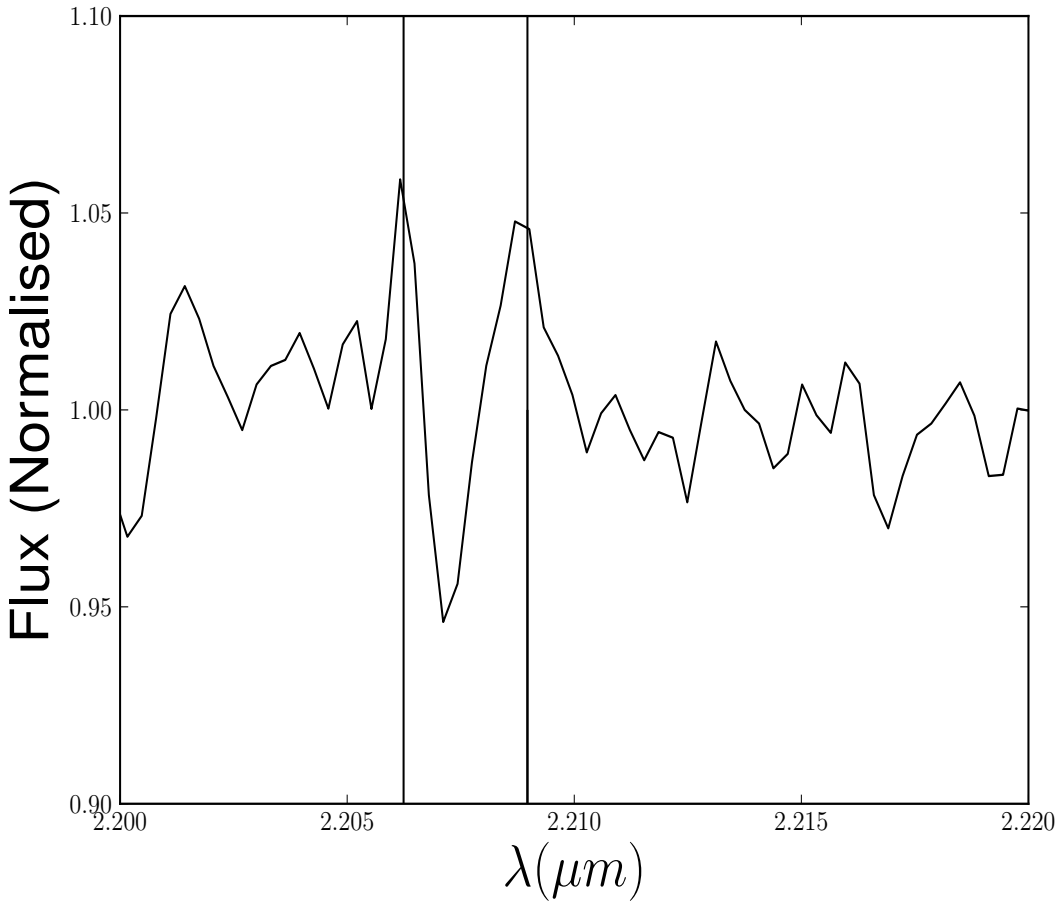

Fig. B.3: Spectrum of *IRAS* 17150-3224showing some points above the continuum at 2.2 µmgives a tentative suggestion of the presence of the Na I doublet (lines indicate theoretical location of doublet). The data for this plot was provided by B. Hrivnak (private communication).

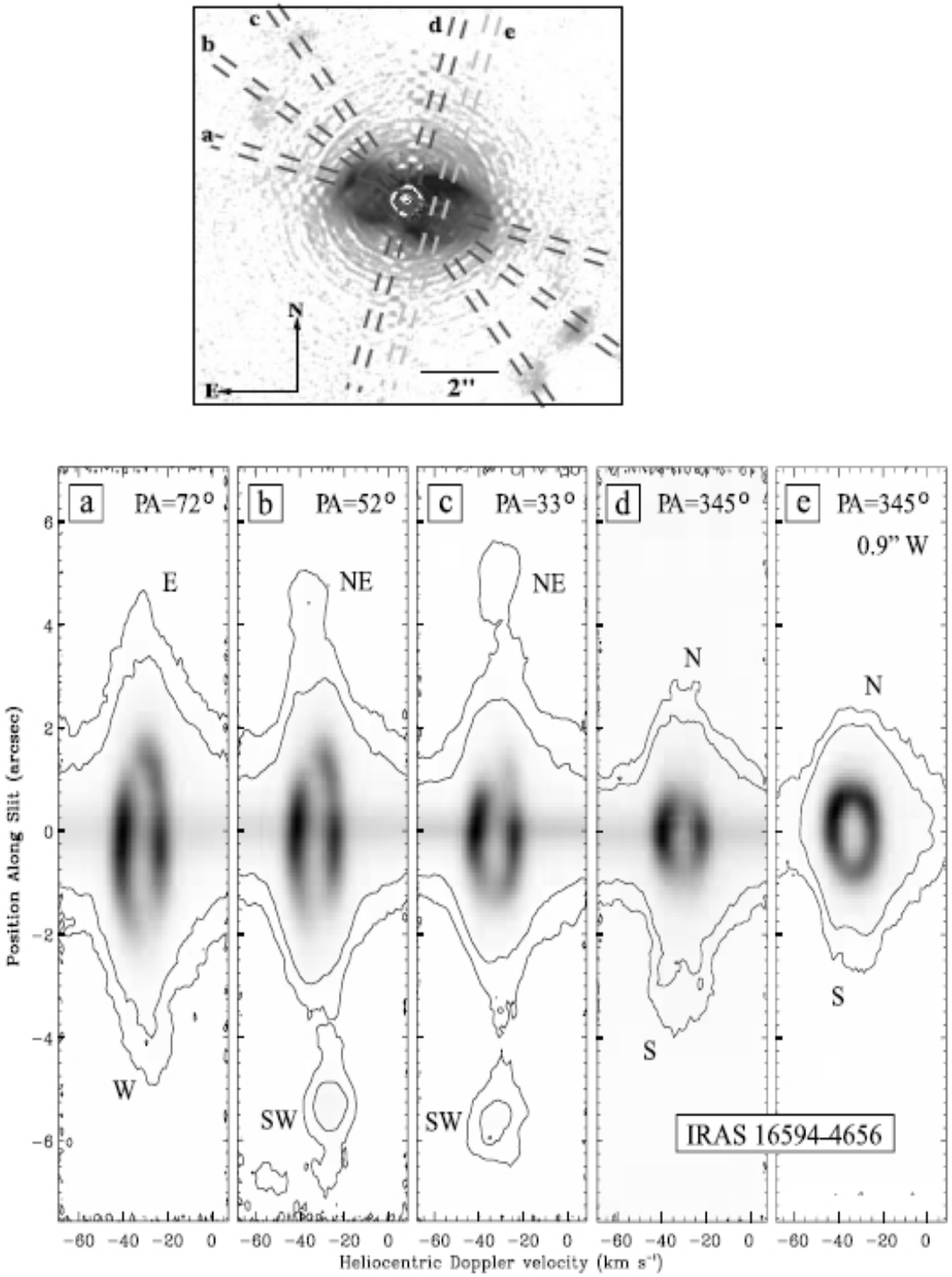

Fig. B.4: (*top*) H_2 image with the slit positions overlaid. Labelling corresponds to the PV diagrams below. (*bottom*) H_2 PV diagram of *IRAS* 16594-4656. Panels (a)-(e) correspond to the different slit positions. Images from Hrivnak et al. (2008).

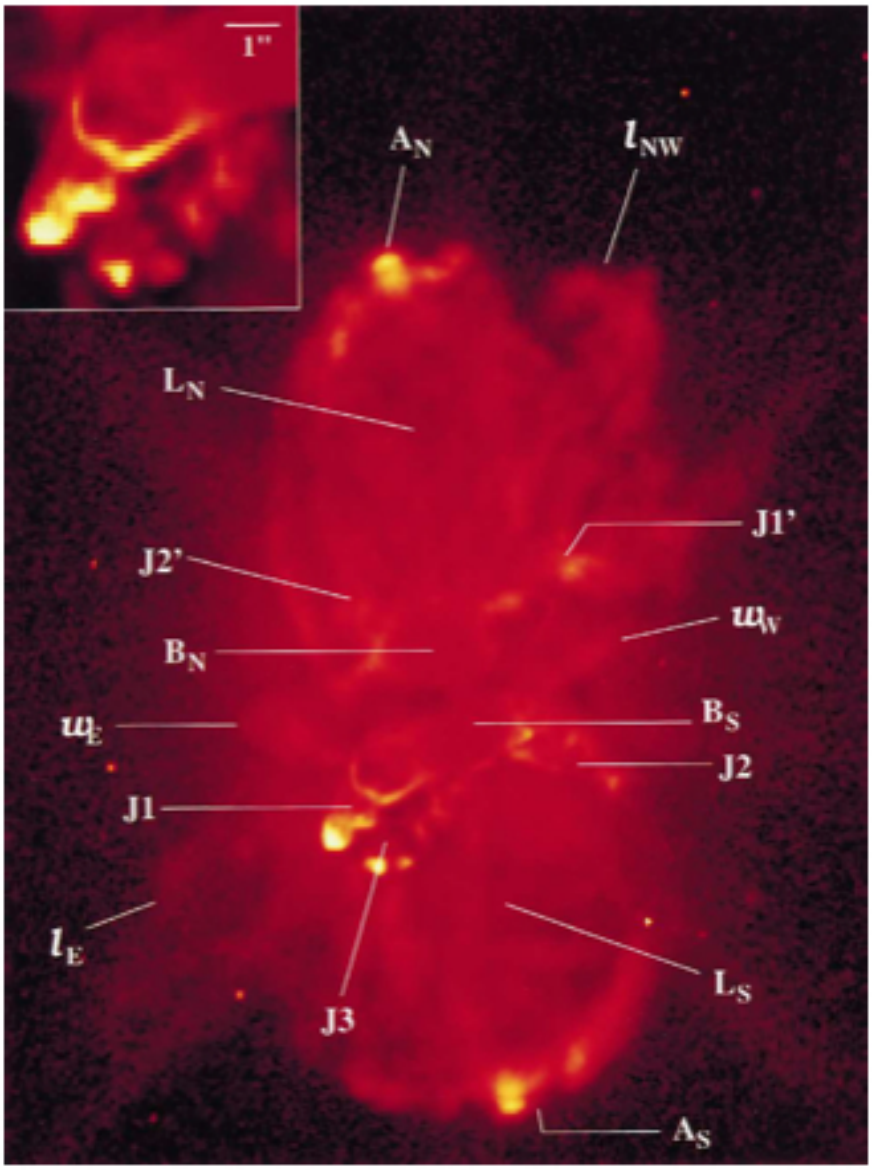

Fig. B.5: False-colour image of Frosty Leo (*IRAS* 09371+1212). Inset shows expanded view of Jets J1 and J3. Image from Sahai et al. (2000).

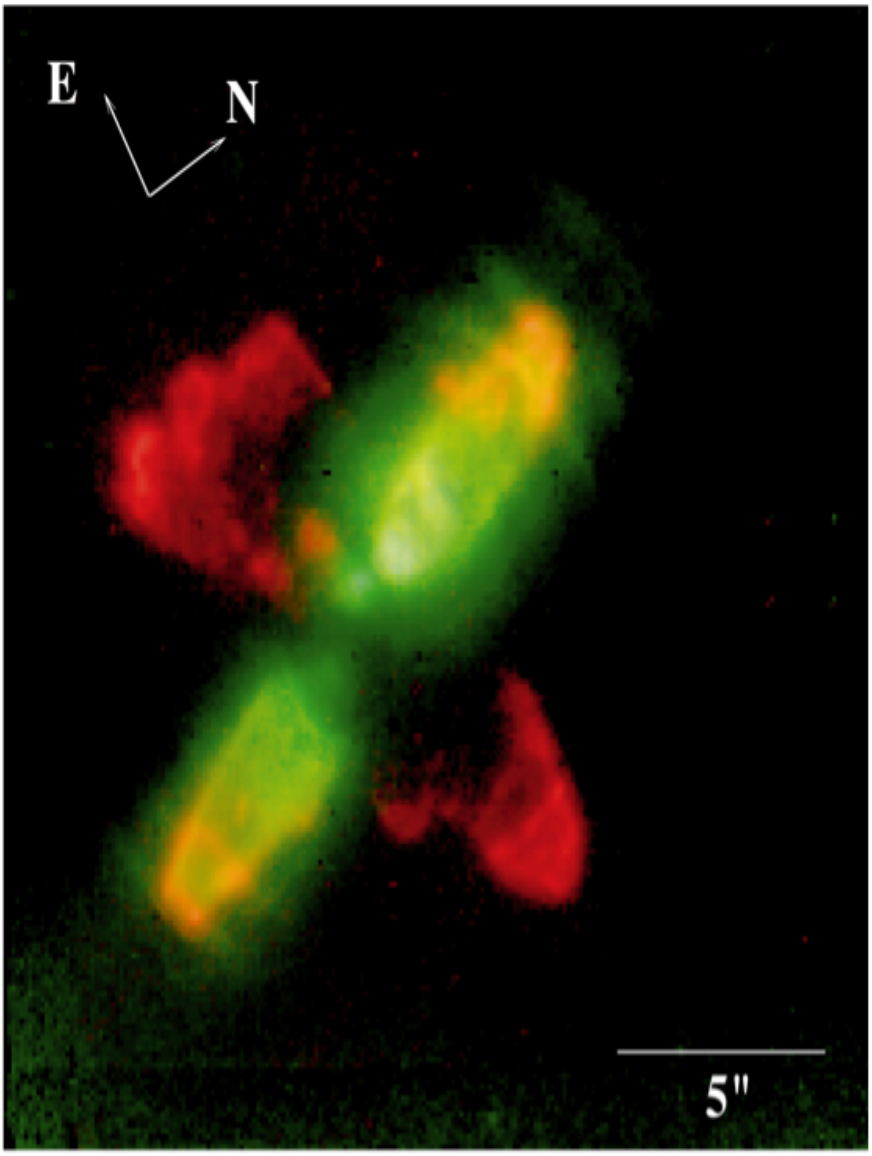

Fig. B.6: H_2 1→0S(1) line emission (red) and nearby 2.15 μm continuum intensity (green) in CRL 2688. Image from Sahai et al. (1998).

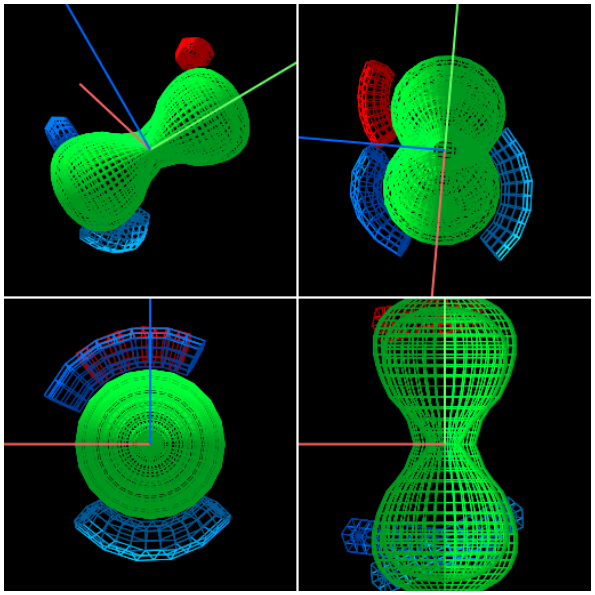

Fig. B.9: Different views of the 3-dimensional mesh

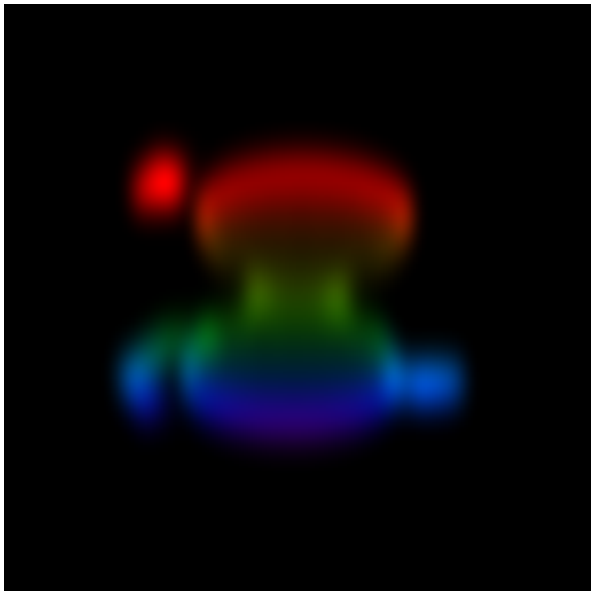

Fig. B.8: Position-velocity diagram

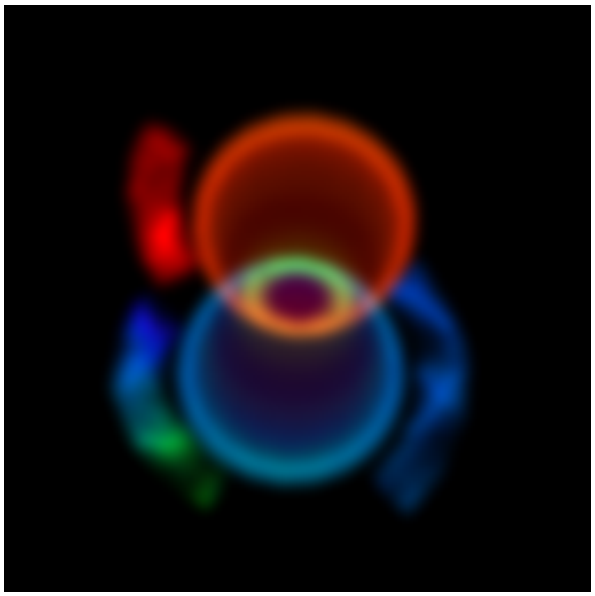

Fig. B.7: A 2-dimensional view of the nebula

Index